School of Science and Computing

Oxidative Dissolution of Chalcopyrite in Ferric Media: An X-ray Photoelectron Spectroscopy Study

Andrew Donald Parker

This thesis is presented for the Degree of

Doctor of Philosophy

of

Curtin University of Technology

August 2008

Declaration

To the best of my knowledge and belief this thesis contains no material previously published by any other person except where due acknowledgement has been made. This thesis contains no material which has been accepted for the award of any other degree or diploma in any university.

Andrew Donald Parker

Publications

Klauber, C., A. Parker, W. van Bronswijk, and H. R. Watling, (2001). Sulphur speciation of leached chalcopyrite surfaces determined by X-ray photoelectron spectroscopy. *International Journal of Mineral Processing. 62*(1-4), 65-94.

Parker, A., C. Klauber, A. Kougianos, H. R. Watling, and W. van Bronswijk (2003). An x-ray photoelectron spectroscopy study of the mechanism of chalcopyrite leaching. *Hydrometallurgy. 71*(1-2), 265-276.

Acknowledgements

I acknowledge the efforts of Prof. Wilhelm van Bronswijk (Curtin University of Technology), Dr. Craig Klauber (CSIRO Minerals) and Ms. Felicia Lee (Curtin University of Technology).

The X-ray photoelectron spectrometer was provided by CSIRO Minerals (Waterford).

Financial support was provided by Curtin University of Technology and the Parker Cooperative Research Centre for Integrated Hydrometallurgy Solutions for 3.5 years and by a friend and a family member for 7 years.

Abstract

The oxidative dissolution of chalcopyrite in ferric media often produces incomplete copper recoveries. The incomplete recoveries have been attributed to inhibition caused by the formation of a metal deficient sulphide and the deposition of elemental sulphur and jarosite. Although these phases have been qualitatively identified on the surface of chalcopyrite, none have been quantitatively identified. The aim of the project was to quantitatively analyse the surface before and after oxidative dissolution, with X-ray photoelectron spectroscopy (XPS), and to use the phases identified as the basis for mechanisms of dissolution and inhibition.

XPS analysis was performed on chalcopyrite massive fractured under anaerobic atmosphere and chalcopyrite massive and concentrate oxidised in 0.1 M ferric sulphate (pH 1.9) and 0.2 M ferric chloride (pH 1.6) at 50, 65 and 80°C. Quantitative XPS analysis of the chalcopyrite surfaces required the development of programs that accounted for the observed XPS spectra. The output of these programs was used to construct profiles of the chalcopyrite surfaces and the deposited phases. These surface profiles were correlated with copper recoveries determined for chalcopyrite concentrate dissolution under the same conditions.

The surface of chalcopyrite before oxidative dissolution reconstructs to form a 'pyritic' disulphide phase. This phase is oxidised in ferric media to form thiosulphate via the incorporation of oxygen atoms from the hydration sphere. The thiosulphate reacts in the oxidising conditions of low pH to form elemental sulphur, sulphite and sulphate. The sulphate complexes with ferric to produce hydronium jarosite. This reaction occurs at the surface during the initial stages of dissolution and in the bulk solution during the

latter stages. This precipitation of hydronium jarosite during the latter stages of dissolution corresponds to inhibition of the dissolution reaction. It is therefore concluded hydronium jarosite is responsible for inhibiting the oxidative dissolution of chalcopyrite in ferric media.

The identification of hydronium jarosite as the inhibiting phase is consistent with the industrial practice of removing 'excess' iron from the ferric solution before oxidative dissolution. However, additional iron and sulphate are generated at the chalcopyrite surface during oxidative dissolution. These high iron and sulphate concentrations combine with the low pH and high temperatures favoured for the oxidative dissolution of chalcopyrite to produce ideal conditions for jarosite precipitation. Therefore, pH must be lowered further to prevent jarosite precipitation and enhance copper recoveries from chalcopyrite in ferric media.

Table of Contents

List of Figures

List of Tables

Chapter 1

Introduction

Chalcopyrite is often processed hydrometallurgically because of the high quality of copper produced and the economic viability of processing low grade ores (Wallis and Chlumsky, 1999). Hydrometallurgical processing of low grade ores can be performed in heaps or dumps on-site, while processing of high grade ores can be performed in stirred tank reactors off-site. The lixiviant commonly used is sulphuric acid; however, extraction rates are improved by the use of an oxidant (Dutrizac and MacDonald, 1974).

The most commonly used oxidant for extracting copper from chalcopyrite is a ferric medium in the form of either ferric sulphate or ferric chloride. Ferric sulphate has a number of advantages, but one major drawback. The principal advantage of ferric sulphate is the ability to use microbes to regenerate the ferric ions. This is because microbes have a high tolerance for sulphate but a low tolerance for chloride (Brierley and Brierley, 1999). Microbes enable ferric sulphate to be used for processing low grade ores, which increases the amount of ore that can be processed economically. Ferric sulphate solutions are also less corrosive on equipment and produce higher quality copper from electrowinning (Roman and Benner, 1973; Wallis and Chlumsky, 1999). However, ferric sulphate solutions incur either incomplete copper recoveries or lengthy residence times (Letowski, 1979). The incomplete recoveries in ferric sulphate have been attributed to inhibition of oxidative dissolution (Munoz et al., 1979).

Inhibition has been attributed to three principal phenomena: alteration of the chalcopyrite surface; deposition of phases onto the chalcopyrite surface; and variation of the solution potential at the chalcopyrite surface. The alteration of the chalcopyrite surface involves the preferential dissolution of iron to produce a metal deficient sulphide that dissolves at a slower rate than chalcopyrite (Baur et al., 1974). The commonly cited alternative to inhibition by metal deficient sulphide formation is the deposition of oxidation product phases onto the chalcopyrite surface. These phases include elemental sulphur, polysulphides and jarosites. Although they have all been qualitatively identified on the surface of chalcopyrite using X-ray photoelectron spectroscopy, none have been confirmed quantitatively (Buckley and Woods, 1984; Mikhlin et al., 2004; Sandstrom et al., 2005). Therefore, the presence and inhibiting ability of these phases remains unresolved. Inhibition of dissolution has also been attributed to changes in solution potential, with low dissolution rates observed at high solution potentials (Kametani and Aoki, 1985). Although alteration of the chalcopyrite surface, phase deposition, or solution potential could each affect dissolution rates, it is possible a combination of these phenomena is responsible for inhibiting dissolution.

Improving copper extraction from the hydrometallurgical processing of chalcopyrite in ferric media requires an understanding of the mechanisms of dissolution and inhibition. The mechanisms should be based on the phases identified by quantitative surface analysis of chalcopyrite before and after dissolution. The surface coverage and deposition rate of these phases should be correlated with kinetics data to establish the phase responsible for inhibition. The kinetics analysis should also investigate the importance of solution potential on dissolution rates. The implications of the mechanisms on the oxidative dissolution of chalcopyrite in ferric media in general, and in microbially assisted systems in particular, can then be discussed.

Chapter 2

Literature review

2.1 Chemical and physical properties of chalcopyrite

The chemical and physical properties of chalcopyrite have been reviewed to assist interpretation of kinetic data acquired during oxidative dissolution and surface analysis data acquired before and after oxidative dissolution.

2.1.1 Stoichiometry and oxidation states

Chalcopyrite is composed of copper, iron and sulphur in a ratio of 1:1:2 and oxidation states of (I), (III) and (-II), respectively. The oxidation states of copper and iron have been confirmed by magnetic moment determinations, with copper and iron displaying moments of 0 and 3.85 μ_B, respectively (Donnay et al., 1958). The moment for iron is lower than the 5.0 μ_B expected for iron (III) because the moments are ordered by the bridging sulphur atoms (Hall and Stewart, 1973). The oxidation states of copper and iron have been confirmed further by Mössbauer and X-ray photoelectron spectroscopies (Raj et al., 1968; Klauber, 2003).

2.1.2 Bulk and surface structures

The chalcopyrite bulk structure is derived from the zinc-blende structure, with the zinc atoms replaced by iron and copper atoms (Figure 2.1)(Hall and Stewart, 1973). The copper and iron atoms are each bonded to four sulphur atoms and the cubic symmetry of the zinc blende structure is replaced by tetragonal symmetry. The symmetry changes because the differing metal radii cause the sulphur to move towards the iron and away from the copper (Fe-S 2.257 Å, Cu-S 2.302 Å). The chalcopyrite structure has bond angles of 109.47° (S-Fe-S), 111.06° and 108.68° (S-Cu-S) that leave the iron perfectly tetrahedral but the copper distorted along the z-axis (Hall and Stewart, 1973).

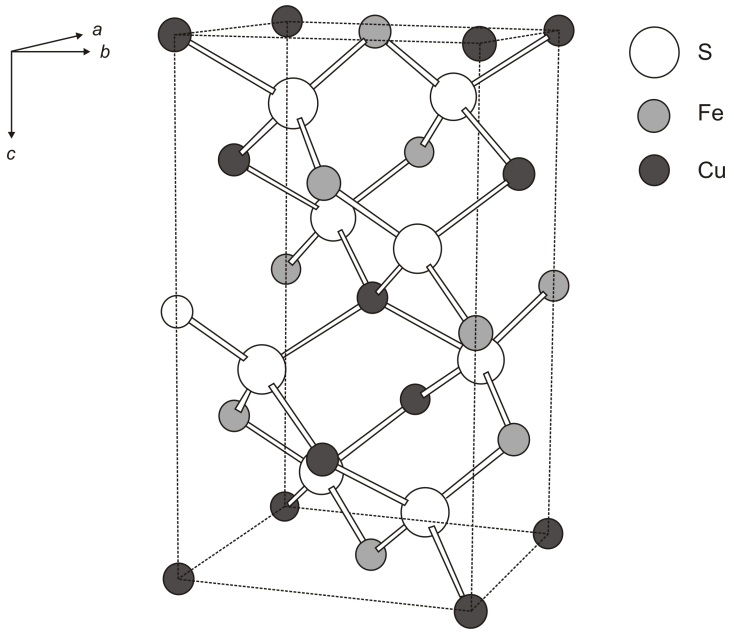

Figure 2.1: *Chalcopyrite bulk structure (Hall and Stewart, 1973).*

The chalcopyrite surface structure differs from the bulk structure because of reconstruction. The chalcopyrite surface reconstructs to form a 'pyritic' phase $FeS_2.0.5Cu_2O$, as described by Klauber (2003). This phase is analogous to pyrite but has only 50% of the density of naturally occurring pyrite. The pyrite structure is derived from the sodium chloride structure, with iron atoms replacing the sodium atoms and sulphur atoms re-

placing the chloride ions. The iron is bonded to six sulphur atoms in a slightly distorted octahedral coordination (Hyde and O'Keefe, 1996). The 'pyritic' phase forms on the surface of chalcopyrite as the chalcopyrite (001) face reconstructs to adopt a similar arrangement to the pyrite (100) face (Klauber, 2003). This reconstruction requires the sulphur ions above and below the cation plane in the chalcopyrite (001) face to shift 2.20 and 1.25 Å, respectively, while the iron atoms only require minor shifts because of the similarity of the surface unit dimensions for the pyrite (100) and chalcopyrite (001) faces (5.418 and 5.289 Å, respectively) (Klauber, 2003).

2.1.3 Semiconductor properties and band structures

Chalcopyrite is an extrinsic semiconductor with either impurities or metal substitution imparting conduction because of an excess of electrons (n-type) or a deficiency of electrons (p-type)(Pridmore and Shuey, 1976). Most natural chalcopyrite samples are n-type, although p-type have also been identified (Austin et al., 1956; Pridmore and Shuey, 1976; McMillan et al., 1982). The semiconductor type of chalcopyrite is often the result of metal substitution, with p-type produced by iron substituting for copper and n-type produced by copper substituting for iron. Metal substitution is estimated to be $\sim$ 0.1 % based on the range of resistivities of a suite of natural samples (0.26 - 1.9 $\times$ 10^{-3} ohm per metre) determined by Pridmore and Shuey (1976).

The band structure of the chalcopyrite bulk is complex because of the lack of symmetry inherent with tetragonal coordination. Self consistent charge calculations have determined the upper valence band is composed of Cu 3d, Fe 3d and S 3p orbitals, while the conduction band is composed of Cu 4s, Fe 4s, Fe 4p and S 3p orbitals (Hamajima et al., 1981). Additional Fe 3d orbitals reside in the forbidden energy gap between the valence and conduction bands, with minor admixture of S 3p orbitals; although it is not stated by Hamajima et al. (1981), the tetragonal coordination implies the Fe 3d (t_{2g}) orbitals reside in the valence band and the Fe 3d (e_g) orbitals reside in the forbidden energy gap. The presence of orbitals within the forbidden energy gap introduces a second adsorption edge for chalcopyrite: one occurs at 0.6 eV for the transfer of electrons

between the valence band and the Fe 3d (e_g) orbitals in the forbidden energy gap and another occurs at 3.2 eV for the transfer of electrons between the valence band and the conduction band (Oguchi et al., 1980). The lower adsorption edge (0.6 eV) corresponds to the commonly cited band gap of chalcopyrite (Oguchi et al., 1980).

The band structure of the chalcopyrite surface is analogous to the band structure of pyrite because of the 'pyritic' reconstruction phase. Self consistent charge calculations have determined the upper valence band of pyrite is composed of Fe 3d (t_{2g}) and S 3p orbitals, with minor admixture of S 3d orbitals, while the conduction band is composed of Fe 3d (e_g), S 3p and S 3d orbitals (Eyert et al., 1998). Although the Fe 3d orbitals are the predominant contributor to the upper valence band, the S 2p orbitals also contribute (Opahle et al., 1999). The contribution of both iron and sulphur orbitals to the upper valence band suggests either element may be oxidised.

2.2 Oxidative dissolution of chalcopyrite

The oxidative dissolution of chalcopyrite depends on the interaction of the atoms and band structure of the surface with water molecules and ferric ions.

2.2.1 Interfacial structure of chalcopyrite before oxidative dissolution

The chalcopyrite surface is hydrated in aqueous solutions to neutralise the surface charge. Chalcopyrite is neutralised below pH 2 (Bebie et al., 1998), which implies the surface is negatively charged and therefore dominated by protonated sulphur atoms.

The surface charge also affects the potential energies of the valence and conduction bands. The incomplete bonding at the surface increases the potential energies of the valence and conduction bands. This increase in energy is known as band bending and the associated region is known as the space charge region (Morrison, 1977). The extent of band bending is the potential difference (V_s) between the bulk and the surface and can be considered a measure of the activation energy required to transfer an electron

from the bulk to the surface (Figure 2.2). The extent of bending is influenced further by factors that alter the amount of charge present in the space charge region, including the semiconductor type of the mineral, the pH of the solution, and the potential energies of the species in solution. The amount of charge present in the space charge region is also altered as charge is transferred during oxidative dissolution (Morrison, 1977).

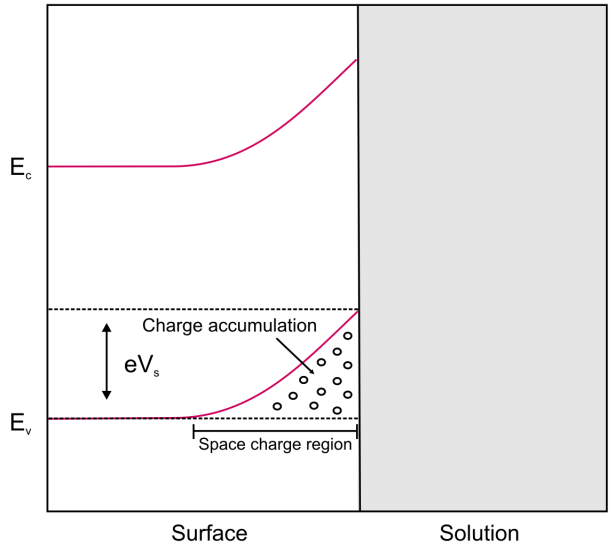

Figure 2.2: *Band bending of the mineral surface in vacuo, with an accumulation of charge at the surface. The figure is adapted from Morrison (1977).*

2.2.2 Interfacial structure of chalcopyrite during oxidative dissolution

The band structure of the surface influences the rate of oxidative dissolution because oxidation requires overlap of the mineral and oxidant energy levels. The importance of this overlap is reflected in the enhanced dissolution rates observed during the oxidative dissolution of chalcopyrite at low solution potential. Kametani and Aoki (1985) observed chalcopyrite dissolution rates were optimal between 0.40 and 0.43 V. These potentials were achieved by the addition of potassium permanganate, which oxidised the iron released from the chalcopyrite. Kametani and Aoki (1985) also observed solution potential – the ratio of ferric to ferrous – was the critical factor determining dissolution

rates, rather than the iron concentrations used to achieve the solution potential. Enhanced dissolution rates of chalcopyrite at low solution potential were also observed by Hiroyoshi et al. (1997) in a comparison of the dissolution rate of chalcopyrite in ferric sulphate solution (high potential) and oxygenated ferrous sulphate solution (low potential). The higher rates achieved in the oxygenated ferrous solution were attributed to the oxidation of chalcopyrite by dissolved oxygen and the catalysis of this reaction by ferrous ions (Hiroyoshi et al., 1997). However, it is more likely the dissolved oxygen oxidised the ferrous ions to ferric ions and these ferric ions were responsible for oxidation of the chalcopyrite. This interpretation is consistent with ferric ions remaining the active oxidant in oxygen pressure leaching, with the oxygen oxidising the ferrous ions back to ferric (Roman and Benner, 1973). Furthermore, Hiroyoshi et al. (1997) do not explain the catalytic role of ferrous ions, and the proposed equation includes ferrous ions as a product of dissolution. This implies the reaction is autocatalytic and the addition of ferrous ions should have little to no effect on dissolution rates. Thus, the enhanced dissolution rates observed by Kametani and Aoki (1985) and Hiroyoshi et al. (1997) are attributable to the low solution potentials, with ferric ions as the oxidant.

Understanding the phenomenon of enhanced dissolution at low solution potentials requires consideration of the fundamentals of solution potential. The solution potential is the ratio of the oxidising agent and its complementary reduced species, as described by the Nernst equation:

$$E_h = E^0 - \frac{RT}{nF} ln \frac{[Oxidising]}{[Reduced]} \tag{2.1}$$

Although the traditional view of solution potential considers electron exchange within the solution to be analogous to exchange within a semiconductor, with the formation of discrete bands and a Fermi level, this overemphasises the electronic interaction between ions (Bockris and Khan, 1985). It is more appropriate to regard the solution potential as a combination of the potentials associated with the individual ions because the band

levels of the mineral are influenced by interaction of the ions in the Helmholtz layer and the protons and hydroxide ions adsorbed at the mineral surface (Morrison, 1977). This concept enables consideration of reactions at the atomic level and accounts for band bending at different potentials, without implying a unified semiconductor solution or changes to the oxidising potential of the ions.

The solution potential revision of Bockris and Khan (1985) and the band theory of Morrison (1977) can account for the enhanced rate of chalcopyrite dissolution at low solution potentials reported by Kametani and Aoki (1985) and Hiroyoshi et al. (1997) because the ratio of ferric to ferrous ions at the surface affects the band bending of the chalcopyrite (Figure 2.3). High ratios of ferric to ferrous (high potential) draw electrons to the surface and increase the potential difference between the surface and the bulk of the chalcopyrite. Conversely, low ratios of ferric to ferrous (low potential) fail to draw as many electrons to the surface because of the lower relative electron affinity of ferrous ions. The enhanced dissolution rates at low potential reported by Kametani and Aoki (1985) imply the lower extent of band bending leads to greater overlap of the bands of the chalcopyrite surface and the ferric ion in solution.

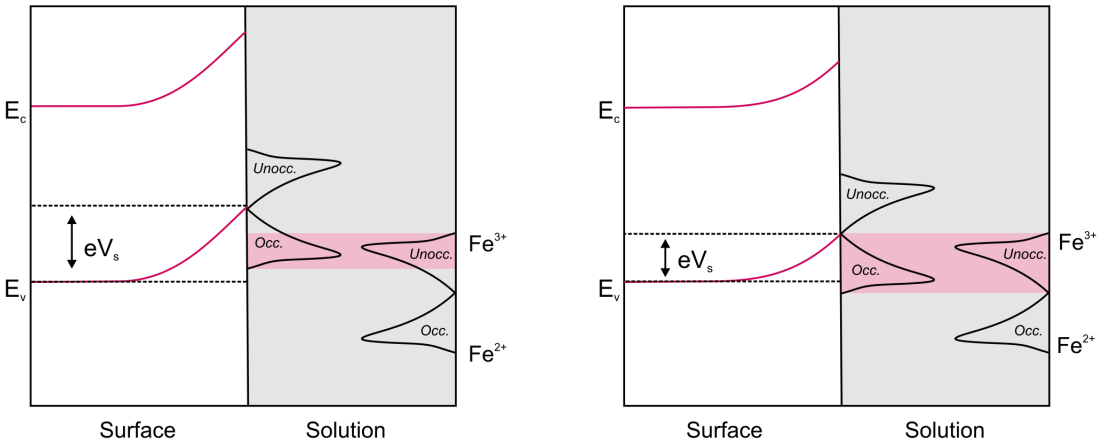

Figure 2.3: *Band bending of the mineral surface in ferric media as a result of (a) high solution potential, and (b) low solution potential, due to differing concentrations of ferrous and ferric ions. The figure is adapted from Morrison (1978) and Bockris and Khan (1985).*

Dissolution rate is also determined by the energy distributions associated with the hydration sheaths surrounding the mineral surface and the oxidant. In particular, rate is determined by the extent of energy distribution overlap and the density of the occupied and unoccupied states of the mineral and the oxidant, respectively (Morrison, 1978). Both factors are influenced by reaction temperature, because higher temperatures broaden the energy distributions of the hydration sheaths and promote electrons to the top of the mineral valence band. The energy distributions arise from fluctuations of the hydration sheaths and may be up to several tenths of an eV (Morrison, 1977). Although the energy distribution has been described as Gaussian by Morrison (1978), the anharmonic oscillation of the water molecules produce a Boltzmann distribution [Bockris and Khan (1985) and Figure 2.3]. The extent of energy distribution overlap determines the rate because energy differences must be minimised for electron transfer to occur. This difference is minimised by the rearrangement of the hydration sheaths to adopt identical configurations (Sacher and Laidler, 1963). The small amount of energy required for this rearrangement is counteracted by the energy released after electron transfer when the hydration sheaths re-orient to compensate for the adjustment in charge. The small amounts of energy involved ensure the conservation of energy law is obeyed.

2.3 Principal products of the oxidative dissolution of chalcopyrite in ferric media

The principal products of the oxidative dissolution of chalcopyrite in ferric sulphate and chloride media are elemental sulphur and sulphate (Jones and Peters, 1976; Dutrizac, 1978):

$$CuFeS_2 + 4\,Fe^{3+} \longrightarrow Cu^{2+} + 5\,Fe^{2+} + 2\,S^0 \tag{2.2}$$

$$CuFeS_2 + 16\,Fe^{3+} + 8\,H_2O \longrightarrow Cu^{2+} + 17\,Fe^{2+} + 2\,SO_4^{2-} + 16\,H^+ \tag{2.3}$$

These equations are proposed to account for the various percentages of elemental sulphur and sulphate reported for both media. The percentage of sulphide presenting as elemental sulphur (rather than sulphate) varies between 65-100% and 95-100% for ferric sulphate and ferric chloride media, respectively (Sullivan, 1933; Dutrizac et al., 1969; Jones and Peters, 1976; Dutrizac, 1990). This variation has been attributed to errors involved in the determination of elemental sulphur and sulphate, including the physical loss of elemental sulphur, the insolubility of amorphous elemental sulphur in carbon disulphide, the precipitation of sulphate, and the production of thiosalts rather than sulphate (Jones and Peters, 1976; Dutrizac, 1978).

2.4 Mechanisms of the oxidative dissolution of (chalco)pyrite in ferric media

The proposed mechanisms of oxidative dissolution of chalcopyrite in ferric media involve depictions of bulk chalcopyrite (Equations 2.2 and 2.3). However, the chalcopyrite surface reconstructs to form a 'pyritic' phase. Hence, it is more appropriate to consider mechanisms of pyrite oxidative dissolution in ferric media.

Moses et al. (1987) have proposed the oxidative dissolution of pyrite in ferric media via the transfer of a hydroxyl radical from a hexaqua-ferric ion to the terminal sulphur atom of the sulphide (Equation 2.4). Once an additional hydroxyl radical has been transferred to the terminal sulphur atom (Equation 2.5) dehydration occurs and an oxygen atom remains bonded to the terminal sulphur atom (Equation 2.6). Moses et al. (1987) proposed this addition and dehydration process is repeated three times, leaving three oxygen atoms on the terminal sulphur atom and producing thiosulphate. However, this process is unlikely to be sterically favourable because the final addition and dehydration step requires four oxygen atoms to be bonded to the terminal sulphur atom.

$$\mathrm{Fe{-}S^{-}{-}S^{-}\cdots H_2O{-}Fe^{3+}{-}(H_2O)_5 \longrightarrow Fe{-}S^{-}{-}S{-}OH^{-}} \tag{2.4}$$

$$\mathrm{Fe{-}S^{-}{-}S{-}OH^{-}\cdots H_2O{-}Fe^{3+}{-}(H_2O)_5 \longrightarrow Fe{-}S^{-}{-}S{-}(OH)_2^{-}} \tag{2.5}$$

$$\mathrm{Fe{-}S^{-}{-}S{-}(OH)_2^{-} \longrightarrow Fe{-}S^{-}{-}S{-}O^{-} + H_2O} \tag{2.6}$$

Luther (1987) has proposed a similar mechanism for the oxidation of pyrite in ferric media via the addition of oxygen atoms to the terminal sulphur atom. However, the intervening water molecules are removed and direct contact between the terminal sulphur atom and the ferric ion is assumed.

The first stage of the mechanism is the formation of a sulphur radical via the removal of an electron from a terminal sulphur atom by a ferric ion (Equation 2.7). The sulphur radical is oxidised by another ferric ion and an oxygen atom is incorporated (Equation 2.8). This process is repeated until the thiosulphate group is formed (Luther, 1987).

$$\mathrm{Fe_A{}^{II}{-}S{-}S{-}Fe_B{}^{III}(H_2O)_5{}^{3+} \xrightarrow{e^{-}\ \text{transfer}} Fe_A{}^{II}{-}S{-}S^{\cdot+}{-}Fe_B{}^{III}(H_2O)_5{}^{2+}} \tag{2.7}$$

$$\mathrm{Fe_A{}^{II}{-}S{-}S^{\cdot+}{-}Fe_B{}^{III}(H_2O)_5{}^{2+} + Fe(H_2O)_6{}^{3+} + 2\,H_2O \longrightarrow} \tag{2.8}$$
$$\mathrm{Fe_A{-}S{-}S{-}O + 2\,Fe(H_2O)_6^{2+} + 2\,H^{+}}$$

The source of the oxygen atoms (and the mechanism of the incorporation) is not stated; however, they are presumably derived from water molecules, despite the absence of intervening water molecules between the terminal sulphur atom and the ferric ion. Luther (1987) proposes the absence of intervening water molecules because it enables direct contact between the pyrite surface and the ferric ion, and the establishment of consistent Π orbital overlap between the ferric ion and the terminal sulphur atom. This consistent orbital overlap is deemed necessary for the rapid electron transfer responsible for the high dissolution rates observed. However, the complete absence of hydration

spheres from the surface and ferric ion is unlikely because they will attract water molecules to neutralise the inherent charge.

Mishra and Osseo-Asare (1988) have proposed another mechanism of pyrite oxidation in ferric media, involving the progressive incorporation of oxygen atoms onto the terminal sulphur atoms by hydroxyl radicals. These hydroxyl radicals are produced by the interaction of water molecules with the iron moiety of the pyrite, which possesses a hole (Equation 2.9). The hole is presumably created after an electron has been removed from the iron moiety by a ferric ion; however, the role of the ferric ion is not stated. The hydroxyl radicals react with the terminal sulphur atom (Equation 2.10) until three oxygen atoms are incorporated and the thiosulphate group is formed (Equation 2.11).

$$FeS_2 + H_2O \longrightarrow Fe(OH)S_2 + H^+ + e^- \tag{2.9}$$

$$Fe(OH)S_2 \longrightarrow FeS_2(OH) \tag{2.10}$$

$$FeS_2(OH) + 2\,H_2O \longrightarrow Fe^{2+} + S_2O_3^{2-} + (5)\,H^+ + 5\,e^- \tag{2.11}$$

Note: Equation 2.11 has been balanced.

It was proposed the terminal sulphur reacts with a hydroxyl radical because only a highly reactive radical would overcome the electrostatic repulsion between two negatively charged species. The generation of the hydroxyl radical by water interacting with the oxidised iron of pyrite assumes only the iron in pyrite is available for oxidation because the uppermost valence band is composed of the Fe 3d (t_{2g}) orbitals (Mishra and Osseo-Asare, 1988). However, this assumption neglects the overlap of the Fe 3d (t_{2g}) orbitals with the S 3p and 3d orbitals discussed earlier in Section 2.1.3. Furthermore, the hydroxyl radical is unlikely to be stable in the presence of iron because of the high stability of iron oxides/oxyhydroxides.

Despite inconsistencies in the proposed mechanisms of the oxidative dissolution of pyrite, the production of thiosulphate has been confirmed experimentally by Gold-

haber (1983), Moses et al. (1987) and Bonnissel-Gissinger et al. (1998). The detection of thiosulphate was only possible, however, under weakly oxidising conditions (0.001 M ferric or dissolved oxygen) of high pH (6-9) and low temperature (20-30°C) because of the extreme reactivity of thiosulphate under acidic and oxidative conditions. Thus, it may not be possible to detect thiosulphate during the oxidative dissolution of chalcopyrite because of the strongly oxidising conditions (> 0.1 M ferric) of low pH (< 2) and high temperature (50-80°C).

2.5 Kinetics of the oxidative dissolution of chalcopyrite in ferric media

The oxidative dissolution of chalcopyrite in ferric media is characterised by a dramatic decrease in dissolution rate with time and the emergence of a second stage. This second stage is attributed to inhibition of the dissolution reaction. Although the dissolution rate is observed to eventually increase after the second stage, most studies focus on the first two stages because the inhibition producing the second stage is the issue of most interest (Ferreira and Burkin, 1975; Dutrizac, 1981).

The emergence of the second stage has been attributed to a change in kinetic model from surface to diffusion controlled dissolution (Dutrizac et al., 1969; Beckstead et al., 1976; Munoz et al., 1979). The kinetic model can be determined from the rates of dissolution in the kinetic data. Surface (aka chemical reaction) controlled kinetics imply the rate limiting step is the restructuring of bonds at the surface-solution interface. Diffusion controlled kinetics imply the rate limiting step is the diffusion of reactants or products from the surface-solution interface through either the solution or a solid state interface. The kinetic model can be established by applying diffusion or surface control equations, or both, to each stage of the kinetic data (Sharp et al., 1966; Galwey and Brown, 1995). A linear relationship implies a strong correlation between the data and the model.

Kinetic model equations have been applied to the kinetic data of chalcopyrite dissolution in ferric sulphate by Dutrizac et al. (1969), Beckstead et al. (1976) and Munoz et al.

(1979). These studies applied diffusion control equations and assumed one stage of dissolution. However, close inspection of their data indicates the possibility of surface control kinetics and two stages of dissolution. Although the diffusion control plots are reasonably linear, surface control plots have not been produced for comparison, despite a degree of curvature in the plots at 86 and 94°C obtained by Dutrizac et al. (1969). The curvature in these plots also suggests the possibility of two stages of dissolution. Beckstead et al. (1976) and Munoz et al. (1979) acknowledge a second stage, with the kinetics changing from surface to diffusion controlled; however, this interpretation is not reflected in their data analysis. Thus, chalcopyrite dissolution in ferric sulphate might occur in two stages – particularly at higher temperatures – and at least one of these stages may be surface controlled, but this has not been confirmed.

The kinetic model can also be determined from the activation energy. The activation energy is calculated from the ratio of the rate constants produced at different temperatures. These rate constants can be obtained from the gradients of various stages of the surface or diffusion control plots. Therefore, the activation energy determination depends on identifying the number of dissolution stages, applying the model equations to each stage exclusively, and assuming the reaction rate for each stage is governed by the one reaction.

The activation energies reported for the oxidative dissolution of chalcopyrite in ferric media vary according to the conditions, but all are high and correspond to surface controlled kinetics (Table 2.1); all energies above 20 kJ mol^{-1} are attributable to surface control according to Wadsworth and Miller (1979). The apparent contradiction between the diffusion controlled kinetics assumed for the rate constant determination and the surface controlled kinetics implied by the activation energies has been acknowledged, but remains unresolved (Warren, 1958; Roman and Benner, 1973; Rimstidt et al., 1994). Although the high activation energy has been attributed to solid state diffusion by Ammou-Chokroum et al. (1979), the phase created by solid state diffusion has not been identified. The high activation energy has also been attributed to the transfer of electrons via elemental sulphur by Munoz et al. (1979) and Klauber (2008). However, this does not account for the variation of activation energies for both ferric sulphate and

ferric chloride systems or the consistently lower activation energies reported for ferric chloride systems (Table 2.1). Indeed, these lower activation energies – sometimes as low as 38 kJ mol^{-1} – are reported despite more elemental sulphur being generated in ferric chloride than ferric sulphate systems (Section 2.3). If electron transfer via elemental sulphur, which has an activation energy of 96.3 kJ mol^{-1} (Munoz et al., 1979), was responsible for the high activation energies, ferric chloride systems would have much higher activation energies.

Table 2.1: *Activation energies (kJ mol^{-1}) reported for the oxidative dissolution of chalcopyrite in ferric sulphate and ferric chloride systems.*

Sample	**Lixiviate**	**Temperature range**	**E_a**	**Reference**
Natural	$FeCl_3$	60 to 106°C	50	Ermilov et al. (1969)
Synthetic	$FeCl_3$	25 to 75°C	38 +/- 4	Ammou-Chokroum et al. (1977)
Synthetic	$FeCl_3$	50 to 100°C	46 +/- 4	Dutrizac (1978)
Natural	$FeCl_3$	30 to 100°C	42 +/- 4	Dutrizac (1978)
Natural	$FeCl_3$	40 to 100°C	63 +/- 8	Dutrizac (1981)
Natural	$FeCl_3$	40 to 60°C	63	Rimstidt et al. (1994)
Synthetic	$Fe_2(SO_4)_3$	50 to 94°C	71 +/- 13	Dutrizac et al. (1969)
Natural	$Fe_2(SO_4)_3$	32 to 50°C	75	Lowe (1970)
Natural	$Fe_2(SO_4)_3$	27 to 92°C	84	Baur et al. (1974)
Natural	$Fe_2(SO_4)_3$	60 to 93°C	84	Beckstead et al. (1976)
Natural	$Fe_2(SO_4)_3$	60 to 90°C	84	Munoz et al. (1979)
Synthetic	$Fe_2(SO_4)_3$	30 to 95°C	38 - 63	Dutrizac (1978)
Natural	$Fe(NO_3)_3$	25 to 40°C	59	Linge (1976)

Source: Most activation energies (E_a) taken from Dutrizac (1981).

Semiconductor type is expected to influence chalcopyrite dissolution in ferric media because it affects charge accumulation at the surface and therefore the extent of band bending (Section 2.2.2). However, this influence has not been confirmed experimentally. Dissolution rates of chalcopyrite from different locations have been compared by Linge (1976), Munoz et al. (1979), Dutrizac (1982), McMillan et al. (1982) and Hiroyoshi et al. (1997); however, only Dutrizac (1982) and McMillan et al. (1982) reported the semiconductor type. Dutrizac (1982) compared the dissolution rates of

one p-type and six n-type chalcopyrite samples and concluded dissolution rate is independent of semiconductor type. However, the comparison is not definitive because the p-type was only declared weak to moderate. Furthermore, the diffusion control (parabolic) rate equation was applied to the whole suite of data points, which does not account for the possibility of surface controlled kinetics or multiple stages of dissolution. This approach also assumed the dissolution rate close to time zero was governed by the overall dissolution reaction, although oxidation products are usually removed and the solution temperature is usually attained within the initial stage of dissolution (Galwey and Brown, 1998). McMillan et al. (1982) compared the dissolution rates of one p-type and one n-type chalcopyrite sample and concluded the dissolution rate is higher for the n-type sample. However, this comparison is not definitive because the n-type sample contains 8.1 % pyrite and 117 ppm silver; pyrite enhances chalcopyrite dissolution via galvanic interaction and silver catalyses chalcopyrite dissolution (Hiskey and Wadsworth, 1975; Miller and Portillo, 1981). Thus, the results of Dutrizac (1982) and McMillan et al. (1982) are inconclusive and the influence of semiconductor type on dissolution rates is unresolved.

Lixiviate influences chalcopyrite dissolution with higher rates observed in ferric chloride than ferric sulphate (Jones and Peters, 1976; Dutrizac, 1978; Ammou-Chokroum et al., 1977). Dutrizac (1978) proposed the different rates occur because of a difference in the mechanism of dissolution. However, the different rates may be caused by a different mechanism of inhibition or different extent of inhibition. Kinetic model equations have been applied to kinetic data of chalcopyrite dissolution in ferric chloride by Jones and Peters (1976), Dutrizac (1978) and Ammou-Chokroum et al. (1977). Dutrizac (1978) applied a surface control equation to the data acquired at various temperatures and assumed one stage of dissolution. Linearity was observed for a sample oxidised at 50°C; however, Dutrizac (1978) noted slight curvature in samples oxidised at higher temperatures. Curvature is also evident in the dissolution data of Jones and Peters (1976); nonetheless, they too applied a surface control equation to the data and assumed one stage of dissolution. Ammou-Chokroum et al. (1977) observed similar curvature to Jones and Peters (1976) but concluded dissolution occurs in two stages. The first stage

was attributed to surface controlled kinetics, while the second stage was attributed to inhibition; it was not stated whether the second stage was surface or diffusion controlled. Dutrizac (1978) attributed the change in kinetics observed by Ammou-Chokroum et al. (1977) to the rapid dissolution of fines during the first stage and the slower dissolution of coarse particles during the second stage; however, this argument does not address the curvature apparent in the data produced using sized fractions performed by Jones and Peters (1976). The curvature in the data suggests chalcopyrite dissolution in ferric chloride may undergo inhibition but to a lesser extent than in ferric sulphate. The possibility of inhibition – along with ferric remaining the oxidant in both systems – suggests the mechanisms of dissolution and inhibition are common, but the extent of inhibition is different, because of the associated anions. This is compatible with the detrimental effect of sulphate addition on dissolution rates in ferric chloride systems and the beneficial effect of chloride addition on dissolution rates in ferric sulphate systems (Ferreira and Burkin, 1975; Dutrizac, 1981).

2.6 Inhibiting phases of the oxidative dissolution of chalcopyrite in ferric media

Inhibition of the oxidative dissolution of chalcopyrite in ferric sulphate has been attributed to the establishment of diffusion control kinetics (Section 2.5). These kinetics are due to either modification of the chalcopyrite surface or deposition of phases onto the chalcopyrite surface. The surface modification is believed to produce a metal deficient sulphide phase, while the phases believed to deposit onto the surface include polysulphides, elemental sulphur and jarosite. The feasibility of these phases as inhibitors is considered according to stability under the oxidising conditions of low pH used for the dissolution of chalcopyrite in ferric media. The arguments reported for inhibition by each of the phases are also reviewed.

2.6.1 Metal deficient sulphide

Metal deficient sulphides are formed by the disproportionate release of iron from chalcopyrite (Baur et al., 1974). The metal deficient sulphides proposed for chalcopyrite can be divided into two groups: stoichiometric and non-stoichiometric. The stoichiometric phases proposed include subtle variations [haycockite ($Cu_4Fe_5S_8$), mooihoeckite ($Cu_9Fe_9S_{16}$) and talnakhite ($Cu_9Fe_8S_{16}$) and dramatic variations [covellite (CuS), bornite (Cu_5FeS_4) and chalcocite (Cu_2S)] (Biegler and Swift, 1979; Warren et al., 1982, 1985). The non-stoichiometric phases are usually ill-defined and described as either CuS_x or $Cu_{1-x}Fe_{1-y}S_{2-z}$ (Hiskey and Wadsworth, 1981; Buckley and Woods, 1984; Nava and Gonzalez, 2006).

Stoichiometric and non-stoichiometric metal deficient sulphides are not viable candidates for inhibiting phases based on stability relative to chalcopyrite. The stoichometric phases proposed (including the subtle and dramatic stoichiometric variations) are less stable and more readily oxidised than chalcopyrite (Letowski, 1979; Yin et al., 1995; Vaughan et al., 1997). The relative stability of non-stoichometric phases is harder to discern because they do not have specific stoichiometries. Nonetheless, issues including the extent of iron depletion, charge neutrality and the oxidation states of the remaining ions raise questions about the stability of non-stoichiometric phases. Furthermore, the mechanism of formation — the preferential loss of iron — implies a gradual change in dissolution rate, rather than the sudden change responsible for the second stage of dissolution (Section 2.5).

Despite these reservations, inhibition of chalcopyrite dissolution has been widely attributed to the formation of metal deficient sulphides (Baur et al., 1974; Linge, 1976; Ammou-Chokroum et al., 1979; Biegler and Swift, 1979; Biegler and Horne, 1984). These studies report the preferential loss of iron during the initial stages of dissolution, followed by a decrease in dissolution rate. However, this initial dissolution accounts for only $\sim$ 1% of chalcopyrite dissolution before stoichiometric release is observed. Although these phenomena are attributed to the establishment of a metal deficient sulphide, they may be the result of sample preparation, because all studies involved

chalcopyrite ground or polished in air. These preparation methods produce iron oxides on the surface of chalcopyrite and induce disorder in the crystal lattice (Remond et al., 1983; Farquhar et al., 2003; Velasquez et al., 2005). The dissolution of these iron oxides would produce the preferential iron release, while the disordered lattice would produce the rapid initial dissolution rate. Once the iron oxides and the disordered lattice are removed, slower stoichiometric release would be observed. These conclusions are consistent with an electrochemical study on the initial (or pre-wave) dissolution of chalcopyrite by Biegler and Swift (1979), which observed the initial dissolution behaviour was dependent on whether the electrode was ground or polished. Biegler and Swift (1979) also observed the behaviour was not reproduced on repeated scans (i.e., it was only observed immediately following grinding or polishing). The effect of polishing chalcopyrite and the nature of the underlying sulphide after oxidative dissolution need to be examined to verify metal deficient sulphide formation.

2.6.2 Polysulphides

Polysulphides are polymers of sulphur atoms with chain length inversely proportional to pH (Giggenbach, 1972). The polymer is initiated by oxidation of HS^- to $HS^{\cdot -}$, which then deprotonates and reacts with another $HS^{\cdot -}$ to form $HSS^{\cdot 2-}$ (Steudel, 1996). This polymerisation continues until the polysulphides oxidise or disproportionate and stable rings of S_8 (elemental sulphur) precipitate. The instability of polysulphides is reflected in the sulphur-oxygen stability diagram (Figure 2.4), which shows that hydrogen sulphide, thiosulphate and elemental sulphur are the stable forms of sulphur under the low pH conditions used for oxidative dissolution of chalcopyrite. Furthermore, these conditions promote polysulphide polymerisation (and therefore elemental sulphur precipitation) because ferric and cupric ions are catalysts for the oxidiation of HS^- to $HS^{\cdot -}$ (Fischer, 1984). Thus, polysulphides are likely to form during oxidative dissolution of chalcopyrite, but they are unlikely to persist long enough to deposit from solution and inhibit dissolution.

Despite being unstable under dissolution conditions, polysulphides have been proposed as inhibiting phases for the oxidative dissolution of chalcopyrite (Linge, 1976; Hackl

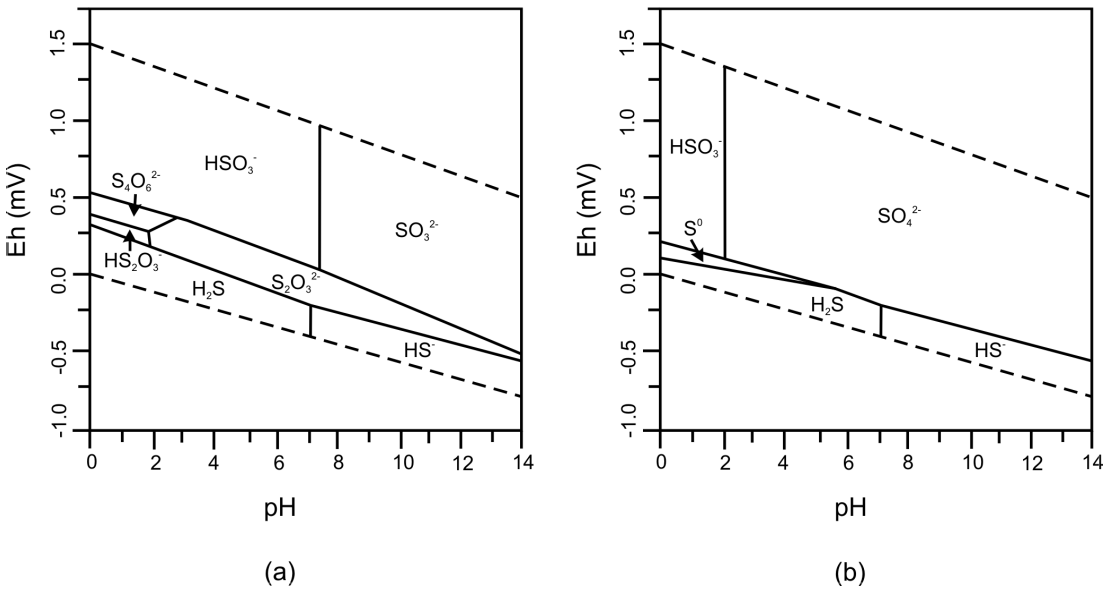

Figure 2.4: *Sulphur-oxygen stability diagram; a) shows figure without sulphate, bisulphate or elemental sulphur, while b) shows figure with sulphate, bisulphate and elemental sulphur (Williamson, 1992).*

et al., 1995). However, these polysulphides form by the same mechanism as metal deficient sulphides; this mechanism has been addressed in the metal deficient sulphide section (Section 2.6.1). The inhibiting ability of polysulphides deposited from solution has been investigated by Kougianos (2000). It was determined polysulphides are not stable and rapidly oxidise in air to form elemental sulphur. Kougianos (2000) also compared Raman spectra of polysulphide standards and chalcopyrite surfaces after oxidative dissolution and concluded polysulphides were not present.

2.6.3 Elemental sulphur

Elemental sulphur has three principal allotropes: S_λ, S_μ and S_π (Barnes, 1969). Although the proportion of these allotropes depends on solution conditions, the S_λ (aka S_8) is the most stable and hence the most commonly observed. The mechanism of elemental sulphur formation under acidic conditions involves the oxidation of hydrogen sulphide to polysulphides, which either oxidise or disproportionate to elemental sulphur (Section 2.6.2). The elemental sulphur molecules coalesce to produce droplets. These

droplets grow with the addition of more molecules or the combination of other droplets until the droplet contacts a crystal of sulphur (Steudel, 1996). This behaviour has been noted in morphological studies of chalcopyrite surfaces after oxidative dissolution, with globules of elemental sulphur depositing onto pre-existing crystals of elemental sulphur (Hirato et al., 1987; Dutrizac, 1989). This deposition mechanism accounts for the islands of elemental sulphur observed on the surface of chalcopyrite during oxidative dissolution by Warren (1978), Hirato et al. (1987) and Dutrizac (1989).

Although elemental sulphur is stable under dissolution conditions, and it deposits onto chalcopyrite surfaces, its ability to inhibit is unresolved. Attempts to improve dissolution rates by physically removing elemental sulphur from chalcopyrite surfaces using solvents have met with mixed results (Parker et al., 1981; Dutrizac, 1989; Buttinelli et al., 1990; Havlik and Kammel, 1995; Krishna et al., 1999). These mixed results may be caused by the formation of various elemental sulphur allotropes and the solubility of these allotropes in the solvents. The allotrope formed during chalcopyrite dissolution in ferric media was soluble in carbon tetrachloride and carbon disulphide according to Dutrizac (1989), Buttinelli et al. (1990) and Havlik and Kammel (1995), with Buttinelli et al. (1990) observing a three-fold improvement in dissolution rate after treatment with carbon tetrachloride. However, the allotrope formed during chalcopyrite oxidative dissolution in electrochemcial studies was insoluble in carbon disulphide according to Biegler and Swift (1979) and Krishna et al. (1999). This latter observation accounts for the failure of Parker et al. (1981) to improve dissolution rates by treating an electrode with carbon disulphide.

In addition to allotropy, morphology of elemental sulphur may also affect its inhibiting ability, with porous deposits producing a diminished diffusion barrier for reactants and products. Increased porosity of elemental sulphur formed in ferric chloride systems is believed responsible for the enhanced dissolution of chalcopyrite observed relative to the dissolution in ferric sulphate systems of the same iron concentration and solution potential (Majima et al., 1985; Dutrizac, 1989). Indeed, Dutrizac (1989) observed enhanced dissolution occurred despite the greater amount of elemental sulphur produced in the ferric chloride system (Dutrizac, 1989). Because the difference in porosity is un-

likely to result from the interaction of polar anions with non-polar elemental sulphur, it is presumably due to the difference in the initial dissolution rate. Therefore, the greater initial dissolution rate of chalcopyrite in ferric chloride produces a greater rate of elemental sulphur formation, which in turn produces a deposit of greater porosity. The formation of elemental sulphur of greater porosity during the initial stages presumably aids the greater dissolution observed during the latter stages (Section 2.5).

2.6.4 Jarosites

Jarosites are iron sulphate complexes with a general formula of $MFe_3(SO_4)_2(OH)_6$, where M is usually a monovalent cation such as potassium, sodium, ammonium or hydronium. The formation of these jarosites is dependent on pH, ferric and sulphate concentrations, monovalent cation concentration, temperature and seeding. Jarosites are stable between pH 1 and 2.5 (Figure 2.5). If the pH falls below 1, jarosite will not form, while if the pH rises above 2.5, both jarosite and iron oxides will form. Jarosites may be formed in solutions with ferric concentrations of 0.001 M, but concentrations between 0.025 and 3.0 M are typically used to improve yields for jarosite synthesis (Das et al., 1996). Ferric concentration is more important than sulphate concentration in ferric sulphate because ferric is the limiting reagent in these solutions. However, sulphate concentration becomes limiting at the extremely low levels present in ferric chloride solutions. Nonetheless, Dutrizac (1981) observed jarosite formation in a ferric chloride solution 0.5 M in ferric and 0.025 M in sulphate (i.e., a ferric to sulphate ratio of 20:1); although this jarosite also contained the iron oxide goethite, a solution 0.05 M in sulphate formed jarosite exclusively. In the presence of sufficient ferric and sulphate concentrations, the jarosite formed depends on the monovalent cations present. The stability of the jarosite is proportional to the size of the monovalent cation, with potassium the most stable and hydronium the least. Thus, potassium jarosite will form before other jarosites, but all solutions will eventually form hydronium jarosite. Although jarosite formation is thermodynamically favourable at 25°C, it is kinetically favourable at temperatures above 80°C, and precipitation is almost complete after a few hours (Dutrizac, 1983). The kinetics of jarosite precipitation can be enhanced further

with the addition of seed (Dutrizac, 1996). Furthermore, the stability of jarosite at the pH values, temperatures and ferric sulphate concentrations often used for chalcopyrite dissolution suggest jarosite is a candidate for the inhibiting phase.

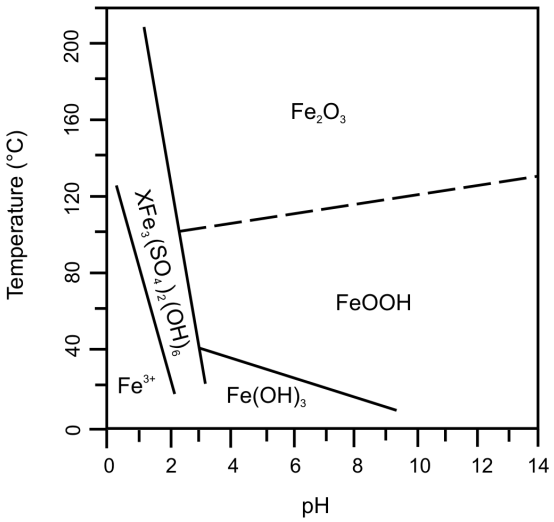

Figure 2.5: *Iron-sulphur-oxygen stability diagram (Das et al. 1996).*

Jarosite is formed on sulphide ores during natural weathering and has been identified on chalcopyrite ores oxidised in heap leaching operations (Bladh, 1982; Robles et al., 1994). It has also been identified on the surface of chalcopyrite oxidised in dissolution studies under laboratory conditions (Sandstrom et al., 2005). However, the ability of jarosite to inhibit the dissolution of chalcopyrite is unresolved. In a study of the oxidative dissolution of chalcopyrite under potentials controlled by the addition of potassium permanganate, Sandstrom et al. (2005) attributed inhibition to potassium jarosite, which was identified using XRD and XPS. Ferreira and Burkin (1975) also identified a 'jarosite-type' phase, in addition to goethite, during the oxidative dissolution of chalcopyrite in ferric sulphate at temperatures between 50 and 95°C. Jarosite and goethite in ferric sulphate at elevated temperatures is consistent with XRD analysis of the hydrolysis products of 0.03 M ferric sulphate at 90°C (Music et al., 1994). The enhanced kinetics of jarosite formation at elevated temperatures may be responsible for the erratic dissolution rates noted by Dutrizac (1981), which are attributed to 'invisible iron' despite the use of low pH to prevent iron hydrolysis. Indeed, many studies have

been performed at low pH in an attempt to prevent precipitation of either jarosite or goethite (Dutrizac et al., 1969; Munoz et al., 1979; Majima et al., 1985). These studies have still reported inhibition of dissolution, leaving the inhibiting ability of jarosite in doubt. However, the prevention of jarosite formation in these studies is uncertain.

Inhibition by jarosite would account for the dissolution rates in ferric chloride being dependent on ferric concentration and the dissolution rates in ferric sulphate being independent of ferric concentration above 0.01 M (Dutrizac et al., 1969). Although Dutrizac et al. (1969) attributed this phenomenon to different mechanisms for the two systems, Beckstead et al. (1976) attributed the phenomenon to the relatively unchanging ferric ion activity at concentrations above 0.01 M because of the greater ion pairing of ferric and sulphate. This detrimental effect of sulphate has been observed in other studies, with the addition of sulphate diminishing dissolution rates and the addition of chloride improving dissolution rates (Dutrizac, 1981). Furthermore, the effect of sulphate was more dramatic with the addition of ferrous sulphate than with other sulphate salts. These results suggest an iron sulphate – such as jarosite – may be responsible for inhibiting dissolution.

2.6.5 Summary

The commonly proposed inhibiting phases of oxidative dissolution of chalcopyrite have been considered in terms of the persistence and inhibiting ability of these phases under oxidative conditions of low pH. The instability of polysulphides and stoichiometric metal deficient sulphides under these conditions makes them unlikely candidates for inhibiting phases, while the kinetics of dissolution reported suggest a non-stoichiometric metal deficient sulphide is not responsible for inhibition. The mechanisms of formation of the remaining two candidates – elemental sulphur and jarosite – are consistent with the reported dissolution kinetics; however, the inhibiting abilities are unresolved.

2.7 X-ray Photoelectron Spectroscopy (XPS)

X-ray photoelectron spectroscopy is a surface analysis technique that provides chemical speciation of the uppermost 2 to 5 nm of a sample, depending on the sample matrix, the kinetic energy of the photoelectron of interest, and the instrumentation used (Klauber, 1995). The technique involves irradiating the sample with monochromated X-rays *(E_{X-ray})* to produce photoelectron emission. The kinetic energies *(E_K)* of the emitted photoelectrons are measured relative to the spectrometer work function *(Φ_{spec})* to determine the binding energies *(E_{BE})* (Klauber, 1995):

$$E_K = E_{X-ray} - E_{BE} - \Phi_{spec} \tag{2.12}$$

Photoelectron binding energies can be used to identify elements and electronic environments. These environments influence the binding energy of the photoelectron because it is determined by the electrostatic attraction between the emerging photoelectron and the inner electron shell. The electrostatic interaction is always attractive because the loss of the electron leaves the inner electron shell less stable. The extent of the attraction depends on the inner electron shell's ability to recover from the loss by acquiring electrons from outer orbitals. If the inner electron shell recovers quickly, the attraction will be weak, the kinetic energy loss will be small, and the photoelectron will contribute at low binding energy. Conversely, if the inner electron shell recovers slowly, the attraction will be strong, the kinetic energy loss will be large, and the photoelectron will contribute at higher binding energy. Therefore, oxidised species produce peaks at high binding energy and reduced species produce peaks at low binding energy. In addition to binding energy, the electronic environment also influences peak width, analyser resolution and atomic vibrational freedom (Klauber, 1995).

Photoelectron intensity at any particular binding energy for an element *(A)* is a function of the kinetic energy *(E)*, atom density *(N)*, depth *(χ)*, incident flux *(J)*, partial

photoelectron cross section *(σ_{PA})*, angular asymmetry of the intensity of the photoemission *[L(A)]*, and the product of the analyser transmission efficiency and the sample area analysed *[$G(E_A)$]* (Seah, 1981):

$$I_A = J_0 \sigma_{PA} L(A) G(E_A) D(E_A) X \int_0^\infty N_A(\chi) e^{[-\chi/\lambda_M(E_A)\cos\Theta]} dx \tag{2.13}$$

Photoelectron intensity is diminished by spin-orbit splitting, which produces two peaks in the spectrum. Spin orbit splitting occurs for p, d and f orbitals because the electron remaining after photoelectron emission will have a spin state either parallel or anti-parallel to the orbital angular momentum. The different energies of the two spin states cause the photoelectron binding energy to change and two peaks to appear in the spectrum. The energy separation of the two peaks and the ratio of the peak areas will remain constant for each core level of an element, enabling mathematic removal of the splitting during spectral processing for simple photoelectron lines such as S 2p. For more complex photoelectron lines, such as those of transition metals, the energy separation and ratios of the peak areas are too complex and mathematic removal is not reliable (Klauber, 1995).

X-ray photoelectron spectra also display photoelectron satellite structure. Satellite structure arises from unmonochromated X-ray sources, shake-up and shake-off processes and characteristic energy losses. Unmonochromated Mg K_α and Al K_α X-ray sources produce eight satellite peaks: two intense and six weak. The two intense satellite peaks ($K_{\alpha 1}$ and $K_{\alpha 2}$) cannot be resolved, and thus impart asymmetry to the principal peaks, including the photoelectron peaks. The six weak satellite peaks produce structure of varying intensity, with the most intense occurring within approximately 20 eV of the main peaks. Shake-up satellite peaks occur when emitted photoelectrons are exposed to the ion in an excited state and subsequently lose energy. This energy loss corresponds to a spectral contribution appearing at binding energies above the main photoelectron peak. The intensity of shake-up satellite peaks correlates with paramagnetism and provides a simple diagnostic for cuprous (diamagnetic) and cupric (paramagnetic) because

only cupric display intense shake-up satellite peaks (Frost et al., 1972; Yin et al., 1972). Shake-off satellite structure occurs when the incident photon is partitioned between two or more photoelectrons. These photoelectrons have kinetic energies significantly lower than the photoelectrons of the main peak and contribute peaks at higher binding energies. Lastly, characteristic energy losses arise when a photoelectron imparts energy to a permitted electron transition between orbitals. Because of the finite energy of the orbital transition, the energy loss is observed at a fixed binding energy separation from the main peak. This fixed binding energy separation enables identification of characteristic energy losses in a system because the losses are observed for all photoelectron peaks.

In addition to photoelectron peaks, X-ray photoelectron spectra display Auger transition peaks. Auger transitions occur when an electron from an outer orbital fills a vacancy created by the emission of a photoelectron from a core level orbital and the energy difference is imparted to a third electron. This electron is known as an Auger electron. The binding energy of the Auger electron is independent of the X-ray source that created the initial vacancy because the energy of the transition is a function of the two orbitals. The Auger transitions may involve core levels exclusively, or a combination of core and valence levels. Because of the possible combinations, Auger transition peaks always occur in series for elements with atomic numbers of five and above.

Auger electron intensity at any particular binding energy for an element *(A)* is a function of the kinetic energy *(E_A)*, atom density *(N_A)*, depth *(χ)*, incident electron beam current *(I_0)*, total Auger cross section per atom A *(σ_{AA})*, the backscatter factor *(r_M)*, analyser transmission function *[$T(E_A)$]*, analyser detection efficiency *[$D(E_A)$]*, the inelastic mean free path of the electrons in the matrix *[$\lambda_M(E_A)$]* and the angle of emission off-normal (Seah, 1981):

$$I_A = I_0\sigma_{AA}[1 + r_M(E_A)]T(E_A)D(E_A)X\int_0^\infty N_A(\chi)e^{[-\chi/\lambda_M(E_A)\cos\Theta]}dx \tag{2.14}$$

2.7.1 XPS studies of chalcopyrite

XPS has been used extensively to study chalcopyrite dissolution and flotation for the minerals industry. However, this review focuses on studies analysing chalcopyrite before and after oxidative dissolution at low pH. Studies that have not provided sufficient detail (Llanos et al., 1995), or practiced appropriate care with sample preparation (Pratesi and Cipriani, 2000), or instrument operation (Mielczarski et al., 1996), are not included. In particular, results from ion-sputtering are not discussed because of the possibility of preferential sputtering and interface smearing, and the difficulty of estimating the extent of these effects.

2.7.1.1 Unoxidised chalcopyrite

Examination of unoxidised chalcopyrite requires the analysis of an unreacted surface produced under anaerobic atmosphere, either inside the spectrometer or inside a glove box/bag directly attached to the spectrometer. This requirement has been met unambiguously by Klauber (2003) and Harmer et al. (2004). Both studies have concluded chalcopyrite surfaces reconstruct to form either a sulphur dimer or a sulphur polymer. The study by Klauber (2003) discusses the S 2p, Fe 2p and Cu 2p spectra, while the study by Harmer et al. (2004) focuses on the S 2p spectra. Although the peaks identified in both studies are similar, the chemistry concluded is different.

Klauber (2003) fractured chalcopyrite under anaerobic atmosphere and identified two layers of surface reconstruction. The reconstruction is consistent with the phases identified in the S 2p, Cu 2p and Fe 2p spectra. The S 2p spectrum was fitted with three peaks: bulk sulphide (161.15 eV), disulphide (161.81 eV), and characteristic loss structure (163.32 eV). The bulk sulphide peak was attributed to the underlying bulk chalcopyrite. The disulphide was attributed to neighbouring sulphur atoms oxidised from -2 to -1 and dimerised to form S_2^{2-} at the surface. The characteristic loss structure was attributed to the interband transition between the S 3p and Fe 3d orbitals, with a corresponding energy loss of $\sim$ 2.6 eV, in accordance with Hamajima et al. (1981). The identification of additional peaks at $\sim$ 2.6 eV above the main S 2p, Cu 2p

and Fe 2p photoelectron peaks is consistent with characteristic loss structure. Additionally, the greater intensity of the characteristic loss structure in the S 2p and Fe 2p spectra is consistent with the involvement of the S 3p and Fe 3d orbitals. The Fe 2p spectrum also revealed the sulphur dimers were associated with the iron of the mineral, which was reduced from +3 to +2 to produce a 'pyritic' phase (FeS_2) with $\sim$ 50 % the density of natural pyrite. The reduction of the iron was confirmed by comparing the Fe 2p spectra of anaerobically fractured pyrite and chalcopyrite standards, with the two spectra revealing significant overlap at the binding energy corresponding to +2 oxidation state. According to Klauber (2003), the reduction of one iron atom and the oxidation of two sulphur atoms produces a residual electron. This residual electron reduces the atmospheric oxygen present in trace quantities inside the anaerobic chamber. The reduced oxygen reacts with the copper of the mineral to form cuprite (Cu_2O). The formation of cuprite is consistent with the monovalent copper of the Cu 2p spectrum and the small oxide peak of the O 1s spectrum. The proposed structure of the surface reconstruction of chalcopyrite is $FeS_2.0.5Cu_2O$, with inelastic mean free path (IMFP) calculations predicting two layers above bulk chalcopyrite (Klauber, 2003).

Harmer et al. (2004) identified similar reconstruction peaks in the S 2p spectra of a chalcopyrite fracture surface produced under anaerobic atmosphere; however, the proposed chemistry associated with the reconstruction is different. The S 2p spectrum produced using a conventional X-ray source was composed of three peaks at similar binding energies to those reported by Klauber (2003): bulk sulphide (161.35 eV), polmeric sulphur (161.90 eV), and loss structure (163-166 eV). The peak at 161.90 eV is speculatively attributed to polymeric sulphur, with more than two sulphur atoms bonding to each other, rather than the disulphide. This assertion was based on the breadth of the peak and reports of similar polymerisation for arsenides, including gallium arsenide and iron arsenide. However, while the polymerisation of trivalent arsenide (-III) is feasible, the polymerisation of monovalent sulphur atoms (-I) beyond a dimer is not. The model proposed by Harmer et al. (2004) differs further from the model proposed by Klauber (2003) because the sulphur dimer/polymer is associated with copper. However, spectroscopic evidence of this association is not presented and neither the Cu 2p nor the

Fe 2p spectrum is displayed or discussed. Harmer et al. (2004) proposes the sulphur polymer is unreactive and protects the copper from oxidation, while the unprotected iron is oxidised. However, this proposal is unlikely because the sulphur at the surface of chalcopyrite reacts to form elemental sulphur and sulphate (Section 2.3).

2.7.1.2 Chalcopyrite oxidised in air with and without polishing

XPS analysis has confirmed the rapid oxidation of chalcopyrite in air (Buckley and Woods, 1984; Brion, 1980) is exacerbated by polishing (Remond et al., 1983; Farquhar et al., 2003; Velasquez et al., 2005). Studying the effect of air-oxidation on chalcopyrite establishes the surface initially exposed to oxidative dissolution.

Air oxidation of chalcopyrite for brief periods produces iron oxide/oxyhydroxide and metal deficient sulphide, according to Buckley and Woods (1984). They proposed an iron deficient sulphide forms as the iron within the chalcopyrite lattice migrates to the surface and forms an iron oxide ($Fe_2O_3.xH_2O$). The iron oxide on the surface was identified with a contribution to the Fe 2p spectrum at $\sim$ 711 eV. The metal deficient sulphide peak was identified at 163.8 eV in the S 2p spectrum, above the main sulphide peak at 162.0 eV. The proposed metal deficient sulphide has a stoichiometry of CuS_2; however, Buckley and Woods (1984) do not believe the structure compares to pure CuS_2 because the metal deficient sulphide peak is fitted 1.8 eV above the main sulphide peak and CuS_2 standards display peaks significantly closer to the main sulphide peak. Thus, Buckley and Woods (1984) conclude the metal deficient sulphide has a structure comparable to chalcopyrite, with iron vacancies and undimerised sulphur atoms at the surface.

Air-oxidation of chalcopyrite for extended periods produces iron oxide/oxyhydroxide, sulphate, and possibly metal deficient sulphide, according to Brion (1980) and Buckley and Woods (1984). Buckley and Woods (1984) extended the model proposed for brief periods of air-oxidation with modification of the metal deficient sulphide and the appearance of sulphate. They proposed the metal deficient sulphide loses copper to form $Cu_{1-x}S_{2-x}$. This coincides with copper sulphate forming at the surface, based

on the emergence of a peak near 168.4 eV in the S 2p spectrum and the emergence of satellite structure in the Cu 2p spectrum. Brion (1980) also examined chalcopyrite oxidised in air for extended periods and attributed a peak near 168.6 eV to sulphate, but did not observe satellite structure in the Cu 2p spectrum. Therefore, unlike Buckley and Woods (1984), Brion (1980) proposes the sulphate is associated with iron, as a basic iron sulphate comparable to jarosite, based on peak positions in the Fe 2p and O 1s spectra. Brion (1980) did not propose a metal deficient sulphide, preferring to speculate the higher binding energy contribution in the S 2p spectrum at 162.6 eV is due to sulphur dimers forming a structure comparable to pyrite. Thus, there is consensus that oxidising chalcopyrite for extended periods produces iron oxide/oxyhydroxide and sulphate, but the production of the metal deficient sulphide and the association of sulphate are disputed.

Air-oxidation of chalcopyrite during polishing produces iron oxide/oxyhydroxide, sulphate and metal deficient sulphide according to Remond et al. (1983), Farquhar et al. (2003) and Velasquez et al. (2005). Remond et al. (1983) and Farquhar et al. (2003) both identified iron oxide/oxyhydroxide on the surface of polished chalcopyrite based on the Fe 2p and O 1s spectra, respectively. Despite the significant quantities of iron oxide evident in the Fe 2p spectra of Remond et al. (1983), neither study declared the iron oxide/oxyhydroxide. Sulphate has also been identified as a product of polishing, but it doesn't appear to persist in water. Remond et al. (1983) identified sulphate on the chalcopyrite surface polished with a silicone oil based diamond polish but not on the surface polished with a water based chromic oxide polish. This solubility in water accounts for the absence of sulphate in the studies of Farquhar et al. (2003) and Velasquez et al. (2005) because both washed the surface with water before analysis. Remond et al. (1983) proposed the sulphate is associated with iron rather than copper, based on the position of the peak in the Fe 2p spectrum and the absence of satellite structure in the Cu 2p spectrum, but did not identify the iron sulphate. All three studies propose a metal deficient sulphide underlying the iron oxide or sulphate, but these proposals are based on questionable analyses. Remond et al. (1983) proposed an iron deficient sulphide based on analysis after ion sputtering, which often produces

concentration gradients because of preferential sputtering. Velasquez et al. (2005) also proposed an iron deficient sulphide, because of an apparent decrease in iron and sulphur intensities. This decrease could be due to the dissolution of an iron sulphate at the surface during the washing procedure. However, it may also be due to changes in the relative intensities for each of the photoelectron lines, caused by surface roughness; comparison of the Fe 2p spectra of fractured and polished chalcopyrite by Farquhar et al. (2003) shows diminished definition of the main Fe 2p peak after polishing, which indicates surface disorder/roughness. Surface roughness might also be responsible for changes of intensity that led Farquhar et al. (2003) to conclude a copper and iron deficient sulphide forms as a result of polishing. Firmer conclusions cannot be drawn because of the sparse details of the intensity determination and the lack of curve fitting performed on the S 2p spectra in all three studies. Furthermore, none of the studies identified sulphur dimers or loss structure in the S 2p spectra; Remond et al. (1983) identified a peak at 164 eV for the water based chromic oxide polished sample but did not attribute it to a phase, while Farquhar et al. (2003) identified a peak at 163.25 eV and attributes it to neutral sulphur but did not propose a phase. Thus, polishing chalcopyrite produces iron oxide/oxyhydroxide and sulphate, but the production of a metal deficient sulphide is unresolved.

Chalcopyrite is very susceptible to air-oxidation, forming iron oxides/oxyhydroxides initially. This oxidation is exacerbated by polishing, which produces sulphates, in addition to iron oxides/oxyhydroxides. Metal deficient sulphides have also been proposed for air-oxidation of chalcopyrite; however, these proposals do not consider the persistence of the sulphur dimer/polymer and loss structure contributions identified on unoxidised chalcopyrite by Klauber (2003) and Harmer et al. (2004) (Section 2.7.1.1).

2.7.1.3 Chalcopyrite oxidised in ferric media

XPS has been used to study chalcopyrite surfaces oxidised in ferric media under various conditions (Buckley and Woods, 1984; De Filippo et al., 1988a; Hackl et al., 1995; Mikhlin et al., 2004; Sandstrom et al., 2005). These studies have focussed on the S

2p spectra because of the relative intractability of the Fe 2p and Cu 2p spectra. The reported S 2p spectra fits vary in the number of the peaks, the binding energies of the peaks, and the phases attributed to the peaks (Table 2.2). This conjecture is partially because of the overlap of peaks in the S 2p spectra. Despite this variation, almost all studies identified metal deficient sulphide, elemental sulphur and sulphate in the S 2p spectra. There is also consistency in the state of the copper and iron, but the Cu 2p and Fe 2p analyses remain inconclusive.

Table 2.2: *S 2p binding energies (eV) reported for spectra of chalcopyrite after oxidative dissolution in ferric media.*

Chalcopyrite	M.D.S.	Elemental sulphur	Loss structure	Sulphate	Reference
161.0	163.1	163.5	-	168.1	Buckley and Woods (1984)*
161.6	-	163.2	-	169.0	De Filippo et al. (1988a)†
161.0	162.0, 162.9	163.9	-	-	Hackl et al. (1995)‡
160.4	161.4-164.1	-	-	168.6	Mikhlin et al. (2004)
161.3	162.3	163.4	165.4	168.9	Sandstrom et al. (2005)

Note: M.D.S = metal deficient sulphide. All binding energies calibrated to C 1s (284.6 eV) or Au 4f (83.9 eV)

*Buckley and Woods (1984) binding energies are based on the binding energy for chalcopyrite interpreted by the author and the binding energy shifts for the other features reported by Buckley and Woods (1984).

†De Filippo et al. (1988a) assigned the peak at 163.4 eV to the C=S bonds of the xanthate flotation agent adsorbed to the surface of the chalcopyrite.

‡Hackl et al. (1995) did not display the S 2p spectral region required to confirm the presence of sulphate.

Metal deficient sulphide

Metal deficient sulphides have been identified on the surface of chalcopyrite after oxidative dissolution based on relative intensity determinations (De Filippo et al., 1988a; Mikhlin et al., 2004; Sandstrom et al., 2005). However, these determinations may not take account of the spectral contributions from both the underlying sulphide and the deposition phases. Sandstrom et al. (2005) identified metal deficient sulphide formation during oxidation in ferric media at high and low solution potentials. Oxidation

at high solution potential produced iron deficiency, while oxidation at low solution potential produced copper deficiency. These deficiencies are based on relative intensities determined after the removal of 'non-sulphide lattice' contributions including elemental sulphur, sulphate, ferric and cupric. However, the method of removal is not described and the exclusion of ferric (which is the form of iron in bulk chalcopyrite) may not be appropriate. The difference in deficiency might be the result of different levels of deposition phases on the surface and attenuation of the signal by these phases. Mikhlin et al. (2004) also identified metal deficient sulphide formation on the surface of chalcopyrite oxidised in ferric media, after oxidation in ferric chloride and ferric sulphate solutions. They asserted both solutions produce a sulphur rich surface, with the Fe:Cu ratio higher after dissolution in ferric sulphate, than in ferric chloride. These elemental ratios were determined using peak areas, without apparent discrimination between the spectral contribution from the underlying sulphide and the deposition phases. Thus, the sulphur enrichment may be due to the deposition of elemental sulphur or sulphate (in the form of jarosite) on the surface. The latter proposal would account for the higher iron to copper ratio observed in the ferric sulphate solution because of the greater amounts of jarosite formed in ferric sulphate solutions (Section 2.6.4). It would also be consistent with the decrease in copper intensity observed by De Filippo et al. (1988a) after the precipitation of jarosite onto the surface of the chalcopyrite during oxidation in microbial ferric media. Similar to Mikhlin et al. (2004), De Filippo et al. (1988a) attributed the change of intensity to the formation of a metal deficient sulphide but did not discriminate the spectral contributions arising from the underlying sulphide and the deposition phases.

Metal deficient sulphides have also been identified on the surface of chalcopyrite after oxidative dissolution, based on the binding energies of the S 2p spectra (Buckley and Woods, 1984; Hackl et al., 1995; Mikhlin et al., 2004). However, there are inconsistencies in the binding energies and the associated oxidation states. Buckley and Woods (1984) attributed a peak at $\sim$ 163.0 eV to a metal deficient sulphide, with the sulphur atoms possessing a nominal oxidation state between -0.4 and 0. Although this peak increased as a function of reaction time, it was not attributed to elemental sulphur be-

cause it was assumed all elemental sulphur would volatilise under vacuum. Hackl et al. (1995) assumed elemental sulphur persisted under vacuum and contributed a peak at 164.3 eV, in addition to the metal deficient sulphide peaks at 163.3 and 162.4 eV, with nominal oxidation states between -1 to -0.5, and -0.5 to 0, respectively. Mikhlin et al. (2004) attributed three and four peaks to the sulphur atoms within a metal deficient sulphide formed by chalcopyrite dissolution in ferric sulphate and ferric chloride, respectively; the three peaks for the ferric sulphate system occured at 161.8, 163.4 and 164.5 eV, while the four peaks for the ferric chloride system occured at 161.8, 162.9, 163.7 and 164.6 eV. The metal deficient sulphide was considered analogous to a polysulphide, with the peaks at 161.8, 162.9 - 163.7, and 164.5 - 164.6 eV possessing oxidation states of -1, 0 and either +1 or +2, respectively. However, the presence of positively charged polysulphides contradicts XPS studies of polysulphide standards that only identify -1 and 0 oxidation states (Termes et al., 1987; Smart et al., 1999; Kougianos, 2000). Furthermore, the reliability of the binding energies and oxidation states proposed by Mikhlin et al. (2004) is uncertain because of the changing binding energy assignments.

Elemental sulphur

Elemental sulphur has been identified in the S 2p spectra of chalcopyrite after oxidative dissolution (Buckley and Woods, 1984; Hackl et al., 1995; Mikhlin et al., 2004; Sandstrom et al., 2005). The range of binding energies reported for elemental sulphur (163.0 - 164.3 eV) may reflect the different approaches to curve fitting, or the breadth of the elemental sulphur peak due to different bonding associations. Buckley and Woods (1984) examined the S 2p spectra of chalcopyrite after oxidative dissolution, before and after 24 hours under vacuum, and observed that despite most of the peak at 163.0 eV being lost, a minor amount remained. Although the lost peak was attributed to elemental sulphur, the remaining peak was attributed to a metal deficient sulphide. This proposal does not consider that the bonding between the elemental sulphur and the surface may be greater than the bonding between the elemental sulphur and itself. Different bonding associations might cause binding energy shifting of the elemental sulphur peak, depending on the amount of elemental sulphur present on the surface during

analysis; this depends on the amount of elemental sulphur produced during oxidative dissolution and the time the sample spends under ultra high vacuum before analysis. The inconsistent binding energies reported for elemental sulphur have implications for the assignment of peaks in the S 2p spectrum.

Sulphate

Sulphate has been identified in the S 2p spectra of chalcopyrite after oxidative dissolution (Buckley and Woods, 1984; De Filippo et al., 1988a; Mikhlin et al., 2004; Sandstrom et al., 2005). Although Buckley and Woods (1984) and Mikhlin et al. (2004) did not attribute the sulphate to a phase, Sandstrom et al. (2005) and De Filippo et al. (1988a) both attributed the sulphate to jarosite; Sandstrom et al. (2005) confirmed the identification of jarosite by X-ray diffraction analysis. Hackl et al. (1995) do not mention sulphate in reference to either the S 2p or the Fe 2p spectra and the S 2p spectrum does not include the spectral region required to confirm its presence.

Iron

Iron oxides and jarosites have been identified in the Fe 2p spectra of chalcopyrite after oxidative dissolution (De Filippo et al., 1988a; Hackl et al., 1995; Sandstrom et al., 2005). However, these identifications are not based on fitting of the Fe 2p spectra, presumably because of the complexity of the Fe 2p spectral region. Hackl et al. (1995) noted iron oxide on the surface decreased after oxidative dissolution; however, despite speculating hematite, magnetite and goethite may be present, no iron oxide was definitively identified. Both Buckley and Woods (1984) and Mikhlin et al. (2004) attributed some of the Fe 2p intensity to iron associated with oxygen, but they did not identify the iron oxide. Neither De Filippo et al. (1988a) nor Sandstrom et al. (2005) identified iron oxides, but they did identify jarosite. De Filippo et al. (1988a) identified jarosite on the surface of chalcopyrite oxidised in microbial ferric media, based on the presence of sulphate in the S 2p spectrum, the presence of hydroxide in the O 1s spectrum, and reports of jarosite in other microbial studies. Sandstrom et al. (2005) identified jarosite

on samples oxidised in microbial and non-microbial ferric media, in the presence of potassium. The identification of jarosite was confirmed by XRD analysis.

Copper

Chalcopyrite or metal deficient sulphide have been explicitly or implicitly identified in the Cu 2p spectra of chalcopyrite after oxidative dissolution (Buckley and Woods, 1984; De Filippo et al., 1988a; Hackl et al., 1995; Mikhlin et al., 2004; Sandstrom et al., 2005). Although all of the studies proposed metal deficient sulphide formation, the analyses of the Cu 2p spectra were restricted to the identification of satellite structure to determine whether the copper is monovalent or divalent. De Filippo et al. (1988a), Hackl et al. (1995) and Mikhlin et al. (2004) observed monovalent copper exclusively, while Buckley and Woods (1984) and Sandstrom et al. (2005) observed monovalent and divalent copper. However, Sandstrom et al. (2005) only identified divalent copper in one sample oxidised in microbial ferric media at high potential; the sample oxidised in microbial ferric media at low potential, and the samples oxidised in non-microbial ferric media at high and low potentials, displayed monovalent copper. Nonetheless, neither Buckley and Woods (1984) nor Sandstrom et al. (2005) attributed the divalent copper to phases other than chalcopyrite and metal deficient sulphide.

2.7.2 Summary

X-ray photoelectron spectroscopy has been used to study chalcopyrite surfaces after fracture under anaerobic atmosphere, aerial oxidation and oxidative dissolution. Although similar phases have been proposed for surfaces produced under each set of conditions, these proposals have not been confirmed by quantitative analysis.

2.8 The aims of this study

The aim of the study was to establish mechanisms of dissolution and inhibition for the oxidative dissolution of chalcopyrite in ferric media. The mechanisms were deduced

from kinetic analysis of chalcopyrite during dissolution and quantitative surface analysis of chalcopyrite before and after dissolution.

Kinetic analysis determined the kinetics model (surface or diffusion) of n- and p-type chalcopyrite dissolution in ferric sulphate via rate equations and activation energies. Dissolution rates of n- and p-type chalcopyrite were compared to establish the effect of solution potential. Kinetic models of p-type chalcopyrite dissolution in ferric sulphate and ferric chloride were determined via rate equations and compared to establish the effect of lixiviate on dissolution and inhibition.

Surfaces of chalcopyrite before and after oxidative dissolution were quantitatively analysed by correlating the speciation and relative intensities of the S 2p, Cu 2p and Fe 2p spectra of surfaces fractured in nitrogen, polished in air and oxidised in ferric media. The ferric media included ferric sulphate and ferric chloride at various temperatures and pH values to establish the effect of these conditions on dissolution and inhibition.

The mechanisms of dissolution and inhibition were based on the surface coverage and deposition rate of phases identified by quantitative surface analysis and correlated with changes in dissolution rate identified by kinetics analysis. The mechanisms were also used to account for various phenomena reported for the oxidative dissolution of chalcopyrite in ferric media.

Chapter 3

Experimental

3.1 Chalcopyrite samples for oxidative dissolution

Oxidative dissolution was performed on n- and p-type chalcopyrite flotation concentrates (Con-n and Con-p) and p-type chalcopyrite massive (Mass-p). Con-n was sourced from the Northern Hemisphere, while Mass-p and Con-p were sourced from the Southern Hemisphere. Con-n consisted of 81 % chalcopyrite, 4 % pyrite, 8 % oxides and sulphides and 7 % inert gangue materials (predominantly quartz). The particles had a size range of 1-200 μm, mean particle size of 33 μm, and surface area of 0.421 m^2g^{-1} (determined by nitrogen BET). Con-p consisted of 88 % chalcopyrite, 4 % pyrite and 8 % inert gangue materials (predominantly quartz). The particles had a size range of 1-200 μm, mean particle size of 31 μm, and surface area of 0.268 m^2g^{-1} (determined by nitrogen BET). Mass-p was of high purity and only contained minor inclusions of quartz (Figure 3.1).

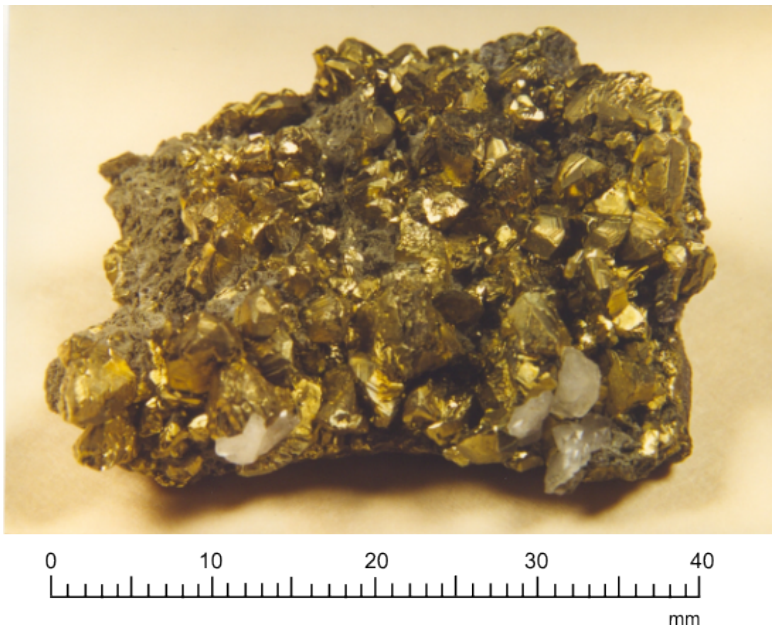

Figure 3.1: *Chalcopyrite massive (Mass-p) used for oxidative dissolution.*

3.2 Chalcopyrite washing and sizing procedures

The chalcopyrite concentrates were washed to remove xanthate flotation reagents and sized to ensure reproducible results before oxidative dissolution. The initial washing and sizing procedures were performed by Dr. Matthew Stott (CSIRO, Minerals) and the final washing procedures were performed by the author.

400 g of chalcopyrite concentrate was added to 4 L of 10% ethanol (GR grade) in de-ionised water (v/v) at room temperature. The concentrate was stirred for 5 minutes and allowed to settle for 10 minutes before the solution was decanted. The remaining concentrate was filtered through a Buchner funnel and then returned to the decanted solution. This washing procedure was repeated twice to ensure thorough mixing of the concentrate and the solution.

The 400 g of chalcopyrite concentrate was then washed with 4 L of de-ionised water at 80°C. Initially, 1 L of de-ionised water was added in increments of 100–200 mL, with stirring and vacuum filtration performed after each addition. Then, 1 L of de-ionised water was added during constant vacuum filtration. This two stage procedure

was repeated. Finally, the concentrate was dried at 60°C overnight and sealed in a polythene bag.

The washed and dried chalcopyrite concentrates were wet sieved to 25-37 μm and analysed using a Malvern Mastersizer 2000. The Con-p particles had a size distribution of 11-90 μm and a mean particle size of 32 μm, while the Con-n particles had a size distribution of 0.5-80 μm and a mean particle size of 33 μm.

20 g of sized chalcopyrite concentrate was washed twice with 200 mL of 10% ethanol (AR grade) in MilliQ® water (v/v) and once with 100 mL of MilliQ® water, both at 80°C. The concentrate was stirred with each addition and then filtered. After the final filtration, the concentrate was washed thoroughly with MilliQ® water at room temperature. Appropriate quantities of concentrate were then weighed and introduced into flasks for oxidative dissolution.

3.3 Chalcopyrite semiconductor typing

The semiconductor typing of the chalcopyrite samples was performed by Dr. Craig Klauber (CSIRO, Minerals) according to the procedure of Shive (1959).

Chalcopyrite concentrate typing was performed on concentrate compacted into 1 cm path length cells (typically used for UV-visible spectroscopy), with electrical contact via gold rods inserted into each end of the cell (Table 3.1). Chalcopyrite massive typing was performed on a sawn piece of known dimensions, with electrical contact via gold rods applied to each end of the massive (Table 3.1).

Table 3.1: *Semiconductor typing of chalcopyrite massive and concentrate samples.*

Sample	**Type**	**Carrier conc. (m^{-3})**	**Mobility ($m^2\ V^{-1}\ s^{-1}$)**	**Resistivity (ohm m)**
Mass-p	p	30.0×10^{21}	2.37×10^{-4}	8.77×10^{-1}
Con-p	p	9.00×10^{21}	7.63×10^{-4}	9.08×10^{-1}
Con-n	n	3.26×10^{21}	1.57×10^{-4}	122×10^{-1}

3.4 Oxidative dissolution of chalcopyrite in ferric media

Solutions for oxidative dissolution were prepared from ferric sulphate and ferric chloride (AR grade) and MilliQ® water. The appropriate pH adjustments were performed using acids of the corresponding anion (AR grade) and a TPS-LC80A pH-mV-temp meter. Solutions were prepared immediately before each set of experiments.

3.4.1 Dissolution of concentrate for kinetic analysis under aerobic atmosphere

3 g of chalcopyrite concentrate was added to 250 mL conical flasks containing 100.0 mL of the appropriate ferric sulphate or ferric chloride solution. The flasks were covered with parafilm to limit evaporation and stirred at 160 rpm in an Innova 4080 incubator shaker maintained at 50, 65 or 80°C. Solution volumes were adjusted for evaporation by addition of MilliQ® water before sampling. 1.00 mL samples were drawn using a Boeco micropipette and acidified with 1.00 mL of concentrated hydrochloric acid (AR Grade) before being analysed for copper using ICP-AES. The copper concentrations reported in Chapter 4 are the averages of experiments performed in duplicate.

3.4.2 Dissolution of concentrate for kinetic analysis under anaerobic atmosphere

3 g of chalcopyrite concentrate and 2.7 g of ferric chloride (AR Grade) were added to 250 mL Schott bottles before insertion into the glove-box. The Schott bottles and pipettes were washed with H_2O or D_2O and then dried at 80°C for a minimum of three hours before use. The glove-box was purged with high purity nitrogen for 2.5 hours. 100.0 mL of H_2O or D_2O was added to each Schott bottle before they were sealed with rubber bungs and screw-top lids. An initial 1.00 mL sample was drawn using a syringe before the bottles were stirred at 160 rpm in an Innova 4080 incubator shaker at 50°C. This sample, along with all subsequent samples, was acidified with 1.00 mL of concentrated hydrochloric acid (AR Grade) before being analysed for copper using

ICP-AES. The copper concentrations reported in Section 7.1.3 are the averages of experiments performed in duplicate.

3.4.3 Dissolution of concentrate for XPS analysis

1 g of pre-washed chalcopyrite concentrate (Section 3.2) was washed twice with 10 mL of 10% ethanol (AR grade) in MilliQ® water (v/v) and once with 10 mL of MilliQ® water, both at 80°C. The concentrate was stirred and filtered after each addition and washed three times with 5 mL of MilliQ® water at room temperature.

0.5 g of the washed chalcopyrite concentrate and 10.00 mL of 0.1 M ferric solution were added to 25 mL conical flasks. The solutions were then stirred at 160 rpm in an Innova 4080 incubator shaker maintained at 50, 65 or 80°C. After the dissolution period, the concentrate was filtered through a 0.3 μm millipore filter paper and washed three times with 5 mL of MilliQ® water at room temperature. The concentrate was then pressed into a stainless steel ESCALAB powder stub and immediately introduced into the spectrometer under laboratory atmosphere.

The pressing dies and stainless steel ESCALAB powder stubs were sonicated in MilliQ® water containing Decon 90® and then rinsed thoroughly with MilliQ® water to prevent cross-contamination between concentrate samples.

3.4.4 Dissolution of massive for XPS analysis

Chalcopyrite massive was sawn into pieces (approximately 1-2 cm^2) using a low-speed, low-pressure diamond saw, mounted onto standard XPS stubs using silver dag, and cured for 3 days. The massive surface was polished using 2000 grit silicon carbide paper that had been sonicated and rinsed in MilliQ® water to remove particulates.

Oxidative dissolution of chalcopyrite massive in ferric sulphate was performed under aerobic atmosphere. The ferric sulphate solution was introduced to the 'in-house' designed overflow-cell made by Dennis Clair (Allirra Glassblowing, Pty Ltd)(Figure 3.2).

The overflow cell contained inner and outer chambers that enabled the solution in the inner chamber to be kept at a constant level. This overcame minor losses of solution from evaporation and ensured the solution remained in contact with the massive for the duration of the dissolution period. The solution was agitated by the constant pumping of the solution and the stirring of a magnetic stirrer bar in the inner chamber. The solution temperature was maintained at 50°C using an IKAMAG RCT Basic hotplate and an external IKATRON ETS-D4 Fuzzy temperature probe. The massive was suspended onto the meniscus of the ferric sulphate solution in the overflow cell and surface tension was used to minimise contact between the solution and the silver dag adhesive and stainless steel stub (Figure 3.2). After the dissolution period, the massive was removed, washed with MilliQ® water (pH 1.9), dried with compressed air, and immediately introduced into the spectrometer under laboratory atmosphere.

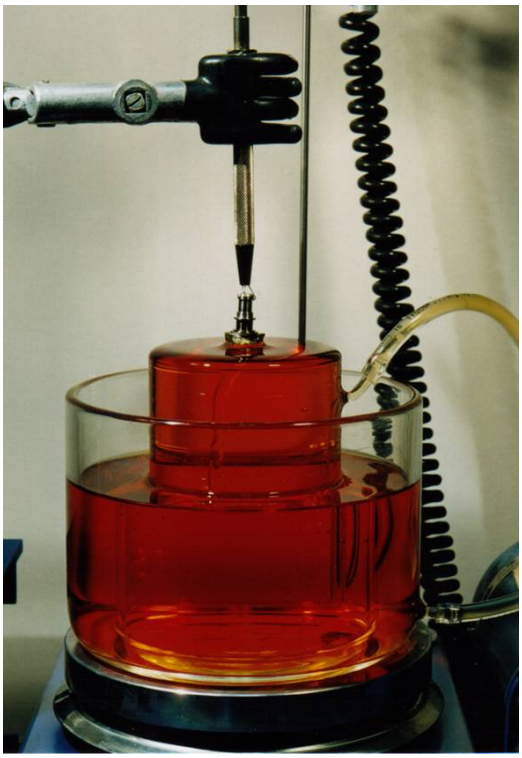

Figure 3.2: *Temperature controlled overflow cell containing ferric sulphate solution in contact with chalcopyrite massive sample.*

Oxidative dissolution of chalcopyrite massive in ferric chloride was performed under anaerobic atmosphere, in a glove-box attached directly to the spectrometer. The glove-box was purged with high purity nitrogen for 90 minutes, with all containers opened, before the ferric chloride solution was prepared. The ferric chloride solid was introduced to the overflow cell and dissolved in MilliQ® water that had been purged with high purity nitrogen for 30 minutes before being introduced into the glove-box. The solution was agitated by the constant pumping of the solution and the stirring of a magnetic stirrer bar in the inner chamber. The solution temperature was maintained at 50°C using an IKAMAG RCT Basic hotplate and an external IKATRON ETS-D4 Fuzzy temperature probe. The massive was suspended onto the meniscus of the ferric chloride solution (as per Figure 3.2). After the dissolution period, the massive was removed, washed with MilliQ® water (pH 1.6), dried with high purity nitrogen, and immediately introduced into the spectrometer under high purity nitrogen atmosphere.

3.5 Standards for XPS analysis

A series of natural and synthetic standards were analysed using XPS (Table 3.2).

Table 3.2: *Origin of the natural and synthetic standards used in the study.*

Standard	Origin	Standard	Origin
Chalcopyrite	Mount Isa, Australia	Hydronium jarosite*	Synthesized 'in-house'
Chalcopyrite	Mount Lyell, Australia	Potassium jarosite*	Synthesized 'in-house'
Chalcopyrite†	Unknown region, Zambia	Sodium jarosite*	Synthesized 'in-house'
Covellite†	Butte, United States of America	Ammonium jarosite*	Synthesized 'in-house'
Bornite	Mary Kathleen, Australia	Ferric sulphate‡	Ajax Chemicals, ¿ 95 %
Chalcocite	Unknown	Potassium sulphite†	Aldrich, 95 %
Cuprite	Unknown	Potassium thiosulphate†	Aldrich, 95 %
Hematite†	Unknown	Potassium sulphate	B.D.H., 99.5 %
Magnetite†	Unknown	Calcium carbonate	B.D.H., 99.5 %
Goethite†	Unknown	Titanium dioxide	Aldrich, 99.9 %
Alumina	Alcoa World Alumina, Australia		

*Jarosite standards synthesized by Ms. Felicia Lee (Lee, 2001).

†Standard spectra acquired by Dr. Craig Klauber.

‡Ferric sulphate analysed immediately after being kept at 80°C for 24 hours.

The natural standards, mortar and pestle, stainless steel ESCALAB powder stubs, pressing dies, spatula and tweezers were sonicated in MilliQ® water containing Telcon® (a neutral pH detergent) before being dried with compressed air and inserted into the glove-box attached directly to the spectrometer. The glove-box was then purged with high purity nitrogen for 90 minutes. After this period, each sample was crushed using the mortar and pestle and pressed into a stainless steel ESCALAB powder stub. The sample was then transferred directly into the spectrometer under high purity nitrogen atmosphere.

The synthetic standards were also pressed into stainless steel ESCALAB powder stubs. The stainless steel ESCALAB powder stubs, pressing dies, spatulas and tweezers, were sonicated in MilliQ® water containing Telcon® (a neutral pH detergent) before the standards were pressed. Once pressed, the standards were transferred directly into the spectrometer under laboratory atmosphere.

The standard spectra are presented in Appendices A and B.

3.6 Analytical Techniques

Solid samples were analysed using X-ray photoelectron spectroscopy. Solution samples were analysed using Raman, infrared and ultraviolet-visible spectroscopy. Solubilised copper was measured using ICP-AES.

3.6.1 X-ray photoelectron spectroscopy

X-ray photoelectron spectra were obtained using a VG ESCALAB Mk II (nominal base pressure $< 10^{-10}$ mbar) retrofitted with multiple channeltron electron detection and an SSI Al K_α monochromated source, in addition to the original Mg K_α and Al K_α twin anode source. Mg K_α (1253.6 eV) spectra were obtained at a source power of 300 W irradiated over the whole sample. Mg K_α radiation was used to avoid overlap of the Fe 2p photoelectron line ($\sim$ 710 eV) with the Cu $L_3M_{4,5}M_{4,5}$ Auger line ($\sim$ 712 eV, using

Al K_α radiation). Analyser slits of 6 mm and a constant analyser pass energy of 20 eV were used. The spectrometer was calibrated using the Ag $3d_{5/2}$ line at 368.29 eV, the Au $4f_{7/2}$ line at 84.00 eV (Seah, 1989), and a wide range linearity check using the Cu 2p line. In all cases argon etched polycrystalline foils were used for calibration.

All samples were analysed within 90 minutes of introduction into the spectrometer. This time constraint was imposed by the degassing of samples in each of the chambers. The fast entry lock chamber was evacuated to 10^{-5} mbar, before the sample was transferred to the preparation chamber; the sample was kept at ambient temperature in both chambers. Once the pressure in the preparation chamber was 10^{-7}–10^{-8} mbar, the sample was transferred to the analysis chamber and onto the cooling stage ($\sim$ 150 K). The cooling stage was used to minimise volatilisation, thermal effects and radiation damage. The analysis was begun once the pressure was in the 10^{-10} mbar range, and cooling was maintained for the duration of the analysis.

The spectral regions were examined as follows: S 2p, Cu 2p, Fe 2p, O 1s, Cu $L_3M_{4,5}M_{4,5}$, O $KL_{2,3}L_{2,3}$, C 1s and full survey. This sequence minimised radiation damage to the sulphur species before acquisition of the S 2p spectra. The remaining order was determined by the relative interest of each spectrum. Spectra were obtained with a 0.1 eV channel width and a 100 ms dwell time per channel. The number of channels and scans used for each region were varied to ensure all high energy X-ray satellite structure was acquired. The regions scanned were at least 30 eV for S 2p, O 1s, O $KL_{2,3}L_{2,3}$ and C 1s spectra, 80 eV for Cu 2p and Fe 2p spectra, and 40 eV for Cu $L_3M_{4,5}M_{4,5}$ spectra. Samples were irradiated over a 90 minute period, with the S 2p spectra acquired within the first 12 minutes.

Static charging shifts were not observed for chalcopyrite samples, with both Con-p concentrate and Mass-p massive displaying excellent surface and bulk conductivity. However, this does not preclude minor spectrometer work function shifts altering observed binding energies, despite regular calibration.

3.6.2 Raman Spectroscopy

Raman spectra were acquired using a Dilor Labram-1B spectrometer. Solution samples were introduced into a 1 cm path length quartz cell and placed in a solution sample holder fitted with a spherical back-reflecting mirror. An argon (514.532 nm) laser was used at up to 30 mW. All spectra were acquired using an 1800 g mm^{-1} grating. Wavelength calibrations were performed using a neon lamp.

3.6.3 Infrared Spectroscopy

Solid spectra were acquired using a Bruker IFS-66 Fourier Transform Infrared Spectrometer over 256 scans at 4 cm^{-1} resolution with an MCT detector. Freeze dried oxidative dissolution residues were spread across potassium bromide plates that had been pressed under 3200 kg cm^{-2}.

Solution spectra were acquired using a Bruker IFS-66 Fourier Transform Infrared Spectrometer over 256 scans in absorbance mode at 4 cm^{-1} resolution with an MCT detector and a Grasby Specac AMTIR ATR accessory. The chamber was purged at 1000 L h^{-1} for 5 minutes, followed by 100 L h^{-1} for 5 minutes. Background and sample spectra were recorded until water and carbon dioxide levels were constant within 1-2 milli absorbance units. A blank of MilliQ® water was run before the first sample. MilliQ® water was also used to clean the ATR crystal before each sample.

3.6.4 Ultraviolet-visible Spectroscopy

Solution spectra were acquired using a Hewlett Packard 8452 A Diode Array-Spectrometer and a 1 cm path length glass cell.

3.6.5 Inductively Coupled Plasma-Atomic Emission Spectroscopy

Solutions were analysed for copper using a Varian Liberty 220 Inductively Coupled Plasma-Atomic Emission Spectroscopy. The solution uptake time was 18 seconds, and the solution washout time was 15 seconds. The spectra were recorded with the plasma located in the axial position.

Chapter 4

Kinetics of the oxidative dissolution of chalcopyrite in ferric media

The kinetics of chalcopyrite dissolution in ferric sulphate and ferric chloride were investigated to address aspects of dissolution, including the contrary reports of diffusion controlled kinetic models and surface controlled activation energies, the enhanced dissolution at low solution potential, and the enhanced dissolution in ferric chloride, relative to ferric sulphate. The kinetic models and the associated activation energies were determined for the oxidative dissolution of n- and p-type chalcopyrite (Con-n and Con-p, respectively) in ferric sulphate. Additionally, the kinetic model for the oxidative dissolution of p-type chalcopyrite in ferric chloride was determined and compared with the model determined for dissolution in ferric sulphate. The determinations were analysed to provide insight into the mechanisms of chalcopyrite dissolution and inhibition in ferric media.

4.1 Oxidative dissolution of chalcopyrite concentrate in ferric sulphate

The copper releases of Con-n and Con-p dissolution in 0.1 M ferric sulphate (pH 1.9) for 72 hours at 30, 50, 65 and 80°C compare favourably with reported data (Section 2.5), displaying a dramatic decrease in dissolution rate and the emergence of a second stage, depending on the extent of dissolution (Figures 4.2 - 4.1). The dissolution rates increase with temperature, but are also dependent on semiconductor type, with Con-n and Con-p displaying 15 and 5 % copper release, respectively, after 72 hours at 50°C. However, the effect of semiconductor type is not evident at higher temperatures, with Con-n and Con-p both displaying $\sim$ 30 % copper release after 72 hours at 80°C.

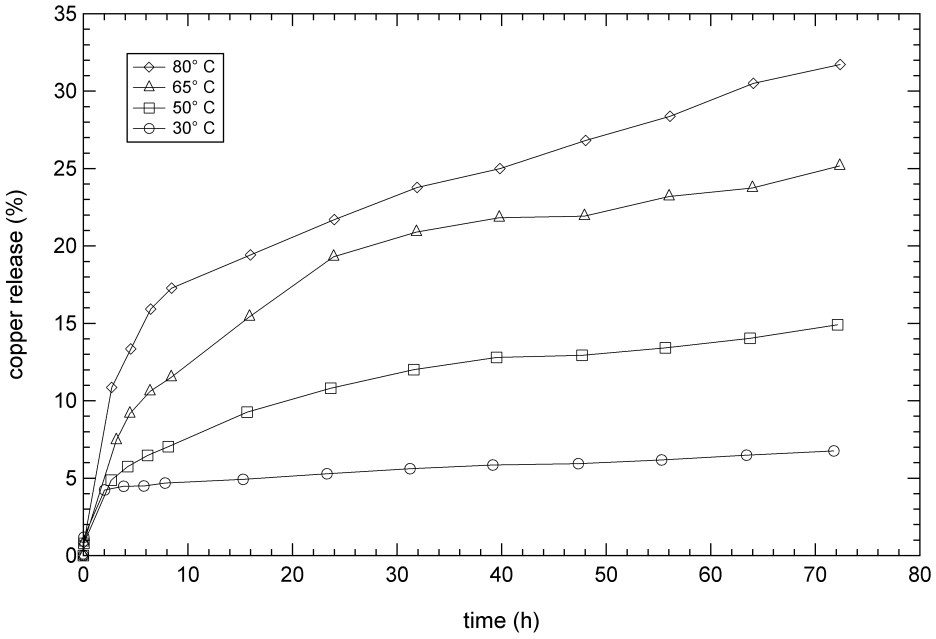

Figure 4.1: *Copper release of chalcopyrite (Con-n) during oxidative dissolution in 0.1 M ferric sulphate (pH 1.9) at 30, 50, 65 and 80° C for 72 hours.*

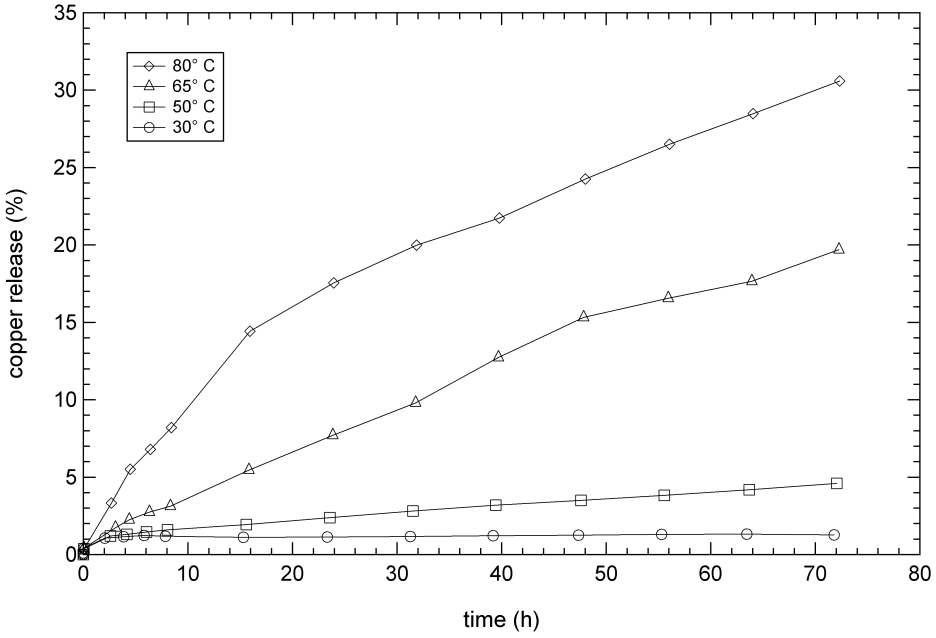

Figure 4.2: *Copper release of chalcopyrite (Con-p) during oxidative dissolution in 0.1 M ferric sulphate (pH 1.9) at 30, 50, 65 and 80° C for 72 hours.*

4.2 Kinetic model determination

The kinetic model of each dissolution stage (surface vs. diffusion control) was assessed by applying rate equations to the copper release data and establishing whether linear relationships were displayed. The equations were also used to determine whether dissolution was in 2- or 3-dimensions (Sharp et al., 1966; Galwey and Brown, 1995):

Surface control:	$1-(1-\alpha)^{1/2}$	(2-dimensions)	(4.1)
Surface control:	$1-(1-\alpha)^{1/3}$	(3-dimensions)	(4.2)
Diffusion control:	$(1-\alpha)ln(1-\alpha)+\alpha$	(2-dimensions)	(4.3)
Diffusion control:	$[1-(1-\alpha)^{1/3}]^2$	(3-dimensions)	(4.4)

Where α = fraction reacted.

The surface and diffusion control equations were applied to the copper release data observed for Con-n and Con-p dissolution at 50, 65 and 80°C; the copper release data observed at 30°C was deemed too low for reliable analysis. The initial copper release data points for all samples were excluded to ensure the analysis was based on data acquired once the samples had reached thermal equilibrium, lost possible surface contaminants, and commenced the governing reaction.

The surface and diffusion plots reveal all of the copper release data obeys surface control in 3-dimensions (Figures 4.4 - 4.7). The surface control plots display strong linear relationships for either one or two stages, depending on the extent of dissolution. The diffusion control plots are non-linear and display an increase over time, which is consistent with the diffusion plots previously reported (Section 2.5).

A second stage of dissolution was observed for Con-n at 50, 65 and 80°C, and Con-p at 65 and 80°C. The emergence of a second stage is attributed to partial coverage of the chalcopyrite surface by an inhibiting deposition phase. Although the exposed chalcopyrite surface available for dissolution is diminished, the dissolution reaction remains governed by surface control kinetics (Figure 4.9). The abrupt decrease in copper release rate (after 16–48 hours) implies the phase deposits rapidly, but only on parts of the surface, rather than forms slowly over the entire surface. If surface coverage becomes complete, the kinetics may become diffusion controlled; however, the kinetics observed for the second stage of dissolution – equating to $\sim$ 30 % copper release after 72 hours at 80°C – remain surface controlled.

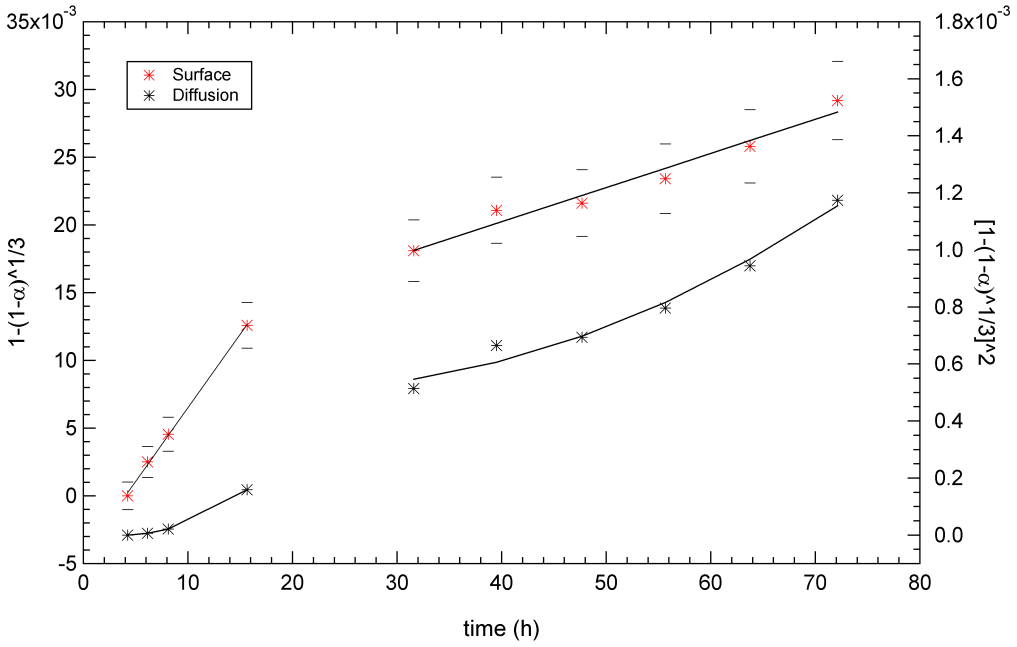

Figure 4.3: *Surface and diffusion control plots of copper release of chalcopyrite (Con-n) during oxidative dissolution in 0.1 M ferric sulphate (pH 1.9) at 50° C.*

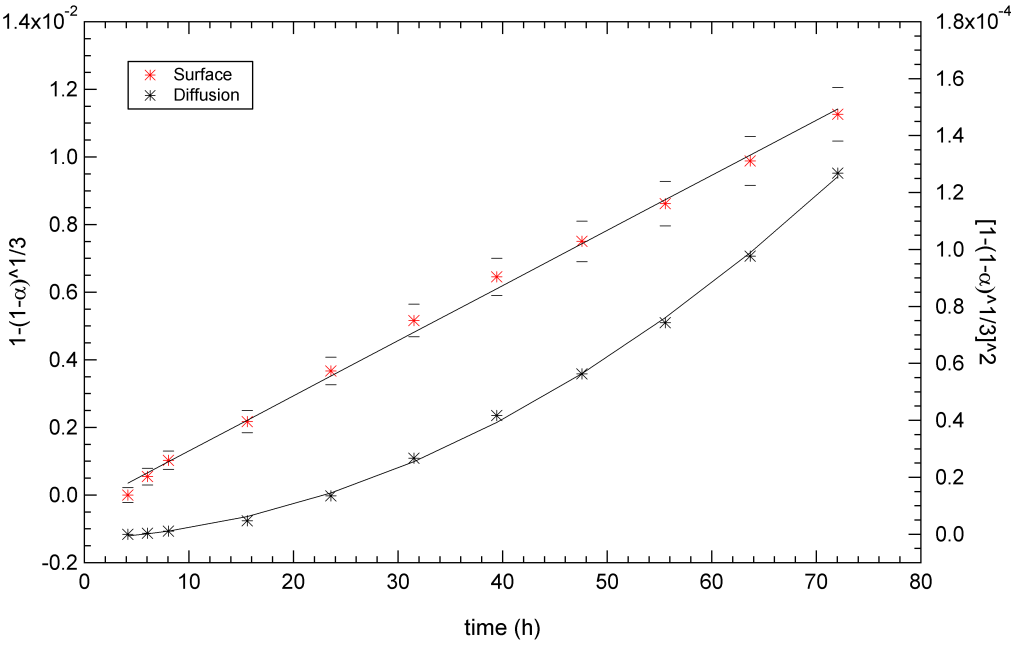

Figure 4.4: *Surface and diffusion control plots of copper release of chalcopyrite (Con-p) during oxidative dissolution in 0.1 M ferric sulphate (pH 1.9) at 50° C.*

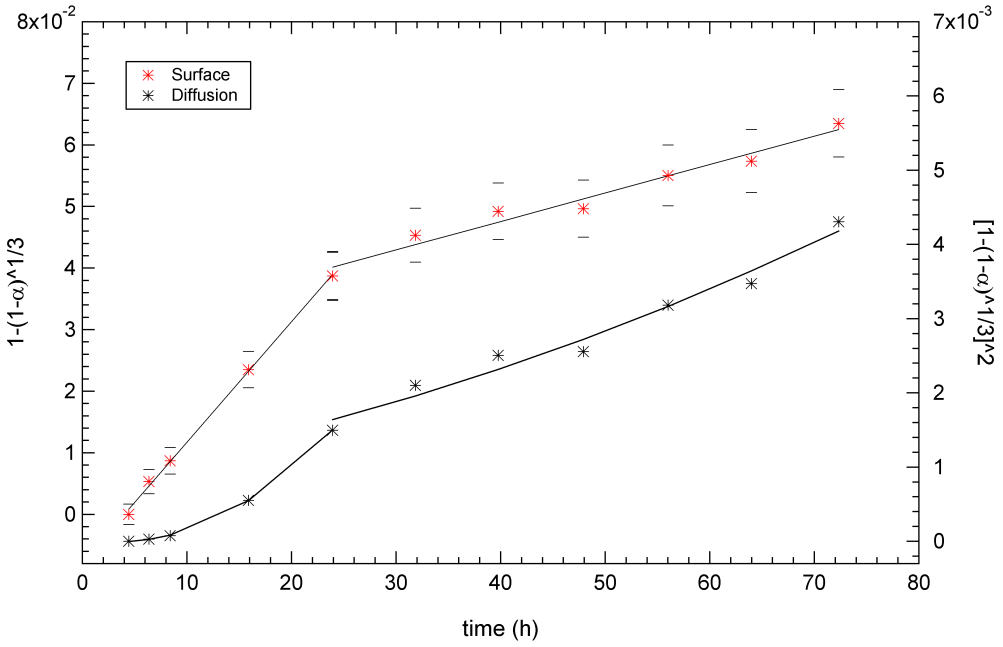

Figure 4.5: *Surface and diffusion control plots of copper release of chalcopyrite (Con-n) during oxidative dissolution in 0.1 M ferric sulphate (pH 1.9) at 65° C.*

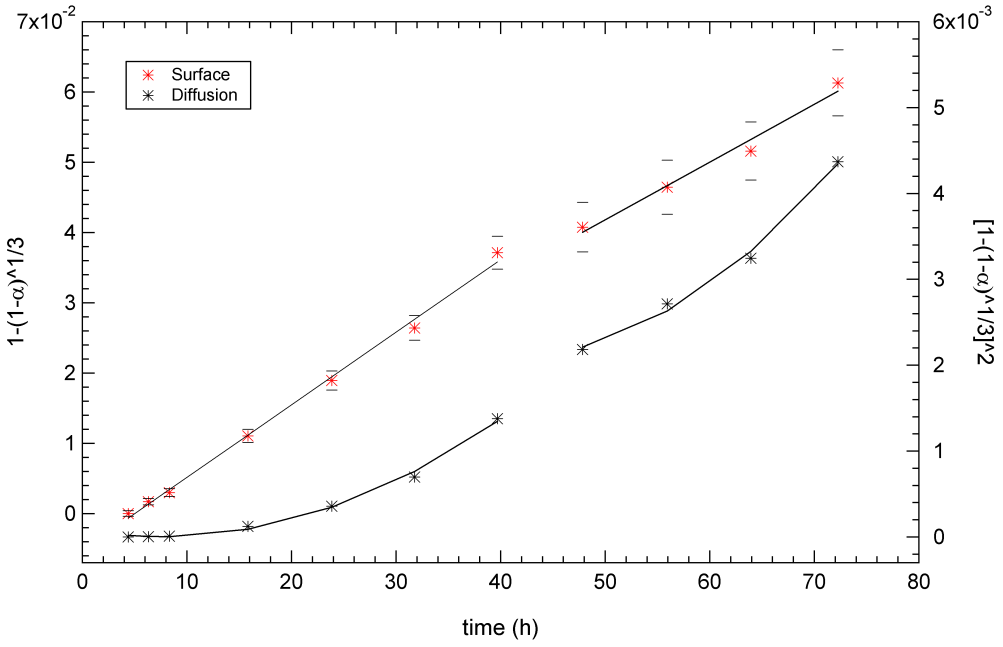

Figure 4.6: *Surface and diffusion control plots of copper release of chalcopyrite (Con-p) during oxidative dissolution in 0.1 M ferric sulphate (pH 1.9) at 65° C.*

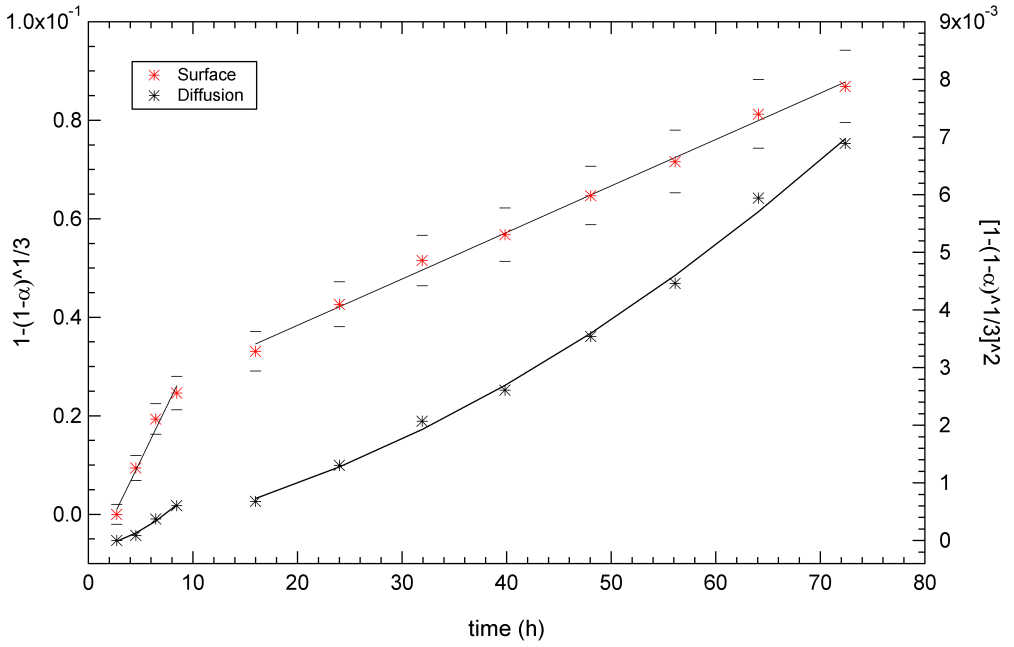

Figure 4.7: *Surface and diffusion control plots of copper release of chalcopyrite (Con-n) during oxidative dissolution in 0.1 M ferric sulphate (pH 1.9) at 80° C.*

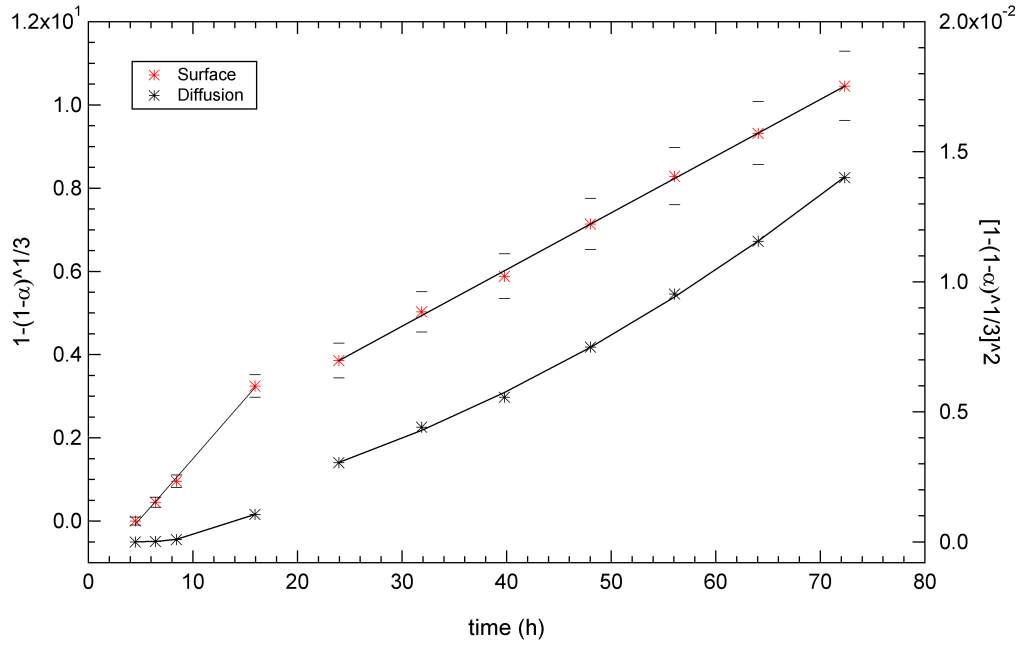

Figure 4.8: *Surface and diffusion control plots of copper release of chalcopyrite (Con-p) during oxidative dissolution in 0.1 M ferric sulphate (pH 1.9) at 80° C.*

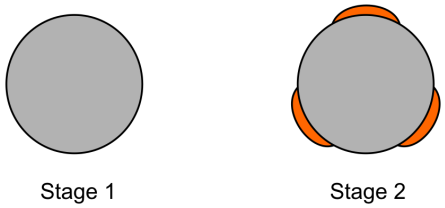

Figure 4.9: *Chalcopyrite surface area decrease after phase deposition to establish Stage 2 of dissolution.*

4.3 Activation energy determination

Activation energies were calculated for Stages 1 and 2, at both temperature combinations (50 & 65°C and 65 & 80°C), for Con-n, but only Stage 1, at both temperature combinations, for Con-p. Although a second stage was identified at 65°C for Con-p (Figure 4.6), the subtle change in dissolution rate suggests this stage may be transitional. The activation energies determined (36–112 kJ mol^{-1}, Table 4.1) compare favourably with reported energies (38–84 kJ mol^{-1}, Table 2.1) and confirm each stage of dissolution obeys surface control kinetics.

Table 4.1: *Activation energies (kJ mol^{-1}) observed for the oxidative dissolution of chalcopyrite (Con-n and Con-p) in 0.1 M ferric sulphate (pH 1.9).*

Sample	Stage	50°C, 65°C	65°C, 80°C
Con-n	**1**	36 +/- 3	53 +/- 9
	2	39 +/- 11	48 +/- 7
Con-p	**1**	112 +/- 3	68 +/- 4

The activation energies of Con-n for both stages, at each temperature combination (50 & 65°C and 65 & 80°C), are within experimental error of each other (Table 4.1). This implies one reaction is governing both stages of dissolution at each temperature. However, the activation energies for both stages increase for the higher temperature combination. Although the increases are only marginally beyond the experimental error, the trend is consistent with the results of Ferreira and Burkin (1975), which show

a dramatic increase in activation energy with an increase in temperature. Ferreira and Burkin (1975) attribute this increase to a change in dissolution kinetics from diffusion control at low temperatures to surface control at high temperatures. Although this is consistent with their activation energies (6.3 and 83 kJ mol^{-1}), the activation energies and kinetic models determined in this study do not suggest a change in kinetic model is appropriate.

The increase in activation energy observed for Con-n with an increase in temperature is attributed to the deposition of an inhibiting phase onto the mineral surface. This deposition produces a decrease in dissolution rate because partial coverage of the surface diminishes the effective surface area available for dissolution but ensures the kinetics remain surface controlled for both stages. The partial coverage means the dissolution rate does not increase commensurately with the increase in temperature, and the associated activation energy (which is determined by the dissolution rates), increases (Figure 4.10). The partial coverage of the surface – which has been confirmed by XPS analysis (Chapter 6) – implies the inhibiting phase deposits from solution onto particular surface phases. This suggests a nucleation mechanism with the inhibiting phase forming a non-impervious layer at the surface before nucleation. The increase in activation energy with an increase in temperature implies the stability of this inhibiting phase increases with temperature.

The activation energies of Con-p also displayed a similarly strong relationship with temperature; however, a decrease was observed for the higher temperature combination. This decrease can be attributed to the effect of semiconductor type and temperature on dissolution rates.

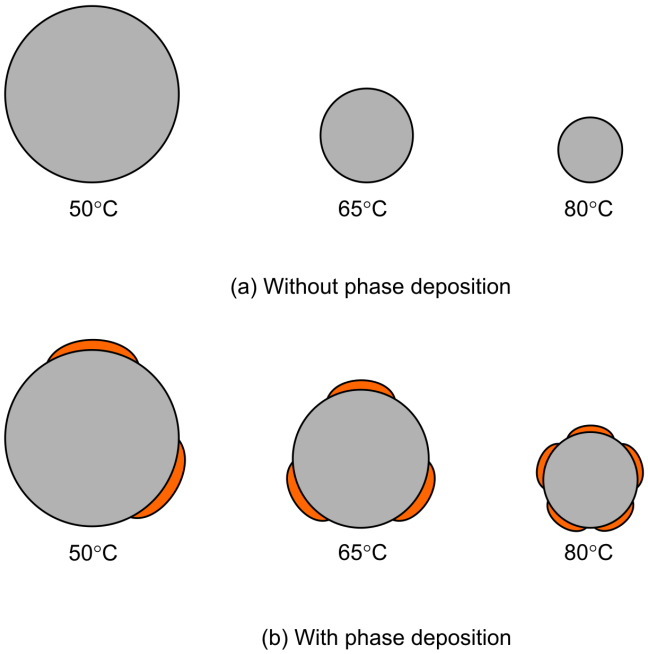

Figure 4.10: *Chalcopyrite surface area decrease after phase deposition at 50, 60 and 80° C after time x of oxidative dissolution: a) without phase deposition the dissolution rate is proportional to the surface area of the sphere; while b) with phase deposition the dissolution rate is proportional to the partial surface area of the sphere.*

4.4 Effect of semiconductor type and temperature on oxidative dissolution

The activation energies determined for Stages 1 and 2 reveal a strong relationship between temperature and semiconductor type, and dissolution rate. At low temperatures (50 & 65°C) the rate of dissolution of Con-n (n-type) produced an activation energy less than half that observed for Con-p (p-type). This is consistent with the higher resistivity of Con-n (Section 3.3) because resistivity is imparted by crystal defects, which imbue greater reactivity (Majima et al., 1985; Vaughan, 1995). However, at higher temperatures (65 & 80°C) the reactivities become comparable, with the Stage 1 activation energies for Con-n and Con-p almost within experimental error of each other.

Table 4.2: *Reaction rates (k) observed for the oxidative dissolution of chalcopyrite (Con-n and Con-p) in 0.1 M ferric sulphate (pH 1.9) at 50, 65 and 80° C.*

Stage	Sample	50°C	65°C	80°C
1	**Con-n**	1.088	1.957	4.638
	Con-p	0.163	1.033	2.873
	Ratio	**6.671**	**1.894**	**1.614**
2	**Con-n**	0.322	0.608	1.254
	Con-p	0.148	0.822	1.364
	Ratio	**2.176**	**0.739**	**0.919**

The comparable dissolution rates of Con-n and Con-p at 80°C suggest temperature has an additional role for Con-p. This additional role is the promotion of electrons to the top of the valence band because the removal of these electrons determines the rate of dissolution (Section 2.2.2). The high rate of dissolution for the n-type chalcopyrite is because of its excess of electrons, which ensures the top of the valence band is filled with electrons. However, the top of the valence band for the p-type chalcopyrite only becomes occupied at higher temperatures because of its deficiency of electrons. The increase in dissolution rate observed as the upper valence band of the p-type chalcopyrite becomes occupied is consistent with the greater dissolution observed at low solution potentials, due to the greater overlap of the occupied states of the valence band and unoccupied states of the ferric ion (Section 2.2.2).

The effect of semiconductor type and temperature (along with crystal defects and solution potential) on dissolution rate decreases during Stage 2, after the deposition of the inhibiting phase. Although the ratios of the Con-n and Con-p dissolution rates are large during Stage 1 (6.67, 1.89, 1.61), they are much smaller during Stage 2 (2.18, 0.74, 0.92) at 50, 65 and 80°C, respectively (Table 4.2). Therefore, optimal dissolution rates depend on establishing conditions that delay and diminish (if not eliminate) deposition of the inhibiting phase.

4.5 Effect of lixiviate on oxidative dissolution

The kinetics of Con-p dissolution in ferric chloride and ferric sulphate systems were compared to determine whether the enhanced dissolution reported for ferric chloride systems is because of a difference in the mechanisms of dissolution and inhibition, or the extent of inhibition (Section 2.5).

The copper releases of Con-p dissolution in ferric chloride and ferric sulphate (both 0.2 M in ferric) at pH 1.6 and 1.9, respectively, and 50°C are ~ 9 % and ~ 4 %, respectively, and confirm the enhanced dissolution reported for ferric chloride (Figure 4.11, Section 2.5). The greater dissolution in the ferric chloride system produces a second stage of dissolution, while only one stage is observed in the ferric sulphate system.

The kinetic model determination for the ferric chloride system reveals both stages are surface controlled (Figure 4.12). Although the kinetic model plots are not definitive, the higher dissolution rates imply largely unimpeded dissolution, and the reported activation energies for ferric chloride systems, which correspond to surface control (Table 2.1), all suggest dissolution in ferric chloride is surface controlled. The second stage of dissolution implies that contrary to previous reports (Section 2.5), ferric chloride systems do undergo inhibition. This inhibition is assumed to be comparable to the inhibition observed in the ferric sulphate system, with the mineral surface partially covered by deposition phases. However, the dissolution rates of the ferric chloride system ($k = 1.37$ and 0.22 for Stages 1 and 2, respectively) indicate the inhibition is less than in the ferric sulphate system ($k = 0.16$ for Stage 1) (Table 4.3). Thus, the inhibition mechanism is common to both systems, but the extent of inhibition is lower in the ferric chloride system.

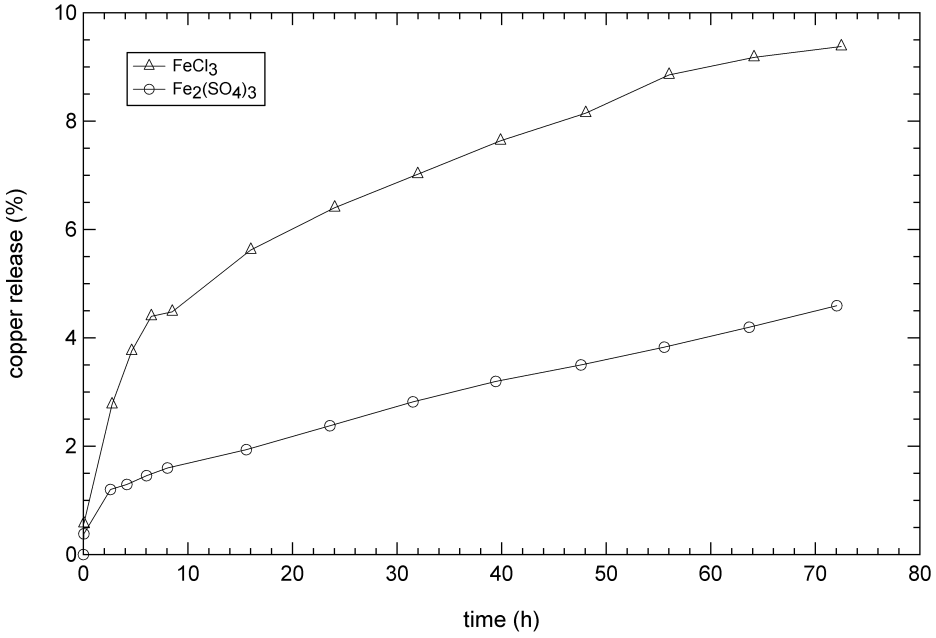

Figure 4.11: *Copper release of chalcopyrite (Con-p) during oxidative dissolution in 0.2 M ferric chloride (pH 1.6), and 0.1 M ferric sulphate (pH 1.9), at 50° C.*

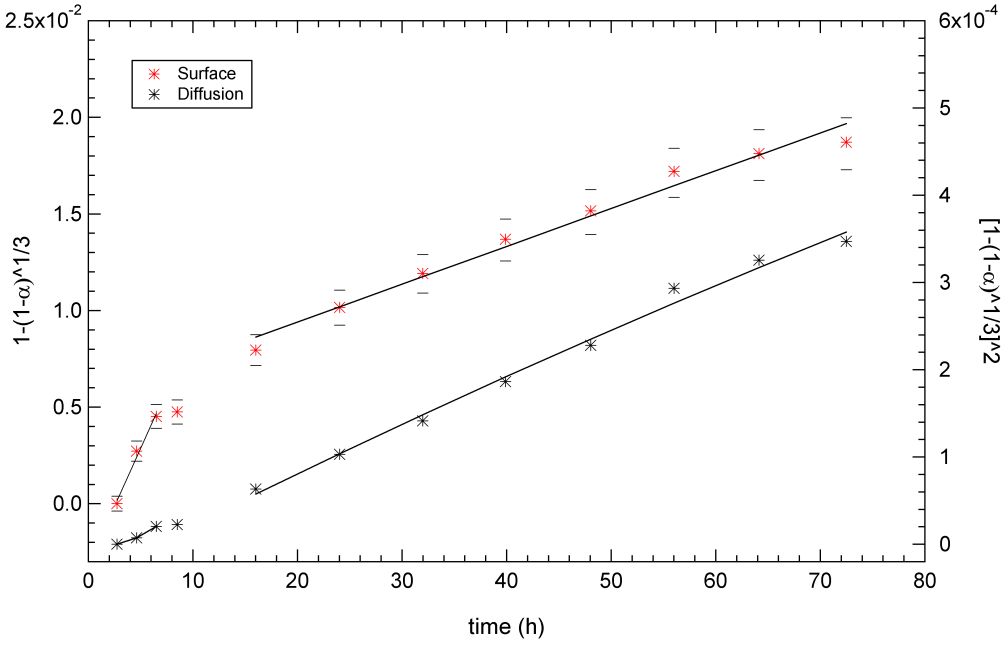

Figure 4.12: *Surface and diffusion control plots of copper release of chalcopyrite (Con-p) during oxidative dissolution in 0.2 M ferric chloride (pH 1.6) at 50° C. The data point at 8 hours has not been fitted because it is considered an outlier.*

Table 4.3: *Reaction rates (k) observed for the oxidative dissolution of chalcopyrite (Con-p) in 0.2 M ferric chloride (pH 1.6) and 0.1 M ferric sulphate (pH 1.9) at 50° C.*

Lixiviate	Stage 1	Stage 2
$\mathbf{FeCl_3}$	1.369	0.224
$\mathbf{Fe_2(SO_4)_3}$	0.163	-

The presence of two surface controlled dissolution stages in ferric chloride and ferric sulphate systems implies the mechanisms of dissolution and inhibition are common to both systems. Furthermore, the lower inhibition of the ferric chloride system implies an iron sulphate is responsible for inhibition. Therefore, the mechanism of inhibition involves an iron sulphate depositing onto the chalcopyrite surface and decreasing the surface area available for dissolution. The enhanced dissolution rate of the ferric chloride system is attributed to lower quantities of the iron sulphate, which only exists in the ferric chloride system after oxidation of the chalcopyrite (Section 2.3). This conclusion is consistent with reports of the deleterious effect of sulphate addition to the dissolution rates observed in ferric chloride systems (Section 2.5).

4.6 Summary

The kinetics of the oxidative dissolution of chalcopyrite reveal the rates are largely governed by an inhibiting deposition phase. This deposition produces two distinct stages because partial coverage of the surface reduces the effective surface area available for dissolution. The partial coverage ensures the kinetics remain surface controlled, which is consistent with the kinetic model and activation energy determinations. The effect of the deposition is apparent in the comparison of the oxidative dissolution of Con-n (n-type) and Con-p (p-type) chalcopyrite. Although dissolution of Con-n is favoured during the first stage, the dissolution of Con-p becomes comparable during the second stage, after deposition, particularly at high temperatures. The dissolution rates of the ferric sulphate and ferric chloride systems also become closer during the second stage, after deposition. Before deposition, however, the dissolution rate in the

ferric chloride system is much greater. This enhanced dissolution rate is attributed to the diminished deposition of the inhibiting phase, which is speculated to be an iron sulphate.

Chapter 5

XPS data analysis

Quantitative analysis of chalcopyrite before and after oxidative dissolution required the correlation of observed and predicted photoelectron intensities. The photoelectron intensities were ascertained by determining the spectral envelopes and relative intensities of each photoelectron line, for both standards and samples. Once the spectral envelope was determined, curve fitting or factor analysis was performed to establish the phase contributions. The curve fitting and factor analysis were based on a suite of standards, including chalcopyrite and deposition phases. The predicted photoelectron intensities were determined using inelastic mean free path (IMFP) and spectrometer calculations. These calculations were adjusted to correlate the observed and predicted intensities for the suite of standards. The adjusted IMFP and spectrometer calculations were then used to predict the relative contribution of each phase towards each photoelectron line, for a suite of models composed of deposition phases overlaying chalcopyrite. These models were based on the spectral analysis of chalcopyrite fractured under anaerobic atmosphere and polished under aerobic atmosphere. The intensities associated with each model, determined using the IMFP and spectrometer calculations, were then used to establish the suite of models required to produce the photoelectron intensities observed for each sample. The suite of models were combined to construct profiles of the chalcopyrite surface after oxidative dissolution in ferric media.

5.1 Determining spectral envelopes

Spectral envelopes were determined by background removal, and in some cases spin-orbit splitting and X-ray source asymmetry removal, using an 'in-house' program (SpecProc). This processing determined spectral intensities and produced spectral envelopes for further analysis. The spectral envelopes include the S 2p, Cu 2p, Fe 2p, O 1s photoelectron lines and the O $KL_{2,3}L_{2,3}$ Auger line.

5.1.1 S 2p spectral analysis

The S 2p spectral envelopes and intensities were determined by Shirley background removal, X-ray source asymmetry removal, spin-orbit splitting removal, and the intensity removal of silicon peaks for concentrate samples. An adjusted Shirley background (SpecProc) containing a Shirley background in combination with a linear segment was applied to all spectra (Figure 5.1). The adjustment minimised the dip observed at higher binding energies produced with the unadjusted Shirley background correction. While there was no fundamental basis for the introduction of the linear segment, it produced a more accurate reflection of the contribution for a broad peak at $\sim$ 169 eV. The background correction boundary points were at higher binding energies to the peak at $\sim$ 169 eV and at lower binding energies to the satellite structure at $\sim$ 148 eV (Figure 5.1). Once the background was subtracted, the spin-orbit splitting and X-ray source asymmetry were removed. The spin orbit splitting removal was performed with a separation of 1.19 eV and an intensity ratio of 2:1 for the S $2p_{3/2}$ and S $2p_{1/2}$ lines. The X-ray source asymmetry removal was performed with a Fourier de-convolution of an appropriate response function developed by Klauber (1993). This processing produced the final envelope for all samples, except chalcopyrite concentrate samples. The processed S 2p spectra of chalcopyrite concentrate (Con-p) samples contained residual Si 2s peaks from silica between 150 eV and 155 eV. The intensity of these residual peaks was determined and subtracted from the total S 2p envelope intensity to produce the intensity of the sulphur peaks exclusively.

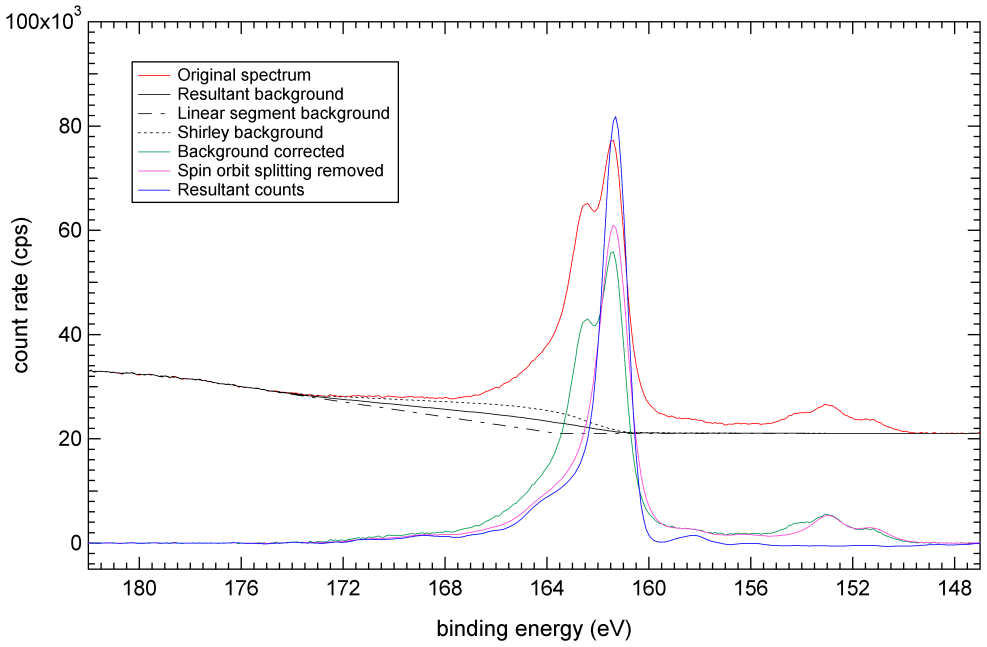

Figure 5.1: *S 2p spectrum processing procedure.*

5.1.2 Fe 2p spectral analysis

The Fe 2p spectral envelopes and intensities were determined by unadjusted Shirley background removal (SpecProc) because the multiple state contributions to the spectra made spin-orbit splitting and X-ray source asymmetry removal relatively intractable (Figure 5.2). The boundary points for the unadjusted Shirley background were at lower binding energies to the satellite structure at $\sim$ 690 eV, and at 759.3 eV. The boundary point at 759.3 eV was determined from quantitative analysis of anaerobically fractured chalcopyrite (Section 5.3) because the broad contribution of O $KL_{23}L_{23}$ Auger peaks towards the Fe 2p spectral envelope made the high binding energy boundary point difficult to identify. The unadjusted Shirley background was used for the Fe 2p spectra because of the breadth of the spectral envelope and the peaks it contained.

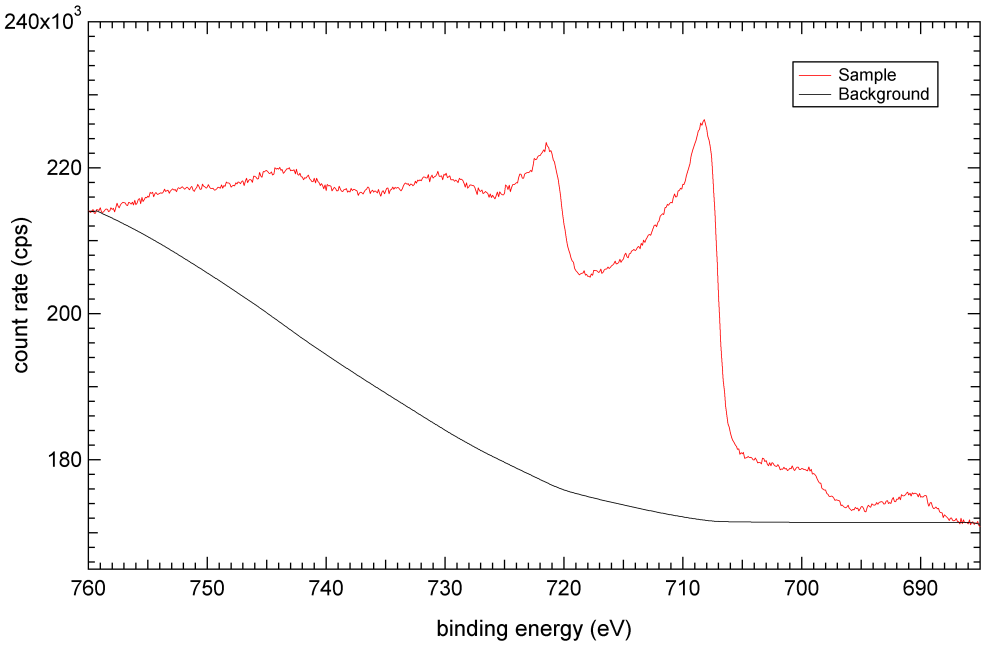

Figure 5.2: *Fe 2p spectrum processing procedure.*

5.1.3 Cu 2p spectral analysis

The Cu 2p spectral envelopes and intensities were determined by adjusted Shirley background removal and X-ray source asymmetry removal (SpecProc)(Figure 5.3). Spin orbit splitting was not removed because of multiple state contributions to the spectra and because peak fitting was not performed on the subsequent spectral envelope. The boundary points for the adjusted Shirley background were 16.00 eV to the lower binding energy of the Cu $2p_{3/2}$ peak and 8.00 eV to the higher binding energies of the Cu $2p_{1/2}$ peak. These boundary points ensured all major satellite structure was included, and all intensities were comparable, regardless of the binding energy of the Cu $2p_{3/2}$ and Cu $2p_{1/2}$ peaks. The adjusted Shirley background was used for consistency with the S 2p spectrum processing involved in Cu 2p cross section adjustment (Section 5.5.1.3), although the effect of the background adjustment is negligible.

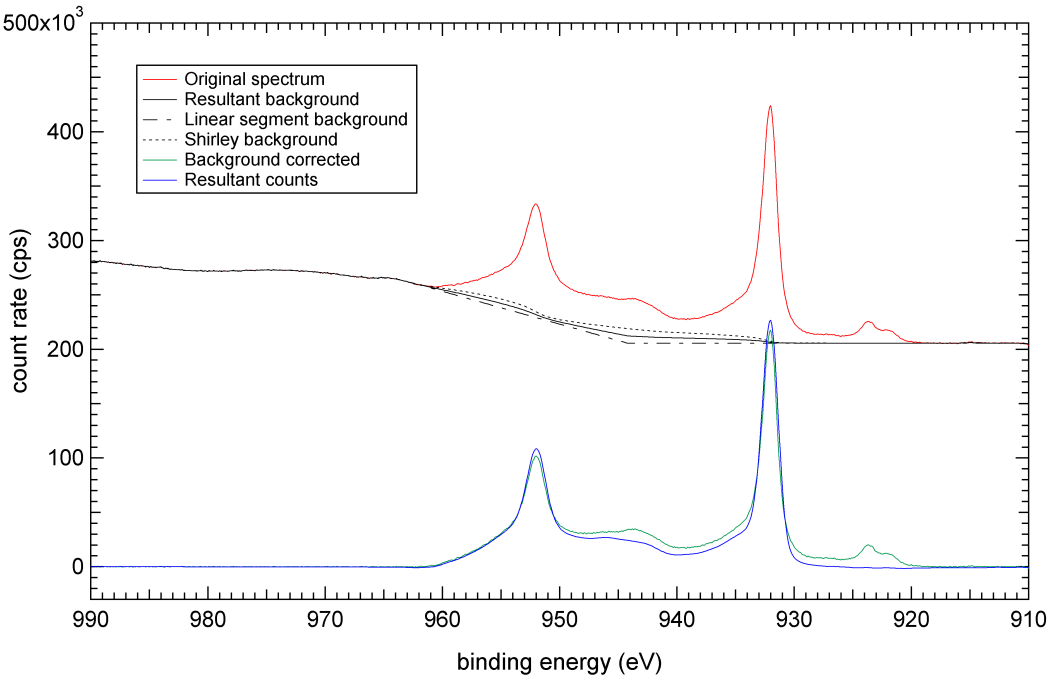

Figure 5.3: *Cu 2p spectrum processing procedure.*

5.1.4 O 1s spectral analysis

The O 1s spectral envelopes and intensities were determined by unadjusted Shirley background removal (SpecProc) to account for the breadth of the peaks and to ensure consistency for all background corrections used for the Fe 2p cross section adjustment including the Fe 2p, O 1s and O $KL_{2,3}L_{2,3}$ spectra (Figure B.11 and Section 5.5.1.3).

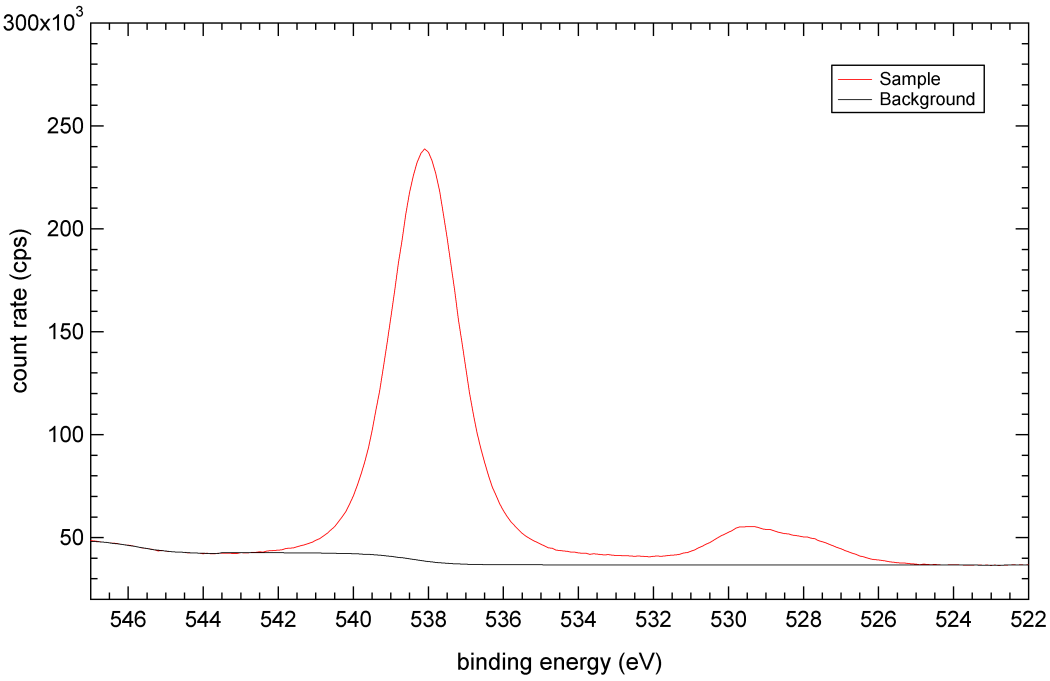

Figure 5.4: *O 1s spectrum processing procedure.*

5.1.5 C 1s spectral analysis

The C 1s spectra binding energies were determined using a Gaussian peak maximum function (SpecProc). Shirley background corrections were not performed before these determinations.

5.1.6 Auger spectral analysis

The O $KL_{2,3}L_{2,3}$ spectral envelopes and intensities were determined by unadjusted Shirley background removal (SpecProc) to account for the breadth of the peaks and to ensure consistency for all background corrections used for the Fe 2p cross section adjustment including the Fe 2p, O 1s and O $KL_{2,3}L_{2,3}$ spectra (Figure B.12, Section 5.5.1.3).

The Cu $L_3M_{4,5}M_{4,5}$ spectra were analysed in terms of lineshape and binding energy, with the latter used for Auger parameter determination (Appendix D). The binding energies were obtained using a Gaussian peak maximum function (SpecProc). Shirley

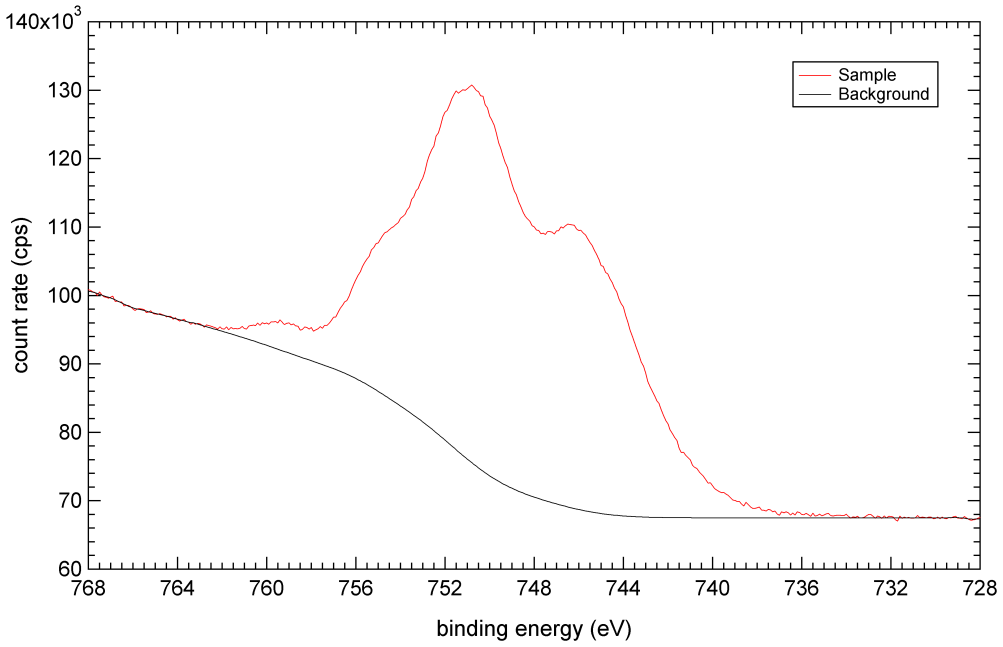

Figure 5.5: *O $KL_{2,3}L_{2,3}$ spectrum processing procedure.*

background corrections were not performed before these determinations. Although other Cu LMM transitions occur, the Cu $L_3M_{4,5}M_{4,5}$ remains the most intense and hence the most analysed.

The Fe Auger peaks were not analysed because they are very broad and offer little discrimination, while the S Auger peaks occur at binding energies (1103 eV) above the binding energies collected (0-1100 eV).

5.2 Fitting spectral envelopes

Fitting was performed on S 2p, O1s and Fe 2p spectral envelopes. The S 2p and O 1s spectral envelopes of standards and chalcopyrite samples were fitted iteratively with Gaussian peaks (SpecProc). The Fe 2p spectral envelopes of chalcopyrite samples were fitted iteratively with standard spectra using Eclipse (Thermo VG Scientific, Pty. Ltd.) and FeFit (an 'in-house' program developed in Excel), which perform factor analysis by non-linear least squares (NLLS) reduction (Section 5.4.2).

5.3 Qualitative analysis of chalcopyrite before oxidative dissolution in ferric media

The surfaces of chalcopyrite fractured under anaerobic atmosphere and polished under aerobic atmosphere were analysed to establish the composition of the chalcopyrite surface before oxidative dissolution. The observed lineshapes of the S 2p, Fe 2p, Cu 2p and O 1s spectra have been compared with reported lineshapes and the observed intensities have been compared with predicted intensities. Furthermore, the spectra of chalcopyrite surfaces fractured under anaerobic atmosphere and polished under aerobic atmosphere were compared to establish the changes induced by polishing, including lineshape degradation and phase formation.

5.3.1 Chalcopyrite fractured under anaerobic atmosphere

The S 2p spectrum was fitted with peaks attributed to bulk sulphide (161.28 eV), disulphide (161.99 eV) and loss structure (163.73 eV), in accordance with similar fitting by Klauber (2003)(Figures 5.6 and 5.7). Similar binding energies were determined for three additional samples to establish average binding energy separations for the fitting of the S 2p spectra of chalcopyrite after oxidative dissolution (Table 5.1). The S 2p fitting of chalcopyrite fractured under anaerobic atmosphere produced a disulphide peak intensity consistent with the surface reconstruction phase proposed by Klauber (2003). The fractional contribution of the disulphide peak towards the S 2p spectrum (0.204) suggests two layers of the reconstruction phase (0.232) rather than one layer (0.124), according to IMFP and spectrometer calculations (presented in Section 5.5.1).

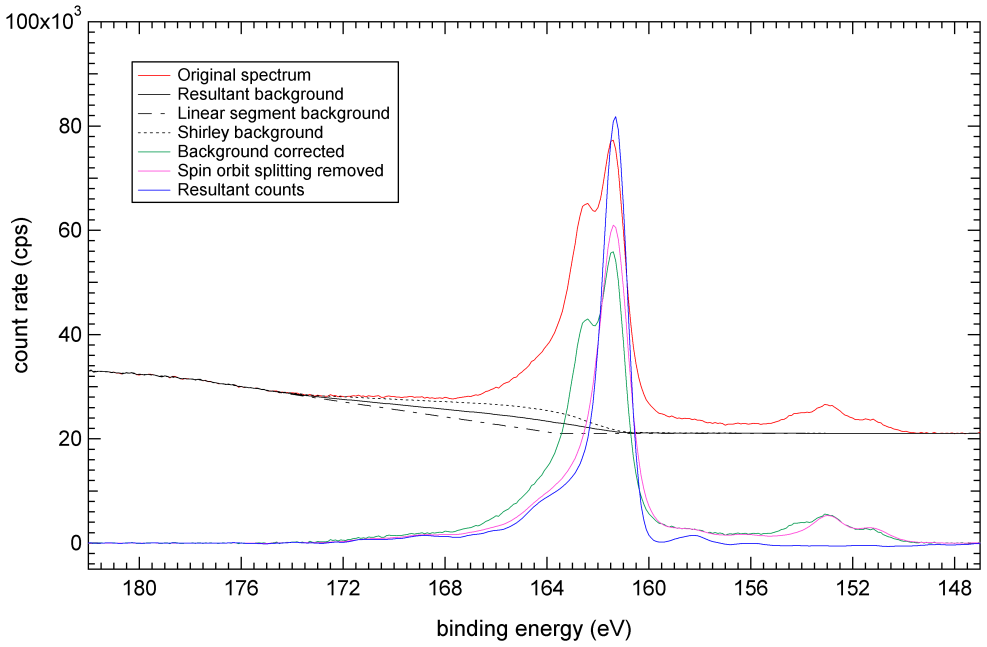

Figure 5.6: *S 2p spectrum of chalcopyrite (Mass-p) fractured under anaerobic atmosphere.*

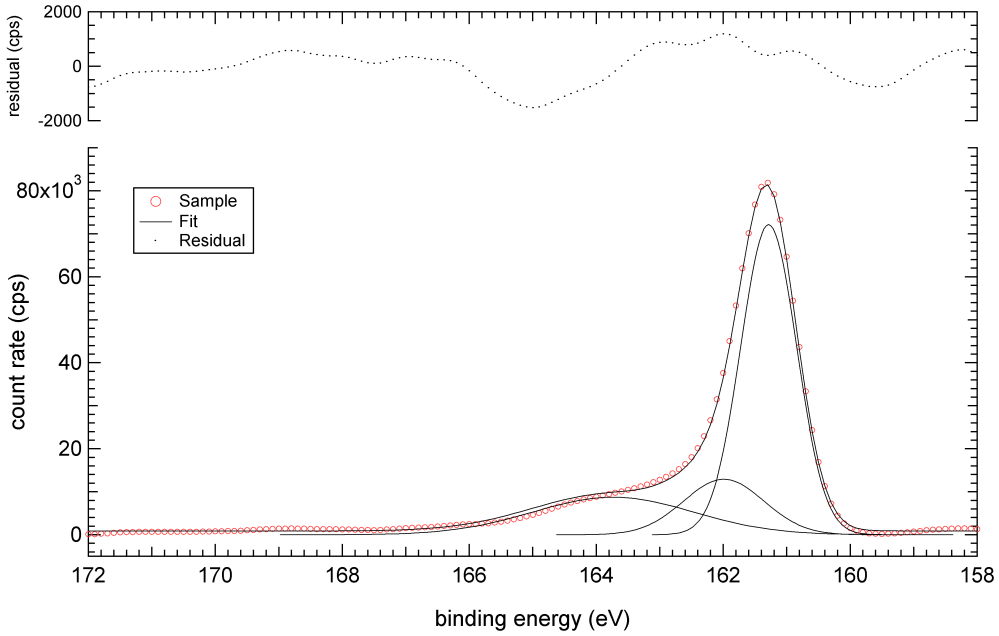

Figure 5.7: *Fit of the S 2p spectrum of chalcopyrite (Mass-p) fractured under anaerobic atmosphere.*

Table 5.1: *S 2p binding energy separations (eV) of the sulphide (S^{2-}), disulphide (S_2^{2-}) and loss structure (l.s.) peaks of a series of chalcopyrite standards fractured under anaerobic atmosphere.*

S 2p peaks	Sample 1	Sample 2	Sample 3	Sample 4	Average
$\mathbf{S^{2-} - S_2^{2-}}$	0.71	0.81	0.68	0.72	0.73
$\mathbf{S^{2-}}$ **– l.s.**	2.45	2.48	2.64	2.48	2.51

The Fe 2p spectrum displays excellent definition, with peaks attributed to Fe $2p_{3/2}$ and Fe $2p_{1/2}$ photoelectron lines (708 and 721 eV, respectively) and Fe $2p_{3/2}$ and Fe $2p_{1/2}$ loss structure (730 and 742 eV, respectively)(Figure 5.8). The Fe $2p_{3/2}$ binding energy observed (708.33 eV) compares favourably with the binding energy reported ($\sim$ 708 eV) by Klauber (2003). The definition of this photoelectron peak indicates the lattice structure has been maintained, while minimal oxidation is indicated by the relative absence of O $KL_{2,3}L_{2,3}$ peaks ($\sim$ 743 eV). Thus, the Fe 2p spectrum is considered appropriate for factor analysis (Section 5.4.2).

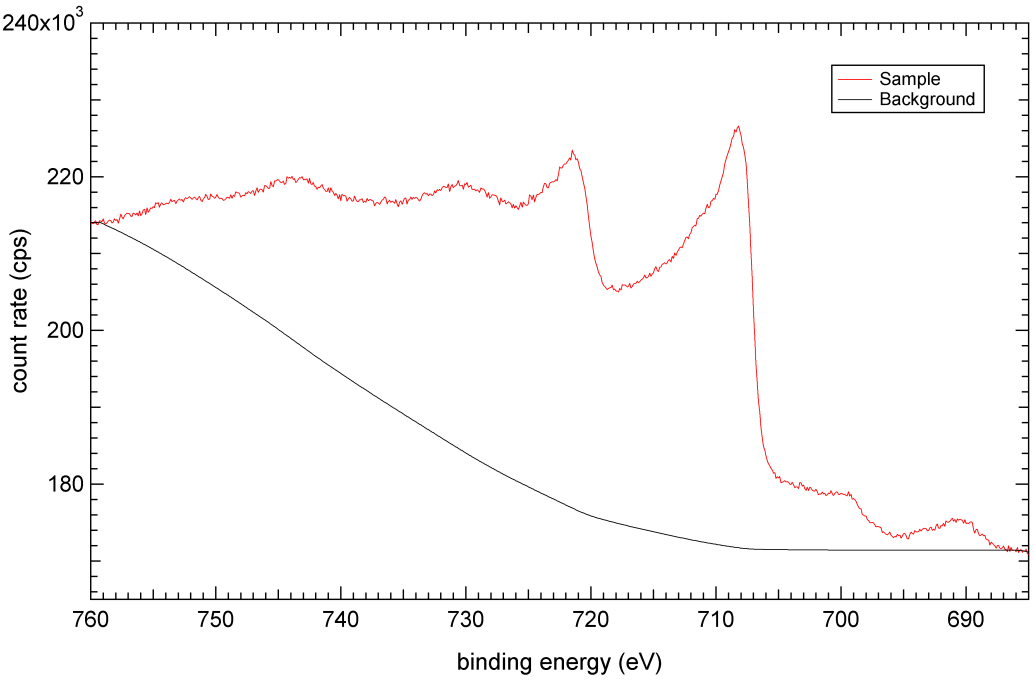

Figure 5.8: *Fe 2p spectrum of chalcopyrite (Mass-p) fractured under anaerobic atmosphere.*

The Cu 2p spectrum displays excellent definition and the absence of satellite structure is consistent with monovalent copper (Figure 5.9). The Cu $2p_{3/2}$ binding energy observed (932.05 eV) compares favourably with the binding energy reported (931.92 eV) by Klauber (2003).

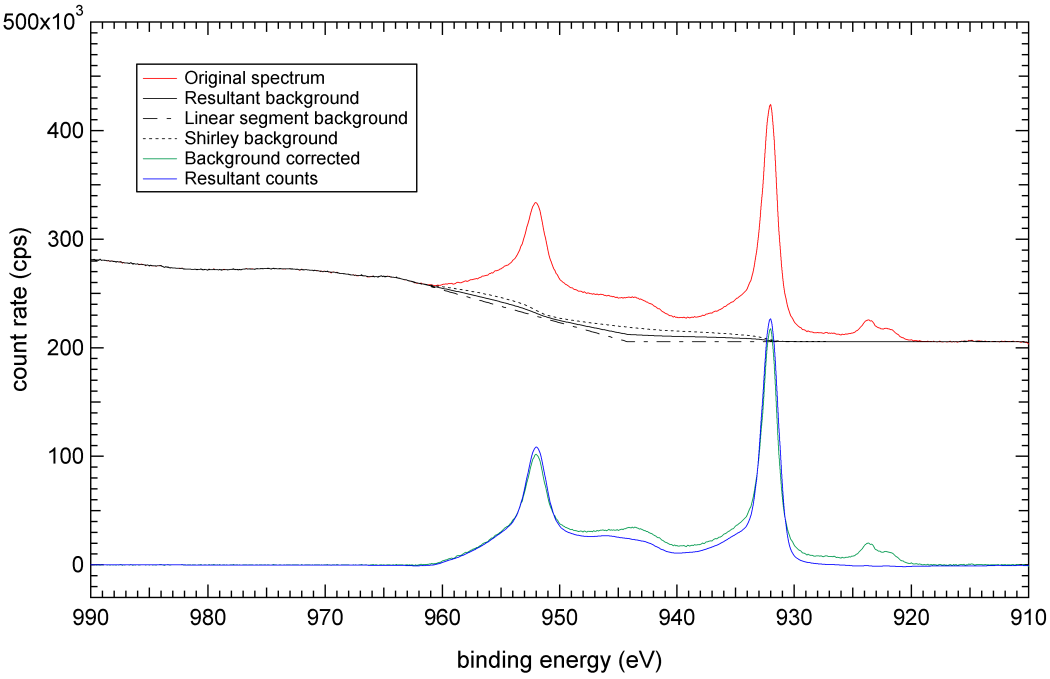

Figure 5.9: *Cu 2p spectrum of chalcopyrite (Mass-p) fractured under anaerobic atmosphere.*

The O 1s spectrum displays poor definition and low intensity, which indicates minimal oxidation (Figure 5.10). The spectrum consists of three peaks speculatively attributed to cuprite, iron oxide, and either adsorbed water or degraded hydrocarbons.

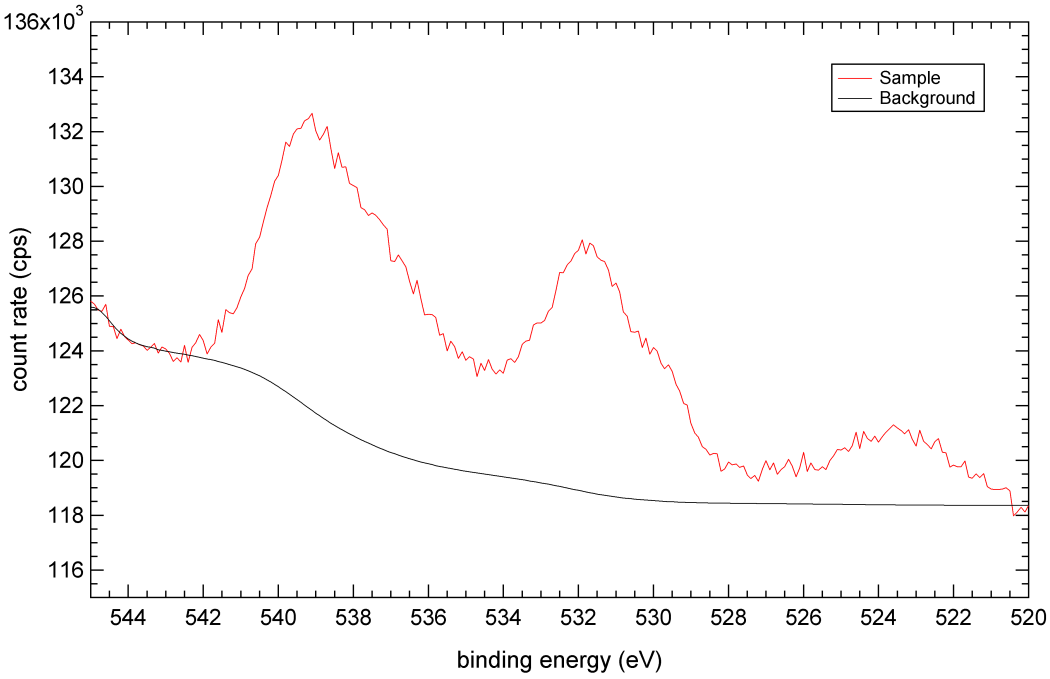

Figure 5.10: *O 1s spectrum of chalcopyrite (Mass-p) fractured under anaerobic atmosphere.*

The observed S 2p, Fe 2p and Cu 2p spectra lineshapes (Figures 5.6 - 5.10) compare favourably with reported spectra. The observed and reported S 2p spectra of unreacted chalcopyrite all display the spin-orbit splitting of the main sulphide peak, and the high binding energy tail. The definition of spin-orbit splitting observed in this study using Mg K_α compares favourably with Klauber (2003) but not with Yin et al. (1995) or Farquhar et al. (2003). This difference may be the result of improved instrumentation used by the latter two studies. Improved definition of spin-orbit splitting acquired using Al K_α was reported by Buckley and Woods (1984), Zachwieja et al. (1989), McCarron et al. (1990) and Harmer et al. (2004). The Fe 2p spectrum compares favourably with the spectrum reported by Klauber (2003) and displays better definition of the Fe $2p_{3/2}$ peak at 708 eV than the spectra reported by Yin et al. (1995) and Farquhar et al. (2003), principally because of their poor signal to noise. The definition of the Fe $2p_{3/2}$ peak acquired using Al K_α is severely impaired by oxidation of the sample in the studies of Buckley and Woods (1984) and Zachwieja et al. (1989), despite their attempts to minimise oxygen exposure. The Cu 2p spectrum compares favourably with those

reported by Fujisawa et al. (1994) and Yin et al. (1995), with all three displaying an absence of satellite structure and remaining consistent with monovalent copper. Thus, the lineshapes of the S 2p, Fe 2p and Cu 2p spectra of this study confirm the high purity of the sample and the rigour of the sample preparation and spectral acquisition. The O 1s spectrum could not be compared with reported spectra because of an absence of the latter. Nonetheless, the observed and predicted Cu 2p:S 2p and Fe 2p:S 2p spectral intensity ratios compare favourably (Table 5.2).

Table 5.2: *Observed and predicted Cu 2p:S 2p and Fe 2p:S 2p spectral intensity ratios of the chalcopyrite standard fractured under anaerobic atmosphere.*

	Cu 2p:S 2p	**Fe 2p:S 2p**
Observed	7.25	8.33
Predicted	7.52	8.31

Note: The intensities predicted for the chalcopyrite standard were based on a model consisting of two layers of the surface reconstruction phase above the bulk chalcopyrite.

5.3.2 Chalcopyrite polished under aerobic atmosphere

Polishing chalcopyrite massive oxidised the surface and degraded the spectral lineshapes. Comparison of the S 2p, Fe 2p, Cu 2p and O 1s spectra of chalcopyrite polished under aerobic atmosphere and fractured under anaerobic atmosphere reveals minor oxidation in the S 2p spectrum, considerable oxidation in the Fe 2p and O 1s spectra, and no oxidation in the Cu 2p spectrum (Figures 5.11 - 5.14).

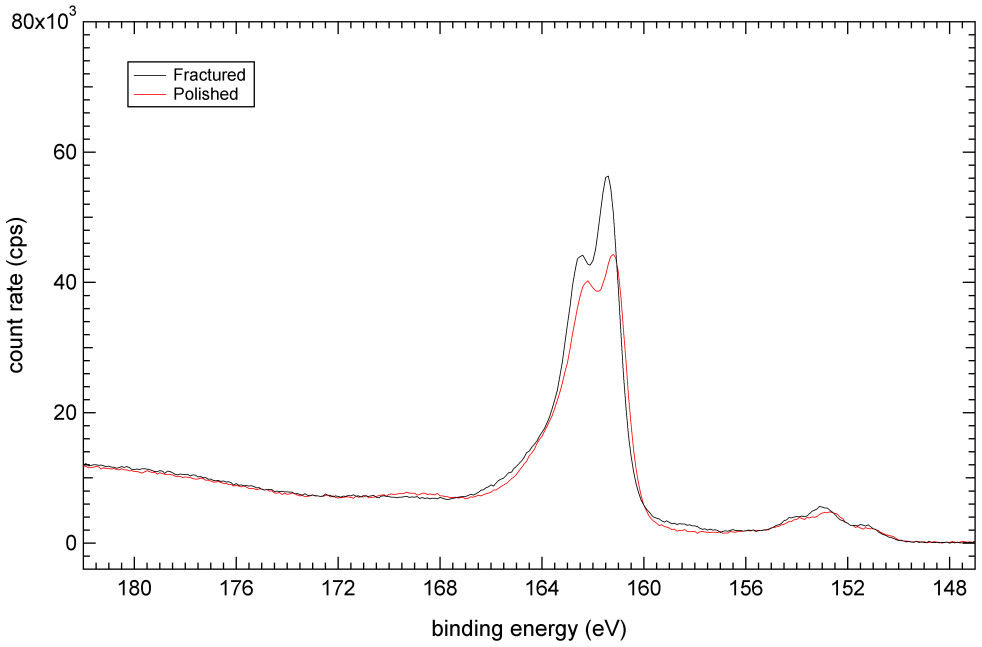

Figure 5.11: *S 2p spectra of chalcopyrite (Mass-p) fractured under anaerobic atmosphere and polished under aerobic atmosphere.*

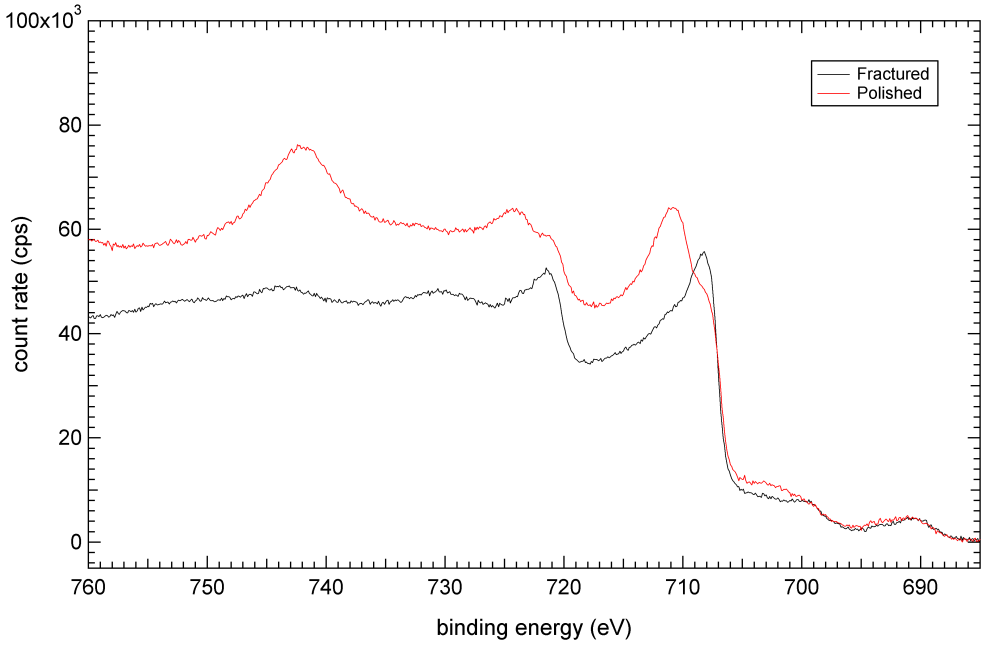

Figure 5.12: *Fe 2p spectra of chalcopyrite (Mass-p) fractured under anaerobic atmosphere and polished under aerobic atmosphere.*

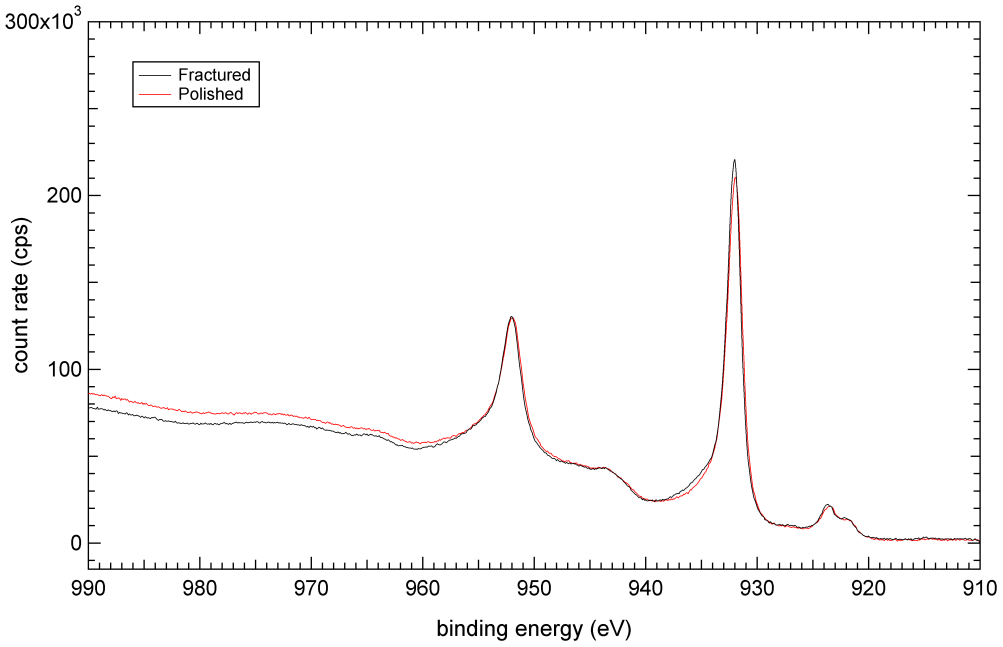

Figure 5.13: *Cu 2p spectra of chalcopyrite (Mass-p) fractured under anaerobic atmosphere and polished under aerobic atmosphere.*

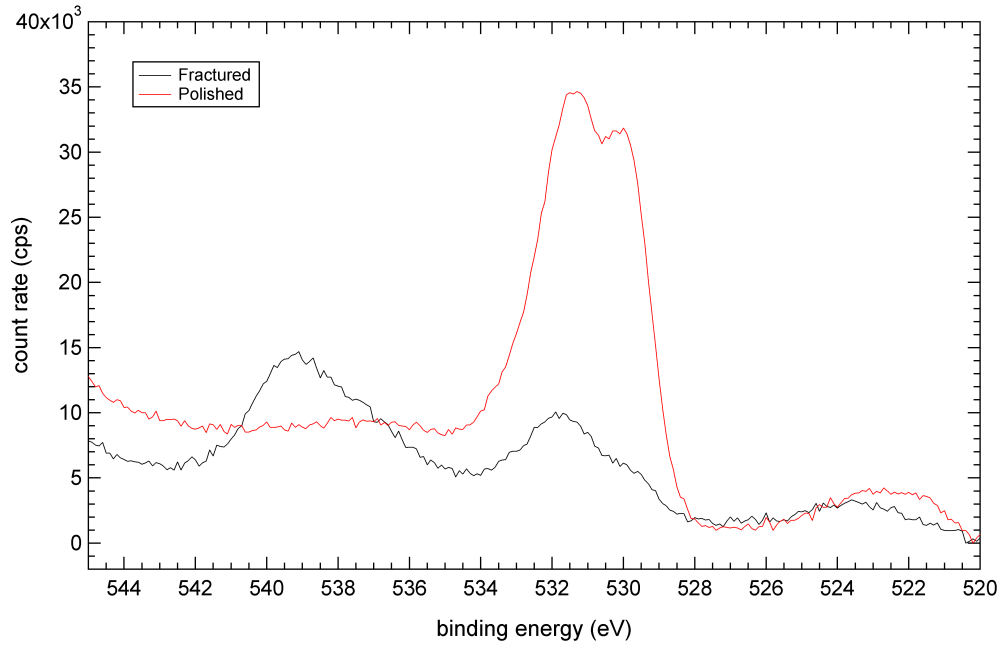

Figure 5.14: *O 1s spectra of chalcopyrite (Mass-p) fractured under anaerobic atmosphere and polished under aerobic atmosphere.*

The oxidation identified in the Fe 2p and O 1s spectra is attributed principally to the formation of goethite, based on non-linear least squares (NLLS) analysis of the Fe 2p spectrum (Figure 5.15). The NLLS analysis rejected the hematite (Fe_2O_3) and magnetite (Fe_3O_4) standards in favour of goethite (FeOOH), despite the proposals of magnetite or goethite by Holloway (1982) and hematite by Buckley and Woods (1984) (Section 2.7.1.2). The similarity of the Fe 2p spectra of the three iron standards (Section A.2.1) indicates an approach such as NLLS is necessary to distinguish between standards. The goethite is not intimately associated with the chalcopyrite surface and is easily removed in dilute sulphuric acid (pH 1.9) at 50°C after 15 minutes (Figure 5.16).

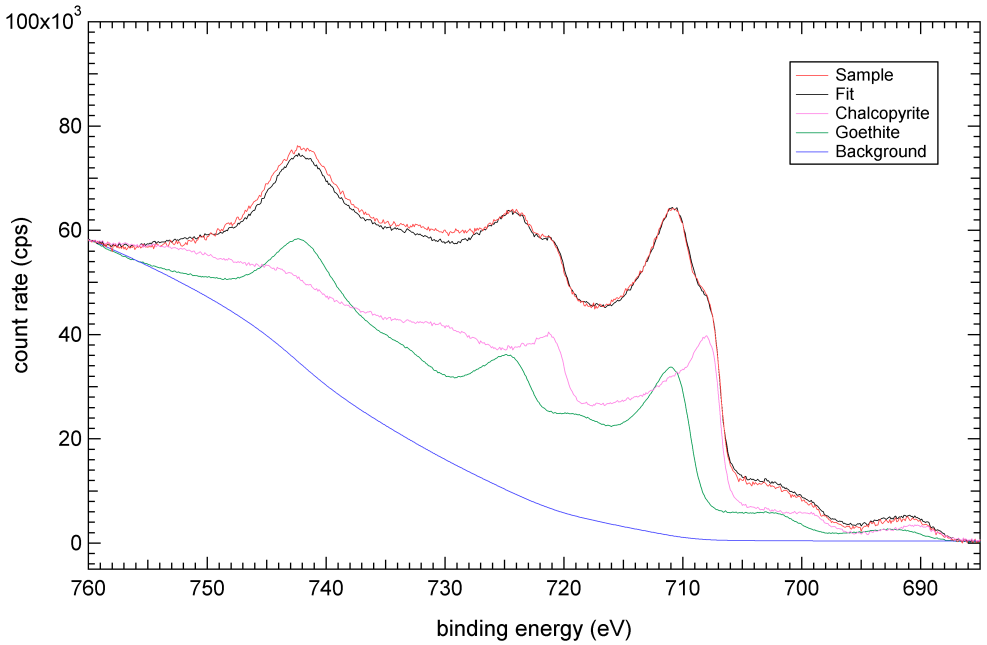

Figure 5.15: *Fit of the Fe 2p spectrum of chalcopyrite (Mass-p) polished under aerobic atmosphere. Note: The O $KL_{2,3}L_{2,3}$ fit is excellent relative to the fits observed for chalcopyrite after oxidative dissolution (Appendices C) because of the lack of water in the standards.*

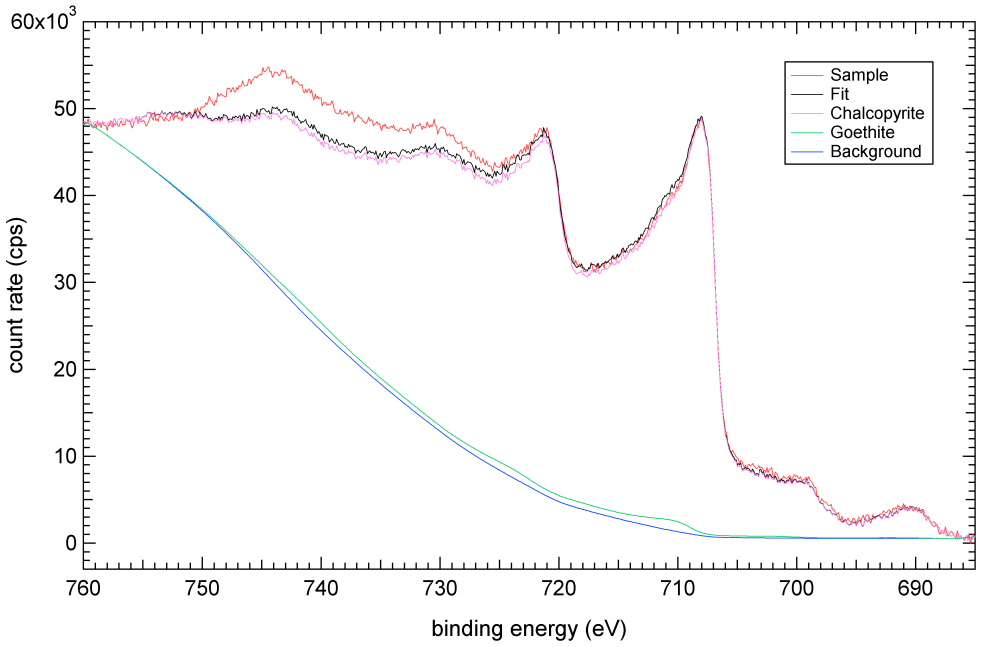

Figure 5.16: *Fit of the Fe 2p spectrum of chalcopyrite (Mass-p) after dissolution in sulphuric acid (pH 1.9) at 50° C for 15 minutes.*

The oxidation identified in the S 2p spectrum, with a peak corresponding to sulphur (VI), is attributed to oxidation of the 'pyritic' reconstruction phase (Figure 5.11). Although sulphate has been reported on the surface of polished chalcopyrite (Section 2.7.1.2), the absence of copper (II) in the Cu 2p spectrum, and the fitting of the Fe 2p spectrum with only chalcopyrite and goethite, implies neither copper nor iron sulphates are responsible for the sulphur (VI) identified in the S 2p spectrum. Rather, it is concluded the sulphur (VI) is produced by oxidation of the terminal sulphur atom of the 'pyritic' surface reconstruction phase while it remains associated with the sulphur dimer, in a form analogous to thiosulphate (Fe-S-SO_3). This proposal enables the bridging and terminal sulphur atoms of the dimer to assume the oxidation states (-II and VI) identified in the S 2p spectrum. Furthermore, the thiosulphate proposal ensures the oxygen atoms bond with the terminal sulphur exclusively, as opposed to the sulphate proposal which requires the bridging and terminal sulphur atoms of the dimer to be bridged by an oxygen atom.

The oxidation identified in the Fe 2p and S 2p spectra has been combined with the absence of oxidation in the Cu 2p spectrum in the proposed oxidised 'pyritic' reconstruction phase ($FeS_2O_3.0.5Cu_2O$). The Fe 2p spectrum of the chalcopyrite standard accounts for the iron, while the oxidation states of -II and VI observed in the S 2p spectrum of the chalcopyrite standard account for the sulphur. The increase of the sulphur (VI) intensity in the S 2p spectrum of chalcopyrite after dissolution in dilute sulphuric acid (pH 1.9) at 50°C for 15 minutes (Figures 5.12 and 5.17) is attributed to the diminished attenuation of the intensity caused by the removal of goethite from the surface (Figure 5.16). Lastly, the Cu 2p spectrum is unchanged in lineshape and intensity, implying the copper remains as cuprite within the first few layers of surface reconstruction. It is therefore concluded the polished surface exposed to solution consists of chalcopyrite underlying partially oxidised 'pyritic' reconstruction phase that is partially overlaid with goethite.

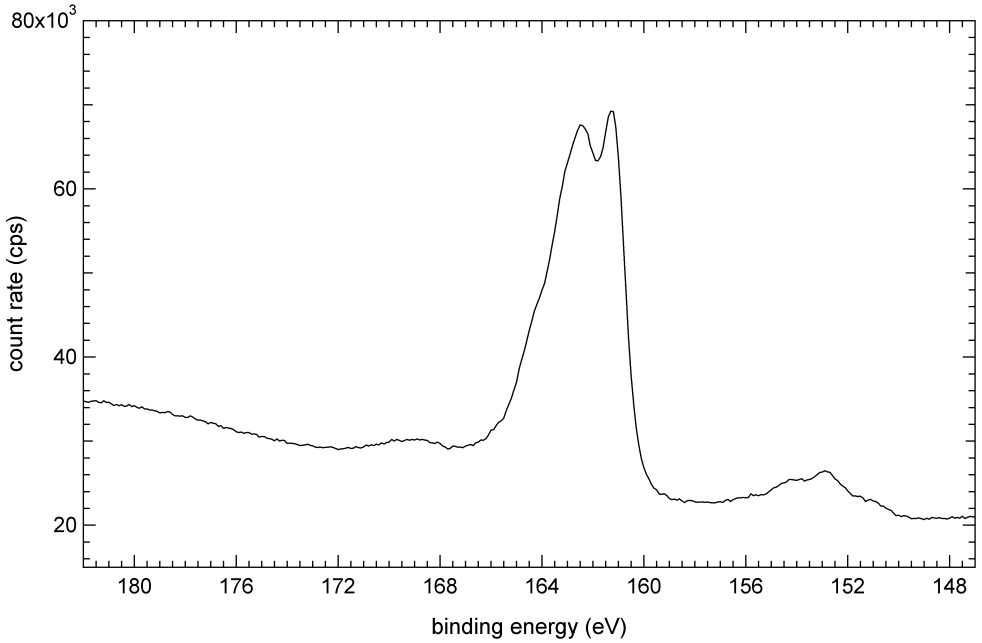

Figure 5.17: *S 2p spectrum of chalcopyrite (Mass-p) after dissolution in sulphuric acid (pH 1.9) at 50° C for 15 minutes.*

5.3.3 Summary

The XPS spectra of chalcopyrite fractured under anaerobic atmosphere and polished under aerobic atmosphere were analysed to determine the nature of the surfaces before oxidative dissolution. Analysis of the spectra of chalcopyrite fractured under anaerobic atmosphere revealed minor oxidation and well defined peaks. Thus, the parameters of the peaks identified in the S 2p spectrum were deemed appropriate for analysis of S 2p spectra of chalcopyrite samples after oxidative dissolution and the Fe 2p spectrum was deemed appropriate for use as a standard for the analysis of Fe 2p spectra of chalcopyrite samples after oxidative dissolution. Analysis of the spectra of chalcopyrite polished under aerobic atmosphere revealed oxidation of the iron and sulphur. The oxidised iron (goethite) is easily removed in low pH solutions, but the oxidised sulphur is intimately associated with the 'pyritic' reconstruction phase. Thus, the quantitative analysis of chalcopyrite massive requires consideration of the oxidised 'pyritic' reconstruction phase.

5.4 Qualitative analysis of chalcopyrite after oxidative dissolution in ferric media

XPS spectra of chalcopyrite after oxidative dissolution were analysed to determine the fractional contributions of oxidation states towards the S 2p spectra and the phase contributions towards the Fe 2p spectra.

5.4.1 S 2p spectral analysis

The S2p spectra were fitted iteratively with peaks based on the S 2p analysis of the chalcopyrite standard (fractured under anaerobic atmosphere) and commonly cited deposition phases.

The S 2p spectra were fitted with six Gaussian peaks attributed to oxidation states of -II, -I, 0, IV and VI, and loss structure (Figure 5.18). The oxidation states of -II and -I

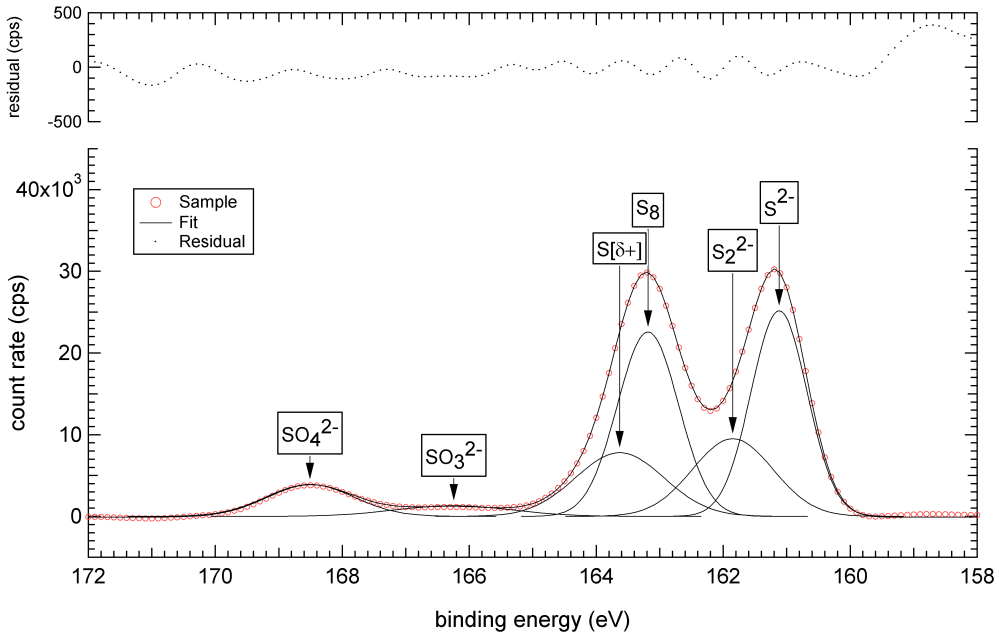

Figure 5.18: *Fit of the S 2p spectrum of chalcopyrite (Con-p) after oxidative dissolution in ferric media.*

were attributed to the sulphide (S^{2-}) and disulphide ($S_2{}^{2-}$). These species, in addition to loss structure ($S^{\delta+}$), were identified in the S 2p fit of the chalcopyrite standard (Section 5.3.1). The oxidation states of 0, IV and VI were attributed to elemental sulphur (S_8), sulphite ($SO_3{}^{2-}$) and sulphate ($SO_4{}^{2-}$), respectively. Elemental sulphur and sulphate are commonly cited products of chalcopyrite oxidation (Section 2.3), while sulphite has been identified on pyrite oxidised in ferric chloride by Sasaki et al. (1995). The persistence of elemental sulphur under vacuum (Section 2.7.1.3) was confirmed with a loss at $\sim$ 163.5 eV for chalcopyrite oxidised in ferric sulphate analysed before and after 128 hours under the ultrahigh vacuum of the spectrometer (Figure 5.19). This binding energy compares favourably with 163.6 eV for bulk elemental sulphur reported by Termes et al. (1987) and is within the range of 163.2 and 163.9 eV reported for elemental sulphur on chalcopyrite (Section 2.7.1.3). The binding energy of the sulphite ($\sim$ 166.2 eV) compares favourably with 166.4 eV reported by Sasaki et al. (1995), while the binding energy of the sulphate ($\sim$ 168.5) is within the range of 168.1 - 169.0 eV reported for sulphate (Section 2.7.1.3). The six peaks were present in all S 2p

spectra, with only the relative intensities changing as a result of the oxidation conditions (Appendices C).

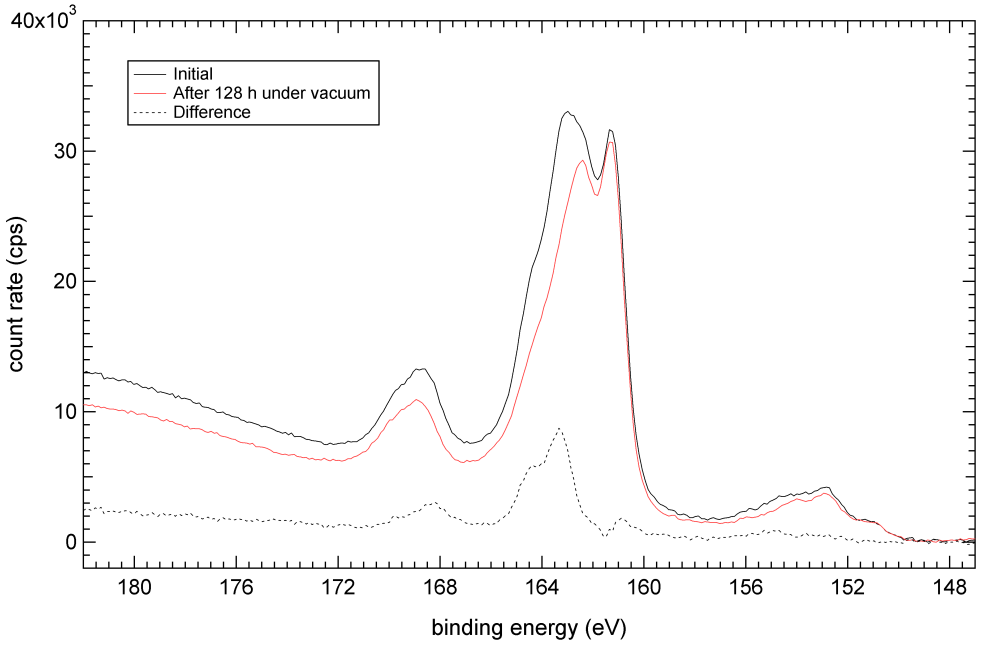

Figure 5.19: *S 2p spectrum of chalcopyrite (Con-p) after oxidative dissolution in 0.1 M ferric sulphate (pH 1.9) at 50° C for 2 hours, before and after 128 hours under vacuum. Note: The minor peaks at ∼ 161.0 eV (sulphide) and ∼ 168.5 eV (sulphate) are because of the difference in spectral backgrounds and not the evaporation of charged species.*

The fit parameters for the peaks attributed to the underlying sulphide (sulphide, disulphide and loss structure) were based on the S 2p fit for the chalcopyrite standard fractured under anaerobic atmosphere (Table 5.3, Section 5.3.1). In particular, the widths of the sulphide and disulphide peaks and the binding energy separations between the sulphide, disulphide and loss structure peaks were all held. The binding energy of the sulphide peak was determined by the low binding energy edge of the spectrum envelope and allowed to free fit. The binding energies of the disulphide and loss struture peaks were then set relative to this peak. Although a binding energy separation of 0.73 eV was used for the sulphide and disulphide peaks, different separations were required for

the loss structure and sulphide peaks for chalcopyrite massive and chalcopyrite concentrate. The separation for the chalcopyrite massive fits was maintained at 2.51 eV, in accordance with the average separation observed for the chalcopyrite standard (Table 5.1). However, initial attempts to fit the S 2p spectra of chalcopyrite concentrate using this separation were deemed unrealistic because the intensity of the loss structure approached that of the sulphide peak, rather than the expected level of less than 50 % of the sulphide peak. To overcome this, the S 2p spectra for chalcopyrite concentrates were fitted with the separation held at 2.60 eV – still within the experimentally observed range – and the loss structure peak intensity was held at 50 % of the parent peak. This variation in binding energy is not surprising because of the breadth of the loss structure peak and the uncertainty of its true position.

Table 5.3: *S 2p binding energies and binding energy separations (eV) for S 2p fits of chalcopyrite after oxidative dissolution.*

Peak	$\mathbf{S^{2-}}$	$\mathbf{S_2{}^{2-}}$	$\mathbf{S_8}$	**l.s.**	$\mathbf{SO_3{}^{2-}}$	$\mathbf{SO_4{}^{2-}}$
Binding energy	$\sim$ 161.1	$\sim$ 161.8	$\sim$ 163.1	$\sim$ 163.6	$\sim$ 166.2	$\sim$ 168.8
Separation from $\mathbf{S^{2-}}$	-	0.73	-	2.51, 2.60	-	-

The fit parameters for the peaks attributed to deposition phases (elemental sulphur, sulphite and sulphate) were largely unconstrained (Table 5.3). The elemental sulphur peak was not constrained in position, width or amplitude and was defined by the spectrum envelope and the surrounding peaks. This freedom accommodated variations in width and position that may result from elemental sulphur associating with conducting phases (e.g., disulphide) and insulating phases (e.g., hydronium jarosite and goethite). The sulphite peak was unconstrained in position and width when the surrounding peaks were well defined. However, when the sulphate peak intensity was low, the sulphite peak either shifted laterally or broadened, and in these cases, the position or the width, or both, were held. The sulphate peak was unconstrained in position and width, and required only one peak to account for intensity, except for two samples that required two peaks. This requirement arose because the high levels of sulphate produced charge shifting and the emergence of a second peak at higher binding energy.

5.4.2 Fe 2p spectral analysis

The Fe 2p spectra were analysed using factor analysis in the form of Non-Linear Least Squares (NLLS). This procedure involved a commercially available program (Eclipse) to determine the suite of standards – and the associated binding energy shifts – required to account for the spectra, and an 'in-house' program (FeFit) to determine the associated scaling factors. The procedure utilised the quick computation of the Eclipse program and the accurate intensity determination of the FeFit program.

The Eclipse program required the importation of the sample spectrum and the standard spectra. The sample background was calculated and applied to the sample and standard spectra. The standard spectra were then iteratively scaled and laterally shifted to minimise the residual of the fit to the sample spectrum over the designated spectral region.

Although the Eclipse program provided an output for the scaled Fe 2p intensities of the standards, these intensities were not consistent with the S 2p and O 1s intensities determined using SpecProc, according to IMFP and spectrometer calculations (Section 5.5.1). This discrepancy is attributed to the different sample spectrum backgrounds calculated by Eclipse and SpecProc; the algorithm for the Shirley background calculated in Eclipse was not available for comparison with the Shirley background calculated in SpecProc. Furthermore, it appears the sample background calculated in Eclipse was applied to the standard spectra during the intensity determination. Thus, if different sample backgrounds were applied to a standard spectrum, the intensities produced would differ, even when the standard spectrum was multiplied by the same scaling factor. To overcome these problems with intensity determination, the FeFit program was developed and used in combination with Eclipse.

The Eclipse program was used to determine the suite of standards and the associated binding energy shifts required to account for the Fe 2p spectra. These standards included sulphide (chalcopyrite), iron oxides (hematite, magnetite, goethite) and iron sulphates (ferric sulphate and hydronium jarosite). Trials involving permutations of all standards were performed with lateral shifts restricted to 0.3 eV for chalcopyrite

massive samples and 0.4 eV for chalcopyrite concentrate samples; the latter range was used to accommodate the increase in sample charging expected from the greater extent of dissolution and hence greater deposition of insulating phases. These lateral shift restrictions accommodated spectrometer drift and ensured consistent and realistic final binding energies for standard spectra.

The Eclipse trials revealed only three standards were required to account for all Fe 2p spectra of the chalcopyrite samples: chalcopyrite, goethite and hydronium jarosite. The identification of goethite was consistent with the Fe-S-O stability diagram for pH values below 2 (Figure 2.5) and the XRD analysis of chalcopyrite oxidised in ferric sulphate performed by Ferreira and Burkin (1975). Goethite was also identified unequivocally despite the similarity of the Fe 2p spectra of iron oxides (Appendices A.2). Confirmation of the iron-oxide by examination of the O 1s intensity was not possible because of the large contribution towards the O 1s spectrum by residual water in the chalcopyrite sample spectra (Section 5.4.4). Hydronium jarosite was consistently selected in preference to ferric sulphate on the basis of the prominent Fe $2p_{1/2}$ peak at 719 eV in the ferric sulphate spectrum (Figure A.33). Only one sample fit produced a smaller residual when ferric sulphate was included with hydronium jarosite. However, the ferric sulphate contribution was extremely minor, and acceptable fits were achieved without it, so the fit including ferric sulphate was rejected in favour of the one including just chalcopyrite, goethite and hydronium jarosite, to ensure consistency between all samples, and because the presence of an iron sulphate richer in sulphate occurring in a ferric chloride system was unlikely. Thus, the standards (chalcopyrite, goethite and hydronium jarosite) and the associated binding energy shifts were established and imported into the FeFit program for intensity determination.

The FeFit program used the Shirley background spectra determined using SpecProc for each standard and sample spectrum. Once the spectra of the sample and the standards – and the associated background spectra – were introduced into the program, the standard spectra were shifted laterally according to the binding energy shifts determined using Eclipse. The standard spectra and sample spectrum were set to zero counts at 685.00 eV and scaled to intersect with the sample background spectrum at

759.30 eV to establish the high and low binding energy boundaries for the baseline (Figures 5.20 - 5.21). The sample background spectrum was then subtracted from the sample spectrum and the standard spectra (Figure 5.22). The standard spectra were iteratively scaled using Excel Solver until the residual of the sample spectrum and the combination of standard spectra was minimised within the spectral region of 725.00 eV to 690.00 eV (Figure 5.23); this region excludes the contribution of water towards the O $KL_{2,3}L_{2,3}$ Auger series between 725 and 760 eV; the effect of water on the O $KL_{2,3}L_{2,3}$ Auger series can be observed in a comparison of the Fe 2p spectra of chalcopyrite after polishing (Figure 5.15) and after oxidative dissolution (Appendix C). The background spectrum for the sample was added to all spectra for purely ascetic reasons (Figure 5.24). The two scaling factors used for each standard spectrum were then used to adjust the original standard spectrum intensity determined in SpecProc (Section 5.4.2) to produce the Fe 2p intensity of each standard towards the Fe 2p spectrum of the sample.

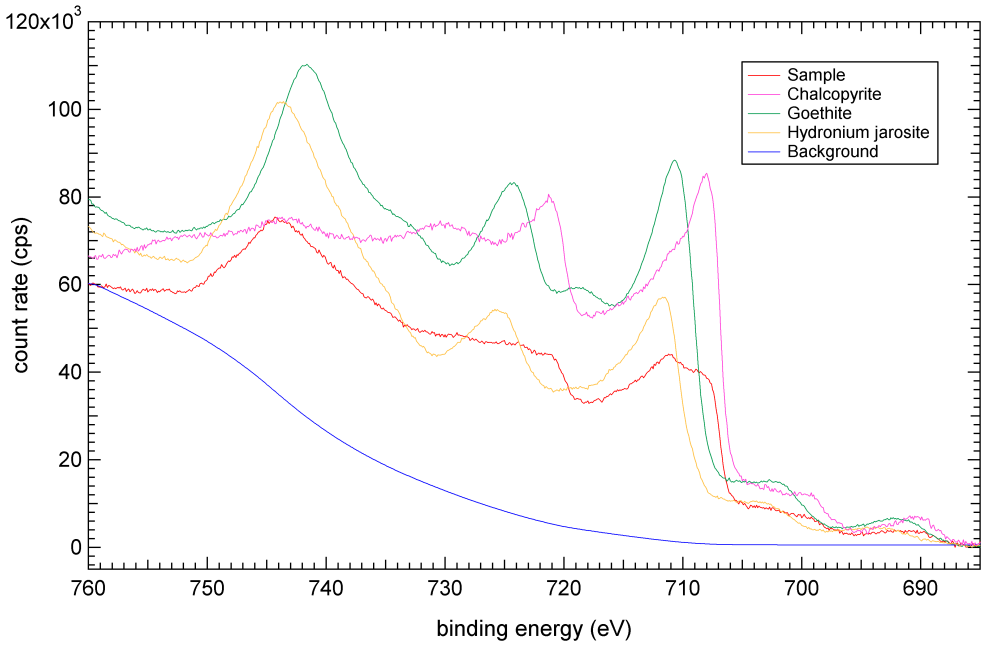

Figure 5.20: *Fit of the Fe 2p spectra: Stage 1.*

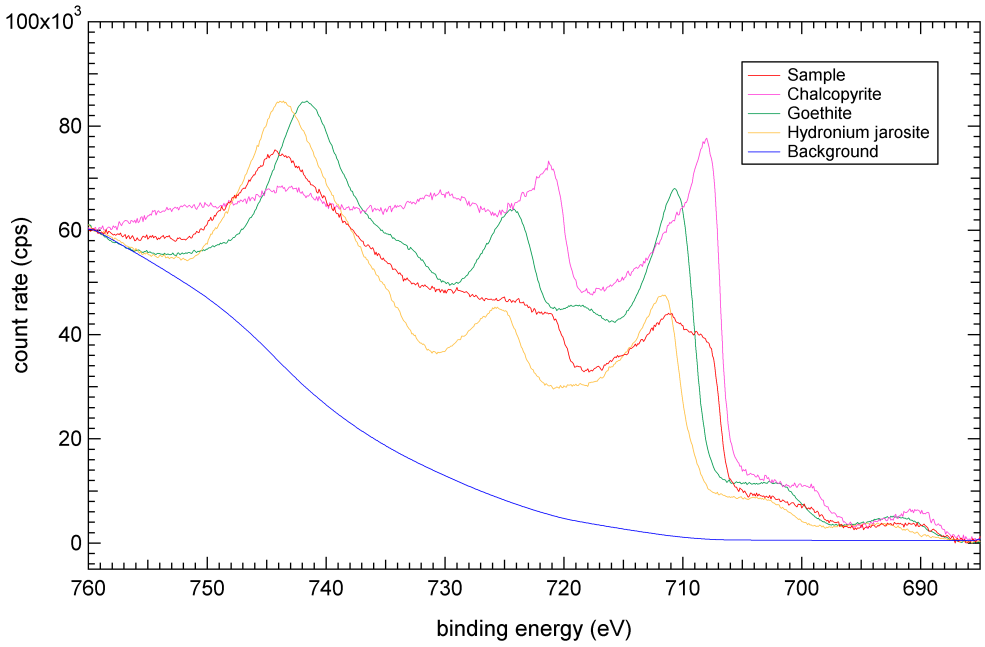

Figure 5.21: *Fit of the Fe 2p spectra: Stage 2.*

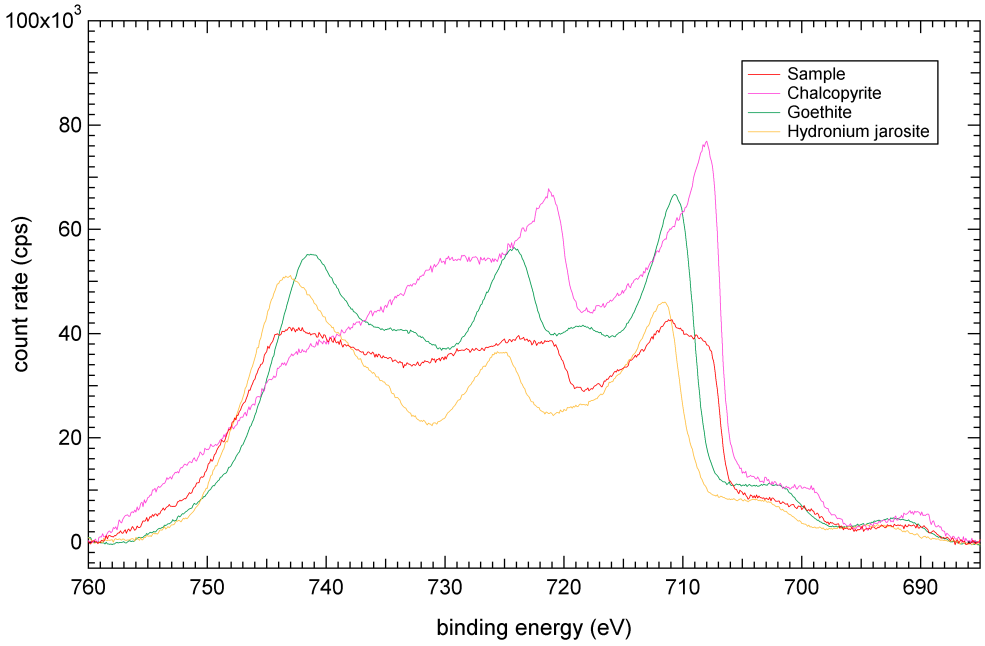

Figure 5.22: *Fit of the Fe 2p spectra: Stage 3.*

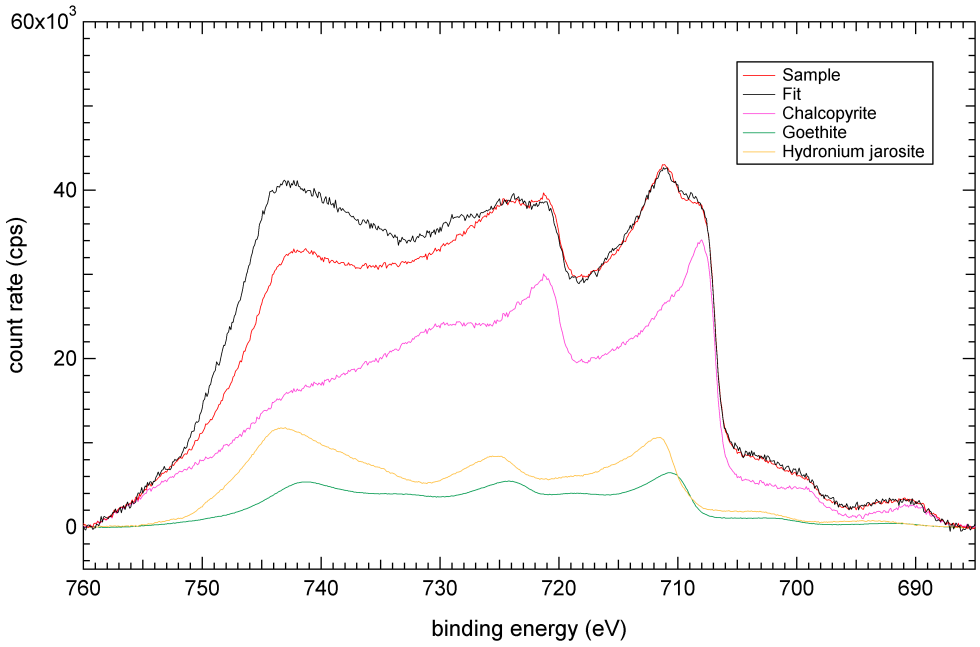

Figure 5.23: *Fit of the Fe 2p spectra: Stage 4.*

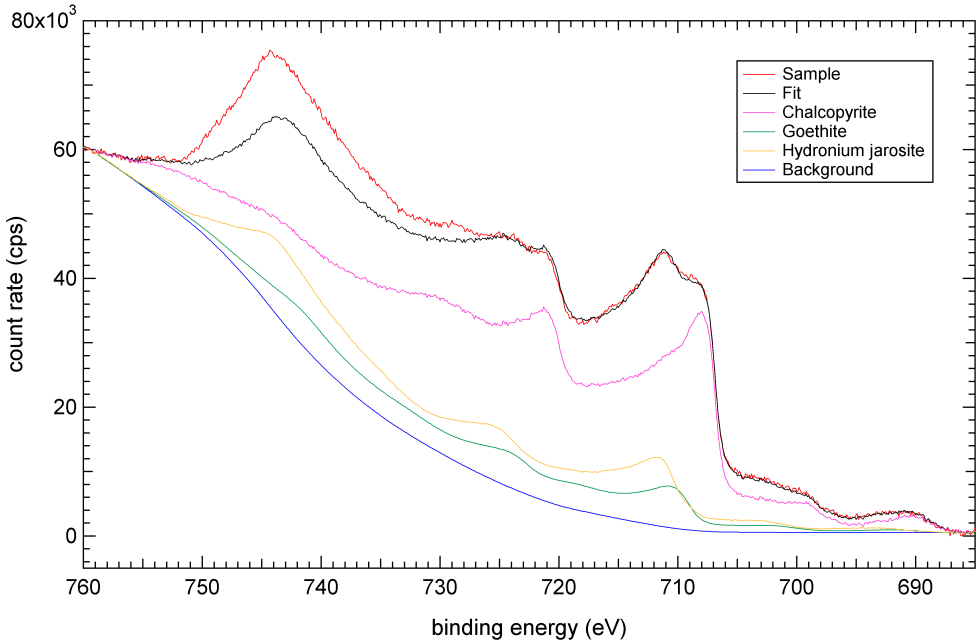

Figure 5.24: *Fit of the Fe 2p spectra: Stage 5.*

The overall procedure —

- required no additional processing of either the sample spectrum or the standard spectra and did not diminish the resolution; original data points were simply shifted and scaled;
- determined the Fe 2p intensity contribution of each standard spectrum towards each sample spectrum, using the one form of Shirley background (SpecProc) in a manner consistent with the S 2p and O 1s intensity determinations and the IMFP and spectrometer calculations;
- used the quick computation of Eclipse to determine valid combinations of standards and appropriate binding energy shifts for each standard;
- used the mathematical removal of the O $KL_{2,3}L_{2,3}$ contribution to the Fe 2p spectra of standards to enable determination of the Fe 2p intensities for each sample without further processing;
- used one background determination for each Fe 2p standard spectrum;
- ensured the background correction used to determine the intensity for each standard spectrum was based on the standard spectrum, rather than the sample spectrum; and
- produced an accurate intensity output that did not require interpretation of the graphical intensity output of Eclipse.

5.4.3 Cu 2p spectral analysis

The Cu 2p spectra were analysed in terms of spectral intensity according to the spectral analysis procedure described in Section 5.1.3; no fitting was performed. The Cu 2p spectra were consistent with the copper remaining monovalent (Appendix C) and the copper was not susceptible to photoreduction during the serial acquisition of twenty individual scans of the Cu 2p spectrum.

5.4.4 O 1s spectral analysis

The O 1s spectra were not analysed because of the spectral contribution by water. The extent of the contribution was determined by analysing a sample of washed chalcopyrite before and after 48 hours under vacuum and performing a spectral subtraction (Figure 5.25). The residual of the spectral subtraction is attributed to water and its width ($\sim$ 4 eV) precludes reliable subtraction for intensity determination. Analysis was complicated further by possible O 1s contributions between 530 and 532 eV from goethite, cuprite, sulphite and hydronium jarosite (Appendices A).

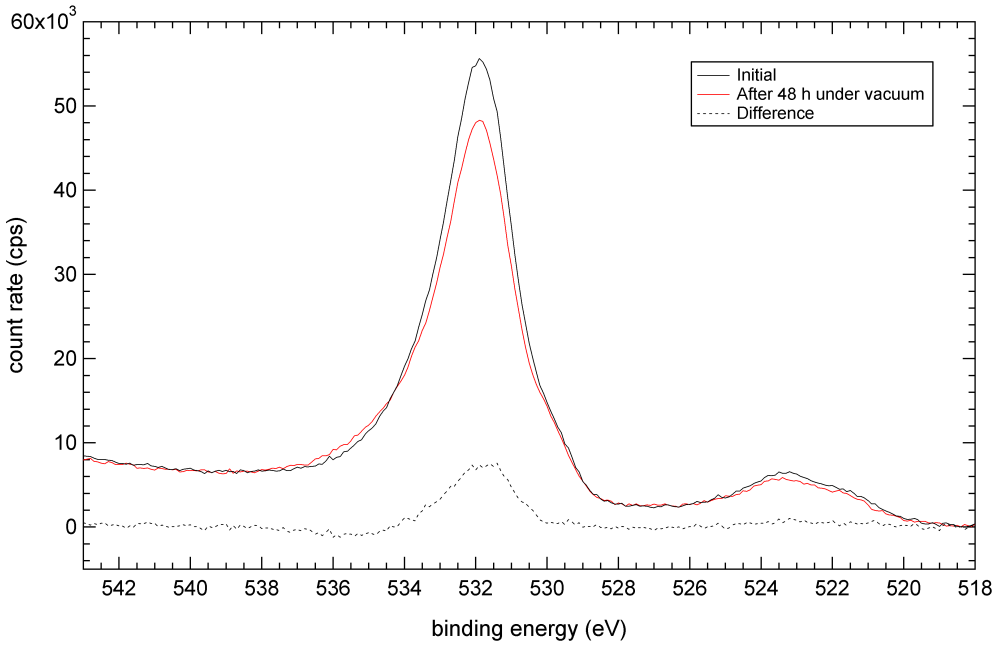

Figure 5.25: *The O 1s spectra of chalcopyrite (washed with MilliQ® water) before and after 48 hours under vacuum.*

5.4.5 C 1s spectral analysis

The C 1s spectra of chalcopyrite samples after oxidative dissolution were not analysed.

5.4.6 Cu $L_3M_{4,5}M_{4,5}$ spectral analysis

The electronic structures of the chalcopyrite samples after oxidative dissolution, according to Cu $L_3M_{4,5}M_{4,5}$ spectral analysis, are consistent with chalcopyrite remaining the only copper sulphide present (Appendix D).

5.4.7 Summary

Analysis of the S 2p spectra revealed the persistence of the sulphide, disulphide and loss structure peaks identified in the chalcopyrite standard, along with the presence of deposition phases, including elemental sulphur, sulphite and sulphate. Analysis of the Fe 2p spectra revealed only chalcopyrite, hydronium jarosite and goethite standard spectra were required to fit all Fe 2p spectra. These phases were used to inform the models constructed for quantitative analysis, while the fractional contributions of oxidation states towards the S 2p spectra and the phase contributions towards the Fe 2p spectra were also used for quantitative analysis.

5.5 Quantitative analysis of chalcopyrite after oxidative dissolution in ferric media

Quantitative analysis has been performed to model the surface of chalcopyrite samples after oxidative dissolution. The analysis was based on the correlation of observed photoelectron intensities of chalcopyrite samples and predicted photoelectron intensities of postulated surface models. The overall procedure required the development of three programs. Programs 1 and 2 consisted of inelastic mean free path (IMFP) and spectrometer calculations to predict the photoelectron intensities of postulated surface models. Program 1 was used to correlate the observed and predicted intensities of standards to establish the photoelectron cross section adjustments required for the IMFP and spectrometer calculations. The adjusted cross sections were introduced into Program 2, which predicted the photoelectron intensities for a suite of postulated surface

models. These model photoelectron intensities were assembled in Program 3, along with the photoelectron intensities observed for the chalcopyrite samples, and used to determine a suite of models that accounted for the observed photoelectron intensities. Finally, the statistical significance of this approach towards quantitative analysis was investigated.

5.5.1 Program 1

The Program 1 prediction of photoelectron intensities was largely dependent on the photoelectron line cross sections used. Although reported cross sections could have been used, it was important to correlate the intensities predicted using these cross sections with the intensities observed for a series of standards. This correlation established the cross section adjustments required for quantitative analysis.

5.5.1.1 Program 1 calculation

Program 1 was developed to predict the relative intensity of each photoelectron line for the uppermost 45 monolayers of a sample because these account for at least 98 % of the photoelectron line contribution of every phase examined. The sample monolayers were assigned to a single phase for the standards and multiple phases for the chalcopyrite samples. The physical properties of the phases, in addition to the energy and cross section of each photoelectron line, were used to calculate the IMFP for each phase and photoelectron line. Once the phase associated with each monolayer of the sample was declared, the fractional contribution of each monolayer towards each photoelectron line was determined as a function of the angle of emission from the sample. These fractional contributions were used to predict the intensity associated with each monolayer for each photoelectron line, based on the transmission function of the spectrometer and the pass energy declared. The intensities for each monolayer were then summed according to the nominated phases to produce intensities of each phase towards each photoelectron line.

5.5.1.2 IMFP and spectrometer calculations

The IMFP and spectrometer calculations were based on the physical properties of a suite of phases (Table 5.4).

The phase densities and band gaps were obtained from published data where possible, with some band gaps approximated according to comparable compounds (e.g., band gaps for insulators were approximated to 4.00 eV). The approximation of band gaps was not critical to the success of the IMFP calculations because of the minor effect they have on the calculations. The density of the speculated phases depended on whether the phases were the combination of two established solid phases. The density of $FeS_2.0.5Cu_2O$ was the average density of FeS_2 and Cu_2O, weighted according to stoichiometry. The density of $FeS_2O_3.0.5Cu_2O$ was the density of $FeS_2.0.5Cu_2O$ divided by the ratio of the molecular weight of $FeS_2O_3.0.5Cu_2O$ and the molecular weight of $FeS_2.0.5Cu_2O$. The density of goethite with either sulphate or sulphite adsorbed was the density of goethite divided by the molecular weight of goethite with either (protonated) sulphate or sulphite adsorbed divided by the molecular weight of goethite without (protonated) sulphate or sulphite adsorbed.

Table 5.4: *Physical properties of the phases used for the inelastic mean free path calculations of Program 1.*

Phase	**MW (g mol^{-1})**	**ρ (cm^3)**	**N$_a$**	**N$_v$**	**E$_g$ (eV)**
$CuFeS_2$	183.525	4.200	4.00	27	0.60*
CuS	95.612	4.760	2.00	15	0.50
Cu_5FeS_4	501.841	5.090	10.00	79	0.50
FeS_2	119.979	5.020	3.00	16	0.92†
0.5 Cu_2O	71.546	3.050	1.50	26	2.00‡
FeS_2.0.5 Cu_2O	191.525	5.423	4.50	29	1.46
$Fe_2(SO_4)_3$	399.885	3.097	17.00	76	4.00
$H_3OFe_3(SO_4)_2(OH)_6$	480.735	3.000	29.00	101	4.00
H_2SO_3	80.064	1.030	6.00	16	4.00
Fe_2O_3	159.692	5.240	5.00	28	1.90§
Fe_3O_4	231.539	5.180	7.00	40	2.50
FeOOH	88.854	4.280	4.00	17	2.50
$FeOOH.0.5H_2SO_3$	129.894	2.160	7.00	26	2.50
$FeOOH.0.25H_2SO_4$	113.374	4.740	5.75	23	2.50
$KFe_3(SO_4)_2(OH)_6$	500.811	3.000	26.00	95	4.00
$NaFe_3(SO_4)_2(OH)_6$	484.702	3.000	26.00	95	4.00
$NH_4Fe_3(SO_4)_2(OH)_6$	479.751	3.000	30.00	103	4.00
K_2SO_4	174.26	3.000	7.00	22	4.00
$CaCO_3$	100.087	3.000	7.00	18	4.00
TiO_2	79.879	4.260	3.00	12	3.20‖
Al_2O_3	101.961	4.020	5.00	12	6.30#
SnO_2	150.709	6.500	7.00	12	4.00
CuO	79.545	6.500	2.00	15	1.85
S_8	256.528	2.070	8.00	32	2.61**

Sources: *Sato and Teranishi (1976); †Karguppikar and Vedeshwar (1988); ‡Olsen et al. (1979); §Morin (1954); ‖Tang et al. (1993); #Ching et al. (1997); and **Abass and Ahmad (1986). All other band gaps were estimated.

Note: MW = molecular weight; ρ = density; N$_a$ = number of atoms; N$_v$ = number of valence electrons; and E$_g$ = band gap.

IMFP calculation

The inelastic mean free path (λ) was calculated for each phase and photoelectron line according to the equations proposed by Tanuma et al. (1991):

$$\lambda = \frac{E}{E^2}\left[\beta \ln(\gamma E) - \left(\frac{C}{E}\right) + \left(\frac{D}{E^2}\right)\right] \tag{5.1}$$

Where

$$E_p = 28.8\left[\frac{N_v \rho_{phase}}{MW_{phase}}\right]$$

$$\beta = -0.1 + \left(\frac{0.944}{\sqrt{E_p^2 + E_g^2}}\right) + 0.069\rho^{0.1}$$

$$\gamma = 0.191\rho_{phase} - 0.50$$

$$U = \frac{E_p^2}{829.4}$$

$$C = 1.97 - 0.91U$$

$$D = 53.4 - 20.8U$$

Where N_v is the number of valence electrons, E_g is the band gap, and E_K is the kinetic energy for each photoelectron line (Table 5.5).

Table 5.5: *Kinetic energy (eV) of photoelectron lines excited using Mg K_α radiation.*

S 2p		**O 1s**		**Fe 2p**		**Cu 2p**	
3 / 2	**1 / 2**	**3 / 2**	**1 / 2**	**3 / 2**	**1 / 2**	**3 / 2**	**1 / 2**
1088.6	1087.6	-	722.6	543.6	530.6	319.6	299.6

Spectrometer calculation

Once the phases associated with each of the 45 monolayers was declared, the fractional contribution of each monolayer towards each photoelectron line was determined *(I_{RPE})*. This required calculation of the monolayer thickness *(a)*, the attenuation per monolayer *(μ)*, the relative photoelectron intensity per monolayer *($I_{R/L}$)*, the cumulative attenuation to escape *($\Sigma\mu_e$)*, the detector intensity per monolayer *($I_{D/L}$)*, and the nett detector intensity *(ΣI_D)*. These calculations were performed as a function of the angle of the crystal face from which the photoelectrons are emitted, known as the angle of emission *(θ)*. Thus:

$$\text{Monolayer thickness } (a) = e^{(ln(MW/\rho\times10^3\times N_a\times NA)/3)\times10^8} \tag{5.2}$$

Where monolayer thickness *(a)* was in nanometers, molecular weight of the phase *(MW)* was in grams per mole, density of the phase *(ρ)* was in grams per cubic centimetres, number of atoms *(N_a)* was dimensionless, and Avogadros Number *(NA)* was 6.022×10^{23}.

$$\text{Attenuation per layer } (\mu) = e^{((-1\times a)/(\lambda cos\theta))} \tag{5.3}$$

Where the attenuation per layer *(μ)* was calculated using the inelastic mean free path *(λ)* for each phase and photoelectron line, the monolayer thickness *(a)*, and the angle of emission *(θ)*, which was in radians.

$$\text{Relative atomic density } (\rho_{RA}) = \rho_A \times 0.250 \times \rho_C \tag{5.4}$$

Where the relative atomic density of element *A* *(ρ_{RA})* was calculated using the density of element *A* *(ρ_A)* and the atomic density of copper in chalcopyrite *(ρ_C)*. These densities were in atoms per cubic centimetre.

$$\text{Relative photoelectron intensity per layer } (I_{R/L}) = \rho_{AN} \times \rho \times (1 - \mu) \tag{5.5}$$

Where the relative photoelectron intensity per layer *($I_{R/L}$)* was calculated using the normalised density of each element in the phase *(ρ_{AN})* in atoms per cubic centimetre, the density of the phase *(ρ)* in atoms per cubic centimetre, and the attenuation per layer *(μ)*.

Cumulative attenuation to escape $(\Sigma\mu_e) = \mu \times \mu_{above}$ (5.6)

Where the cumulative attenuation to escape $(\Sigma\mu_e)$ was calculated using the attenuation per layer (μ) and the attenuation per layer of the layer above (μ_{above}), which was equal to 1 for the first monolayer.

Detector intensity per layer $(I_{D/L}) = I_{R/L} \times \Sigma\mu_e$ (5.7)

Where the detector intensity per layer $(I_{D/L})$ was calculated using the relative intensity per layer $(I_{R/L})$ and the culmulative attenuation to escape $(\Sigma\mu_e)$.

Nett detector intensity $(\Sigma I_D) = \Sigma I_{D/L}$ (5.8)

Where the nett detector intensity (ΣI_D) for each photoelectron line was the sum of the individual detector intensities per layer $(\Sigma I_{D/L})$ for each photoelectron line.

Fraction of the intensity $(I_f) = I_{D/L}/\Sigma I_{D/L}$ (5.9)

Where the fraction of the intensity (I_f) contributed by each monolayer was calculated using the detector intensity $(I_{D/L})$ for each monolayer and the nett detector intensity per monolayer $(\Sigma I_{D/L})$.

The fraction of the intensity (I_f) considered each photoelectron line in isolation and assumed all photoelectron lines were of equal intensity. Thus, the fraction of the intensity was adjusted for the photoelectron cross section, pass energy, and spectrometer transmission function.

Nett observed intensity $(\Sigma I_O) = \Sigma I_D \times \sigma$ (5.10)

Where the nett observed intensity (ΣI_O) for each photoelectron line was calculated using the nett detector intensity (ΣI_D) and the photoelectron cross section (σ) for each photoelectron line (Table 5.6).

Table 5.6: *Photoelectron cross sections for the spectrometer calculations for Mg K_α radiation.*

S 2p		O 1s		Fe 2p		Cu 2p	
3 / 2	**1 / 2**	**3 / 2**	**1 / 2**	**3 / 2**	**1 / 2**	**3 / 2**	**1 / 2**
1.15	0.59	-	2.85	10.54	5.43	15.87	8.18

Note: S 2p and O 1s cross sections taken from Scofield (1976), while Fe 2p and Cu 2p cross sections taken from Section 5.5.1.3.

$$\text{Nett actual intensity } (\Sigma I_A) = E_{PASS} \times 10^{[4-0.21(log(E_{PASS}/E_K)^2)]} \tag{5.11}$$

Where the nett actual intensity (ΣI_A) was calculated using the pass energy (E_{PASS}) and the kinetic energy (E_K), both in eV.

$$\text{Nett relative intensity } (\Sigma I_R) = (\Sigma I_A / \Sigma I_{AFe}) \times \Sigma I_O \tag{5.12}$$

Where the nett relative intensity (ΣI_R) was calculated using the nett observed intensity (ΣI_O) and the nett actual intensity (ΣI_A), which was normalised to the arbitrarily selected nett actual intensity for the Fe $2p_{3/2}$ photoelectron line (ΣI_{AFe}).

The nett relative intensity was then normalised further according to the maximum nett relative intensity.

$$\text{Normalised nett relative intensity } (\Sigma I_{RN}) = (\Sigma I_R \times 100)/\Sigma I_{RM} \tag{5.13}$$

Where the normalised nett relative intensity (ΣI_{RN}) was calculated using the nett relative intensity (ΣI_R) and the maximum nett relative intensity (ΣI_{RM}).

The normalised nett relative intensity for each photoelectron line was used to adjust the fractional contribution of each monolayer towards each photoelectron line, to produce relative intensities for each photoelectron line.

Relative photoelectron intensity $(I_{RPE}) = I_f \times \Sigma I_{RN}$ (5.14)

Where the relative photoelectron intensity (I_{RPE}) was calculated using the intensity fraction (I_f) and the normalised nett relative intensity (ΣI_{RN}).

The monolayer intensity contributions to each photoelectron line were summed according to each phase. These intensities were expressed as intensities or fractional contributions of each phase to each photoelectron line.

5.5.1.3 Cross section adjustment

The suitability of the S 2p, Fe 2p, Cu 2p and O 1s cross sections reported by Scofield (1976) was investigated by comparing the observed and predicted intensities of a series of high purity standards that contribute to the photoelectron lines of interest. The S 2p and O 1s cross sections were assumed to be reliable, but the Fe 2p and Cu 2p cross sections were not, because of extensive multiplet splitting in the Fe 2p and Cu 2p lines.

Fe 2p

Determination of the Fe 2p intensity was complicated by O $KL_{2,3}L_{2,3}$ Auger contributions to the Fe 2p spectral envelope. The O $KL_{2,3}L_{2,3}$ contribution was estimated by the O $KL_{2,3}L_{2,3}$:O 1s spectral intensity ratios observed for a series of oxygen-bearing standards, without additional contributions to the O $KL_{2,3}L_{2,3}$ and O 1s spectral envelopes (Table 5.7).

Table 5.7: *Observed O $KL_{2,3}L_{2,3}$:O 1s spectral intensity ratios of a suite of oxygen-bearing standards, without interfering contributions to either spectral envelope.*

Phase	O $KL_{2,3}L_{2,3}$	O 1s	Ratio
Al_2O_3	3.17×10^4	2.96×10^4	1.07
$CaCO_3$ (# 1)	2.86×10^4	2.72×10^4	1.05
$CaCO_3$ (# 2)	5.62×10^4	5.61×10^4	1.00
K_2SO_4 (# 1)	2.41×10^4	2.42×10^4	1.00
K_2SO_4 (# 2)	4.87×10^4	5.06×10^4	0.96
TiO_2	3.16×10^4	2.74×10^4	1.15
		Ave.	1.04

The average O $KL_{2,3}L_{2,3}$:O 1s spectral intensity ratio (1.04) was used to mathematically remove the O $KL_{2,3}L_{2,3}$ contribution from the Fe 2p spectral envelopes of a series of iron- and oxygen-bearing standards, based on the observed O 1s intensities, to produce observed Fe 2p intensities (Table 5.8).

Table 5.8: *Observed Fe 2p intensity calculated from the observed O $KL_{2,3}L_{2,3}$ + Fe 2p and O 1s intensities for a suite of iron- and oxygen-bearing standards.*

	Obs.		Norm.		Obs.
Phase	**O KLL + Fe 2p**	**O 1s**	**O KLL + Fe 2p**	**O 1s**	**Fe 2p**
$H_3OFe_3(SO_4)_2(OH)_6$	1.96×10^6	6.32×10^5	43.4	14.0	28.8
$KFe_3(SO_4)_2(OH)_6$	2.25×10^6	6.90×10^5	45.7	14.0	31.2
$NaFe_3(SO_4)_2(OH)_6$	2.30×10^6	7.54×10^5	42.7	14.0	28.1
$NH_4Fe_3(SO_4)_2(OH)_6$	2.42×10^6	7.65×10^5	44.3	14.0	29.7
$Fe_2(SO_4)_3$	1.12×10^6	4.09×10^5	32.8	12.0	20.3
Fe_2O_3	3.77×10^6	4.84×10^5	23.4	3.0	20.2
Fe_3O_4	2.91×10^6	3.31×10^5	35.2	4.0	31.1
FeOOH	4.44×10^6	6.83×10^5	13.0	2.0	10.9

The observed Fe 2p intensities were consistently higher than the predicted Fe 2p intensities by a factor of 1.87, using the cross sections reported by Scofield (1976)(Table 5.9). The cross sections used in the IMFP calculation were subsequently adjusted by a

factor of 1.87. Although the adjustment is large, the excellent correlation between the observed and predicted intensities for a range of standards relevant to the study gives a high degree of confidence in this adjustment.

Table 5.9: *Fe 2p cross section adjustment calculated from the observed and predicted Fe 2p intensities of a suite of iron- and oxygen-bearing standards.*

		Unadjusted		Adjusted	
Phase	**Obs.**	**Pred.**	**Obs./Pred.**	**Pred.**	**Obs./Pred.**
$\mathbf{H_3OFe_3(SO_4)_2(OH)_6}$	28.8	15.3	1.89	28.5	1.01
$\mathbf{KFe_3(SO_4)_2(OH)_6}$	31.2	16.4	1.91	30.5	1.02
$\mathbf{NaFe_3(SO_4)_2(OH)_6}$	28.1	16.4	1.72	30.5	0.92
$\mathbf{NH_4Fe_3(SO_4)_2(OH)_6}$	29.7	16.4	1.82	30.6	0.97
$\mathbf{Fe_2(SO_4)_3}$	20.3	10.9	1.86	20.3	1.00
$\mathbf{Fe_2O_3}$	20.2	11.0	1.85	20.4	0.99
$\mathbf{Fe_3O_4}$	31.1	16.4	1.89	30.6	1.01
FeOOH	10.9	5.5	1.99	10.2	1.07
		Ave.	1.87	**Ave.**	1.00

Cu 2p

Determination of the Cu 2p intensity was not complicated by additional contributions to the Cu 2p spectral envelope. The correlation between observed and predicted Cu 2p:S 2p spectral intensity ratios for chalcopyrite and covellite was assessed because of the stability of these phases and the relevance of chalcopyrite to this study. The ratio of the observed and predicted Cu 2p:S 2p spectral intensity ratios was consistently inaccurate, with an average value of 0.863 (Table 5.10). The Cu 2p cross sections used in the IMFP calculation were subsequently adjusted by a factor of 0.863. The smaller adjustment required for the Cu 2p cross sections (relative to the Fe 2p cross sections) is attributed to the simpler multiplet splitting contribution to the Cu 2p spectral envelope. The high correlation between observed and predicted intensities gives confidence in the adjustment.

Table 5.10: *Cu 2p cross section adjustment calculated from the observed and predicted Cu 2p:S 2p spectral intensity ratios of a suite of copper- and sulphur-bearing standards.*

		Unadjusted		Adjusted	
Phase	**Obs.**	**Pred.**	**Obs./Pred.**	**Pred.**	**Obs./Pred.**
$CuFeS_2$	7.25	6.41	1.13	7.46	0.97
CuS	14.9	12.3	1.21	14.5	1.03
		Ave.	1.17	**Ave.**	1.00

5.5.1.4 Summary

Program 1 was used to determine the adjustments required for the photoelectron line cross sections. Comparison of the observed and predicted photoelectron intensities for a series of standards revealed the Fe 2p and Cu 2p cross sections required adjustment. Determination of the Fe 2p cross section adjustment was complicated by O $KL_{23}L_{23}$ contributions to the Fe 2p spectral envelope. However, the O $KL_{23}L_{23}$ contributions were removed mathematically, based on the associated O 1s intensity. This procedure produced a strong correlation between observed and predicted Fe 2p intensities for a suite of iron- and oxygen-bearing standards. Determination of the Cu 2p cross section adjustment was not complicated by additional contributions to the Cu 2p spectral envelope. A strong correlation between observed and predicted Cu 2p intensities for two copper sulphides (including chalcopyrite) was produced by adjustment of the Cu 2p cross sections.

5.5.2 Program 2

Program 2 was developed to generate suites of surface models and predict the photoelectron intensity associated with each phase in each model. These models were composed of chalcopyrite overlaid with the phases identified on the surface of chalcopyrite after oxidative dissolution (Section 5.4). The models were then used in the IMFP and spectrometer calculations of Program 1 (Section 5.5.1), which were modified to account for changes in photoelectron intensity caused by the roughened chalcopyrite

surface produced during oxidative dissolution. The IMFP and spectrometer calculations of Program 1 were modified further with the removal of the normalisation factors, to account for the different total photoelectron intensity associated with each model.

5.5.2.1 Model generation

The models generated by Program 2 were composed of bulk chalcopyrite underneath surface reconstruction phases and deposition phases (Figure 5.26). The surface reconstruction phases and deposition phases were based on species identified qualitatively (Section 5.4), reported data, and consideration of the system chemistry. The deposition phases included elemental sulphur, hydronium jarosite, and goethite (with and without sulphate and sulphite adsorbed). The suites of models generated (composed of 45 monolayers) were permutations of each deposition phase combination overlying each surface reconstruction combination (Table 5.11).

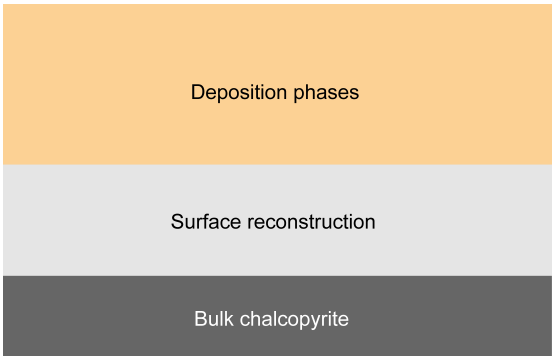

Figure 5.26: *Structure of the models used for quantitative analysis.*

Table 5.11: *Model permutations for Program 2.*

Suite	Elemental sulphur	Hydronium jarosite	Goethite	Goethite w\ sulphate	Goethite w\ sulphite
1	1 - 40	-	-	-	-
2	-	1 - 40	-	-	-
3	-	-	1 - 20	-	-
4	-	-	-	1 - 20	-
5	-	-	-	-	1 - 20
6	1 - 20	1 - 20	-	-	-
7	21 - 30	1 - 10	-	-	-
8	1 - 20	-	-	1 - 20	-
9	21 - 30	-	-	1 - 10	-
10	1 - 20	-	-	-	1 - 20
11	21 - 30	-	-	-	1 - 10
12	-	1 - 20	-	1 - 20	-
13	-	21 - 30	-	1 - 10	-
14	-	1 - 20	-	-	1 - 20
15	-	21 - 30	-	-	1 - 10
16	-	1 - 20	1 - 20	-	-
17	-	21 - 30	1 - 10	-	-
18	1 - 20	-	1 - 20	-	-
19	21 - 30	-	1 - 10	-	-

Note: Suites 1 to 15 were applied to chalcopyrite concentrate and massive. Suites 16 to 19 were applied to chalcopyrite concentrate exclusively.

Surface reconstruction

The surface reconstruction models were based on the analysis of fractured and polished chalcopyrite standards (Section 5.3) and differed for chalcopyrite concentrate and chalcopyrite massive. The surface reconstruction models of chalcopyrite concentrate consisted of one and two layers of $FeS_2.0.5Cu_2O$. Although the S 2p analysis of the chalcopyrite standard fractured under anaerobic atmosphere suggested two layers of $FeS_2.0.5Cu_2O$ were present on the surface, the use of one layer accommodated the possible reaction of the upper layer. It also accommodated the possibility some crystal faces only possessed one layer of surface reconstruction. The surface reconstruction models of chalcopyrite massive also consisted of one and two layers of $FeS_2.0.5Cu_2O$; however, they also consisted of the $FeS_2O_3.0.5Cu_2O$ phase identified on

the surface of polished chalcopyrite massive (Section 5.3.2). These models consisted of one layer of $FeS_2O_3.0.5Cu_2O$ on one and two layers of $FeS_2.0.5Cu_2O$, and two layers of $FeS_2O_3.0.5Cu_2O$ on one layer of $FeS_2.0.5Cu_2O$. The retention of at least one layer of $FeS_2.0.5Cu_2O$ was deemed necessary to produce a realistic combination of phases.

The possibility of stoichiometric metal deficient sulphide phases, including covellite and bornite, as viable replacements for $FeS_2.0.5Cu_2O$ and $FeS_2O_3.0.5Cu_2O$, was dismissed after analysis of Cu $L_3M_{4,5}M_{4,5}$ Auger spectra revealed no copper sulphide forms on chalcopyrite after oxidative dissolution (Appendices D).

Deposition phases

The deposition phase models overlying the surface reconstruction models included elemental sulphur, hydronium jarosite, and goethite (with and without sulphate and sulphite adsorbed).

Elemental sulphur

Elemental sulphur is a product of the direct reaction of the disulphide in $FeS_2.0.5Cu_2O$. Therefore, models including elemental sulphur, for both chalcopyrite concentrate and massive, consisted of elemental sulphur on $FeS_2.0.5Cu_2O$, rather than $FeS_2O_3.0.5Cu_2O$. These assumptions are consistent with the observation of elemental sulphur crystals forming on the surface of chalcopyrite before secondary nucleation of elemental sulphur from solution (Section 2.6.3).

Hydronium jarosite

Hydronium jarosite is a product of iron hydrolysis that was assumed to deposit onto both surface reconstruction phases ($FeS_2.0.5Cu_2O$ and $FeS_2O_3.0.5Cu_2O$). It forms near the surface where the iron and sulphate concentrations are high because of chalcopyrite dissolution and the pH is relatively high because of proton consumption by the chalcopyrite surface. The dramatic increase in hydronium jarosite observed in the

Fe 2p spectra of chalcopyrite after oxidative dissolution (Appendix C) suggests hydronium jarosite is deposited onto all phases, including elemental sulphur.

Goethite

Goethite is another product of iron hydrolysis, which is susceptible to adsorption and incorporation of (protonated) anions such as sulphite and sulphate (Appendix E). Therefore, the models included three forms of goethite: FeOOH, $FeOOH.0.25H_2SO_4$ and $FeOOH.0.5H_2SO_3$. The inclusion of $FeOOH.0.25H_2SO_4$ and $FeOOH.0.5H_2SO_3$ accounted for the additional S(VI) and S(IV) observed in the S 2p spectra, while maintaining the goethite speciation and associated intensity in the Fe 2p spectra. All three forms of goethite are products of iron hydrolysis that deposit onto both reconstruction surface phases ($FeS_2.0.5Cu_2O$ and $FeS_2O_3.0.5Cu_2O$). These phases form near the surface where the iron, sulphate and sulphite concentrations are high because of chalcopyrite dissolution and the pH is relatively high because of proton consumption by the mineral surface. Similar to hydronium jarosite, goethite precipitates from bulk solution; however, a nucleation mechanism could not be discerned from qualitative analysis of the Fe 2p spectra. Because goethite precipitation is intimately associated with hydronium jarosite precipitation (both are products of iron hydrolysis), it was assumed goethite may deposit onto all phases including elemental sulphur and hydronium jarosite; goethite forms after hydronium jarosite precipitation because of the depletion of sulphate from solution. However, the goethite deposited onto the chalcopyrite surface was assumed to be less than the hydronium jarosite deposited because the goethite contribution towards the Fe 2p spectra was always lower and the mole ratio of iron in goethite is higher, so less is required to produce the commensurate Fe 2p intensity. Thus, the maximum number of goethite layers was restricted to twenty. The restricted number of layers was also influenced by the limited number of models permitted by the optimisation program (Section 5.5.3).

5.5.2.2 Surface roughness

Program 2 accounted for surface roughness of the sample by predicting the photoelectron intensities associated with each phase and photoelectron line over a range of angles of emission and scaling these intensities according to the predicted contribution towards the overall spectrum. The prediction is based on the probability of the crystal face of the phase assuming each angle, and the X-ray flux experienced by the crystal face at each angle.

Surface roughening distorts the intensity in two ways. First, intensity is a function of the angle of emission from the crystal face. Second, intensity is proportional to the X-ray flux incident on the crystal face and the X-ray flux is proportional to the area underlying the crystal face. The first factor was addressed by varying the angle of emission (Equation 5.3), while the second factor was addressed by calculating the area underlying the crystal face (of fixed dimensions) as a function of the angle of emission and using these areas as scaling factors for the intensities determined at each angle of emission for each model.

The final angles and areas of the crystal face were determined after rotations in the x- and y-axes (Figure 5.27).

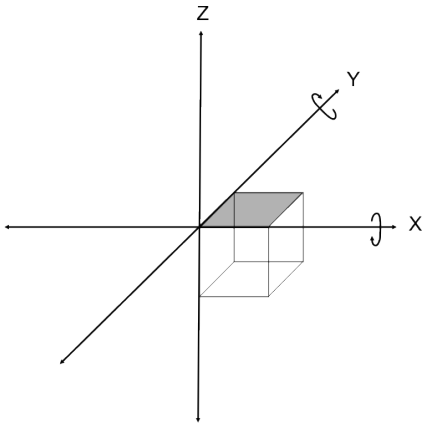

Figure 5.27: *Crystal face before rotations in the x- and y-axes.*

The final angle of the crystal face to the $x - y$ plane, after rotations in the x- and y-axes, was calculated:

$$\text{Final angle} = \text{ArcCosine [Cosine } (x\text{-axis rotation}) \times \text{Cosine } (y\text{-axis rotation})] \tag{5.15}$$

The rotations about the x- and y-axes required for the crystal face to assume a final angle between 0 and 85° at 5° intervals were determined, with the limit of 5° intervals imposed to simplify implementation of the final angle (as the angle of emission) into Program 1. The rotations in the x-axis were further restricted to 5° intervals to limit the number of possible x- and y-axis rotation combinations.

The final area underlying the crystal face (1 μm^2) after these rotations was calculated:

$$\text{Final area} = \text{Cosine } (x\text{-axis rotation}) \times \text{Cosine } (y\text{-axis rotation})] \tag{5.16}$$

The calculated areas revealed the number of x- and y-axis rotation combinations increased and the area underlying the face decreased, with the final angle assumed (Table 5.12). This relationship produced a maximum contribution from a final angle approaching 45°.

Table 5.12: *Rotations about the x- and y-axes required to produce final angles of 0°, 5°, 10° and 15° for a 1 μm^2 crystal face and the associated fractional contribution of each final angle.*

X rotation	Y rotation	Final angle	Final area	Total area	Fractional contribution
0.00	0.00	0.00	1.000	1.000	**0.0115**
0.00	5.00	5.00	0.996		
5.00	0.00	5.00	0.996	1.992	**0.0230**
0.00	10.00	10.00	0.985		
5.00	8.67	10.00	0.985		
10.00	0.00	10.00	0.985	2.954	**0.0341**
0.00	15.00	15.00	0.966		
5.00	14.16	15.00	0.966		
10.00	11.24	15.00	0.966		
15.00	0.00	15.00	0.966	3.864	**0.0446**

Note: Fractional contribution was calculated from the sum of the total areas for final angles 0 to 85°.

The final areas were then summed to produce the fractional contribution of each final angle towards the XPS spectrum (Table 5.13). These contributions were used as scaling factors for the photoelectron intensities associated with each angle of emission used in Program 1.

Table 5.13: *Fractional contribution of each final angle towards the observed spectrum.*

Angle (°)	Fractional contribution	Angle (°)	Fractional contribution
0.00	0.0115	45.00	0.0816
5.00	0.0230	50.00	0.0816
10.00	0.0341	55.00	0.0794
15.00	0.0446	60.00	0.0750
20.00	0.0542	65.00	0.0683
25.00	0.0627	70.00	0.0592
30.00	0.0699	75.00	0.0478
35.00	0.0756	80.00	0.0341
40.00	0.0795	85.00	0.0181

5.5.2.3 Normalisation removal

Program 2 did not include the normalisation steps of Program 1. These steps were removed because the photoelectron intensities associated with each model varied depending on the total number of photoelectrons that emerged from the respective models. For example, one sample composed of one layer of elemental sulphur on infinitely thick chalcopyrite produces a different total number of photoelectrons than a sample composed of two layers of elemental sulphur on infinitely thick chalcopyrite. Therefore, two different models, representing equal quantities of the surface, do not contribute equally to any of the photoelectron lines. Thus, the normalisation equations 5.12 and 5.13 used previously, were replaced with equation 5.17:

$$\text{Nett relative intensity}(\Sigma I_R) = \Sigma I_A \times \Sigma I_O \tag{5.17}$$

Where the nett relative intensity (ΣI_R) was calculated using the nett observed intensity (ΣI_O) and the nett actual intensity (ΣI_A).

5.5.2.4 Summary

The models generated by Program 2 represented possible arrangements of the surface reconstruction and deposition phases on chalcopyrite after oxidative dissolution. The photoelectron intensities associated with each model were predicted for a suite of angles that accounted for the roughened surface of chalcopyrite after oxidative dissolution. Normalisation removal was also performed.

5.5.3 Program 3

Program 3 was developed to determine a suite of models generated by Program 2 that would account for the photoelectron intensities observed for each chalcopyrite sample after oxidative dissolution. The suite of models was then compiled to produce a profile

of the surface. These profiles enabled comparison of chalcopyrite surfaces after oxidative dissolution in ferric media (Chapter 6).

The photoelectron intensities observed for each sample, and predicted for each model, were introduced into Program 3. These intensities addressed the fractional contribution of each oxidation state towards the S 2p spectrum and the fractional contribution of each phase towards the Fe 2p spectrum. The phases attributed to the oxidation states in the S 2p spectra and the phases attributed to the Fe 2p spectra are compiled in Tables 5.14 and 5.15. Additionally, the Cu 2p and S 2p intensities attributed to bulk chalcopyrite and surface reconstruction phases were introduced and expressed as a ratio.

Table 5.14: *Phases attributed to the oxidation states observed in the S 2p spectra of chalcopyrite after oxidative dissolution.*

Oxidation state	Phase
-II	$CuFeS_2$
-I	$FeS_2.0.5Cu_2O$, $0.5 \times FeS_2O_3.0.5Cu_2O$
0	S_8
IV	$FeOOH.0.5H_2SO_3$
VI	$FeOOH.0.25H_2SO_4$, $H_3OFe_2(SO_4)_2(OH)_6$, $0.5 \times FeS_2O_3.0.5Cu_2O$

Note: S 2p intensity of $FeS_2O_3.0.5Cu_2O$ divided equally between S(-II) and S(VI).

Table 5.15: *Phases attributed to the standards observed in the Fe 2p spectra of chalcopyrite after oxidative dissolution.*

Standard	Phase
$CuFeS_2$	$CuFeS_2$, $FeS_2.0.5Cu_2O$, $FeS_2O_3.0.5Cu_2O$
FeOOH	FeOOH, $FeOOH.0.5H_2SO_3$, $FeOOH.0.25H_2SO_4$
$H_3OFe_3(SO_4)_2(OH)_6$	$H_3OFe_3(SO_4)_2(OH)_6$

The residual between the observed and modelled fractional contributions, and the Cu 2p:S 2p ratio, was expressed as the sum of squared residuals and minimised by optimising the scaling factors associated with each of the models. Optimisation was performed using Premium Solver 6.5 and the LP GRG Engine, with the default settings and a

precision of 0.0001. All scaling factors were constrained to remain positive and the sum of the scaling factors was constrained to equal 1.

Once the initial fit was completed, all models with scaling factors lower than 0.004 were discarded. The optimisation was repeated and the model associated with the lowest scaling factor was discarded if the scaling factor was lower than 0.01. This process was repeated until all scaling factors were higher than 0.01. The 0.01 cut off was arbitrary, but was considered a realistic limit to ensure a robust suite of models.

The suite of models for each sample was compiled to produce a profile of the chalcopyrite surface. The profiles consist of the cumulative scalar factors along the x-axis and the phase thickness along the y-axis. The phase thickness was calculated by multiplying the number of phase layers by the monolayer thickness of the phase (Equation 5.2). These phases were grouped according to surface reconstruction phase, and then the overlying deposition phases, to aid interpretation. Thus, although all of the elemental sulphur – for example – is presented on the right hand side of all figures, it is assumed to exist in multiple islands across the surface, in accordance with reported images of oxidised chalcopyrite (Section 2.6.3).

An example of a surface profile is provided in Figure 5.28. The profile is composed of the cumulative surface fraction (totalling 1.0) along the x-axis and the phase thickness (in nm) along the y-axis. The first phase shown, chalcopyrite (black), underlies all of the phases and is assumed to be infinitely thick, although only two layers are shown. The next phase is the 'pyritic' reconstruction (dark grey), which covers approximately each half of the surface with one and two layers, respectively. The one layer of 'pyritic' reconstruction is almost entirely covered by two layers of the oxidised 'pyritic' reconstruction phase (light grey). The oxidised 'pyritic' reconstruction phase is almost entirely covered by neighbouring monolayers of hydronium jarosite (yellow) and goethite with adsorbed sulphite (pink). All of the surface composed of two layers of 'pyritic' reconstruction, and a small amount of the suface composed of one layer of 'pyritic' reconstruction, is covered by elemental sulphur (green) of varying thickness.

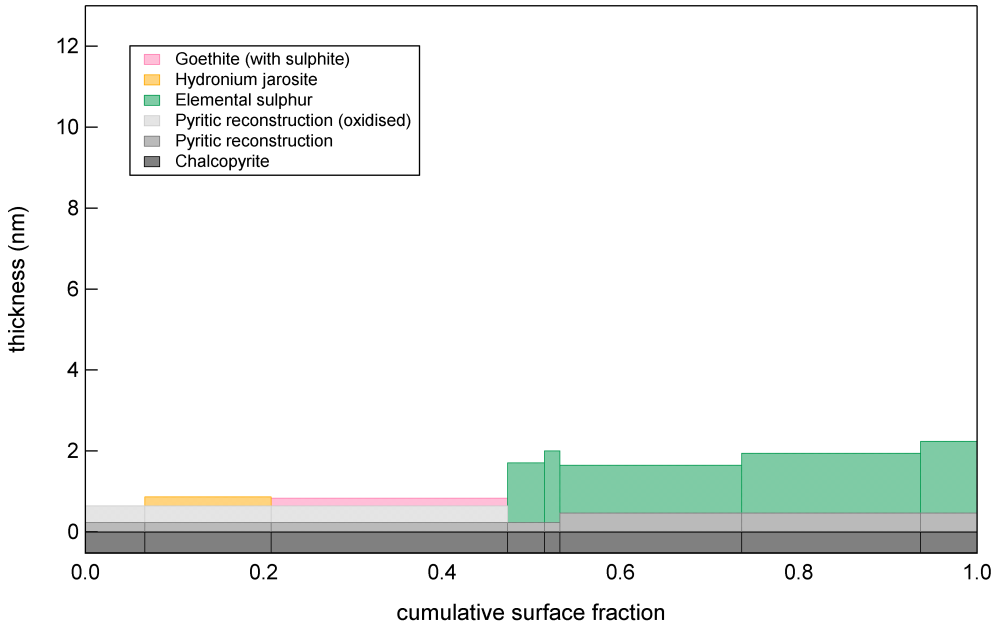

Figure 5.28: *Surface profile of chalcopyrite (Mass-p) after oxidative dissolution in 0.1 M ferric sulphate (pH 1.9) at 50° C for 15 minutes.*

5.5.4 Assessment of the quantitative analysis procedure

The quantitative analysis procedure was assessed because of its complexity and the potential implication of the results. The assessment addressed the limitations of the models generated in Program 2 and used in Program 3, the quality of fit between the observed and predicted photoelectron intensities, and the robustness of the surface profiles to changes in the spectral fitting procedure.

5.5.4.1 Limitations of the models

The limitations of the models generated in Program 2 and used in Program 3 include the discrete phases required, the 'perfectly rough' surface assumed, and the limited thickness of deposition phases modelled.

The discrete phase limitation is most evident with the fixed sulphite adsorption/incorporation in the proposed $FeOOH.0.5H_2SO_3$ phase. The fixed level meant the sulphite in the S 2p spectrum fit was constrained by the goethite in the Fe 2p spectrum fit, especially when the goethite contribution to the Fe 2p spectrum was low. To enable fits of the sulphite peak in the S 2p spectra, without adversely affecting the fit of the other peaks, a relatively high level of sulphite adsorption/incorporation (50 %) was assumed. The high level was counteracted by introducing pure goethite as a possible phase for chalcopyrite concentrate samples. This produced a dilution effect with the adsorbed/incorporated sulphite assumed to be distributed across all goethite on the surface; this dilution approach was not possible for chalcopyrite massive because of the restricted number of models permitted by the optimisation program. Nonetheless, the high level of sulphite adsorption/incorporation assumed, and the constant low levels of sulphite observed in the S 2p fits, ensured the sulphite S 2p fit was not critical to the overall success of the fits and introduced only $\sim$ 1 % error.

Deviations from the 'perfectly rough' surface assumption were caused by shadowing of neighbouring features. Shadowing arises after extensive dissolution with the emergence of crevices or crevasses along grain boundaries, or the deposition of phases from solution. Both of these processes cause the surface topography to deviate from the 'perfectly rough' assumption of the spectrometer calculations.

The extent of reaction also affects the ability of the spectrometer to detect changes in the surface. This affect is reflected in the 45 monolayer limit used for the models because monolayers residing deeper in the sample remain essentially invisible to the spectrometer. Additionally, phase combinations not included in the suite of models will not be part of the solution. For example, more than 40 monolayers of hydronium jarosite on elemental sulphur will appear to be pure hydronium jarosite to the spectrometer and will be approximated to 40 monolayers of hydronium jarosite on chalcopyrite by Program 3. This restriction will only apply to surfaces after extensive phase deposition.

5.5.4.2 Quality of fits of the models

The quality of fit achieved between the observed and predicted photoelectron intensities was examined to establish the ability of the quantitative procedure to represent the surface of chalcopyrite concentrate and massive after oxidative dissolution.

The observed and predicted intensities were plotted and the regression lines for observed vs. predicted and predicted vs. observed were calculated (Table 5.16). The regression line gradients and intercepts were then averaged and used to calculate new predicted intensities, based on the observed intensities. The error associated with the new predicted intensities was calculated from the squared sum of residuals *(SS_r)* between the original and new predicted intensities. Finally, the upper and lower 95 % confidence intervals for the new predicted intensities were determined:

$$y_{calc} \pm t_{N-2}\sqrt{\frac{SS_r}{N-2}}\sqrt{\frac{1}{N}+\frac{(x-x')^2}{(N-1)S_x^2}} \tag{5.18}$$

Where y is the new predicted intensity, t is 2.365, SS_r is the squared sum of residuals, N is the number of new predicted intensities, x is each new predicted intensity, x' is the average of the new predicted intensities, and S_x is the standard deviation of the new predicted intensities.

Table 5.16: *Example of the data processing performed on the observed and predicted photoelectron intensity data to determine the quality of fit.*

	S 2p					Fe 2p			
	S(-II)	**S(-I)**	**S(0)**	**S (IV)**	**S (VI)**	**$CuFeS_2$**	**H_3O-J**	**FeOOH**	**Cu2p/S2p**
Obs.	0.368	0.161	0.237	0.028	0.207	0.287	0.459	0.255	0.752
Pred.	0.356	0.150	0.238	0.027	0.229	0.303	0.444	0.252	0.734
New Pred.	0.364	0.163	0.237	0.035	0.208	0.285	0.452	0.254	0.736
Conf. Int.	0.011	0.012	0.011	0.017	0.011	0.010	0.013	0.010	0.024
Pred. L95%	0.353	0.151	0.226	0.018	0.197	0.275	0.434	0.244	0.712
Pred. U95%	0.374	0.176	0.248	0.052	0.219	0.295	0.464	0.265	0.760

Note: H_3O-J = Hydronium jarosite; Conf. Int. = confidence interval; L95% = lower 95% confidence interval; U95% = upper 95% confidence interval.

All SS_r were below 0.0005.

The quality of fit was determined for all Mass-p and Con-p samples (Tables 5.17 and 5.18). The predicted and new predicted intensities are within a 95 % confidence limit for all samples, with only a maximum of three outliers for any sample. These outliers remain close to the regression line with standard deviations of the gradients and intercepts not exceeding 0.024 and 0.009, respectively, for all samples (Figure 5.29).

Table 5.17: *Quality of fits for the quantitative analysis of the XPS spectra of chalcopyrite (Mass-p) after oxidative dissolution in 0.1 M ferric sulphate (pH 1.9) at 50° C.*

Time (h)	Grad.	Inter.	$SD_{(Grad.)}$	$SD_{(Inter.)}$	r^2	SS_r	Outliers
0.25	1.010	-0.003	0.013	0.005	0.999	0.001	2
0.50	1.012	-0.003	0.015	0.006	0.999	0.001	2
1.00	1.009	-0.002	0.011	0.004	0.999	0.001	3

Note: Grad. = Gradient; Inter. = Intercept; SD = Standard deviation; r^2 = Correlation coefficient; and SS_r = Sum of squared residuals.

Table 5.18: *Quality of fits for the quantitative analysis of the XPS spectra of chalcopyrite (Con-p) after oxidative dissolution in 0.1 M ferric sulphate and 0.2 M ferric chloride at various pH values and temperatures for 2 hours.*

Lixiviate	pH	T (°C)	Grad.	Inter.	$SD_{(grad.)}$	$SD_{(inter.)}$	r^2	SS_r	Outliers
$Fe_2(SO_4)_3$	1.9	50	0.967	0.008	0.023	0.008	0.997	0.001	2
$Fe_2(SO_4)_3$	1.3	50	0.999	0.000	0.001	0.000	1.000	0.000	0
$Fe_2(SO_4)_3$	1.3	65	1.002	-0.001	0.007	0.003	1.000	0.000	1
$Fe_2(SO_4)_3$	1.3	80	0.995	0.001	0.006	0.002	1.000	0.000	1
$FeCl_3$	1.3	50	0.975	0.005	0.008	0.003	1.000	0.000	2
$FeCl_3$	1.3	65	0.985	0.004	0.024	0.009	0.996	0.002	3
$FeCl_3$	1.3	80	0.966	0.007	0.013	0.005	0.999	0.001	1

Note: Grad. = Gradient; Inter. = Intercept; SD = Standard deviation; r^2 = Correlation coefficient; and SS_r = Sum of squared residuals.

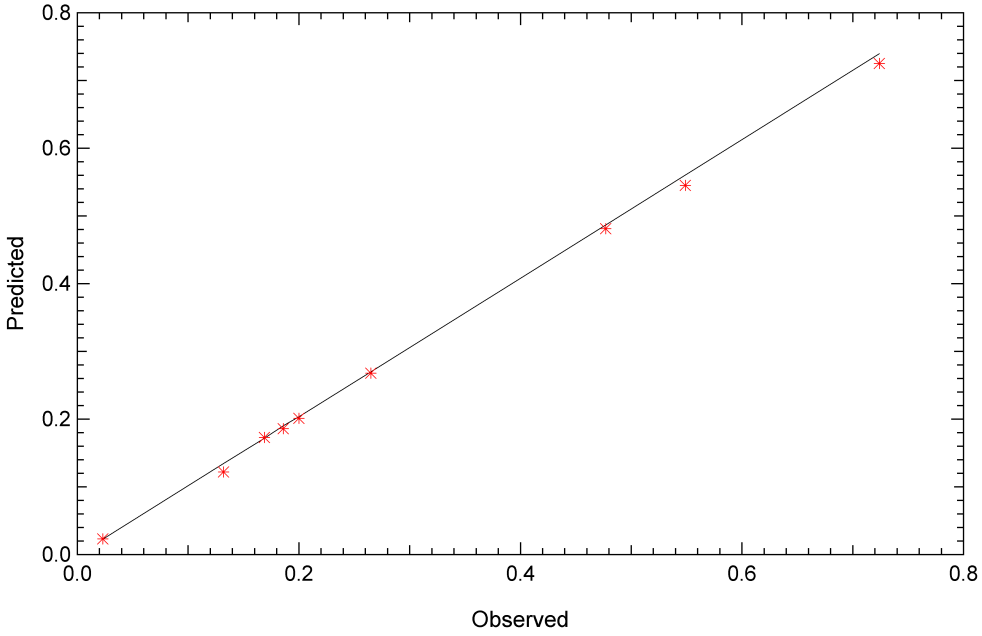

Figure 5.29: *Observed vs. predicted photoelectron intensities of chalcopyrite (Con-p) after oxidative dissolution in 0.1 M ferric sulphate (pH 1.3) at 65° C for 2 hours.*

The high correlation between the predicted and observed photoelectron intensities gives a high degree of confidence in the quantitative procedure to represent the surface of chalcopyrite after oxidative dissolution.

5.5.4.3 Robustness of the models

The robustness of the models reflects the reproducibility of the quantitative analysis procedure and the validity of comparing the profiles of surfaces oxidised under different conditions. Robustness was established by perturbing the S 2p and Fe 2p photoelectron intensities by 5 % and 10 %, determining the suite of models, and calculating the quality of fit. The suite of models produced using the perturbed intensities was then compared with the suite of models produced using the unperturbed intensities.

The perturbations of the chalcopyrite S 2p and Fe 2p photoelectron intensities (5 and 10 %) were distributed towards overlapping photoelectron intensities according to the

approximate extent of overlap. The S 2p perturbation was distributed to the disulphide and elemental sulphur photoelectron intensities in a ratio of 6:4, while the Fe 2p perturbation was distributed to hydronium jarosite and goethite photoelectron intensities in a ratio of 1:1. Additionally, the chalcopyrite S 2p intensity was commensurately perturbed, altering the Cu 2p:S 2p ratio. The perturbation was performed on the intensities observed for chalcopyrite (Con-p) oxidised in ferric chloride (pH 1.3) and ferric sulphate (pH 1.3) at 80° C for 2 hours (Table 5.19).

Table 5.19: *Sum of squared residuals (SS_r) for two chalcopyrite (Con-p) samples after oxidative dissolution in 0.1 M ferric sulphate and 0.2 M ferric chloride (both pH 1.3) at 80 C° for 2 hours, as the original S 2p and Fe 2p photoelectron intensities were perturbed by 5 and 10 %.*

		S 2p				**Fe 2p**			
Sample	**Unper.**	**+ 5 %**	**- 5 %**	**+ 10 %**	**- 10 %**	**+ 5 %**	**- 5 %**	**+ 10 %**	**- 10 %**
'$Fe_2(SO_4)_3$'	0.0107	0.0083	0.0034	0.0137	0.0109	0.0125	0.0256	0.0169	0.0307
'$FeCl_3$'	0.0332	0.0255	0.0425	0.0181	0.0524	0.0370	0.0375	0.0559	0.0430

Note: Perturbation of the intensities increased the sum of squared residuals (SS_r) of the fits substantially for all but two cases, for each of the two samples examined.

The surface profiles for the perturbed and unperturbed intensities, for both samples, consistently reveal greater hydronium jarosite in the ferric sulphate system than in the ferric chloride system (Figures 5.34 - 5.40, and 6.7 and 6.10). This consistency validates the data processing procedure, the phases, the physical properties of the phases, and the quantitative analysis procedure. Furthermore, it confirms the procedure can be used in the comparison of chalcopyrite surfaces oxidised under different conditions.

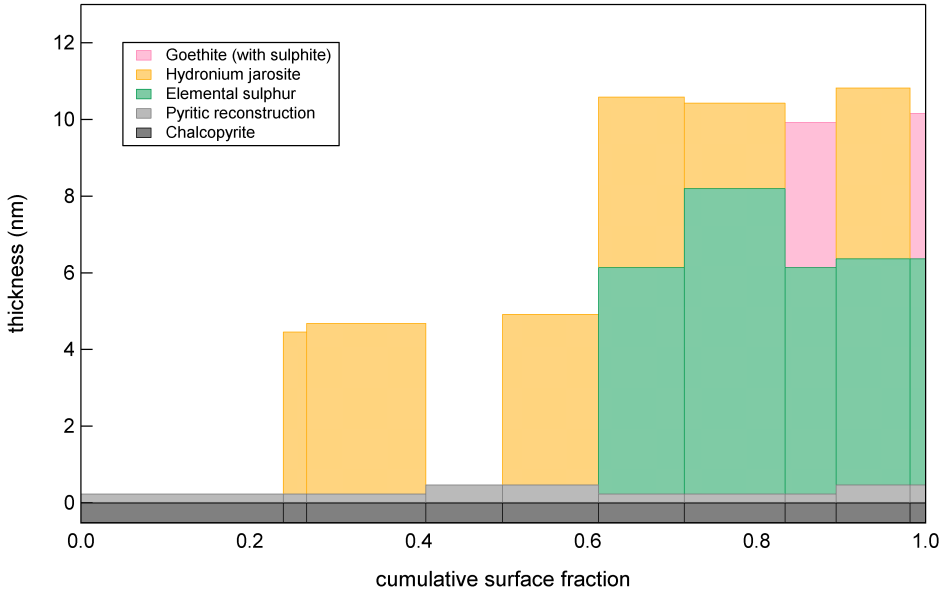

Figure 5.30: *Surface profile of chalcopyrite (Con-p) after oxidative dissolution in 0.1 M ferric chloride (pH 1.3) at 65° C for 2 hours, with 5 % added to the S 2p intensity of chalcopyrite.*

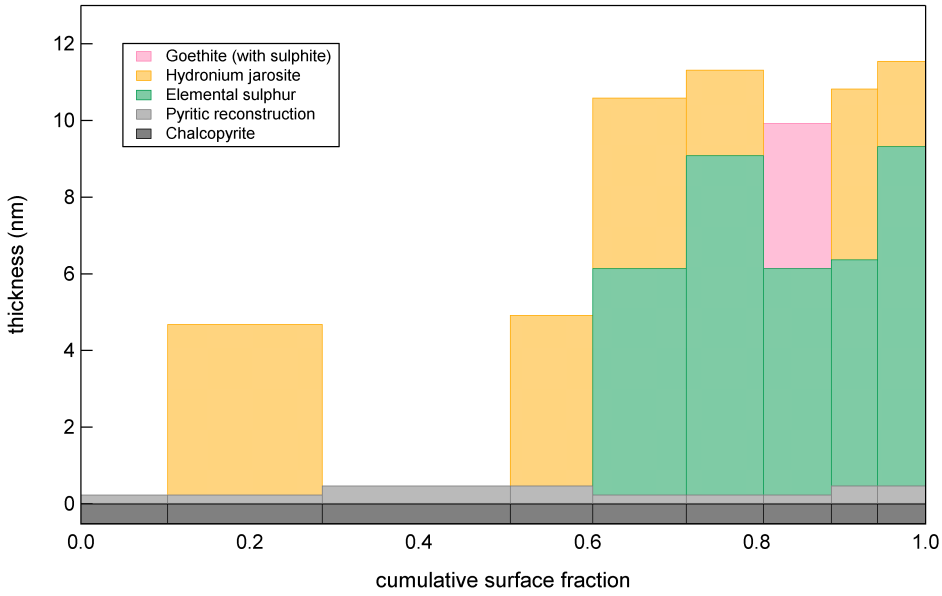

Figure 5.31: *Surface profile of chalcopyrite (Con-p) after oxidative dissolution in 0.1 M ferric chloride (pH 1.3) at 65° C for 2 hours, with 5 % subtracted from the S 2p intensity of chalcopyrite.*

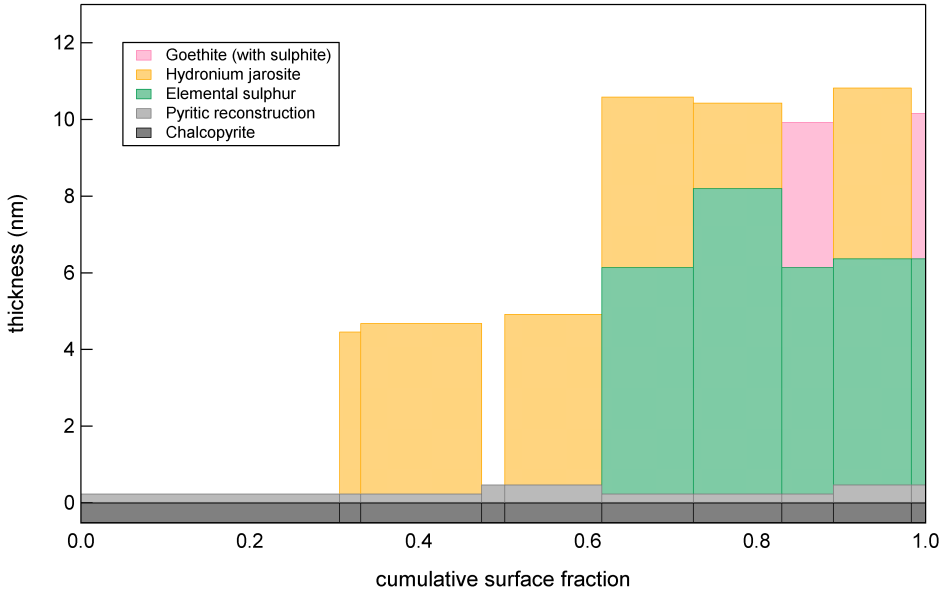

Figure 5.32: *Surface profile of chalcopyrite (Con-p) after oxidative dissolution in 0.1 M ferric chloride (pH 1.3) at 65° C for 2 hours, with 10 % added to the S 2p intensity of chalcopyrite.*

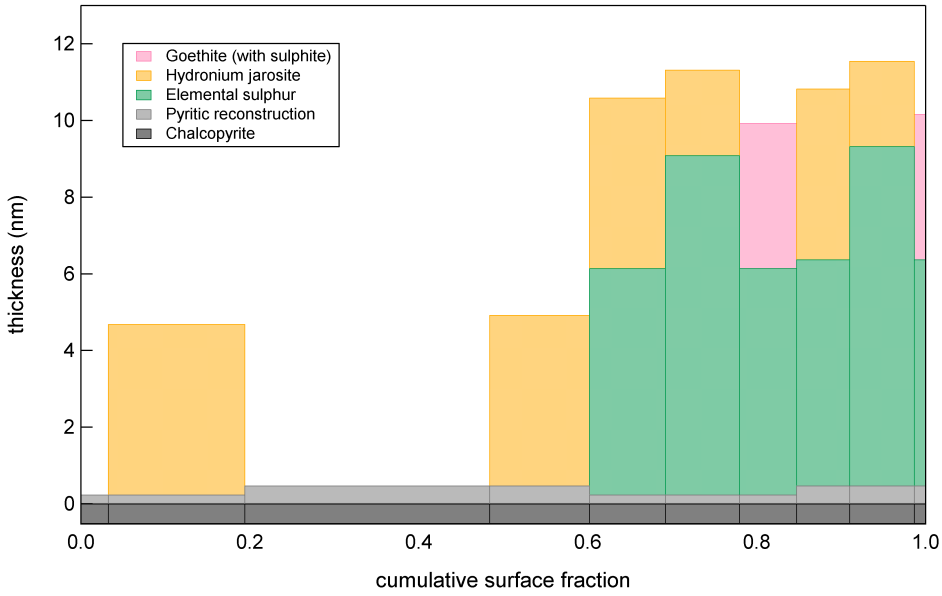

Figure 5.33: *Surface profile of chalcopyrite (Con-p) after oxidative dissolution in 0.1 M ferric chloride (pH 1.3) at 65° C for 2 hours, with 10 % subtracted from the S 2p intensity of chalcopyrite.*

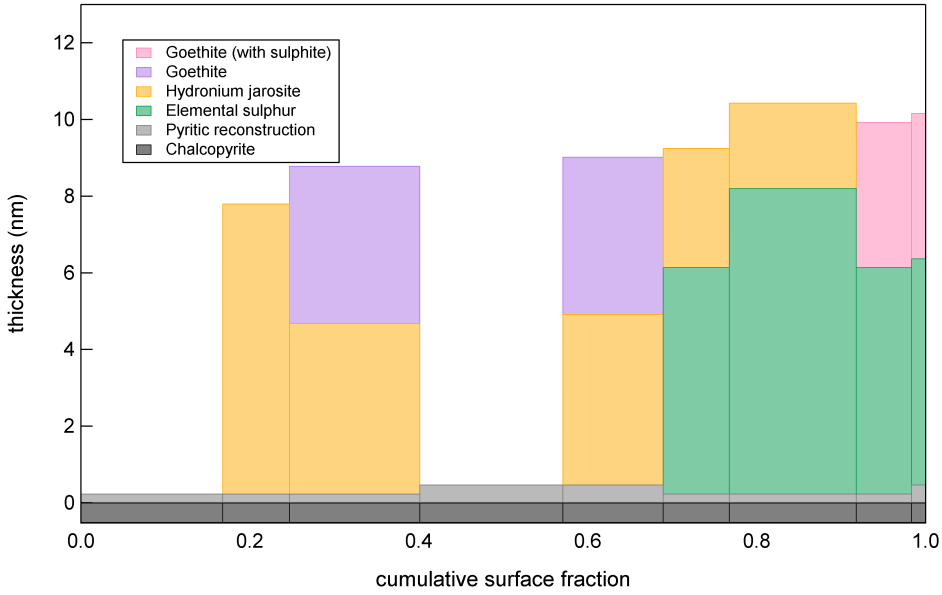

Figure 5.34: *Surface profile of chalcopyrite (Con-p) after oxidative dissolution in 0.1 M ferric chloride (pH 1.3) at 65° C for 2 hours, with 5 % added to the Fe 2p intensity of chalcopyrite.*

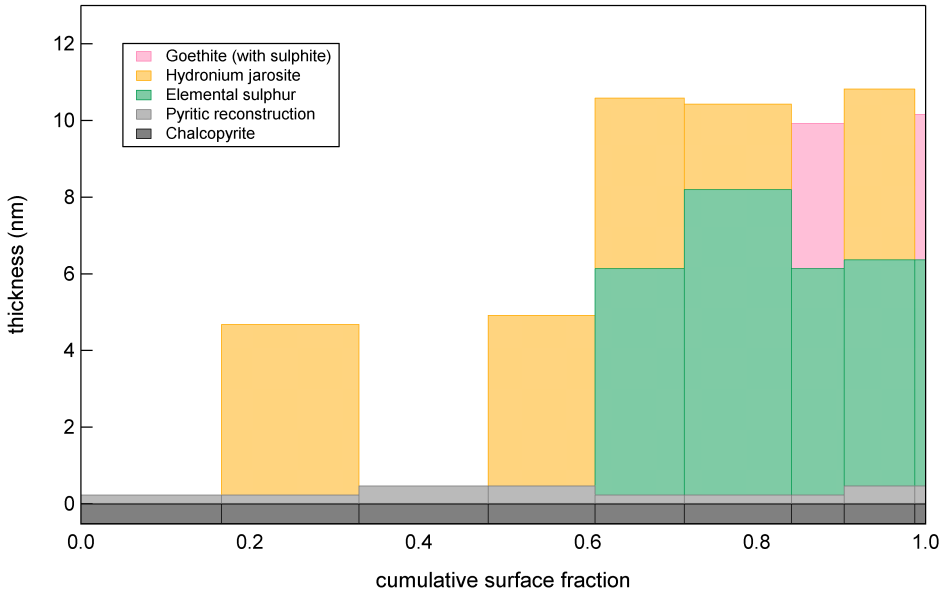

Figure 5.35: *Surface profile of chalcopyrite (Con-p) after oxidative dissolution in 0.1 M ferric chloride (pH 1.3) at 65° C for 2 hours, with 5 % subtracted from the Fe 2p intensity of chalcopyrite.*

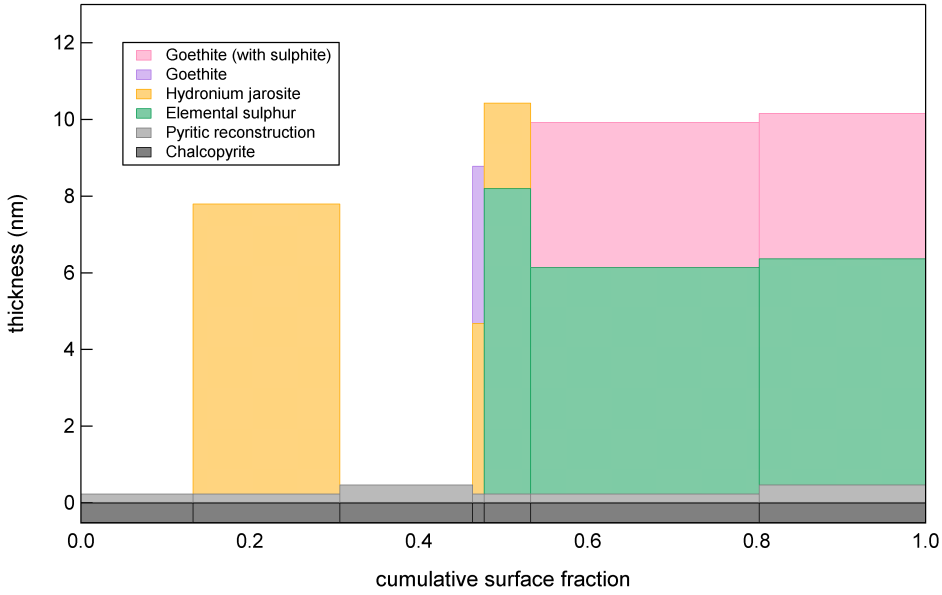

Figure 5.36: *Surface profile of chalcopyrite (Con-p) after oxidative dissolution in 0.1 M ferric chloride (pH 1.3) at 65° C for 2 hours, with 10 % added to the Fe 2p intensity of chalcopyrite.*

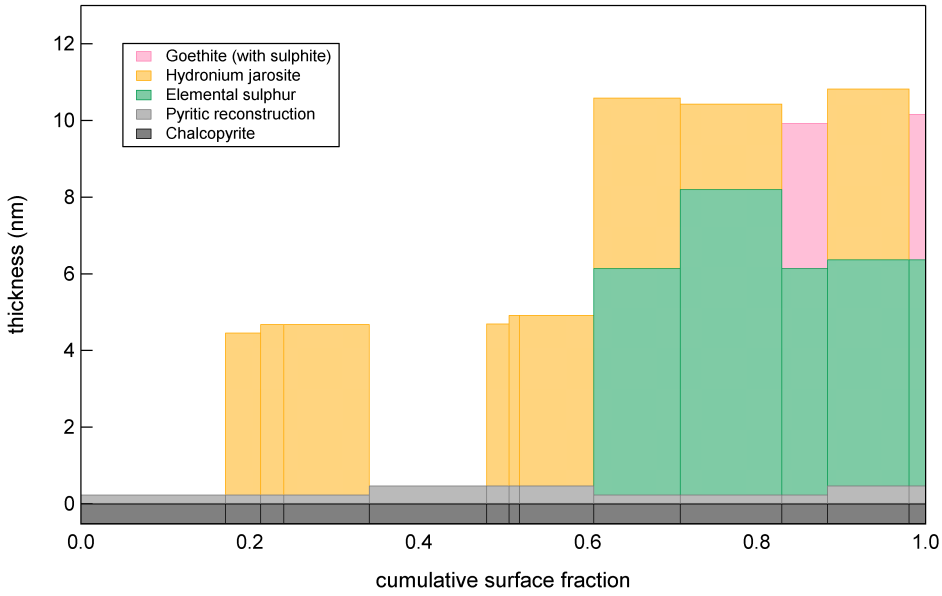

Figure 5.37: *Surface profile of chalcopyrite (Con-p) after oxidative dissolution in 0.1 M ferric chloride (pH 1.3) at 65° C for 2 hours, with 10 % subtracted from the Fe 2p intensity of chalcopyrite.*

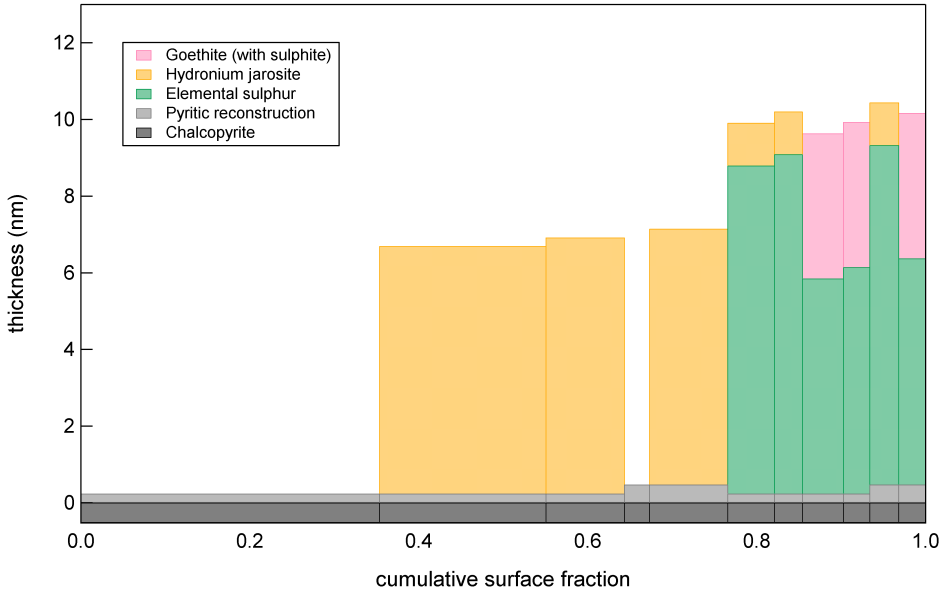

Figure 5.38: *Surface profile of chalcopyrite (Con-p) after oxidative dissolution in 0.1 M ferric sulphate (pH 1.3) at 80° C for 2 hours, with 5 % added to the S 2p intensity of chalcopyrite.*

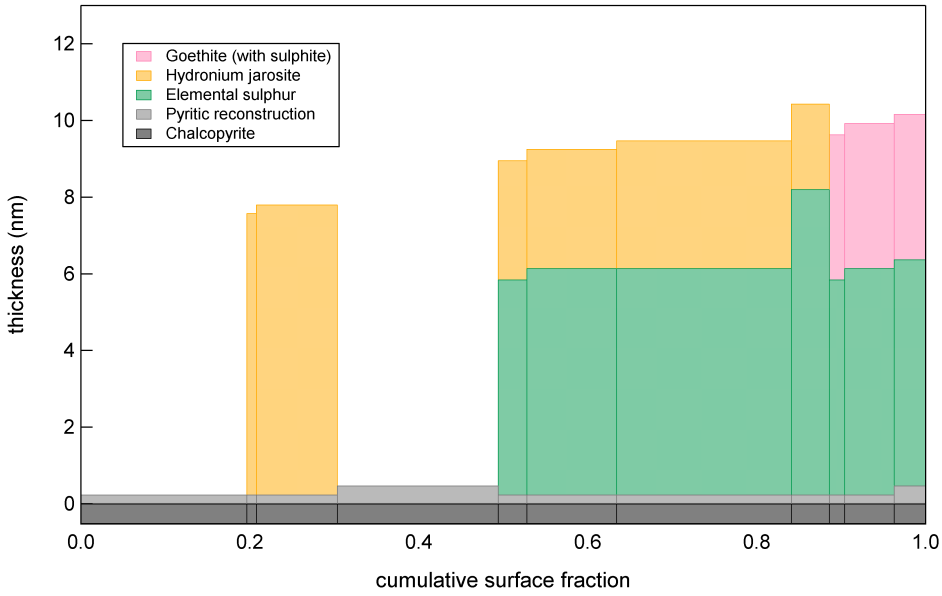

Figure 5.39: *Surface profile of chalcopyrite (Con-p) after oxidative dissolution in 0.1 M ferric sulphate (pH 1.3) at 80° C for 2 hours, with 5 % subtracted from the S 2p intensity of chalcopyrite.*

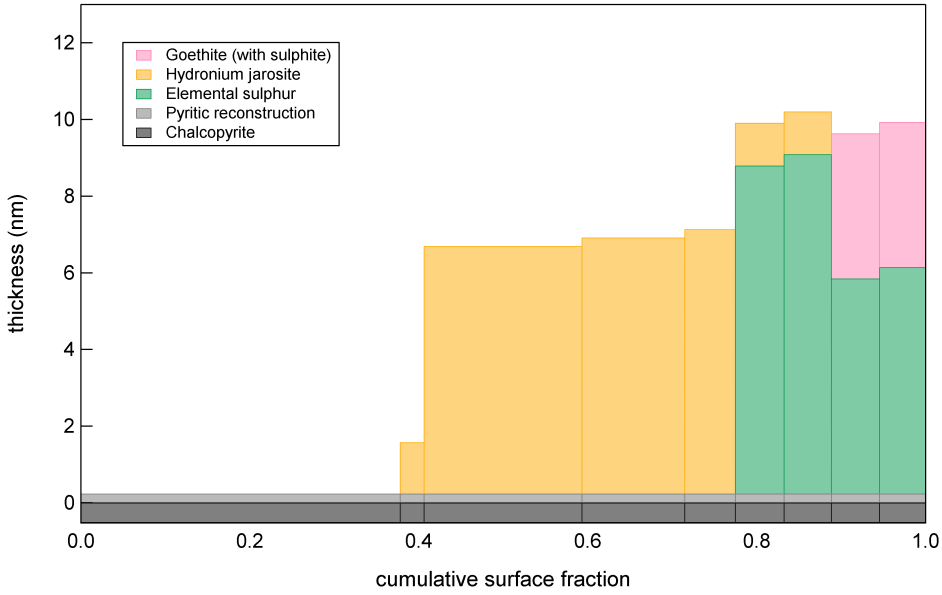

Figure 5.40: *Surface profile of chalcopyrite (Con-p) after oxidative dissolution in 0.1 M ferric sulphate (pH 1.3) at 80° C for 2 hours, with 10 % added to the S 2p intensity of chalcopyrite.*

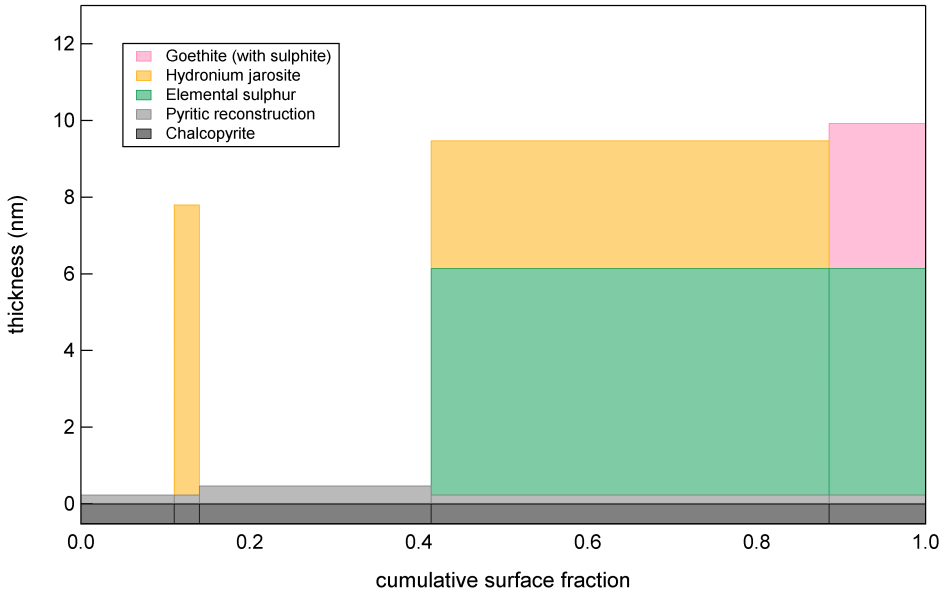

Figure 5.41: *Surface profile of chalcopyrite (Con-p) after oxidative dissolution in 0.1 M ferric sulphate (pH 1.3) at 80° C for 2 hours, with 10 % subtracted from the S 2p intensity of chalcopyrite.*

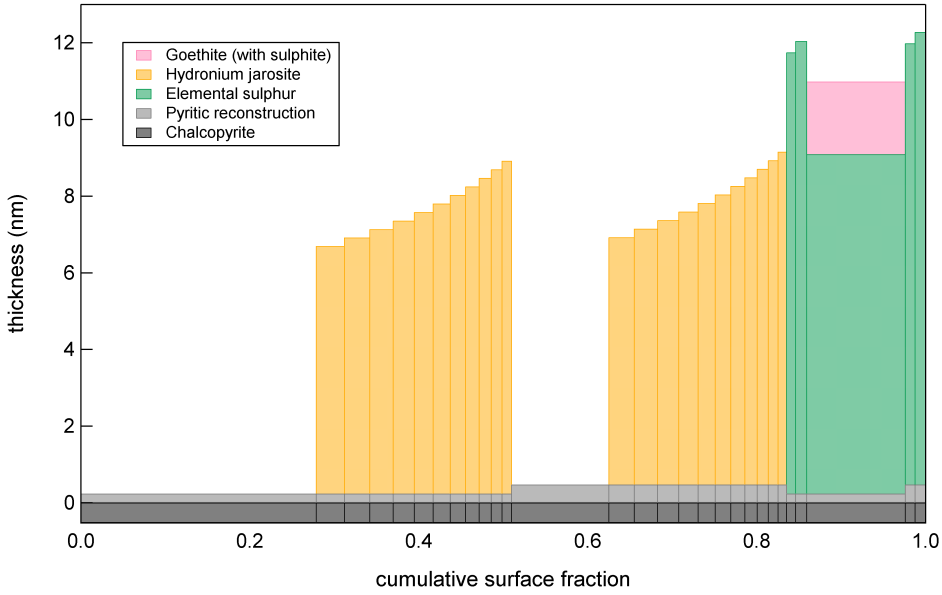

Figure 5.42: *Surface profile of chalcopyrite (Con-p) after oxidative dissolution in 0.1 M ferric sulphate (pH 1.3) at 80° C for 2 hours, with 5 % added to the Fe 2p intensity of chalcopyrite.*

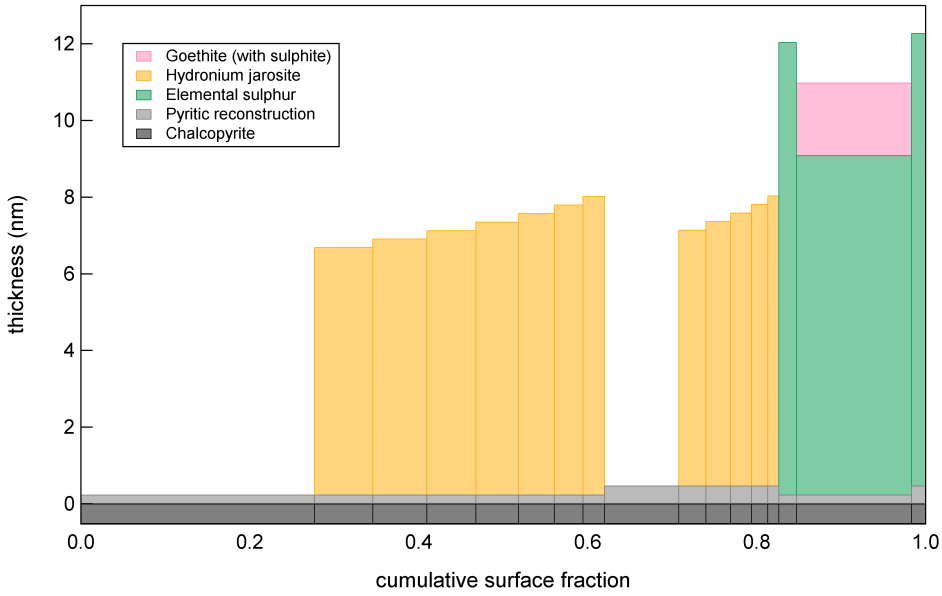

Figure 5.43: *Surface profile of chalcopyrite (Con-p) after oxidative dissolution in 0.1 M ferric sulphate (pH 1.3) at 80° C for 2 hours, with 5 % subtracted from the Fe 2p intensity of chalcopyrite.*

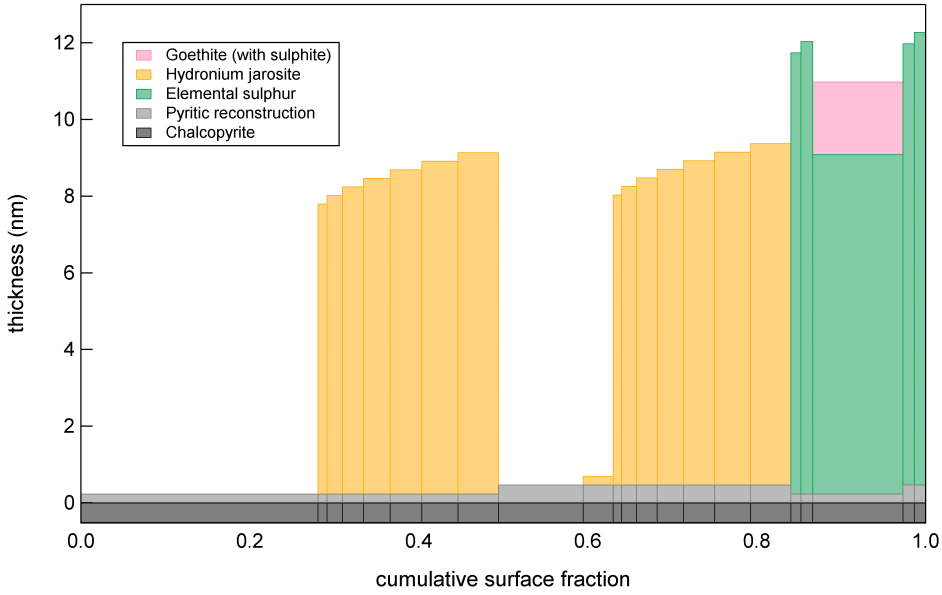

Figure 5.44: *Surface profile of chalcopyrite (Con-p) after oxidative dissolution in 0.1 M ferric sulphate (pH 1.3) at 80° C for 2 hours, with 10 % added to the Fe 2p intensity of chalcopyrite.*

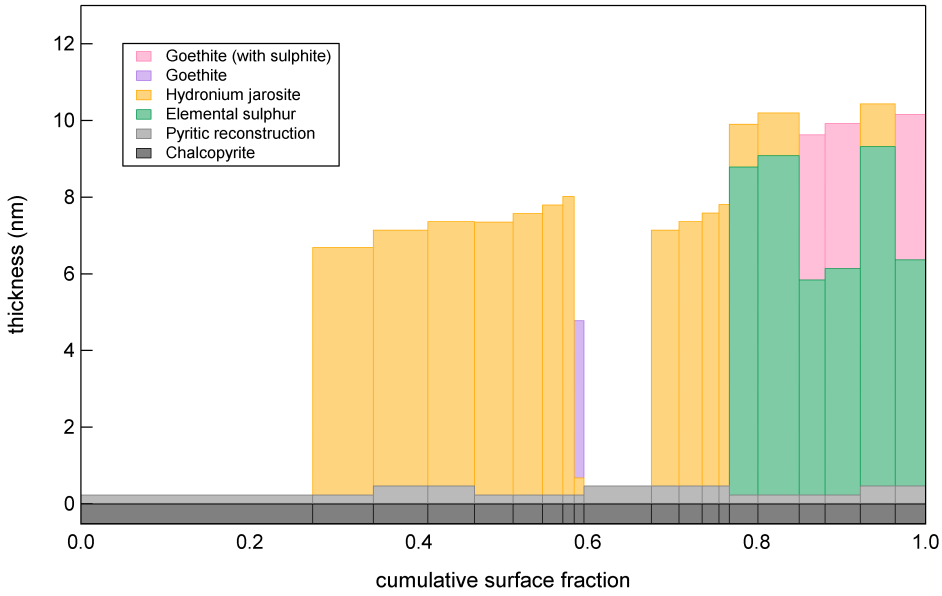

Figure 5.45: *Surface profile of chalcopyrite (Con-p) after oxidative dissolution in 0.1 M ferric sulphate (pH 1.3) at 80° C for 2 hours, with 10 % subtracted from the Fe 2p intensity of chalcopyrite.*

5.5.5 Summary

The procedure developed for the quantitative analysis of chalcopyrite after oxidative dissolution was successful. Program 1 was used to determine the cross section adjustments necessary for the photoelectron intensities predicted by IMFP and spectrometer calculations to correlate with the photoelectron intensities observed for a suite of standards. The adjusted cross sections were then used in Program 2 to generate photoelectron intensities associated with a suite of models that represent the roughened surface of chalcopyrite after oxidative dissolution. These model intensities were then introduced into Program 3, along with the intensities observed for chalcopyrite samples after oxidative dissolution, to determine suites of models that accounted for the observed data. The suites of models were then used to produce surface profiles of each sample. The validity of this quantitative procedure for the analysis of chalcopyrite was confirmed by perturbing the data and recalculating the fits. Despite the limitations of the models, high quality, robust fits were achieved.

Chapter 6

Surface profiles of chalcopyrite after oxidative dissolution in ferric media

The surface profiles of chalcopyrite after oxidative dissolution were analysed to determine the phase responsible for dissolution inhibition. Quantitative analysis revealed elemental sulphur, hydronium jarosite and goethite were present on chalcopyrite surfaces oxidised under all conditions, while the kinetics analysis revealed the inhibiting phase increases in surface coverage and thickness with reaction time. Thus, the surface profiles were examined in terms of the surface coverage and thickness of elemental sulphur, hydronium jarosite and goethite to establish which phase was responsible for dissolution inhibition. These results were then used to account for the kinetic behaviour of chalcopyrite dissolution in ferric media.

Oxidative dissolution was performed on chalcopyrite massive and concentrate to study various stages of dissolution. The initial stages of dissolution were examined using chalcopyrite massive because the relatively low surface area produced slow reaction kinetics. The latter stages of dissolution were examined using chalcopyrite concentrate because the relatively high surface area produced fast reaction kinetics.

6.1 Initial stages

The surface profiles of chalcopyrite oxidised in 0.1 M ferric sulphate (pH 1.9) at 50°C reveal progressive surface coverage by hydronium jarosite, at the expense of elemental sulphur and goethite (Figures 6.1 - 6.3). The surface coverage by hydronium jarosite increases steadily at 15, 18 and 20 % after 15, 30 and 60 minutes. The surface coverage by elemental sulphur is much greater at 55 and 60 % after 15 and 30 minutes, but decreases to 45 % after 60 minutes. This decrease coincides with the elemental sulphur achieving greater thickness, which is consistent with reports of elemental sulphur coalescence (Section 2.6.3). The surface coverage by goethite changes dramatically with 25, 7 and 30 % surface coverage after 15, 30 and 60 minutes, respectively. The erratic surface coverage may be caused by irregular removal of the goethite (produced during polishing, Section 5.3.2) under the oxidising conditions of low pH, rather than irregular deposition of goethite from solution. Although the hydronium jarosite is the favoured candidate for the inhibiting phase because of its steady increase in surface coverage, none of the phases increased in thickness dramatically in accordance with the deposition responsible for the decrease in dissolution rate observed in the kinetics study (Chapter 4).

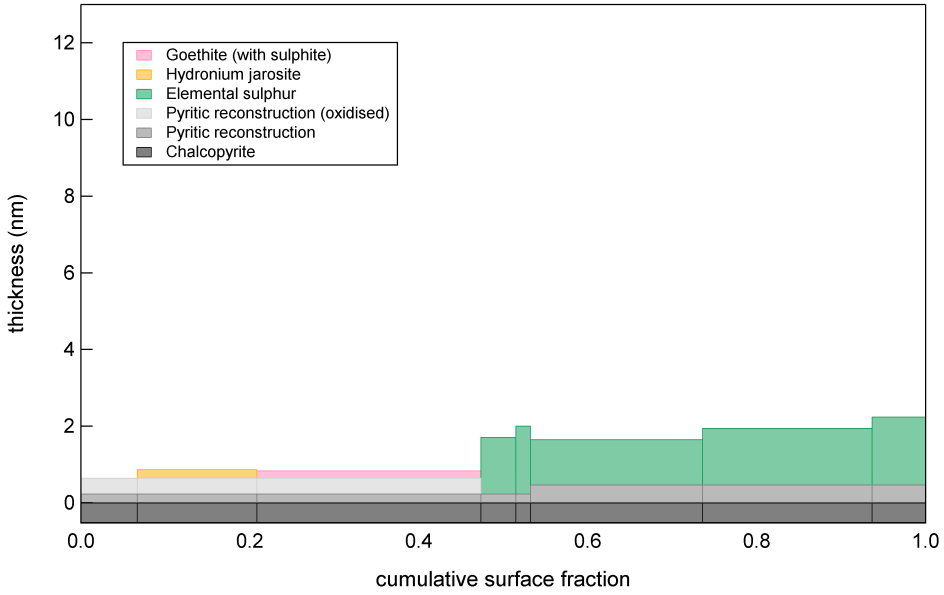

Figure 6.1: *Surface profile of chalcopyrite (Mass-p) after oxidative dissolution in 0.1 M ferric sulphate (pH 1.9) at 50° C for 15 minutes.*

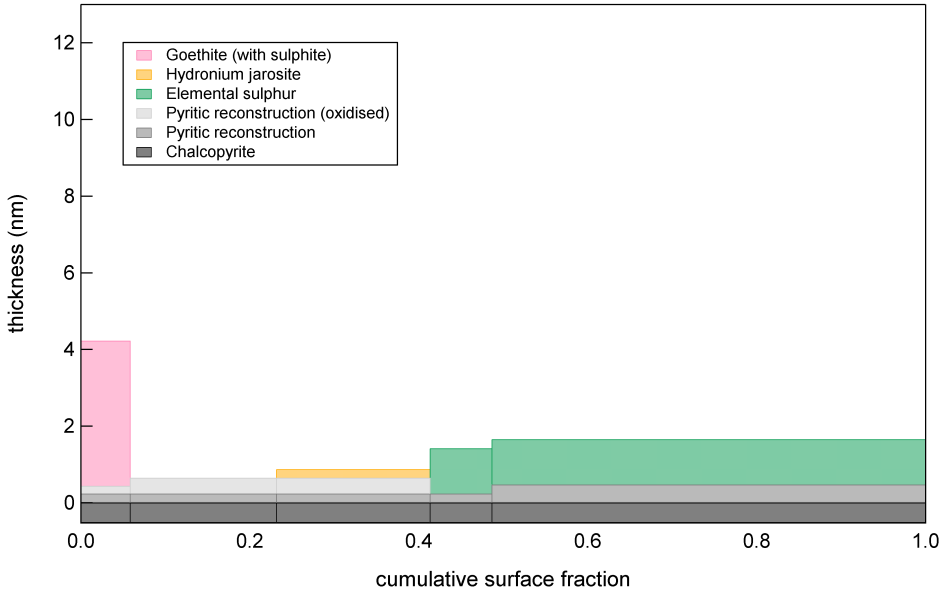

Figure 6.2: *Surface profile of chalcopyrite (Mass-p) after oxidative dissolution in 0.1 M ferric sulphate (pH 1.9) at 50° C for 30 minutes.*

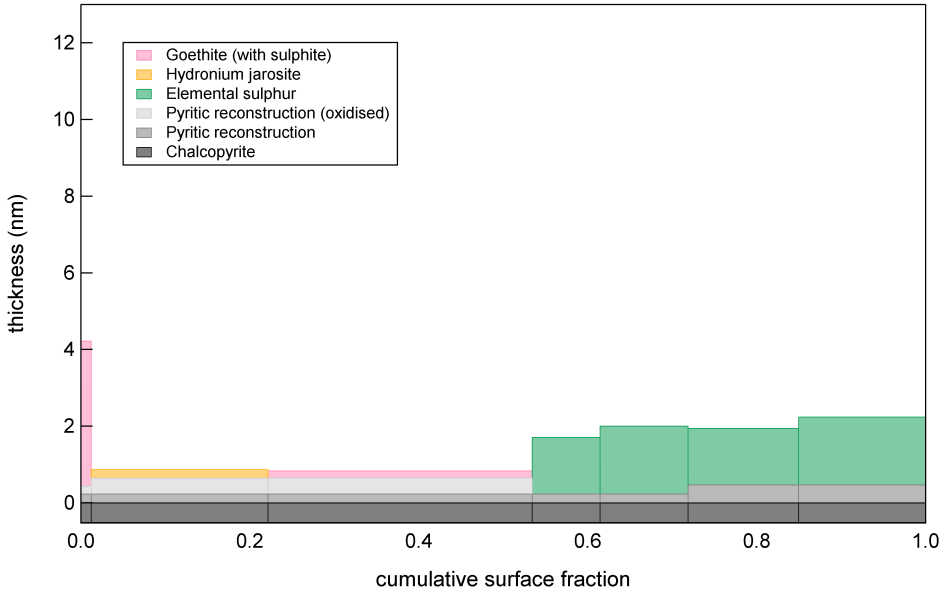

Figure 6.3: *Surface profile of chalcopyrite (Mass-p) after oxidative dissolution in 0.1 M ferric sulphate (pH 1.9) at 50° C for 60 minutes.*

6.2 Latter stages

The surface profiles of chalcopyrite during the initial stages of oxidation in ferric sulphate indicate hydronium jarosite may be responsible for inhibition. Therefore, surface profiles of chalcopyrite during the latter stages of dissolution were examined under conditions that affect the stability of jarosite. These conditions include low pH, high temperature and low sulphate concentration (Section 2.6.4).

The surface profiles of chalcopyrite oxidised in 0.1 M ferric sulphate at pH 1.3 and 1.9 at 50°C for 2 hours reveal the decrease in pH produced a decrease in the surface coverage for all three phases: elemental sulphur (62 to 30 %), goethite (15 to 13 %), and hydronium jarosite (65 to 30 %) (Figures 6.4 - 6.5). The decreases in goethite and hydronium jarosite are consistent with decreased stability of these phases and increased stability of ferric ions at low pH (Figure 2.5). This improved stability of ferric ions produces an increase in the solution potential, which decreases the stability of the elemental sulphur in favour of bisulphite and sulphate at low pH (Figure 2.4).

Although the surface coverage achieved by hydronium jarosite and elemental sulphur are comparable at each pH, the deposition of hydronium jarosite onto the elemental sulphur complies with the additional requirement of the inhibiting phase depositing from solution during the latter stages. The formation of hydronium jarosite despite the low pH implies the presence of a high concentration gradient near the surface. Such a gradient is likely because of the higher pH expected from the consumption of protons by the surface and sulphate ions (to form bisulphate) and the higher concentrations of iron and sulphate at the surface due to oxidative dissolution of the chalcopyrite. Thus, hydronium jarosite is the inhibiting phase above pH 1.3 at 50°C.

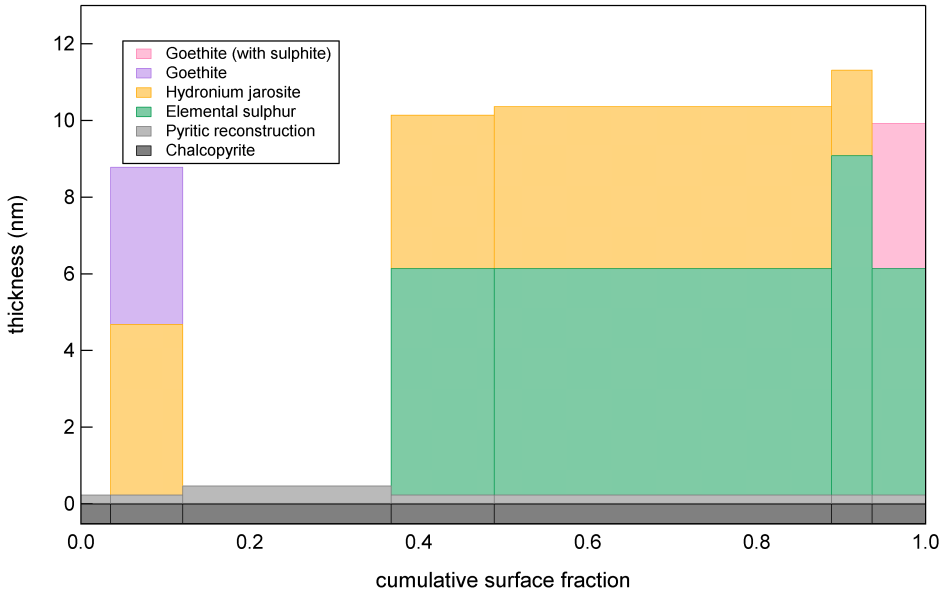

Figure 6.4: *Surface profile of chalcopyrite (Con-p) after oxidative dissolution in 0.1 M ferric sulphate (pH 1.9) at 50° C for 2 hours.*

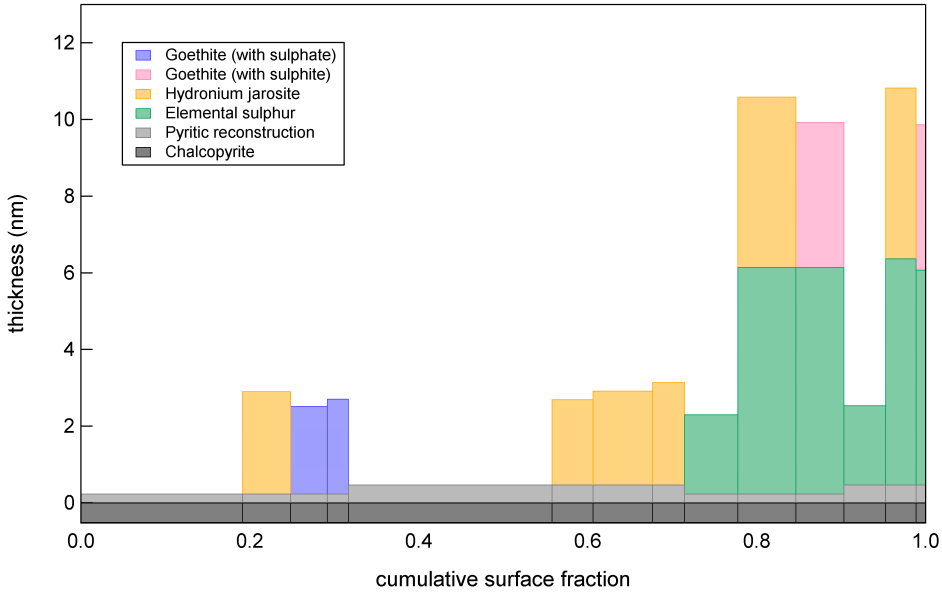

Figure 6.5: *Surface profile of chalcopyrite (Con-p) after oxidative dissolution in 0.1 M ferric sulphate (pH 1.3) at 50° C for 2 hours.*

The surface profiles of chalcopyrite oxidised in 0.1 M ferric sulphate (pH 1.3) at 50, 65 and 80°C for 2 hours reveal an increase in temperature produced a decrease in elemental sulphur precipitation but an increase in iron precipitation (Figures 6.6 - 6.7). The increase in temperature from 50 to 65°C produced a decrease in surface coverage by elemental sulphur (30 to 10 %), but increases by goethite (13 to 15 %) and hydronium jarosite (30 to 40 %). The increase in temperature from 65 to 80°C produced an increase in surface coverage for all three phases (23, 23 and 50 % for elemental sulphur, goethite and hydronium jarosite, respectively). The dominant surface coverage by hydronium jarosite shows the low pH did not counteract the improved kinetics of hydronium jarosite formation at elevated temperatures (Section 2.6.4). The improved kinetics are reflected in the thickness of the hydronium jarosite, with many of the models used containing close to the maximum number of layers permitted (Section 5.5.2). The thickness of the hydronium jarosite could be responsible for the thickness of the elemental sulphur models used because the elemental sulphur may be partially buried by the hydronium jarosite. Thus, the surface coverage by elemental sulphur might be greater than depicted, but the spectrometer may only detect hydronium jarosite,

which is approximated to $\sim$ 40 layers of hydronium jarosite on chalcopyrite. Despite the thickness of hydronium jarosite possibly exceeding the ability of the spectrometer to detect the underlying elemental sulphur, the Cu 2p:S 2p ratio used in Program 3 (Section 5.5.3) ensures the surface coverage is accurately depicted. Regardless of these limitations, the surface profiles are consistent with hydronium jarosite remaining the inhibiting phase above pH 1.3 at 50, 65 and 80°C.

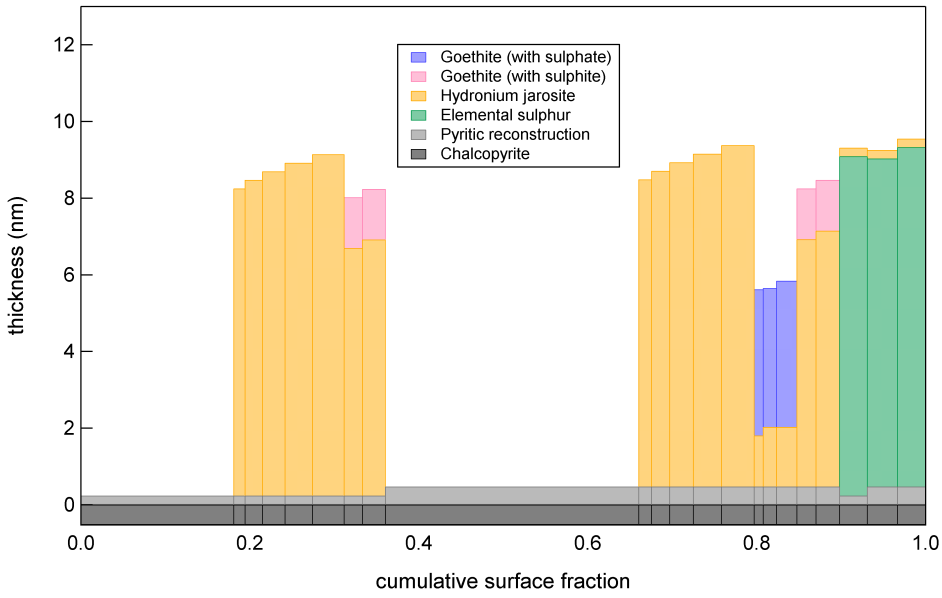

Figure 6.6: *Surface profile of chalcopyrite (Con-p) after oxidative dissolution in 0.1 M ferric sulphate (pH 1.3) at 65° C for 2 hours.*

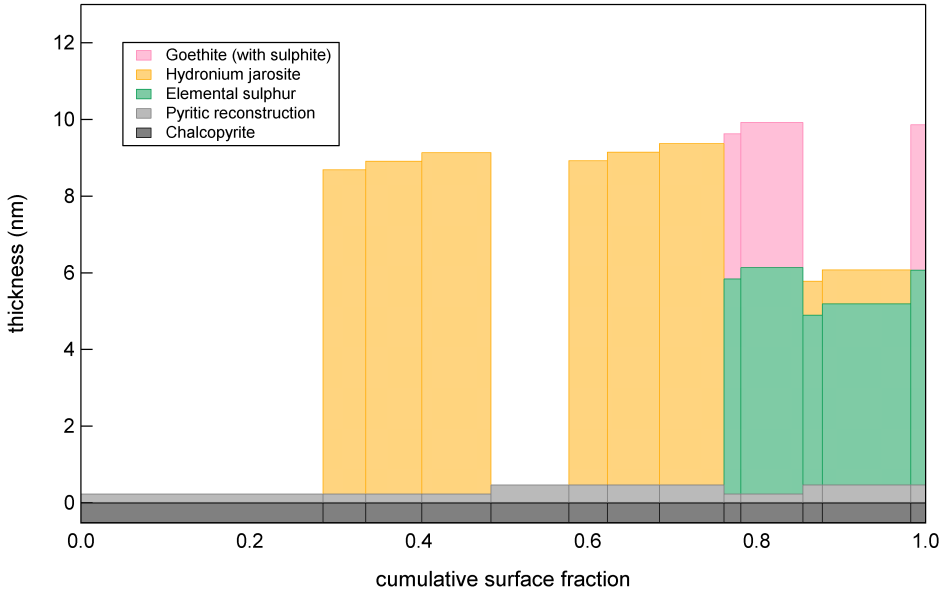

Figure 6.7: *Surface profile of chalcopyrite (Con-p) after oxidative dissolution in 0.1 M ferric sulphate (pH 1.3) at 80° C for 2 hours.*

The surface profiles of chalcopyrite oxidised in 0.2 M ferric chloride (pH 1.3) at 50, 65 and 80°C for 2 hours reveal low sulphate did not prevent hydronium jarosite formation and confirm hydronium jarosite is the inhibiting phase (Figures 6.8 - 6.10). The surface coverage by each phase at 50, 65 and 80°C reveals hydronium jarosite dominates (55, 43 and 58 %) compared with elemental sulphur (45, 42 and 38 %) and goethite (22, 20 and 28 %). Furthermore, hydronium jarosite is deposited onto elemental sulphur in accordance with the deposition mechanism observed in the kinetics study. The formation of hydronium jarosite despite the low pH, and the initial absence of sulphate, confirms the presence of a concentration gradient high in pH, ferric ions and sulphate ions near the surface; the sulphate produced by the oxidative dissolution of the chalcopyrite provides the sulphate required to form jarosite in a chloride system (Dutrizac, 1981). The concentration gradient is also evident from the thickness of hydronium jarosite observed, with greater levels noted on the surface of the chalcopyrite than on the elemental sulphur. These levels also reveal hydronium jarosite obeys the nucleation mechanism observed in the kinetics study by forming initially at the surface before precipitating from solution.

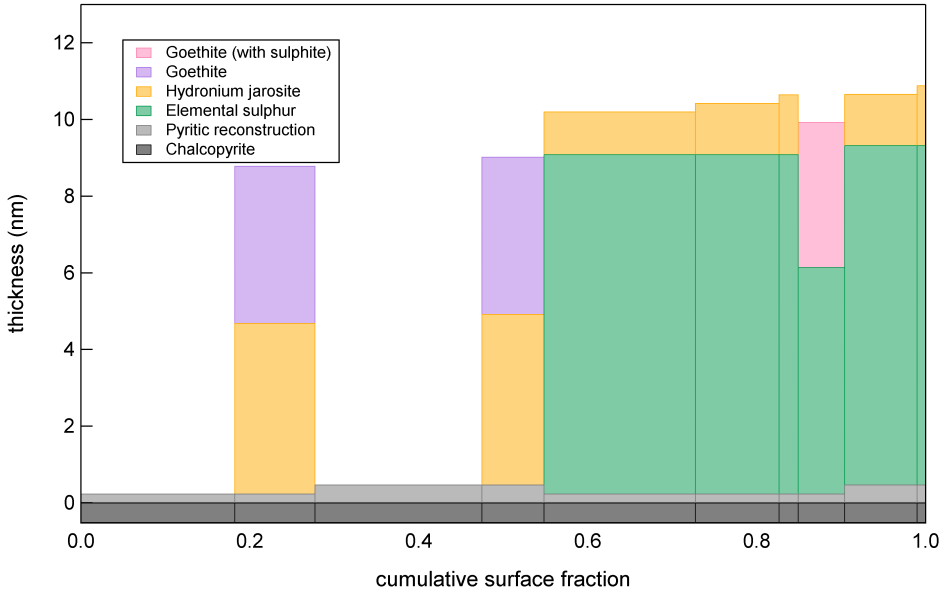

Figure 6.8: *Surface profile of chalcopyrite (Con-p) after oxidative dissolution in 0.2 M ferric chloride (pH 1.3) at 50° C for 2 hours.*

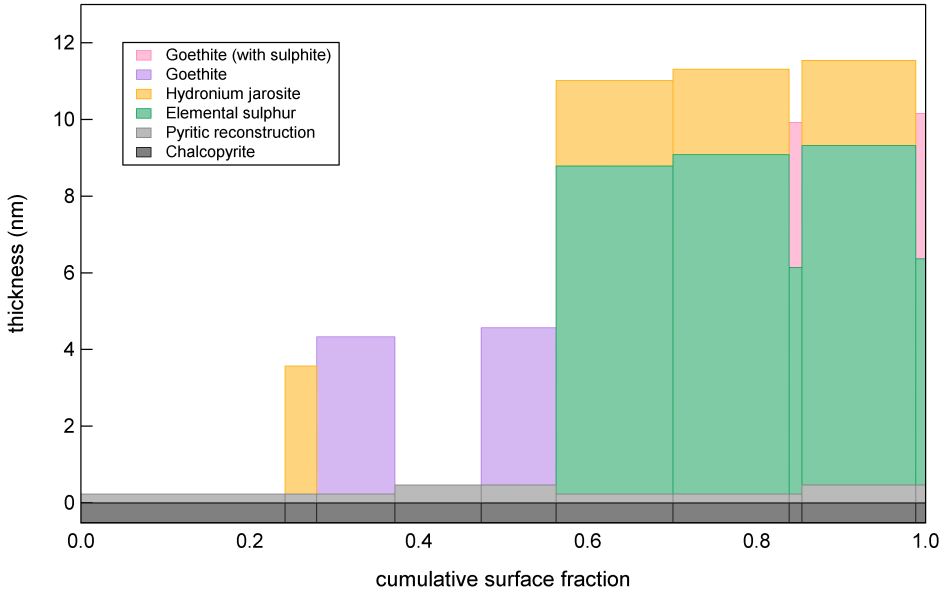

Figure 6.9: *Surface profile of chalcopyrite (Con-p) after oxidative dissolution in 0.2 M ferric chloride (pH 1.3) at 65° C for 2 hours.*

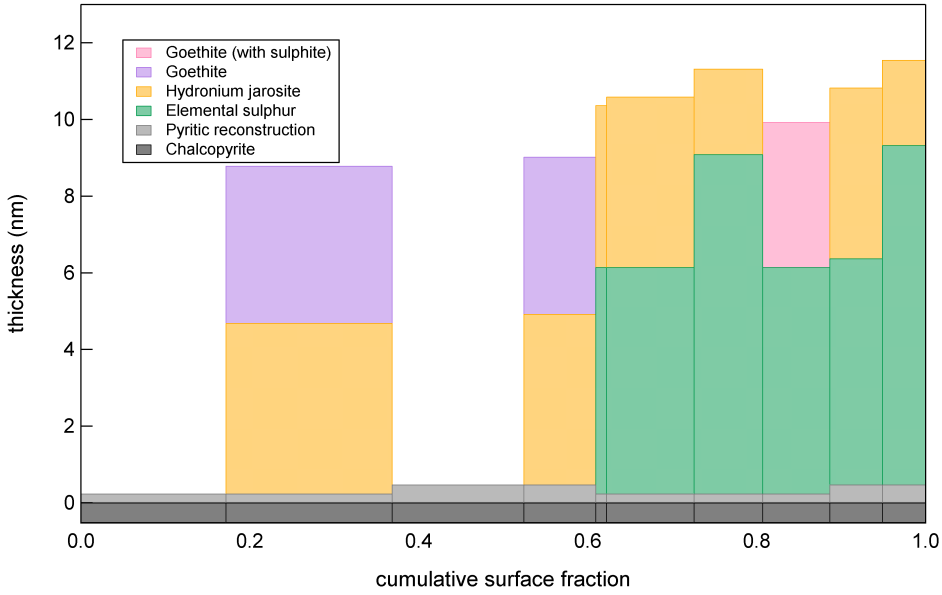

Figure 6.10: *Surface profile of chalcopyrite (Con-p) after oxidative dissolution in 0.2 M ferric chloride (pH 1.3) at 80° C for 2 hours.*

Examination of chalcopyrite after extended dissolution reveals hydronium jarosite is the inhibiting phase. The use of low pH in ferric sulphate systems did not prevent hydronium jarosite formation, nor did low pH counteract the thermodynamic stability of hydronium jarosite at elevated temperatures. The initial absence of sulphate in ferric chloride systems greatly diminished the level of hydronium jarosite. However, low pH and elevated temperatures in ferric chloride systems still produced significant amounts of hydronium jarosite because of the high concentration gradient at the surface.

6.3 Kinetic implications

The surface profiles of chalcopyrite oxidised in ferric media under various conditions display partial coverage of the surface by elemental sulphur, goethite and hydronium jarosite. However, it is the partial coverage of the surface by hydronium jarosite that accounts for the different dissolution rates and activation energies of the ferric sulphate and ferric chloride systems. The higher dissolution rates for ferric chloride systems are

produced by the diminished levels of hydronium jarosite, with greater reaction time required to form hydronium jarosite of adequate thickness to inhibit dissolution. These diminished levels also account for the higher dissolution rate observed for the ferric chloride system during stage two of dissolution when inhibition is present in both systems (Section 4.5). The higher dissolution rates for ferric chloride systems produce lower apparent activation energies (Table 2.1). The variation of reported activation energies for ferric sulphate and ferric chloride systems (Table 2.1) is also addressed by the surface profiles, with different amounts of hydronium jarosite formed by solutions of different ferric and sulphate concentration, and pH (Section 2.6.4). The activation energies also vary according to the temperature combinations used for the determinations because the kinetics of hydronium jarosite change with temperature (Section 2.6.4). Therefore, partial coverage of the surface by hydronium jarosite accounts for the differences in dissolution rate and activation energy reported, without invoking different mechanisms of dissolution or inhibition for the ferric sulphate and ferric chloride systems (Section 2.3). Lastly, the partial coverage of the surface by hydronium jarosite accounts for the persistence of conductivity after inhibition, which has been a justification for attributing inhibition to the formation of a metal deficient sulphide, rather than the deposition of a phase such as hydronium jarosite [Ammou-Chokroum et al. (1979), Warren et al. (1982) and Biegler and Horne (1984)].

6.4 Summary

The surface profiles of chalcopyrite oxidised in ferric sulphate and ferric chloride confirmed hydronium jarosite is responsible for inhibition of oxidative dissolution in both systems. Although hydronium jarosite, elemental sulphur and goethite form near the surface during the initial stages of dissolution, only hydronium jarosite deposits in significant amounts during the latter stages when inhibition is observed. Therefore, inhibition corresponds to the establishment of an imperviously thick layer of hydronium jarosite. Elemental sulphur might cause some degree of inhibition – and hence dissolution rates may be improved by removing elemental sulphur (Section 2.6.3) – but the

inhibiting effect of hydronium jarosite appears much greater. The relatively diminished inhibition by elemental sulphur and goethite might be caused by relative porosity failing to produce diffusion barriers. Inhibition by hydronium jarosite correlates with the diminished levels in ferric chloride systems, which display improved dissolution rates (Section 4.5) and lower reported activation energies (Section 2.5). It is therefore concluded the mechanisms of dissolution and inhibition are common to both ferric sulphate and ferric chloride, with only the extent of inhibition producing different dissolution rates in the two systems.

Chapter 7

Mechanisms of the oxidative dissolution and inhibition of chalcopyrite in ferric media

The mechanisms of chalcopyrite dissolution and inhibition are based on the surface profiles of chalcopyrite after oxidative dissolution. The mechanisms are common to both ferric sulphate and ferric chloride systems and account for the diminished inhibition in the latter.

7.1 Mechanism of dissolution

The mechanism of dissolution is based on oxidation of the disulphide moiety identified on the surface of chalcopyrite before and after oxidative dissolution (Section 5.3.1). The disulphide moiety and the ferric ion are hydrated in solution and electron transfer occurs via bridging water molecules. Oxidation proceeds until the disulphide is oxidised to thiosulphate through the incorporation of oxygen atoms from the hydration sphere. The thiosulphate subsequently decomposes to form products identified on the surface of chalcopyrite, including elemental sulphur, sulphite and sulphate.

7.1.1 Atomic perspective

The first step of the mechanism of dissolution is the removal of an electron from the disulphide moiety via the Grotthuus mechanism. The Grotthuus mechanism involves the transfer of electrons through a chain of bridging water molecules of indeterminate length by proton exchange (De Grotthuus, 1806; Horne and Axelrod, 1964; Tuckerman et al., 2002). Once the electron has been removed from the disulphide moiety, the ferric ion is reduced to ferrous and moves into solution, while the sulphur atom is oxidised and assumes a nominal oxidation state of 0 (Equation 7.1). The loss of negative charge enables overlap of the orbitals between the sulphur atom of the disulphide moiety and the oxygen atoms of the hydration sphere. The sulphur-oxygen bond formed does not experience steric hindrance from hydrogen ions because of the ions small size. The incorporation of oxygen atoms continues as oxidation proceeds, until the disulphide moiety is converted to thiosulphate, in a reaction analogous to pyrite oxidation (Section 2.4). The oxidation states of the sulphur atoms are assigned with the lower oxidation state neighbouring the ferrous of the 'pyritic' reconstruction phase and the higher oxidation state neighbouring the oxygen atom of the water molecule. Although the oxidation states are presented as integers, a degree of charge distribution is assumed.

$$
\begin{aligned}
&S^{-1} - S^{-1} - H \cdots HO - Fe^{3+}(H_2O)_5 + H_2O \longrightarrow S^{-1} - S^{0} - (OH) + Fe^{2+}(H_2O)_6 + H^+ \\
&S^{-1} - S^{0} - OH \cdots HO - Fe^{3+}(H_2O)_5 + H^+ \longrightarrow S^{-1} - S^{+1} - (OH) + Fe^{2+}(H_2O)_6 \\
&S^{-1} - S^{+1} - OH \cdots HO - Fe^{3+}(H_2O)_5 + H_2O \longrightarrow S^{-1} - S^{+2} - (OH)_2 + Fe^{2+}(H_2O)_6 \\
&S^{-1} - S^{+2} - (OH)_2 \cdots HO - Fe^{3+}(H_2O)_5 + H^+ \longrightarrow S^{-1} - S^{+3} - (OH)_2 + Fe^{2+}(H_2O)_6 \\
&S^{-1} - S^{+3} - (OH)_2 \cdots HO - Fe^{3+}(H_2O)_5 + H_2O \longrightarrow S^{-1} - S^{+4} - (OH)_3 + Fe^{2+}(H_2O)_6 \\
&S^{-1} - S^{+4} - (OH)_3 \cdots HO - Fe^{3+}(H_2O)_5 + H^+ \longrightarrow S^{-2} - S^{+6} - (OH)_3 + Fe^{2+}(H_2O)_6
\end{aligned}
\tag{7.1}
$$

Note: The oxidation number of each sulphur atom is arbitrarily assigned. The protons attached to the oxygen atoms bonded to the terminal sulphur are assumed to be in equilibrium with the solution. The groups in parentheses attached to the disulphide represent discrete ligands. The bridging water molecules have not been depicted, for simplicity.

The overall process requires a total of six ferric ions:

$$
FeS_2 + 6\,Fe^{3+} + 3\,H_2O \longrightarrow 7\,Fe^{2+} + S_2O_3^{2-} + 6\,H^+ \tag{7.2}
$$

The oxidation of the disulphide moiety to thiosulphate progressively weakens the bonds of the sulphur atoms to the surrounding iron atoms of the 'pyritic' reconstruction phase. As these bonds become weaker, the bonding within the sulphur moiety becomes increasingly ionic. The assumption of ionic bonding aids hydration and dissolution of the thiosulphate group. The 'pyritic' reconstruction phase reforms and the oxidative dissolution process repeats.

The mechanism resolves some of the outstanding issues concerning the oxidation of a disulphide group in solution, in particular, the invocation of radicals and the incorporation of oxygen atoms (Section 2.4). The hydration of the surface eliminates the requirement of either sulphur or hydroxide radicals to overcome electrostatic repulsion and ensures a maximum of three oxygen groups are bonded to the terminal sulphur of the disulphide moiety at any time.

7.1.2 Orbital perspective

The mechanism of dissolution is consistent with orbital considerations and accounts for the rapid dissolution rates initially observed. These rates require overlap of the orbitals between the iron and sulphur atoms in pyrite (analogous to the 'pyritic' reconstruction phase), the sulphur atoms and the hydration sphere, and the ferric ion and its hydration sphere. Overlap is only possible with consistent bonding between all species. Consistent Π bonding was used by Luther (1987) to justify the direct attachment of the ferric ion to the mineral surface to explain the high dissolution rates. However, consistent σ bonding via hybrid orbitals can account for the dissolution rates observed and enable all of the species to remain hydrated.

The σ bonding of the iron and sulphur within pyrite is consistent with molecular orbital theory and band calculations. The iron in pyrite is Fe^{2+} (d^6) low spin with completely filled t_{2g} orbitals (d_{xy}, d_{xz} and d_{yz}) and completely empty e_g orbitals ($d_{x^2-y^2}$ and d_{z^2}). These empty orbitals overlap with the sp^3 hydrid orbital of the sulphur atom containing a lone pair of electrons to form d^2sp^3 hybrid orbitals, while the other three

sulphur sp^3 orbitals are bonded to other sulphur atoms (Bither et al., 1968). Band calculations confirm the empty Fe e_g orbitals form σ bonds with S sp^3 orbitals, with the former contributing to the conduction band and the latter to the lower valence band (Eyert et al., 1998), while the filled Fe t_{2g} orbitals dominate the upper valence band, remaining essentially non-bonding with only minor π bonding with the S 3d orbitals (Opahle et al., 1999).

The terminal sulphur atom of pyrite in solution is initially bonded to water molecules of the hydration sphere via overlap of the S hybrid sp^3 and H 1s orbitals. However, as electrons are removed, the charge on the terminal sulphur approaches zero. This enables overlap of the hybrid sp^3 orbitals of the terminal sulphur atom in the disulphide with the hybrid sp^3 orbitals of the oxygen in the hydration sphere.

Electron removal occurs via the water molecules that bridge the hydration spheres of the sulphur atoms in pyrite and the ferric ion. The hydration sphere of the ferric ion involves overlap of the O hyrbid sp^3 orbitals of water and the hybrid sp^3d^2 orbitals of the ferric ion. These hybrid sp^3d^2 orbitals form because ferric ions (d^5) are high spin with one electron in each of the t_{2g} and e_g orbitals.

The overlap of hybrid orbitals to form σ bonds between all species ensures the mechanism of dissolution is consistent from an orbital perspective.

7.1.3 Role of water

The mechanism of dissolution involves the incorporation of oxygen from water and the transfer of electrons via bridging water molecules. The former has been investigated by XPS analysis of chalcopyrite after dissolution in an anaerobic ferric chloride system, while the latter has been investigated by comparing the copper release rates for chalcopyrite dissolution in water and deuterated water.

The S 2p spectrum of chalcopyrite oxidised in an anaerobic 0.2 M ferric chloride system (pH 1.3) at 50°C for 2 hours reveals significant quantities of sulphate at $\sim$ 169 eV (Figure 7.1). The presence of sulphate confirms it is a product of oxidative dissolution

and not an artefact of the medium or the aerial oxidation of the elemental sulphur. It also confirms water is the source of oxygen for the sulphate, because of the lack of atmospheric oxygen in the system. This is consistent with the isotopic labelling experiments of Reedy et al. (1991), which revealed over 90 % of the oxygen contained in the sulphate produced by oxidative dissolution of pyrite was derived from water molecules. The incorporation of oxygen atoms from water molecules is also consistent with the chalcopyrite surface remaining hydrated throughout oxidative dissolution.

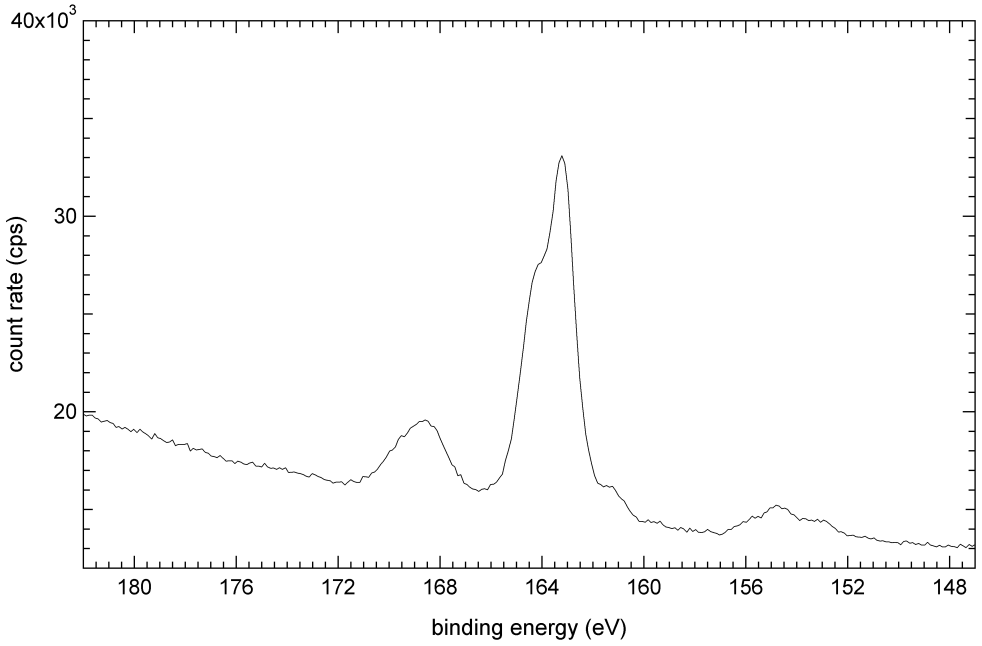

Figure 7.1: *S 2p spectrum of chalcopyrite (Mass-p) after oxidative dissolution in 0.2 M ferric chloride (pH 1.6) at 50° C for 2 hours under anaerobic atmosphere.*

The role of bridging water molecules for electron transfer is displayed in a comparison of the copper release rates of chalcopyrite oxidised in 0.1 M ferric sulphate (pH 1.9) at 50°C for water (H_2O) and deuterated water (D_2O) media (Figure 7.2); the rate constants were determined using the data points before the onset of inhibition (Figures 4.4 and 7.3). The ratio of the water and deuterated water rate constants at 50°C (0.92) is higher than the ratio of the viscosities at 50°C [0.84, Cho et al. (1999)]. This implies copper release is determined by electron transfer via bridging water molecules, rather

than by diffusion of ferric ions through the medium. Furthermore, the similar rate constants suggest the rate limiting step involves the rearrangement of the terminal water molecules, rather than the transfer of electrons across the bridging water molecules (Horne and Axelrod, 1964). Thus, the high copper release rates observed during oxidative dissolution of chalcopyrite do not require intimate contact between the mineral surface and the ferric ion (Section 2.4).

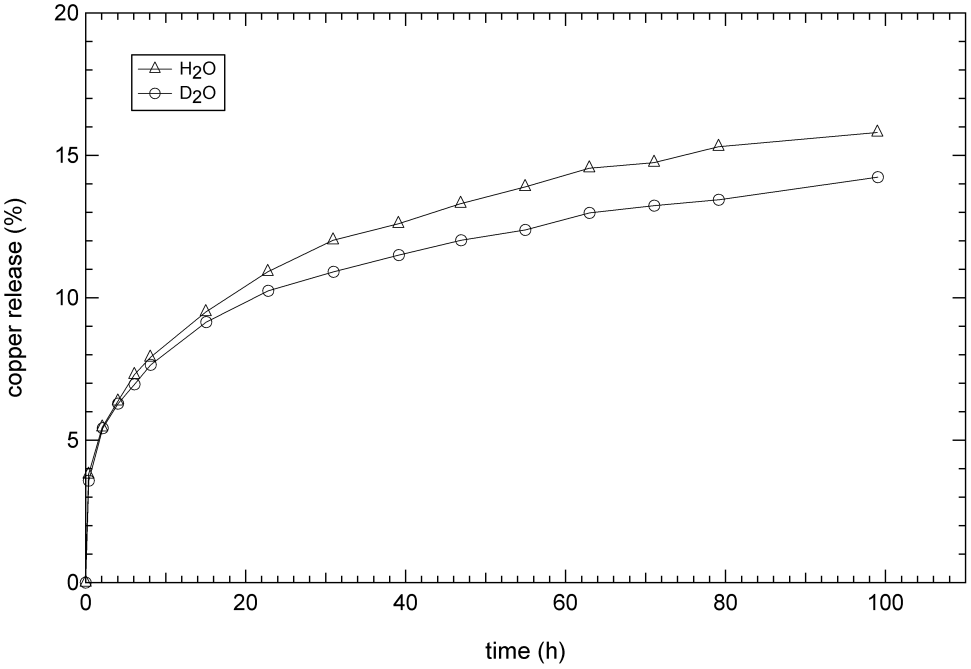

Figure 7.2: *Copper release of chalcopyrite (Con-p) during oxidative dissolution in 0.1 M ferric sulphate (pH 1.9) in H_2O, and D_2O, at 50° C.*

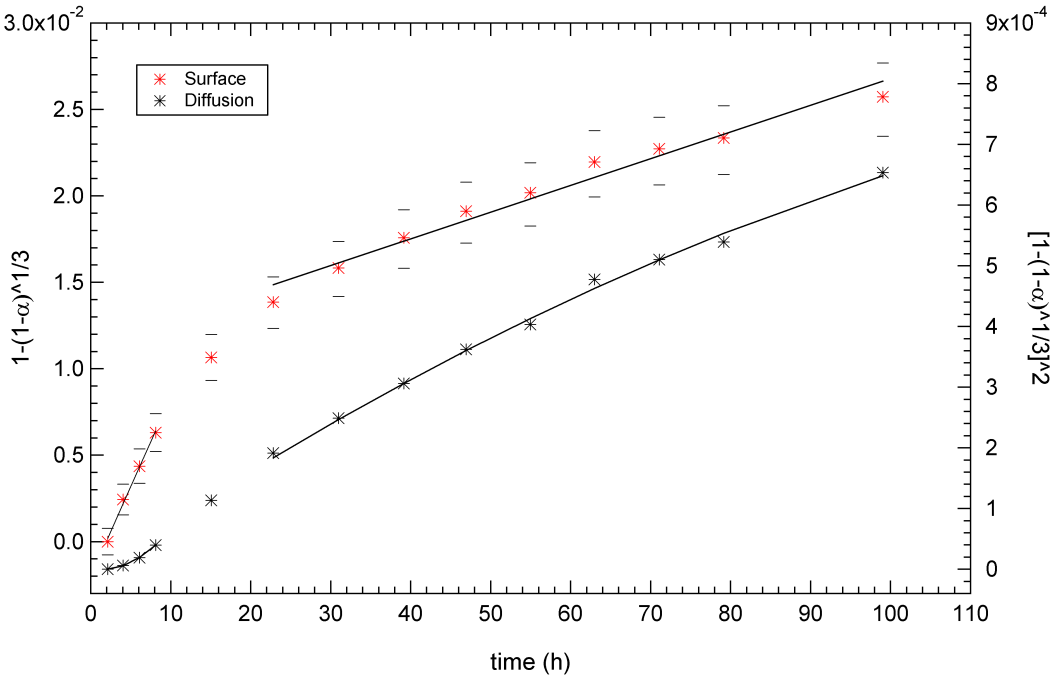

Figure 7.3: *Surface and diffusion control plots of copper release of chalcopyrite (Con-p) during oxidative dissolution in 0.1 M ferric sulphate (pH 1.9) in D_2O at 50° C. Note: The data point at 16 hours has not been fitted because it is considered transitional.*

7.1.4 Final products of oxidation

The mechanism of dissolution ends with the incorporation of oxygen atoms onto the disulphide and the formation of thiosulphate. However, the thiosulphate reacts further, via intermediates, to produce elemental sulphur, sulphite and sulphate.

Thiosulphate may be oxidised by ferric ions, cupric ions and dissolved oxygen to produce tetrathionate (Thatcher, 1904; Rabai and Epstein, 1992; Williamson and Rimstidt, 1993):

$$2\,S_2O_3^{2-} + 2\,Cu^{2+} \longrightarrow 2\,Cu^{+} + S_4O_6^{2-} \tag{7.3}$$

$$2\,S_2O_3^{2-} + 2\,Fe^{3+} \longrightarrow 2\,Fe^{2+} + S_4O_6^{2-} \tag{7.4}$$

$$2\,S_2O_3^{2-} + \tfrac{1}{2}O_2 \longrightarrow O^{2-} + S_4O_6^{2-} \tag{7.5}$$

Oxidation of thiosulphate by dissolved oxygen is much slower than by ferric or cupric ions (Rabai and Epstein, 1992; Williamson and Rimstidt, 1993). Therefore, the principal role of the dissolved oxygen is to regenerate the ferric and cupric ions, rather than oxidise the thiosulphate directly.

Thiosulphate may also be degraded by acid to produce tetrathionate, along with elemental sulphur and (bi)sulphite (Davis, 1958; Mizoguchi et al., 1976):

$$5\,S_2O_3^{2-} + 6\,H^+ \longrightarrow \tfrac{1}{4}S_8 + 2\,S_4O_6^{2-} + 3\,H_2O \tag{7.6}$$

$$S_2O_3^{2-} + H^+ \longrightarrow \tfrac{1}{8}S_8 + HSO_3^- \tag{7.7}$$

Tetrathionate and (bi)sulphite may react further to produce thiosulphate and sulphate (Mizoguchi et al., 1976):

$$4\,S_2O_3^{2-} + 5\,H_2O \longrightarrow 7\,S_2O_3^{2-} + 2\,SO_4^{2-} + 10\,H^+ \tag{7.8}$$

$$4\,HSO_3^- \longrightarrow S_2O_3^{2-} + 2\,SO_4^{2-} + 2\,H^+ + 2\,H_2O \tag{7.9}$$

These reactions account for —

- identification of elemental sulphur, sulphite and sulphate on the surface of chalcopyrite after oxidative dissolution (Section 5.4.1);
- formation of various percentages of elemental sulphur and sulphate in ferric sulphate and ferric chloride systems, without invoking separate mechanisms for elemental sulphur and sulphate formation (Section 2.3);
- formation of more elemental sulphur than sulphate in ferric sulphate and ferric chloride systems (Section 2.6.3) because degradation of thiosulphate by acid is faster than oxidation of thiosulphate by ferric ions (Williamson and Rimstidt, 1993);

- formation of more elemental sulphur in ferric chloride systems than in ferric sulphate systems (Section 2.3) because of the lower pH of the chloride system, which is caused by the dissocation constant of HCl being higher than the dissociation constant of HSO_4^-; and
- detection of no intermediates (including thiosulphate) in solution using UV-visible, Raman or Infrared spectroscopies because of the low stability of these species under the strongly oxidising conditions (0.2 M ferric) of low pH (1.9) and high temperature (50°C) used in this study (Section 2.4).

7.2 Mechanism of inhibition

Surface profiles of chalcopyrite after oxidative dissolution revealed inhibition correlates with the deposition of hydronium jarosite (Section 6). Thus, the mechanism of hydronium jarosite is considered, in addition to the mechanism of goethite, because they are competing products of iron hydrolysis (Section 2.6.4). These mechanisms address the stability of the iron hydrolysis intermediates that determine the extent of hydronium jarosite formation in ferric sulphate and ferric chloride.

7.2.1 Inhibition in ferric sulphate

Hydronium jarosite and goethite levels depend on the iron hydrolysis species present under the reaction conditions. These conditions include temperature, pH and sulphate levels. Although temperature and pH are important, sulphate levels are critical, with high sulphate levels leading to precipitation of hydronium jarosite, low sulphate levels leading to precipitation of either goethite or sulphate adsorbed goethite, and no sulphate leading to precipitation of pure goethite (Appendices E).

In the absence of sulphate, iron hydrolyses to form $Fe(OH)(H_2O)_5^{2+}$, $Fe(OH)_2(H_2O)_4^{+}$ and $Fe_2(OH)_2(H_2O)_8^{4+}$ (Knight and Sylva, 1974):

$$Fe(H_2O)_6^{3+} \rightleftharpoons Fe(OH)(H_2O)_5^{2+} + H^+ \qquad (K_{11} = 1.84 \times 10^{-3}M) \quad (7.10)$$

$$Fe(OH)(H_2O)_5^{2+} \rightleftharpoons Fe(OH)_2(H_2O)_4^{+} + H^+ \qquad (K_{12} = 5 \times 10^{-7}M) \quad (7.11)$$

$$2\,Fe(OH)(H_2O)_5^{2+} \rightleftharpoons Fe_2(OH)_2(H_2O)_8^{4+} + 2\,H_2O \qquad (K_{22} = 1.69 \times 10^{-3}M) \quad (7.12)$$

Because of the stabilities of $Fe(OH)(H_2O)_5{}^{2+}$ and $Fe(OH)_2(H_2O)^{4+}$, and the improved stability of the dimer as a function of temperature (Mulay and Selwood, 1955; Sapieszko, 1977), these species are the basis of the proposed goethite mechanism (Figure 7.4):

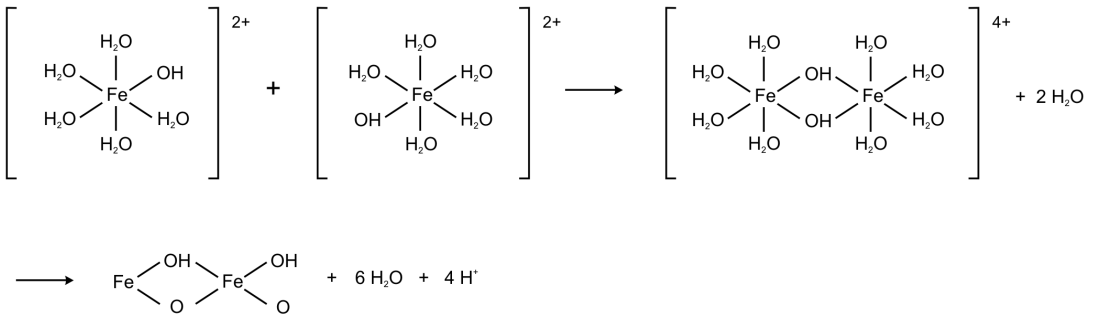

Figure 7.4: *Mechanism of goethite formation adapted from Dutrizac (1980).*

Goethite may precipitate according to this reaction or it may polymerise on addition of $Fe_2(OH)_2(H_2O)^{4+}$ units. The polymer grows until either aging or pH changes cause it to break down and precipitate more goethite (Flynn, 1984).

In the presence of sulphate, iron hydrolyses to form $Fe(OH)(H_2O)_4(SO_4)$ and $Fe_2(OH)_2(H_2O)_6(SO_4)_2$ (Yakovlev et al., 1977; Dutrizac, 1980):

$$Fe(OH)(H_2O)_5^{2+} + SO_4^{2-} \rightleftharpoons Fe(OH)(H_2O)_4(SO_4) + H_2O \qquad (K_{11} = 107M) \quad (7.13)$$

$$2\,Fe(OH)(H_2O)_4(SO_4) \rightleftharpoons Fe_2(OH)_2(H_2O)_6(SO_4)_2 + 2\,H_2O \qquad (K_{22} = 9.33M) \quad (7.14)$$

Because of the stabilities of $Fe(OH)(H_2O)_4(SO_4)$ and $Fe_2(OH)_2(H_2O)_6(SO_4)_2$, and the improved stability of the dimer as a function of temperature (Yakovlev et al., 1977), these species are the basis of the proposed jarosite mechanism (Figure 7.5):

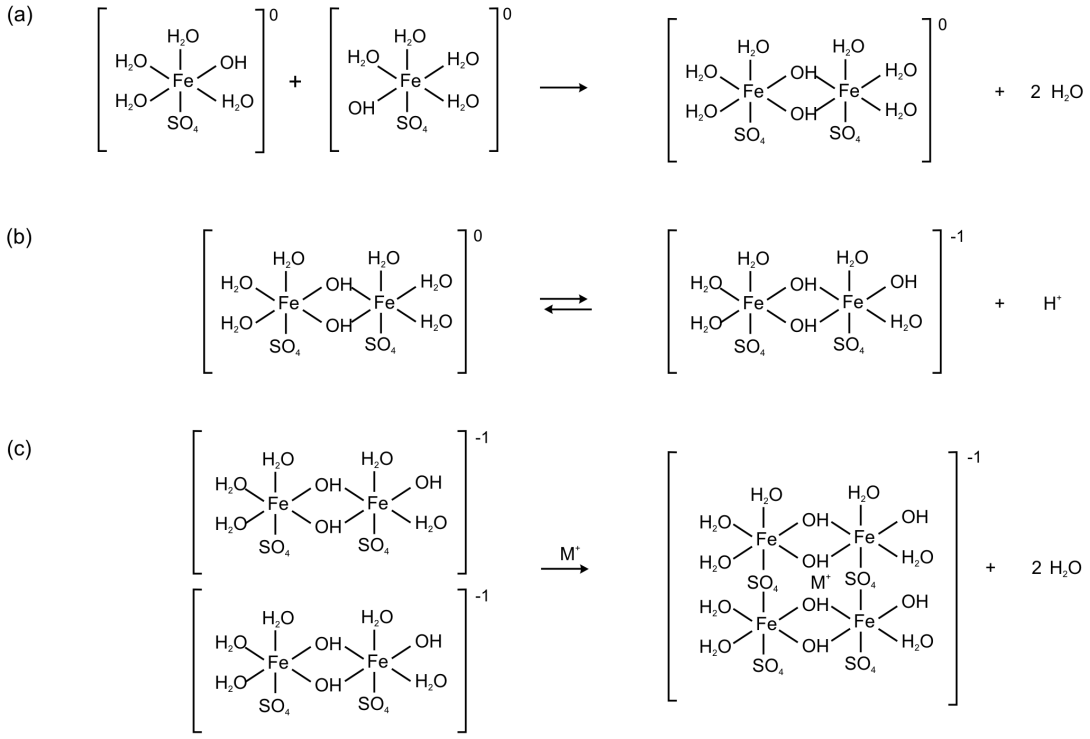

Figure 7.5: *Mechanism of jarosite formation adapted from Lee (2001).*

The $Fe_2(OH)_2(H_2O)_6(SO_4)_2$ dimer is formed by the combination of two $Fe(OH)(H_2O)_4(SO_4)$ units, in a reaction analogous to the dimerisation previously shown (Figure 7.4). The dimers cross link via shared sulphate ligands, with charge

stabilisation by incorporated monovalent cations [M^+]; hydronium ions are incorporated exclusively in the absence of sodium, potassium and ammonium ions (Figure 7.5).

The mechanism is consistent with reported infrared data, which revealed the progressive complexation of sulphate as it transforms from C_{3v} (monodentate) to C_{2v} (bidentate) symmetry (Peak et al., 1999; Lee, 2001).

The goethite and jarosite mechanisms can be expanded to include $Fe(OH)(H_2O)_4(SO_4)$ in the former and $Fe(OH)(H_2O)_5{}^{2+}$ in the latter. These species are present in ferric sulphate systems and might be involved in polymerisation and precipitation reactions. The formation of goethite or jarosite is dependent on the dimers present. The combination of $Fe(OH)(H_2O)_4(SO_4)$ with $Fe(OH)(H_2O)_5{}^{2+}$ produces the $Fe_2(OH)_2(H_2O)_7(SO_4)$ dimer, which may polymerise with other $Fe(OH)(H_2O)_5{}^{2+}$ units and form goethite with sulphate incorporated; this process is believed to be partially responsible for the $FeOOH.0.25H_2SO_4$ species proposed (Appendix E). Alternatively, the $Fe_2(OH)_2(H_2O)_7SO_4$ dimer may acquire an additional sulphate ligand and form jarosite; the $Fe_2(OH)_2(H_2O)_7SO_4$ dimer might be the precursor proposed by Lazaroff et al. (1982), which converts to jarosite on addition of sulphate.

7.2.2 Inhibition in ferric chloride

The extremely low sulphate levels in ferric chloride systems are partially responsible for the low level of hydronium jarosite precipitation; however, the interaction of chloride ions with iron hydrolysis products is another important factor.

The incorporation of anions during iron hydrolysis determines the precipitate formed and hence the dissolution rates. Although ferric chloride systems are dominated by $Fe(H_2O)_5Cl^{2+}$ (Magini and Radnai, 1979), iron sulphate complexes are still apparent at the chalcopyrite surface with identification of hydronium jarosite (Section 6.2). The formation of iron sulphate complexes in ferric chloride systems is attributed to the high concentration gradient at the surface and the greater stability of $Fe(H_2O)_5(SO_4)^+$

relative to $Fe(H_2O)_5(Cl)^{2+}$ (Wendt, 1962). The greater stability implies sulphate may substitute for chloride in existing iron hydrolysis complexes, although the iron sulphate complex concentration is expected to be lower at the surface in ferric chloride systems. Thus, $Fe(H_2O)_5(SO_4)^{+}$ is present at the surface but $Fe(H_2O)_5(Cl)^{2+}$ dominates the bulk solution, with the enhanced dissolution rate observed in ferric chloride systems attributed to delayed hydronium jarosite formation in the bulk solution.

The enhanced dissolution in ferric chloride systems may also be caused by hydration of the anions, with sulphate removing protons from solution and increasing the pH, which favours hydronium jarosite formation. Additionally, the relative hardness of the anions causes greater hydration of chloride, which increases the ferric activity of the solution and therefore enhances dissolution rates.

7.3 Summary

The mechanism of chalcopyrite dissolution involves oxidation of the disulphide moiety through to thiosulphate, with electron exchange occurring via bridging water molecules. This mechanism does not require the invocation of radicals and it ensures the species remain hydrated at all times. Electron exchange between these hydrated species occurs via consistent sigma bonding, which accounts for the high dissolution rates observed. Hydration of the species was confirmed by XPS analysis of chalcopyrite after oxidative dissolution performed anaerobically, while electron exchange via bridging water molecules was confirmed by comparison of the rate constants observed in water and deuterated water. The oxidation through to thiosulphate releases iron and copper into solution, while the thiosulphate reacts further to form elemental sulphur, sulphite and sulphate. The relative amounts of elemental sulphur and sulphate formed depends on the solution conditions, which is consistent with the varying levels reported, without invoking two separate mechanisms.

The mechanism of chalcopyrite inhibition involves the deposition of hydronium jarosite, which forms along with goethite. The hydronium jarosite and goethite mechanisms are

based on the polymerisation of the stable products of iron hydrolysis. In the absence of sulphate, $Fe(OH)(H_2O)_5{}^{2+}$ and $Fe(OH)_2(H_2O)_4{}^{4+}$ form before polymerising to produce goethite. In the presence of sulphate, $Fe(OH)(H_2O)_4SO_4$, $Fe(OH)_2(H_2O)_3SO_4$ and $Fe_2(OH)_2(H_2O)_6(SO_4)_2$ form, before producing either goethite with sulphate incorporated or hydronium jarosite. Therefore, the formation of either goethite or hydronium jarosite is strictly dependent on the sulphate levels in solution. This dependence accounts for the reduced levels of hydronium jarosite present in ferric chloride solutions because of the predominance of $Fe(H_2O)_5(Cl)^{2+}$. However, the enhanced stability of iron sulphate complexes, relative to iron-chloride complexes, accounts for the presence of hydronium jarosite on the surface of chalcopyrite in ferric chloride solutions because of the high concentration of sulphate at the chalcopyrite surface. The mechanism also accounts for the adverse effect of sulphate addition, and the beneficial effect of chloride addition, on chalcopyrite dissolution rates.

Chapter 8

Conclusions

The mechanisms of dissolution and inhibition of chalcopyrite in ferric media have been investigated by studying the rate of copper release during oxidative dissolution and analysing the surface before and after oxidative dissolution.

The surface analysis was performed quantitatively using XPS, which required the analysis of the XPS spectra and the development of three programs.

Spectral analysis involved the S 2p, Fe 2p and Cu 2p spectra recorded for each oxidised chalcopyrite sample. The S 2p spectra were fitted with six peaks that corresponded to sulphide, disulphide, elemental sulphur, loss structure, sulphite and sulphate. These peaks were present in the spectra of samples oxidised under all conditions. The relative contributions of the peaks were determined by iterative fitting of the S 2p spectra using an 'in-house' program (SpecProc). The sulphide, disulphide and loss structure fit parameters were constrained according to the parameters determined during the spectral analysis of chalcopyrite fractured under anaerobic atmosphere. The elemental sulphur, sulphite and sulphate peaks were largely unconstrained. This approach yielded excellent fits for the S 2p spectra of all samples. The Fe 2p spectra were fitted by PCA (as NLLS) with Fe 2p spectra of chalcopyrite, goethite and hydronium jarosite standards. These phases were present in the spectra of samples oxidised under all conditions. The relative contributions of the phases were determined by iterative fitting

of the Fe 2p spectra using Eclipse and an 'in-house' program (FeFit). The binding energy shifts permitted during the fitting procedure were constrained to ensure realistic solutions. The Cu 2p spectra were simply analysed in terms of photoelectron intensity. Thus, the spectra of chalcopyrite samples after oxidative dissolution were fitted using chalcopyrite, elemental sulphur, hydronium jarosite, and goethite (with and without sulphite and sulphate adsorbed or incorporated). These phases accounted for all spectra without requiring the invocation of either metal deficient sulphides or polysulphides.

The first program developed for quantitative analysis used IMFP and spectrometer calculations to predict the intensity ratios associated with monolayer models for pure standards. The theoretical Fe 2p and Cu 2p cross sections used in the calculations were adjusted to ensure the observed and predicted S 2p, Fe 2p, Cu 2p and O 1s intensities were consistent for a range of stable standards.

The second program also used IMFP and spectrometer equations to predict the intensity ratios associated with monolayer models. However, these models were based on possible models of the chalcopyrite surface after oxidative dissolution. Thus, they were based on chalcopyrite, elemental sulphur, hydronium jarosite, and goethite (with and without sulphite and sulphate adsorbed or incorporated). The intensity contribution of each phase towards the S 2p, Fe 2p and Cu 2p spectra was predicted across a range of angles to account for the roughened surfaces of the chalcopyrite samples.

The third program contained these predicted intensity contributions, along with the observed intensity contributions for each sample determined during spectral analysis. This program was used to determine a suite of models that accounted for the observed spectra of each sample. The suite of models was then used to construct a surface profile of the chalcopyrite samples after oxidative dissolution.

Surface profiles of chalcopyrite samples revealed hydronium jarosite is the phase responsible for inhibition, regardless of the pH, temperature or lixiviate. Although elemental sulphur and goethite were also identified on the surface, only hydronium jarosite consistently increased in surface coverage during the initial stages of dissolution. Hydronium jarosite was also the only phase that deposited in large quantities during the latter

stages of dissolution. The consistent increase of surface coverage and rapid deposition during the latter stages of dissolution explain the dramatic decrease in dissolution rate observed during the kinetics study. The deposition of hydronium jarosite onto isolated parts of the surface also accounts for both stages of dissolution, identified during the kinetics study, remaining surface controlled. The identification of hydronium jarosite as the inhibiting phase addresses the higher activation energy observed at higher temperatures, along with the lower activation energies reported for ferric chloride systems that do not produce as much hydronium jarosite because of the relative lack of sulphate. The deposition of hydronium jarosite also accounts for different apparent activation energies for the oxidative dissolution of chalcopyrite in ferric media without invoking different mechanisms of dissolution or inhibition.

The mechanism of the oxidative dissolution of chalcopyrite is based on the progressive oxidation of the disulphide to thiosulphate via the exchange of electrons between the chalcopyrite and the ferric ions through bridging water molecules according to the Grotthuus mechanism. The thiosulphate degrades under the oxidising conditions of low pH to form elemental sulphur, sulphite and sulphate. Iron and copper are also released during oxidation of the disulphide. The mechanism ensures the chalcopyrite surface and ferric ion are hydrated at all times, with consistent sigma bonding between all species accounting for the high dissolution rates. However, the products of dissolution – namely iron and sulphate – are implicated in the mechanism of inhibition.

The mechanism of inhibition of the oxidative dissolution of chalcopyrite involves the deposition of hydronium jarosite onto the surface of the chalcopyrite. The mechanism of hydronium jarosite formation in ferric media is based on the stable iron sulphate species present under the dissolution conditions. This mechanism accounts for the greater hydronium jarosite formation observed in the ferric sulphate system, along with the formation of hydronium jarosite in the ferric chloride system.

The identification of hydronium jarosite on the surface of chalcopyrite oxidised in ferric chloride systems is evidence of a high concentration gradient at the surface. This concentration gradient is produced by the iron and sulphate released at the surface

and the proton consumption by the surface, which diminishes the solubility of iron and sulphate at the surface. The situation is complicated further by the combination of iron hydrolysis and sulphur oxidation reactions that produce and consume protons to maintain the solution pH within a window that appears to favour hydronium jarosite formation, especially at the surface-solution interface. The effect of these reactions and the high concentration gradient was not overcome by the use of low pH or ferric chloride, and hydronium jarosite was still formed at the surface.

Implications

The identification of hydronium jarosite as the inhibiting phase for the oxidative dissolution of chalcopyrite has implications for the hydrometallurgical processing of chalcopyrite. These implications arise because the conditions that produce favourable chalcopyrite dissolution coincide with the conditions that produce favourable jarosite formation. The key determinants for jarosite precipitation include ferric and sulphate concentrations, pH and temperature. Although ferric concentrations need to be sufficient to produce dissolution, they cannot be too high because jarosite will precipitate. Iron concentrations are lowered industrially using precipitation tanks before oxidising the ore with the solution; however, the use of scrap iron for the cementation process of removing copper from solution, introduces more iron into the solution (Canterford et al., 1985). The oxidative dissolution of chalcopyrite also introduces more iron into solution. Sulphate concentrations are initially dependent on the concentration of ferric sulphate used; however, dissolution of chalcopyrite introduces more sulphate into solution. The introduction of more iron and sulphate into solution produces a high concentration gradient at the surface. The precipitation of iron sulphate phases at the surface is difficult to control because the pH at the surface is determined by competing reactions producing and consuming protons (Section 7.1.4). However, it is important to maintain a low pH because it keeps the oxidant in solution and prevents jarosite formation.

The effects of iron and sulphate concentrations, and pH, are exacerbated during microbially assisted oxidative dissolution of chalcopyrite. The microbes typically used for

chalcopyrite dissolution oxidise ferrous to ferric, elemental sulphur to sulphate, or both (Stott et al., 2003). Although the regeneration of ferric ions is advantageous during the early stages of dissolution, it may become a problem during the latter stages of dissolution because of the decrease in the surface area of the chalcopyrite. This decrease will produce an increase of ferric and proton levels in solution, both of which will promote jarosite formation. Furthermore, the increase in ferric levels will produce a higher solution potential, which adversely affects dissolution rates (Section 2.2.2). The situation becomes even worse in the presence of microbes that oxidise elemental sulphur to sulphate because this increases jarosite precipitation rates (Parker et al., 2003). The increase is exacerbated further by the microbes requiring nutrient media containing potassium, ammonium and sulphate because these ions promote the formation of potassium and ammonium jarosites, which are more stable and hence form earlier than hydronium jarosite. Controlling jarosite formation by using low pH has been a problem because microbes usually require pH values above 1.3 (Brierley and Brierley, 1999). However, the recent development of microbes that survive at pH values below 1 should lead to significant improvements in copper recovery rates for microbially assisted dissolution of chalcopyrite in heaps (Plumb et al., 2008).

References

Abass, A. K. and N. H. Ahmad (1986). Indirect band gap investigation of orthorhombic single crystals of sulfur. *Journal of Physics and Chemistry of Solids 47*(2), 143–5.

Ammou-Chokroum, M., M. Cambazoglu, and D. Steinmetz (1977). Soft oxidation of chalcopyrite in acid solution: kinetic study of the reactions. i. chemical models. *Bull. Soc. Fr. Mineral. Cristallogr. FIELD Full Journal Title:Bulletin de la Societe Francaise de Mineralogie et de Cristallographie 100*(3-4), 149–61.

Ammou-Chokroum, M., P. K. Sen, and F. Fouques (1979). Electrooxidation of chalcopyrite in acid chloride medium; kinetics, stoichiometry and reaction mechanism. In J. Laskowski (Ed.), *International Mineral Processing Congress*, Volume 1, Warsaw, Poland, pp. 527–557.

Austin, I. G., C. H. L. Goodman, and A. E. Pengelly (1956). New semiconductors with the chalcopyrite structure. *The Journal of the Electrochemical Society 103*, 609–610.

Barman, S. R. and D. D. Sarma (1992). Investigation of the L_3-$M_{45}M_{45}$ Auger spectra of copper, cuprous oxide and cupric oxide. *Journal of Physics: Condensed Matter 4*(37), 7607–16.

Barnes, M. (1969). Sulfur. In E. Dukes (Ed.), *Kirk-Othmer encyclopedia of chemical technology* (2nd ed.), Volume 19. New York: John Wiley and Sons, Inc.

Basset, H. and W. G. Parker (1951). The oxidation of sulphurous acid. *The Journal of the Chemical Society*, 1540–1560.

Baur, J. P., H. L. Gibbs, and M. E. Wadsworth (1974). Initial stage sulfuric acid

leaching kinetics of chalcopyrite using radiochemical techniques. *U. S. Bureau of Mines*.

Bebie, J., M. Schoonen, M. Fuhrmann, and D. Strongin (1998). Surface charge development on transition metal sulfides: An electrokinetic study. *Geochimica et Cosmochimica Acta 62*(4), 633–642.

Beckstead, L. W., P. B. Munoz, J. L. Sepulveda, J. A. Herbst, J. D. Miller, F. A. Olson, and M. E. Wadsworth (1976). Acid ferric sulfate leaching of attritor-ground chalcopyrite concentrates. In J. C. Yannopoulos and J. C. Agarwal (Eds.), *Extractive Metallurgy of Copper: Hydrometallurgy and Electrowinning*, Volume 2, pp. 611–632. New York, New York: Metallurgical Society, American Institute of Mining, Metallurgical and Petroleum Engineer.

Bhappu, R. B., P. H. Johnson, J. A. Brierley, and D. H. Reynolds (1969). Theoretical and practical studies on dump leaching. *Transactions of the American Institute of Mining, Metallurgical and Petroleum Engineers 244*(3), 307–20.

Biegler, T. and M. D. Horne (1984). The electrochemistry of surface oxidation of chalcopyrite. In *Proceedings of the International Symposium on Electrochemistry in Mineral and Metal Processing*, Volume 84-10, pp. 321–39.

Biegler, T. and D. A. Swift (1979). Anodic electrochemistry of chalcopyrite. *Journal of Applied Electrochemistry 9*, 545–554.

Bither, T. A., R. J. Bouchard, W. H. Cloud, P. C. Donohue, and W. J. Siemons (1968). Transition metal pyrite dichalcogenides. High-pressure synthesis and correlation of properties. *Inorganic Chemistry 7*(11), 2208–20.

Bladh, K. W. (1982). The formation of goethite, jarosite, and alunite during the weathering of sulfide-bearing felsic rocks. *Economic Geology 77*(1), 176–184.

Bockris, J. O. and S. U. M. Khan (1985). On the evolution of concepts concerning events at the semiconductor/solution interface. *Journal of the Electrochemical Society* (November), 2648–2655.

Bonnissel-Gissinger, P., M. Alnot, J. J. Ehrhardt, and P. Behra (1998). Surface oxidation of pyrite as a function of pH. *Environmental Science and Technology 32*(19), 2839–2845.

Brierley, C. L. and J. A. Brierley (1999). Bioheap processes - operational requirements and techniques. In G. V. Jergensen (Ed.), *Copper leaching, solvent extraction, and electrowinning technology*. Littleton: Society for Mining, Metallurgy, and Exploration, Inc.

Brion, D. (1980). Etude par spectroscopie de photoelectrons de la degradation superficielle de FeS_2, $CuFeS_2$, ZnS et PbS a l'air et dans l'eau. *Applied Surface Science 5*, 133–152.

Buckley, A. N., I. C. Hamilton, and R. Woods (1984). Investigation of the surface oxidation of bornite by linear sweep voltammetry and X-ray photoelectron spectroscopy. *Journal of Applied Electrochemistry 14*, 63–74.

Buckley, A. N. and R. Woods (1984). An X-ray photoelectron spectroscopic study of the oxidation of chalcopyrite. *Australian Journal of Chemistry 37*(12), 2403–2413.

Buttinelli, D., R. Lavecchia, C. Lupi, F. Pochetti, A. Geveci, and Y. Topkaya (1990). Ferric chloride leaching of a complex copper-zinc sulphide ore in the presence of a solvent for elemental sulphur. *La Chimica and L'Industria 72*(8-9), 707–712.

Cano, E., M. F. Lopez, J. Simancas, and J. M. Bastidas (2001). X-ray photoelectron spectroscopy study on the chemical composition of copper tarnish products formed at low humidities. *Journal of the Electrochemical Society 148*(1), E26–30.

Canterford, J. H., P. T. Davey, and G. Tsambourakis (1985). Gangue mineral dissolution and jarosite formation in copper solution mining. *Hydrometallurgy 13*(3), 327–343.

Chawla, S. K., N. Sankarraman, and J. H. Payer (1992). Diagnostic spectra for XPS analysis of Cu-O-S-H compounds. *Journal of Electron Spectroscopy and Related Phenomena 61*(1), 1–18.

Ching, W., Y. Xu, and M. Rhle (1997). Ab-initio calculation of yttrium substitutional impurities in α-Al_2O_3. *Journal of the American Ceramic Society 80*(12), 3199–3204.

Cho, C. H., J. Urquidi, S. Singh, and G. W. Robinson (1999). Thermal offset viscosities of liquid H_2O, D_2O, and T_2O. *Journal of Physical Chemistry B 103*(11), 1991–1994.

Clifford, R. K., K. L. Purdy, and J. D. Miller (1975). Characterization of sulfide mineral surfaces in froth flotation systems using electron spectroscopy for chemical analysis. *American Institute of Chemical Engineers Symposium Series 71*(150), 138–147.

Da Silva, L. A. and J. B. De Andrade (2004). Isomorphic series of double sulfites of the $Cu_2SO_3.MSO_3.2H_2O$ (M = Cu, Fe, Mn, and Cd) Type - A review. *Journal of the Brazilian Chemical Society 15*(2), 170–177.

Das, G., S. Acharya, S. Anand, and R. Das (1996). Jarosites: A review. *Mineral Processing and Extractive Metallurgy Review 16*(3), 185–210.

Davey, P. T. and T. R. Scott (1975). Formation of β-FeOOH and α-Fe_2O_3 in the geothite process. *Transactions of the Institution of Mining and Metallurgy 84*, C83–C86.

Davis, R. E. (1958). Displacement reactions at the sulfur atom. I. An interpretation of the decomposition of acidified thiosulfate. *Journal of the American Chemical Society 80*, 3565–3569.

De Filippo, D., A. Rossi, G. Rossi, and P. Trois (1988a). Chalcopyrite bioleaching: An investigation on copper recovery. In *8th International Biotechnology Symposium*, Volume 2, Paris, France, pp. 1131–1145.

De Filippo, D., A. Rossi, G. Rossi, and P. Trois (1988b). Surface modifications in copper sulfide minerals after bioleaching. In *IBS '87: Biohydrometallurgy*, Warwick, England, pp. 245–258.

De Grotthuus, C. J. T. (1806). On the decomposition of water and their solution species using galvanic electricity. *Ann. Chim. (abbreviated) 58*, 54–74.

Deroubaix, G. and P. Marcus (1992). X-ray photoelectron-spectroscopy analysis of copper and zinc-oxides and sulfides. *Surface and Interface Analysis 18*(1), 39–46.

Donnay, G., L. M. Corliss, J. D. H. Donnay, N. Elliott, and J. M. Hastings (1958). Symmetry of magnetic structure: Magnetic structure of chalcopyrite. *Physical Review 112*, 1917–23.

Duret-Thual, C., D. Costa, W. Yang, and P. Marcus (1997). The role of thiosulfates in the pitting corrosion of Fe-17Cr alloys in neutral chloride solution: Electrochemical and XPS study. *Corrosion Science 39*(5), 913–933.

Dutrizac, J. E. (1978). The kinetics of dissolution of chalcopyrite in ferric ion media. *Metallurgical Transactions B 9*(3), 431–439.

Dutrizac, J. E. (1980). The physical chemistry of iron precipitation in the zinc industry. In J. M. Cigan, T. S. Mackey, and T. J. O'Keefe (Eds.), *Lead-zinc-tin '80*, Las Vegas. The Metallurgical Society of AIME.

Dutrizac, J. E. (1981). The dissolution of chalcopyrite in ferric sulfate and ferric chloride media. *Metallurgical Transactions B 12*(2), 371–378.

Dutrizac, J. E. (1982). Ferric ion leaching of chalcopyrites from different localities. *Metallurgical Transactions B 13B*, 303–309.

Dutrizac, J. E. (1983). Factors affecting alkali jarosite precipitation. *Metallurgical Transactions B: Process Metallurgy 14B*(4), 531–9.

Dutrizac, J. E. (1989). Elemental sulphur formation during the ferric sulphate leaching of chalcopyrite. *Canadian Metallurgical Quarterly 28*(4), 337–344.

Dutrizac, J. E. (1990). Elemental sulphur formation during the ferric chloride leaching of chalcopyrite. *Hydrometallurgy 23*, 153–176.

Dutrizac, J. E. (1996). The effect of seeding on the rate of precipitation of ammonium jarosite and sodium jarosite. *Hydrometallurgy 42*, 293–312.

Dutrizac, J. E. and R. J. C. MacDonald (1974). Ferric ion as a leaching medium. *Minerals Science and Engineering 6*(2), 59–100.

Dutrizac, J. E., R. J. C. MacDonald, and T. R. Ingraham (1969). Kinetics of dissolution of synthetic chalcopyrite in aqueous ferric sulfate solutions. *Transactions of the Metallurgical Society of AIME 245*, 955–959.

Ermilov, V. V., O. B. Tkachenko, and A. L. Tseft (1969). Kinetics of the dissolution of chalcopyrite in ferric chloride. *Trudy Instituta Metallurgii I Obogashcheniya Akadmmmmiya Nauk Kazakhskoi SSR 30*, 3–14.

Eyert, V., K. H. Hock, S. Fiechter, and H. Tributsch (1998). Electronic structure of FeS_2: The crucial role of electron-lattice interaction. *Physical Review B: Condensed Matter and Materials Physics 57*(11), 6350–6359.

Farquhar, M. L., P. L. Wincott, R. A. Wogelius, and D. J. Vaughan (2003). Electrochemical oxidation of the chalcopyrite surface: An XPS and AFM study in solution at pH 4. *Applied Surface Science 218*(1-4), 34–43.

Ferreira, R. C. H. and A. R. Burkin (1975). Acid leaching of chalcopyrite. In A. R. Burkin (Ed.), *Leaching and Reduction in Hydrometallurgy*, pp. 54–66. London: The Institute of Mining and Metallurgy.

Fischer, U. (1984). *Sulfur-Its significance for chemistry for the geo-, bio- and cosmosphere and technology.* Amsterdam, The Netherlands: Elsevier.

Flynn, Charles M., J. (1984). Hydrolysis of inorganic iron(III) salts. *Chemical Reviews 84*(1), 31–41.

Folmer, J. C. W. and F. Jellinek (1980). The valence of copper in sulfides and selenides: An X-ray photoelectron spectroscopy study. *Journal of the Less Common Metals 76*(1-2), 153–162.

Frost, D. C., A. Ishitani, and C. A. McDowell (1972). X-ray photoelectron spectroscopy of copper compounds. *Molecular Physics 24*(4), 861–877.

Fujisawa, M., S. Suga, T. Mizokawa, A. Fujimori, and K. Sato (1994). Electronic-structures of $CuFeS_2$ and $CuAl_{0.9}Fe_{0.1}S_2$ studied by electron and optical spectroscopies. *Physical Review B 49*(11), 7155–7164.

Galtayries, A. and J. P. Bonnelle (1995). XPS and ISS studies on the interaction of H_2S with polycrystalline Cu, Cu_2O and CuO surfaces. *Surface and Interface Analysis 23*(3), 171–179.

Galwey, A. K. and M. E. Brown (1995). A theoretical justification for the application of the arrhenius equation to kinetics of solid-state reactions (mainly ionic-crystals). *Proceedings of the Royal Society of London Series A-Mathematical and Physical Sciences 450*(1940), 501–512.

Galwey, A. K. and M. E. Brown (1998). Kinetic background to thermal analysis and calorimetry. In M. E. Brown (Ed.), *Handbook of thermal analysis and calorimetry*, Volume 1. Oxford: Elsevier.

Gebhardt, J. E., J. J. McCarron, P. E. Richardson, A. N. Buckley, and J. P. Bonnelle (1986). The effect of cathodic treatment on the anodic polarization of copper sulphides. *Hydrometallurgy 17*(1), 27–38.

Giggenbach, W. F. (1972). Optical spectra and equilibrium distribution of polysulphide ions in aqueous solution at 20 C. *Inorganic Chemistry 11*(6), 1201–1207.

Goldhaber, M. B. (1983). Experimental study of metastable sulfur oxyanion formation during pyrite oxidation at pH 6-9 and 30 degrees C. *American Journal of Science 283*(3), 193–217.

Grano, S. R., M. Sollaart, W. Skinner, C. A. Prestidge, and J. Ralston (1997). Surface modifications in the chalcopyrite-sulphite ion system. 1. Collectorless flotation, XPS and dissolution study. *International Journal of Mineral Processing 50*(1-2), 1–26.

Haber, J., T. Machej, L. Ungier, and J. Ziolkowski (1978). ESCA studies of copper oxides and copper molybdates. *Journal of Solid State Chemistry 25*, 207–218.

Hackl, R. P., D. B. Dreisinger, E. Peters, and J. A. King (1995). Passivation of chalcopyrite during oxidative leaching in sulfate media. *Hydrometallurgy 39*, 25–48.

Hall, S. and J. Stewart (1973). The crystal structure refinement of chalcopyrite, $CuFeS_2$. *Acta Crystallographica B 29*, 579–585.

Hamajima, T., T. Kambara, K. I. Gondaira, and T. Oguchi (1981). Self-consistent electronic structures of magnetic semiconductors by a discrete variational Xα calculation. III Chalcopyrite $CuFeS_2$. *Physical Review B 24*(6), 3349–3353.

Harmer, S. L., A. R. Pratt, W. H. Nesbitt, and M. E. Fleet (2004). Sulfur species at chalcopyrite ($CuFeS_2$) fracture surfaces. *American Mineralogist 89*(7), 1026–1032.

Harvey, D. T. and R. W. Linton (1981). Chemical characterization of hydrous ferric oxides by X-ray photoelectron spectroscopy. *Analytical Chemistry 53*, 1684–1688.

Havlik, T. and R. Kammel (1995). Leaching of chalcopyrite with acidified ferric chloride and carbon tetrachloride addition. *Minerals Engineering 8*(10), 1125–1134.

Herzog, W., M. Schwarz, H. Sixl, and R. Hoppe (1988). X-ray photoelectron-spectroscopy of the high-temperature superconductor $YBa_2Cu_3O_{7-x}$ and the copper oxides. *Zeitschrift für Physik B - Condensed Matter 71*(1), 19–22.

Hingston, F. J., A. M. Posner, and J. P. Quirk (1972). Anion adsorption by goethite and gibbsite. I. Role of the proton in determining adsorption envelopes. *Journal of Soil Science 23*(2), 177–92.

Hirato, T., H. Majima, and Y. Awakura (1987). The leaching of chalcopyrite with ferric sulfate. *Metallurgical Transactions B 18*(3), 489–496.

Hiroyoshi, N., M. Hirota, T. Hirajima, and M. Tsunekawa (1997). A case of ferrous sulphate addition enhancing chalcopyrite leaching. *Hydrometallurgy 47*, 37– 45.

Hiskey, J. B. and M. E. Wadsworth (1975). Galvanic conversion of chalcopyrite. *Metallurgical Transactions B 6*(1), 183–190.

Hiskey, J. B. and M. E. Wadsworth (1981). Electrochemical processes in the leaching of metal sulfides and oxides. *Process and Fundamental Considerations of Selected Hydrometallurgical Systems*, 303–325.

Holloway, P. H. (1982). Surface and interface characterization of advanced materials. *Ceramic Engineering and Science Proceedings 3*(9-10), 431–49.

Horne, R. A. and E. H. Axelrod (1964). Proton mobility and electron exchange in aqueous media. *Journal of Chemical Physics 40*(6), 1518–22.

Hyde, B. and M. O'Keefe (1996). Marcasite and pyrite (FeS_2). *Australian Journal of Chemistry 49*(8), 867–872.

Jones, D. L. and E. Peters (1976). The leaching of chalcopyrite with ferric sulfate and ferric chloride. *Extractive Metallurgy of Copper: Hydrometallurgy and Electrowinning 2*, 633–653.

Kametani, H. and A. Aoki (1985). Effect of suspension potential on the oxidation rate of copper concentrate in a sulfuric acid solution. *Metallurgical Transactions B 16*(4), 695–705.

Karguppikar, A. M. and A. G. Vedeshwar (1988). Electrical and optical properties of natural iron pyrite (FeS_2). *Physica Status Solidi A 109*(2), 549–558.

Kelsall, G. H., K. E. R. England, D. J. Vaughan, and Q. Yin (1992). Electrochemical oxidation of chalcopyrite ($CuFeS_2$) in alkaline solutions. *Electrochemistry in Mineral and Metal Processing: Proceedings of the 3rd International Symposium (St Louis, Missouri)*, 318–341.

Klauber, C. (1993). Magnesium K-α X-ray line structure revisited. *Applied Surface Science 70-1*, 35–39.

Klauber, C. (1995). X-ray photoelectron and Auger electron spectroscopy. *Microbeam Analysis 4*, 341–368.

Klauber, C. (2003). Fracture-induced reconstruction of a chalcopyrite ($CuFeS_2$) surface. *Surface and Interface Analysis 35*(5), 415–428.

Klauber, C. (2008). A critical review of the surface chemistry of acidic ferric sulphate dissolution of chalcopyrite with regards to hindered dissolution. *International Journal of Mineral Processing 86*(1-4), 1–17.

Knight, R. J. and R. N. Sylva (1974). Precipitation in hydrolyzed iron(III) solutions. *Journal of Inorganic and Nuclear Chemistry 36*(3), 591–7.

Kostikov, Y. P. and D. V. Korolkov (1998). Chemical strucure of copper monosulfide. *Russian Journal of General Chemistry 68*(10), 1547–1549.

Kougianos, A. (2000). *The role of polysulphides in chalcopyrite leaching.* Honours thesis, Curtin University of Technology.

Krishna, N., B. Misra, J. Rawat, and A. Rawat (1999). Characterization of intermediate sulfur layer during acidic oxidation of chalcopyrite using electrochemical impedance spectroscopy (EIS) and atomic force microscope (AFM). In B. Mishra (Ed.), *EPD Congress 1999*, San Diego, USA, pp. 493–507.

Larson, P. E. (1974). X-ray induced photoelectron and Auger spectra of Cu, CuO, Cu_2O and CuS thin films. *Journal of Electron Spectroscopy and Related Phenomena 4*, 213–218.

Lazaroff, N., W. Sigal, and A. Wasserman (1982). Iron oxidation and precipitation of ferric hydroxysulfates by resting thiobacillus ferrooxidans cells. *Applied Environmental Microbiology 43*, 924–938.

Lee, F. A. (2001). *Characterisation of jarosite formed during the bioleaching of chalcopyrite.* Honours thesis, Curtin University of Technology.

Leloup, J., A. Ruaudelteixier, A. Barraud, H. Roulet, and G. Dufour (1993). XPS study of copper sulfides inserted into a Langmuir-Blodgett matrix. *Applied Surface Science 68*(2), 231–242.

Letowski, F. (1979). Acid hydrometallurgical winning of copper and other metals from polish sulfide concentrates. *Prepr. Pap. - Int. Mineral. Process. Congr., 13th 1*, 637–63.

Lianzhong, Z. (1987). Studies of XPS satellites of transition metal compounds. *Journal of Molecular Science 5*(1), 37–43.

Linge, H. G. (1976). Reactivity comparison of Australian chalcopyrite concentrates in acidified ferric solution. *Hydrometallurgy 2*, 219–233.

Llanos, J., A. Buljan, and C. Mujica (1995). Electron transfer in the insertion of alkali metals in chalcopyrite. *Materials Research Bulletin 30*(1), 43–48.

Lowe, D. F. (1970). *Kinetics of the dissolution reactions of copper and copper-iron sulfide minerals using ferric sulfate solutions.* Ph. D. thesis, University of Arizona.

Luther, George W., I. (1987). Pyrite oxidation and reduction: Molecular orbital theory considerations. *Geochimica et Cosmochimica Acta 51*(12), 3193–9.

Magini, M. (1979). Solute structuring in aqueous iron(III) sulphate solutions. Evidence for the formation of iron(III) sulphate complexes. *Journal of Chemical Physics 70*(1), 317–324.

Magini, M. and T. Radnai (1979). X-ray diffraction study of ferric chloride solutions and hydrated melt. Analysis of the iron (III) chloride complexes formation. *Journal of Chemical Physics 71*(11), 4255–4262.

Majima, H., Y. Awakura, T. Hirato, and T. Tanaka (1985). The leaching of chalcopyrite in ferric chloride and ferric sulfate solutions. *Canadian Metallurgical Quarterly 24*(4), 283–291.

McCarron, J. J., G. W. Walker, and A. N. Buckley (1990). An X-ray photoelectron spectroscopic investigation of chalcopyrite and pyrite surfaces after conditioning in sodium sulfide solutions. *International Journal of Mineral Processing 30*(1-2), 1–16.

McIntyre, N. and G. Zetaruk, D (1977). X-ray photoelectron spectroscopic studies of iron oxides. *Analytical Chemistry 49*(11), 1521–1529.

McIntyre, N. S. and M. G. Cook (1975). X-ray photoelectron sturies on some oxides and hydroxides of cobalt, nickel and copper. *Analytical Chemistry 47*(13), 2208–2213.

McMillan, R. S., D. J. MacKinnon, and J. E. Dutrizac (1982). Anodic dissolution of n-type and p-type chalcopyrite. *Journal of Applied Electrochemistry 12*, 743–757.

Mielczarski, J. (1987). XPS study of ethyl xanthate adsorption on oxidized surface of cuprous sulfide. *Journal of Colloid and Interface Science 120*(1), 201–209.

Mielczarski, J. A., J. M. Cases, M. Alnot, and J. J. Ehrhardt (1996). Xps characterization of chalcopyrite, tetrahedrite and tennantite surface products after different conditioning. 1. aqueous solution at ph 10. *Langmuir 12*(10), 2519–2530.

Mikhlin, Y., Y. Tomashevich, I. Asanov, A. Okotrub, V. Varnek, and D. Vyalikh (2004). Spectroscopic and electrochemical characterization of the surface layers of chalcopyrite ($CuFeS_2$) reacted in acidic solutions. *Applied Surface Science 225*(1-4), 395–409.

Miller, J. D. and H. Q. Portillo (1981). Silver catalysis in ferric sulfate leaching of chalcopyrite. *Proceedings of the 13th International Mineral Processing Congress (Warsaw, Poland, 1979) 1*, 691–741.

Mishra, K. K. and K. Osseo-Asare (1988). Aspects of the interfacial electrochemistry of semiconductor pyrite (FeS_2). *Journal of the Electrochemical Society 135*(10), 2502–9.

Mizoguchi, T., Y. Takei, and T. Okabe (1976). The chemical behavior of low valence sulfur compounds. X. Disproportionation of thiosulfate, trithionate, tetrathionate and sulfite under acidic conditions. *Bulletin of the Chemical Society of Japan 49*(1), 70–5.

Morin, F. J. (1954). Electrical properties of α-Fe_2O_3. *Physical Review 93*(6), 1195–1199.

Morrison, S. R. (1977). *The Chemical Physics of Surfaces* (1st ed.). New York: Plenum Press.

Morrison, S. R. (1978). Study of semiconductors using electrochemical techniques. *Journal of Vacuum Science and Technology 15*(4), 1417–21.

Moses, C., D. Nordstrom, J. Herman, and A. Mills (1987). Aqueous pyrite oxidation by dissolved oxygen and by ferric ion. *Geochimica et Cosmochimica Acta 51*, 1561–1571.

Mulay, L. N. and P. W. Selwood (1955). Hydrolysis of Fe^{3+}: Magnetic and spectrophotometric studies on ferric perchlorate solutions. *Journal of the American Chemical Society 77*, 2693–701.

Munoz, P. B., J. D. Miller, and M. E. Wadsworth (1979). Reaction mechanism for the acid ferric sulfate leaching of chalcopyrite. *Metallurgical Transactions B 10*, 149–158.

Music, S., Z. Orehovec, S. Popovic, and I. Czako-Nagy (1994). Structural properties of precipitates formed by hydrolysis of Fe^{3+} ions in $Fe_2(SO_4)_3$ solutions. *Journal of Materials Science 29*(8), 1991–8.

Music, S., S. Popovic, Z. Orehovec, and I. Czako-Nagy (1993). Properties of precipitates formed by hydrolysis of iron(3+) ions in ammonium iron sulfate [$NH_4Fe(SO_4)_2$] solutions. *Journal of Colloid and Interface Science 160*(2), 479–82.

Nakai, I., Y. Sugitani, K. Nagashima, and Y. Niwa (1978). X-ray photoelectron spectroscopic study of copper minerals. *Jounral of Inorganic and Nuclear Chemistry 40*, 789–791.

Nava, D. and I. Gonzalez (2006). Electrochemical characterization of chemical species formed during the electrochemical treatment of chalcopyrite in sulfuric acid. *Mineralogical Journal 51*(25), 5295–5303.

Oguchi, T., K. Sato, and T. Teranishi (1980). Optical reflectivity spectrum of a $CuFeS_2$ single crystal. *Journal of the Physical Society of Japan 48*(1), 123–128.

Olsen, L. C., R. C. Bohara, and M. W. Urie (1979). Explanation for low-efficiency Cu_2O Schottky-barrier solar cells. *Applied Physics Letters 34*(1), 47–49.

Opahle, I., K. Koepernik, and H. Eschrig (1999). Full potential band structure calculation of iron pyrite. *Physical Review B 60*(20), 14035–14041.

Parker, A., C. Klauber, M. Stott, H. R. Watling, and W. van Bronswijk (2003). An X-ray photoelectron spectroscopy study of the mechanism of microbially assisted dissolution of chalcopyrite. In *15th International Biohydrometallurgical Symposium - Biohydrometallurgy: A sustainable technology in evolution.*, Athens, Greece.

Parker, A. J., R. L. Paul, and G. P. Power (1981). Electrochemical aspects of leaching copper from chalcopyrite in ferric and cupric salt solutions. *Australian Journal of Chemistry 34*, 13–34.

Peak, D., R. G. Ford, and D. L. Sparks (1999). An in situ ATR-FTIR investigation of sulfate bonding mechanisms on goethite. *Journal of Colloid and Interface Science 218*(1), 289–299.

Peisert, H., T. Chasse, P. Streubel, A. Meisel, and R. Szargan (1994). Relaxation energies in XPS and XAES of solid sulfur compounds. *Journal of Electron Spectroscopy and Related Phenomena 68*(1-4), 321–8.

Plumb, J. J., R. Muddle, and P. D. Franzmann (2008). Effect of pH on rates of iron and sulfur oxidation by bioleaching organisms. *Minerals Engineering 21*(1), 76–82.

Poulston, S., P. M. Parlett, P. Stone, and M. Bowker (1996). Surface oxidation and reduction of CuO and Cu_2O studied using XPS and XAES. *Surface and Interface Analysis 24*(12), 811–820.

Pratesi, G. and C. Cipriani (2000). Selective depth analyses of the alteration products of bornite, chalcopyrite and pyrite performed by XPS, AES, RBS. *European Journal of Mineralogy 12*(2), 397–409.

Pridmore, D. F. and R. T. Shuey (1976). The electrical resistivity of galena, pyrite and chalcopyrite. *American Mineralogist 61*, 248–259.

Rabai, G. and I. Epstein (1992). Equilibria and kinetics of the fast interaction between copper (II) and thiosulfate ions in aqueous solution. *Inorganic Chemistry 31*, 3239–3242.

Raj, D., K. Chandra, and S. P. Puri (1968). Mössbauer studies of chalcopyrite. *Journal of the Physical Society of Japan 24*(1), 39–41.

Reedy, B. J., J. K. Beattie, and R. T. Lowson (1991). A vibrational spectroscopic oxygen-18 tracer study of pyrite oxidation. *Geochimica et Cosmochimica Acta 55*(6), 1609–14.

Remond, G., P. Picot, R. Giraud, P. H. Holloway, and P. Ruzakowski (1983). Contribution of electron spectroscopies to X-ray spectrometery applied to the geosciences. *Scanning Electron Microscopy 4*, 1683–1706.

Rimstidt, J. D., J. A. Chermak, and P. M. Gagen (1994). Rates of reaction of galena, sphalerite, chalcopyrite, and arsenopyrite with Fe(III) in acidic solutions. In C. N. Alpers and D. W. Blowes (Eds.), *Environmental Geochemistry of Sulfide Oxidation*, Volume 550, pp. 2–13. Washington, D.C.: American Chemical Society.

Roberts, R. F. (1974). X-ray photoelectron spectroscopic characterization of copper oxide surfaces treated with benzotriazole. *Journal of Electron Spectroscopy and Related Phenomena 4*, 273–291.

Robles, E., G. Miller, and D. Readett (1994). Recent experience in bacterial assisted heap leaching of copper ores in Chile. In J. B. Hiskey (Ed.), *An analysis of in-situ solution mining techniques in bioremediation.*

Roman, R. J. and B. R. Benner (1973). The dissolution of copper concentrates. *Minerals Science and Engineering 5*(1), 3–24.

Romand, M., M. Roubin, and J. P. Deloume (1978). ESCA studies of some copper and silver selenides. *Journal of Electron Spectroscopy and Related Phenomena 13*, 229–242.

Rupp, H. and U. Weser (1976). X-ray photoelectron spectroscopy of copper(II), copper(I) and mixed valence systems. *Bioinorganic Chemistry 6*, 45–59.

Sacher, E. and K. J. Laidler (1963). A theory of nonadiabatic electron transfer in aqueous solution. *Transactions of the Faraday Society 59*, 396–402.

Sandstrom, A., A. Shchukarev, and J. Paul (2005). XPS characterisation of chalcopyrite chemically and bio-leached at high and low redox potential. *Minerals Engineering 18*(5), 505–515.

Sapieszko, R. S. (1977). *Monodispersed basic ferric sulfate suspensions - Model systems for atmospheric corrosion studies.* Ph. D. thesis, Clarkson College of Technology.

Sasaki, K., M. Tsunekawa, T. Ohtsuka, and H. Konno (1995). Confirmation of a sulfur-rich layer on pyrite after oxidative dissolution by Fe(III) ions around pH 2. *Geochimica et Cosmochimica Acta 59*(15), 3155–8.

Sato, K. and T. Teranishi (1976). Optical absorption spectrum of a thin chalcopyrite ($CuFeS_2$) film. *Journal of the Physical Society of Japan 40*(1), 297–8.

Scofield, J. H. (1976). Hartree-Slater subshell photoionization cross-sections at 1254 and 1487 eV. *Journal of Electron Spectroscopy and Related Phenomena 8*(2), 129–137.

Seah, M. P. (1981). A quantitative framework for the analysis of surfaces by AES and XPS. *Analusis 9*(5), 171–80.

Seah, M. P. (1989). Post-1989 calibration energies for X-ray photoelectron spectrometers and the 1990 Josephson constant. *Surface and Interface Analysis 14*, 488.

Sharp, J. H., G. W. Brindley, and B. N. N. Achar (1966). Numerical data for some commonly used solid state reaction equations. *Journal of the American Ceramic Society 49*(7), 379–82.

Shive, J. N. (1959). *Properties, physics and design of semiconductor devices*. Princeton, N. J.: Nostrand.

Shuey, R. T. (1975). *Semiconducting Ore Minerals* (1st ed.). New York: Elsevier Scientific Publishing Company.

Siriwardane, R. V. (1989). Interaction of SO_2 and O_2 mixtures with CaO and sodium deposited on CaO. *Journal of Colloid and Interface Science 132*(1), 200–209.

Smart, R. S. C., W. M. Skinner, and A. R. Gerson (1999). XPS of sulphide mineral surfaces: Metal-deficient, polysulphides, defects and elemental sulphur. *Surface and Interface Analysis 28*, 101–105.

Steiner, P., S. Hufner, A. Jungmann, V. Kinsinger, and I. Sander (1989). Photoemision valence band spectra and electronic density of states in copper oxides and copper based ceramic super-conductors. *Zeitschrift für Physik B Condensed Matter 74*, 173–182.

Steudel, R. (1996). Mechanism for the formation of elemental sulfur from aqueous sulfide in chemical and microbiological desulfurization processes. *Industrial and Engineering Chemistry Research 35*, 1417–1423.

Stott, M. B., D. C. Sutton, H. Watling, and P. D. Franzmann (2003). Comparative leaching of chalcopyrite by selected acidophilic bacteria and archaea. *Geomicrobiology Journal 20*(3), 215–230.

Sullivan, J. D. (1933). Chemical and physical features of copper leaching. *Transactions of the American Institute of Mining, Metallurgical Engineers 106*, 515–546.

Tang, H., H. Berger, P. E. Schmid, F. Levy, and G. Burri (1993). Photoluminescence in TiO_2 anatase single crystals. *Solid State Communications 87*(9), 847–850.

Tanuma, S., C. J. Powell, and D. R. Penn (1991). Calculations of electron inelastic mean free paths. II. Data for 27 elements over the 50-2000 eV range. *Surface and Interface Analysis 17*, 911–926.

Temesghen, W. and P. M. A. Sherwood (2002). Analytical utility of valence band X-ray photoelectron spectroscopy of iron and its oxides, with spectral interpretation by cluster and band structure calculations. *Analytical and Bioanalytical Chemistry 373*(7), 601–608.

Termes, S. C., A. N. Buckley, and R. D. Gillard (1987). 2p electron-binding energies for the sulfur-atoms in metal polysulfides. *Inorganica Chimica Acta 126*(1), 79–82.

Thatcher, C. J. (1904). Electrolytic oxidation of sodium thiosulphate and the mechanism of the process. *Zeitschrift für Physikalische Chemie, Stoichiometrie und Verwandtschaftslehre 47*, 641–720.

Tuckerman, M. E., D. Marx, and M. Parrinello (2002). The nature and transport mechanism of hydrated hydroxide ions in aqueous solution. *Nature 417*(6892), 925–929.

Vasquez, R. P. (1998). Cu_2O by XPS. *Surface Science Spectra 5*(4), 257–261.

Vaughan, D. J. (1995). Mineral surfaces: An overview. *Mineral Surfaces*, 1–16.

Vaughan, D. J., U. Becker, and K. Wright (1997). Sulphide mineral surfaces: Theory and experiment. *International Journal of Mineral Processing 51*, 1–14.

Velasquez, P., D. Leinen, J. Pascual, J. R. Ramos-Barrado, R. Cordova, H. Gomez, and R. Schrebler (2001). XPS, SEM, EDX and EIS study of an electrochemically modified electrode surface of natural chalcocite (Cu_2S). *Journal of Electroanalytical Chemistry 510*, 20–28.

Velasquez, P., D. Leinen, J. Pascual, J. R. Ramos-Barrado, P. Grez, H. Gomez, R. Schrebler, R. Del Rio, and R. Cordova (2005). A chemical, morphological, and

electrochemical (XPS, SEM/EDX, CV, and EIS) analysis of electrochemically modified electrode surfaces of natural chalcopyrite ($CuFeS_2$) and pyrite (FeS_2) in alkaline solutions. *Journal of Physical Chemistry B 109*(11), 4977–4988.

Wadsworth, M. E. and J. D. Miller (1979). Hydrometallurgical processes. In H. J. Sohn and M. E. Wadsworth (Eds.), *Rate Processes of Extractive Metallurgy*, pp. 133–241. New York: Plenum Press.

Wagner, C. D. (1975). Chemical shifts of Auger lines, and the Auger parameter. *Faraday Discussions of the Chemical Society 60*, 291–300.

Wagner, C. D. (1978). X-ray photoelectron spectroscopy with X-ray photons of higher energy. *Journal of Vacuum Science and Technology 15*(2), 518–523.

Wagner, C. D. and J. A. Taylor (1982). Contributions to screening in the solid state by electron systems of remote atoms: Effects of photoelectron and Auger transitions. *Journal of Electron Spectroscopy and Related Phenomena 28*, 211–217.

Wallis, T. L. and G. F. Chlumsky (1999). Economic considerations for SX/EW operations. In G. V. Jergensen (Ed.), *Copper leaching, solvent extraction, and electrowinning technology*. Littleton: Society for Mining, Metallurgy and Exploration, Inc.

Walter-Levy, L. and E. Quemeneur (1968). Thermolysis of basic ferric sulfates. *Bulletin de la Societe Chimique de France* (2), 495–503.

Warren, G. W. (1978). *The electrochemical oxidation of $CuFeS_2$.* Ph. D. thesis, University of Utah.

Warren, G. W., H. J. Sohn, M. E. Wadsworth, and T. G. Wang (1985). The effect of electrolyte composition on the cathodic reduction of chalcopyrite ($CuFeS_2$). *Hydrometallurgy 14*(2), 133–49.

Warren, G. W., M. E. Wadsworth, and S. M. El-Raghy (1982). Anodic behavior of chalcopyrite in sulfuric acid. *Hydrometallurgy '82: Research, Development and Plant Practice.*, 261–275.

Warren, I. H. (1958). A study of acid pressure leaching of chalcopyrite, chalcocite, and covellite. *Australian Journal of Applied Science 9*, 36–51.

Wendt, H. (1962). Fast ion reactions in solutions. III. The kinetics of the formation of the binuclear iron(III) hydroxo complex $Fe(OH)_2Fe^{4+}$. *Zeitschrift für Elektrochemie und Angewandte Physikalische Chemie 66*(3), 235–9.

Williamson, M. and J. Rimstidt (1993). The rate of decomposition of the ferric-thiosulfate complex in acidic aqueous solutions. *Geochimica et Cosmochimica Acta 57*, 3555–3561.

Williamson, M. A. (1992). *Thermodynamic and kinetic studies of sulfur geochemistry.* Ph. D. thesis, Virginia Polytechnic Institute and State University.

Yakovlev, Y. B., F. Y. Kul'ba, A. G. Pus'ko, and M. N. Gerchikova (1977). Hydrolysis of iron(III) sulfate in zinc sulfate solutions at 25, 50, and 80 degrees C. *Zhurnal Neorganicheskoi Khimii 22*(1), 53–6.

Yin, L., T. Tsang, I. Adler, and E. Yellin (1972). L-S coupling interpretation of high-resolution LMM Auger spectra of Cu and Zn. *Journal of Applied Physics 43*(8), 3464–3467.

Yin, Q., G. H. Kelsall, D. J. Vaughan, and K. E. R. England (1995). Atmospheric and electrochemical oxidation of the surface of chalcopyrite ($CuFeS_2$). *Geochimica et Cosmochimica Acta 59*(6), 1091–1100.

Yu, X. R., F. Liu, Z. Y. Wang, and Y. Chen (1990). Auger parameters for sulfur-containing-compounds using a mixed aluminum silver excitation source. *Journal of Electron Spectroscopy and Related Phenomena 50*(1-2), 159–166.

Zachwieja, J. B., J. J. McCarron, G. W. Walker, and A. N. Buckley (1989). Correlation between the surface-composition and collectorless flotation of chalcopyrite. *Journal of Colloid and Interface Science 132*(2), 462–468.

Appendices

Appendix A

XPS analysis of standards

The lineshapes, binding energies and spectral intensity ratios of a series of standards were examined to assist interpretation of spectra from chalcopyrite samples after oxidative dissolution. These standards included copper sulphides and oxide, iron oxides, iron sulphates and sulphur-oxygen salts. The quality of the standards was compared with reported studies, with particular attention to the S 2p, Fe 2p, Cu 2p and O 1s spectra. In addition to binding energies, binding energy separations were compared, although this was complicated by variation in the data processing and the sample quality. All spectra of insulating standards presented in this study have been aligned according to C 1s spectra (284.60 eV). The spectral intensity ratios observed for each standard were compared with intensity ratios predicted using the IMFP and spectrometer calculations outlined in Section 5.5.1.

A.1 Copper sulphides and oxide

In addition to chalcopyrite (Section 5.3), bornite, covellite, chalcocite and cuprite have been analysed. The monovalent copper in these standards is consistent with the monovalent copper observed and reported for oxidised chalcopyrite. The quality of these standards is important because bornite, covellite and cuprite were used for Cu $L_3M_{4,5}M_{4,5}$ analysis (Appendices D).

A.1.1 Bornite (Cu_5FeS_4)

A.1.1.1 S 2p spectrum

The observed S 2p spectrum lineshape (Figure A.1) compares favourably with reported spectra (Buckley et al., 1984); however, no fitting of the spectral envelope has been reported. The observed spectrum has been fitted with two peaks in a ratio of 3 to 1, in accordance with the three equivalent sulphur atoms (Figure A.2). The background subtraction was not entirely successful, creating a dip at $\sim$ 159 eV, but the peak positions and widths do not appear significantly affected.

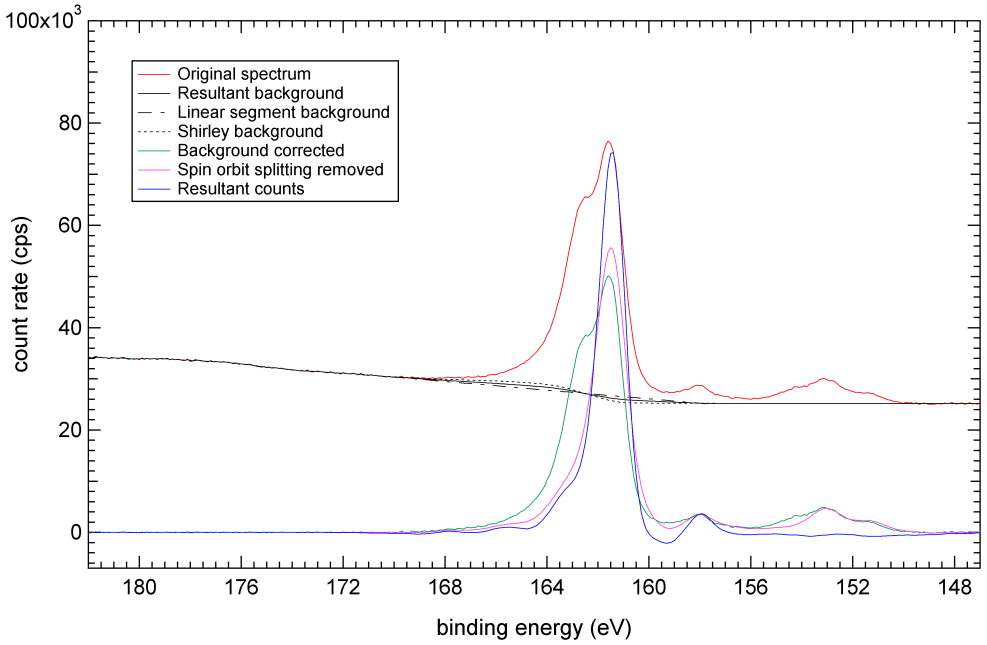

Figure A.1: *S 2p spectrum of the bornite standard.*

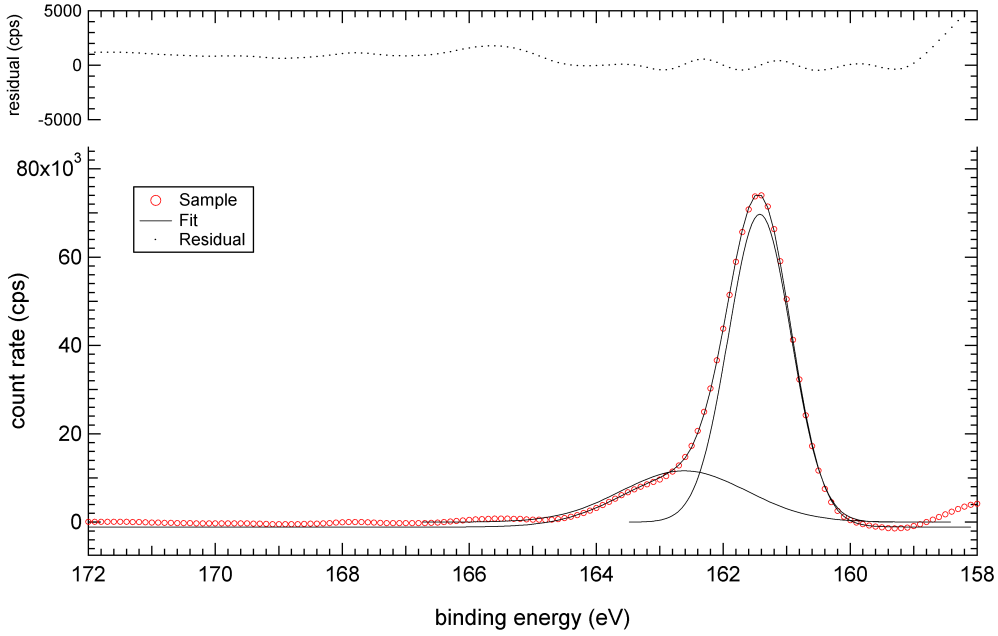

Figure A.2: *Fit of the S 2p spectrum of the bornite standard.*

The absence of fitting and reports of only one peak makes comparisons of S 2p binding energies difficult. Nonetheless, the observed S $2p_{3/2}$ binding energies (161.42 and 162.62 eV) are bisected by the reported energies (Table A.1). The Cu $2p_{3/2}$ to S $2p_{3/2}$ binding energy separation (770.78 eV) is similarly affected.

Table A.1: *Binding energies (eV) of bornite standards.*

Cu $2p_{3/2}$	**Fe $2p_{3/2}$**	**S $2p_{3/2}$**	**Cu $2p_{3/2}$ - S $2p_{3/2}$**	**Reference**
932.20	708.12	161.42, 162.62	770.78	This study
931.85	-	162.09	769.76	Clifford et al. (1975)
932.1	-	161.6	770.5	Nakai et al. (1978)
932.5*	708.2	162.0*	770.5	Buckley et al. (1984)

*Energies interpreted from the reported spectra by the author.

The peak at lower binding energy to the main sulphide peak is attributed to Si 2s from quartz (Figure A.3).

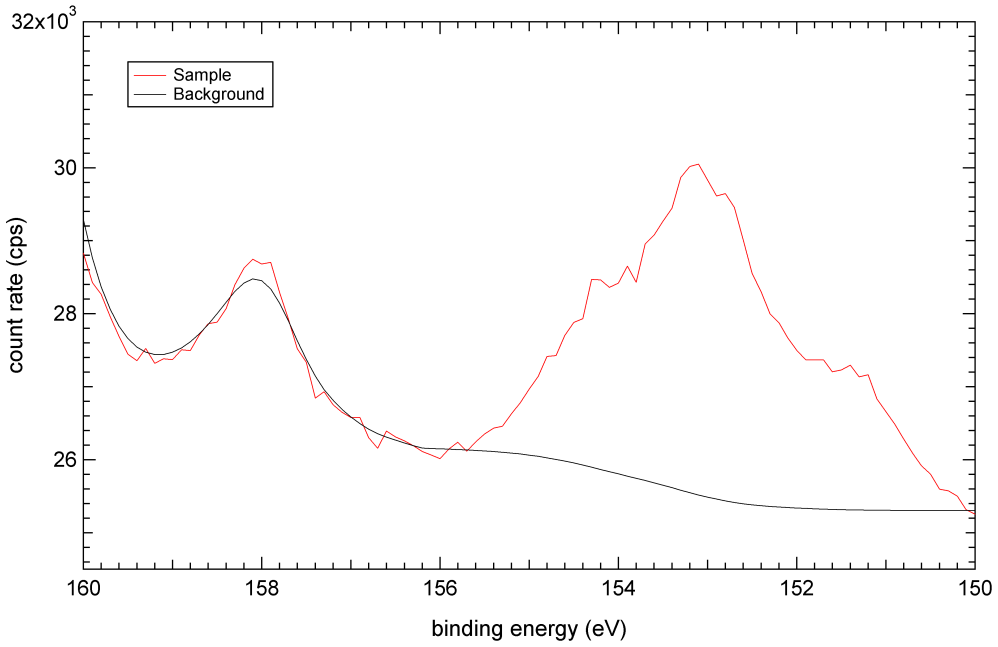

Figure A.3: *Si 2s spectrum of the bornite standard.*

A.1.1.2 Fe 2p spectrum

The observed Fe 2p spectrum lineshape (Figure A.4) displays greater definition of the main peak at 708.12 eV than the spectrum reported by Buckley et al. (1984), despite their attempts to limit oxidation by abrading the sample under liquid nitrogen. Sputtering of bornite samples by Buckley et al. (1984) and Pratesi and Cipriani (2000) also diminished the definition of the peak at 708.2 eV. Despite the lower definition of the reported spectra, the observed Fe 2p binding energy compares favourably with reported energies (Table A.1).

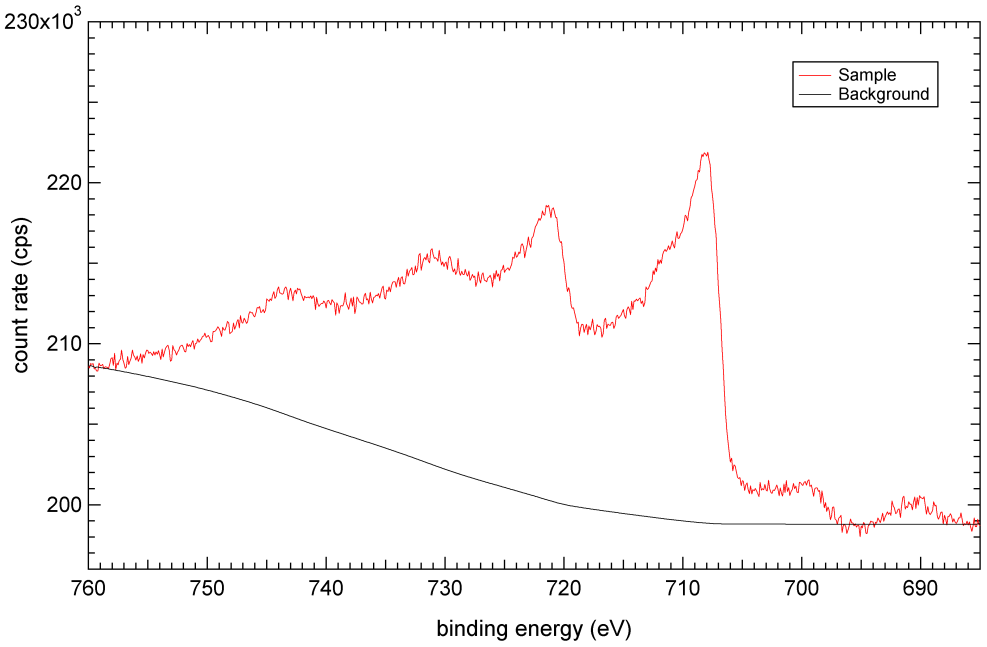

Figure A.4: *Fe 2p spectrum of the bornite standard.*

A.1.1.3 Cu 2p spectrum

The observed Cu 2p spectrum lineshape compares favourably with reported spectra (Buckley et al., 1984) and is consistent with monovalent copper because of the absence of satellite structure (Figure A.5). The Cu $2p_{3/2}$ binding energy (932.20 eV) also compares favourably with reported energies (Table A.1).

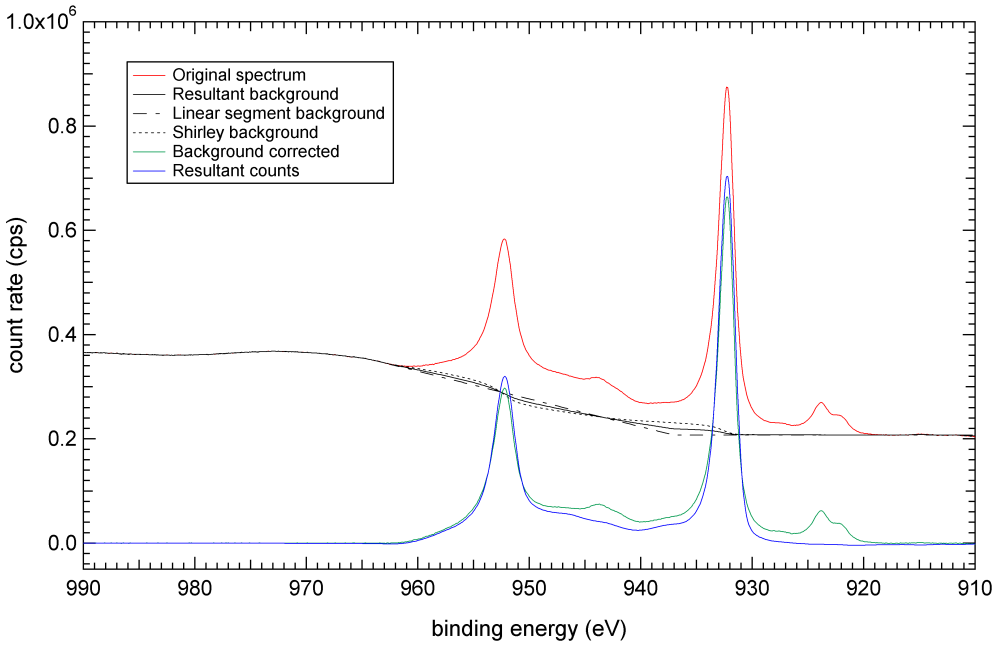

Figure A.5: *Cu 2p spectrum of the bornite standard.*

A.1.1.4 O 1s spectrum

The observed O 1s spectrum lineshape (Figure A.6) reveals minimal oxidation of the sample. The observed spectrum contains additional peaks to the spectrum reported by Buckley et al. (1984), but the low intensities make identification difficult. The observed peaks are speculatively attributed to oxide/oxyhydroxide associated with the mineral surface, adsorbed water and oxidised hydrocarbons.

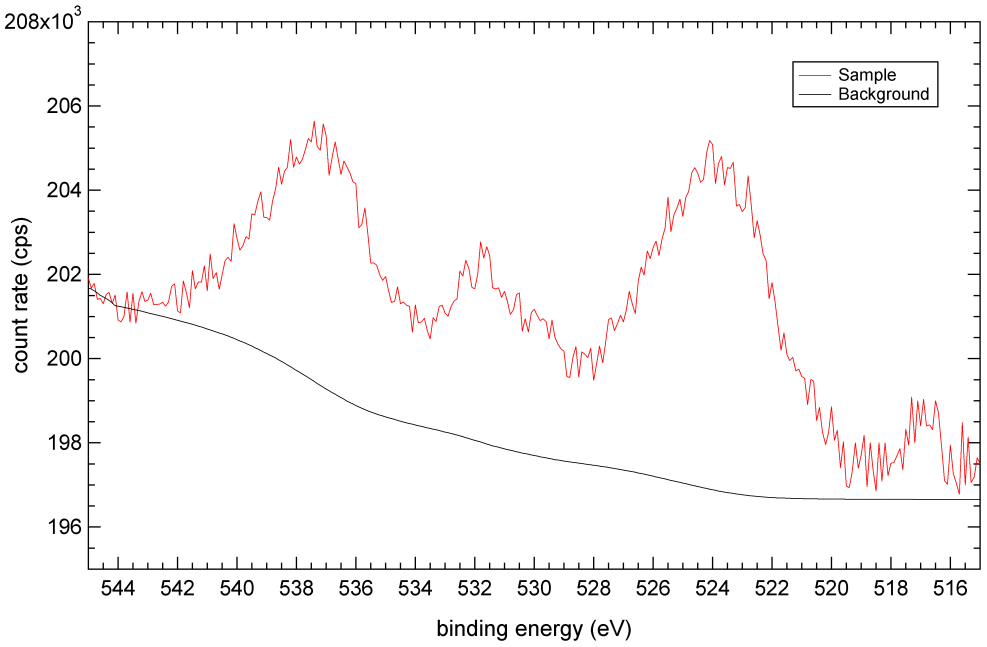

Figure A.6: *O 1s spectrum of the bornite standard.*

A.1.1.5 Spectral intensity ratios

The observed and predicted Cu 2p:S 2p and Fe 2p:S 2p spectral intensity ratios do not compare favourably because of an excess of copper (Table A.2). This copper excess (and minor iron deficiency) is attributed to additional copper sulphide phases such as chalcopyrite, chalcocite or digenite intergrowing with bornite during formation (Shuey, 1975). Bornite has not been used to adjust the Cu 2p or Fe 2p cross sections because of the excess of copper (Section 5.5.1.3).

Table A.2: *Observed and predicted Cu 2p:S 2p and Fe 2p:S 2p spectral intensity ratios of the bornite standard.*

	Cu 2p:S 2p	**Fe 2p:S 2p**
Observed	29.7	3.78
Predicted	18.1	4.10

A.1.2 Covellite (CuS)

A.1.2.1 S 2p spectrum

The observed S 2p spectrum lineshape (Figure A.7) compares favourably with reported spectra (Leloup et al., 1993; Kostikov and Korolkov, 1998); however, the number of peaks used to fit the spectral envelope and the implications of the fit on the structure remains a source of conjecture. The observed S 2p spectrum has been fitted with two peaks in a ratio of 2 to 1 (Figure A.8), in accordance with the proposed structure of $Cu_3^+(S_2)^{2-}S^-$ (Folmer and Jellinek, 1980). Although the fit is noticeably improved with three peaks (Figure A.9), as reported by Leloup et al. (1993), there is no structural basis for this interpretation. Kostikov and Korolkov (1998) proposed the structure of $Cu_2S.Cu_2S_3$, with two inequivalent sulphur atoms in a 3:1 ratio, but no curve fitting was presented to support the proposal.

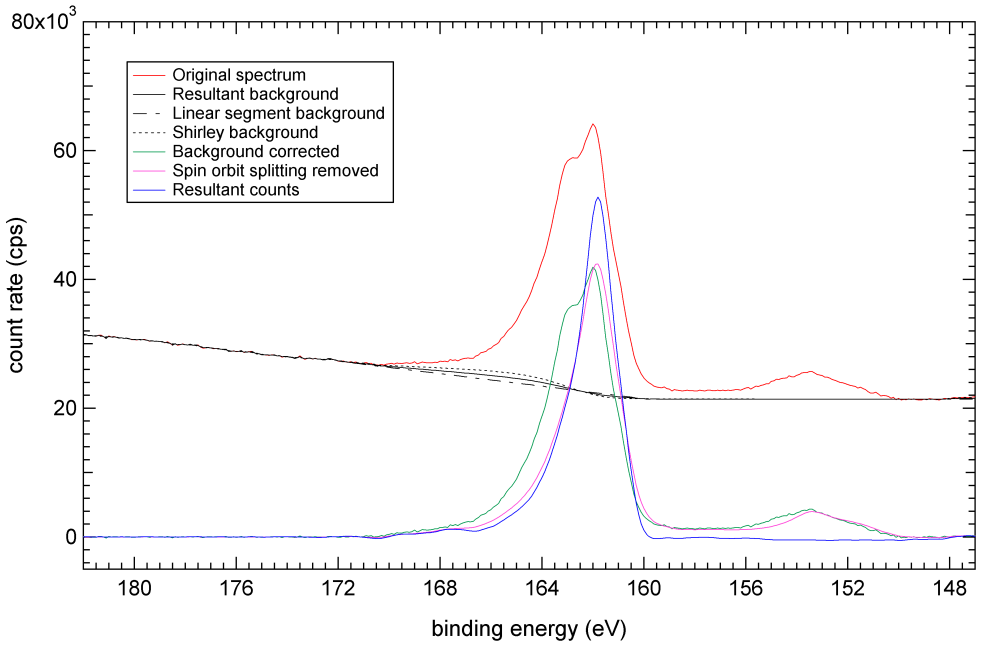

Figure A.7: *S 2p spectrum of the covellite standard.*

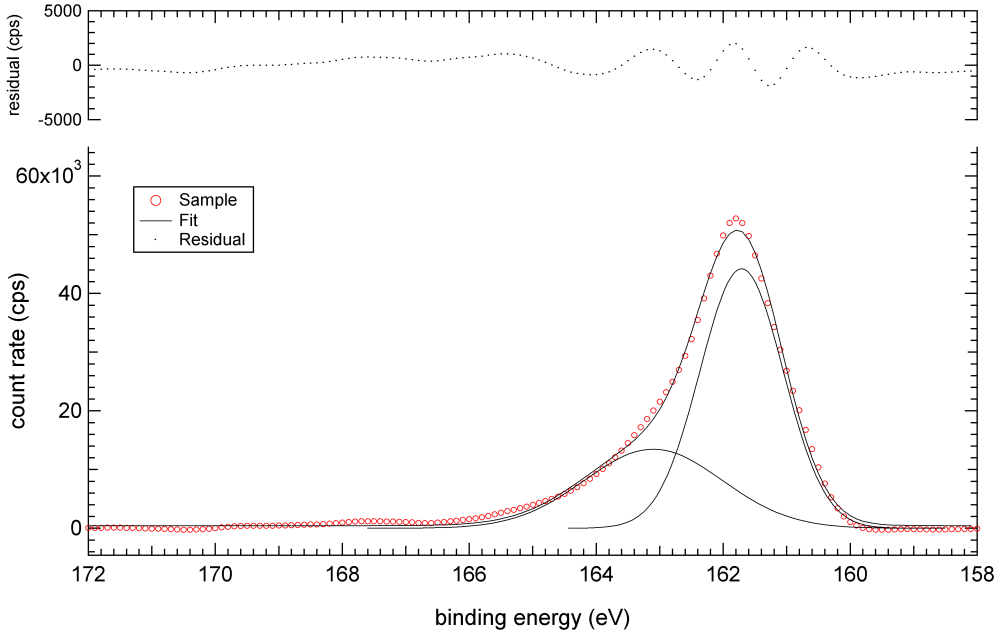

Figure A.8: *Fit of the S 2p spectrum of the covellite standard: two peaks.*

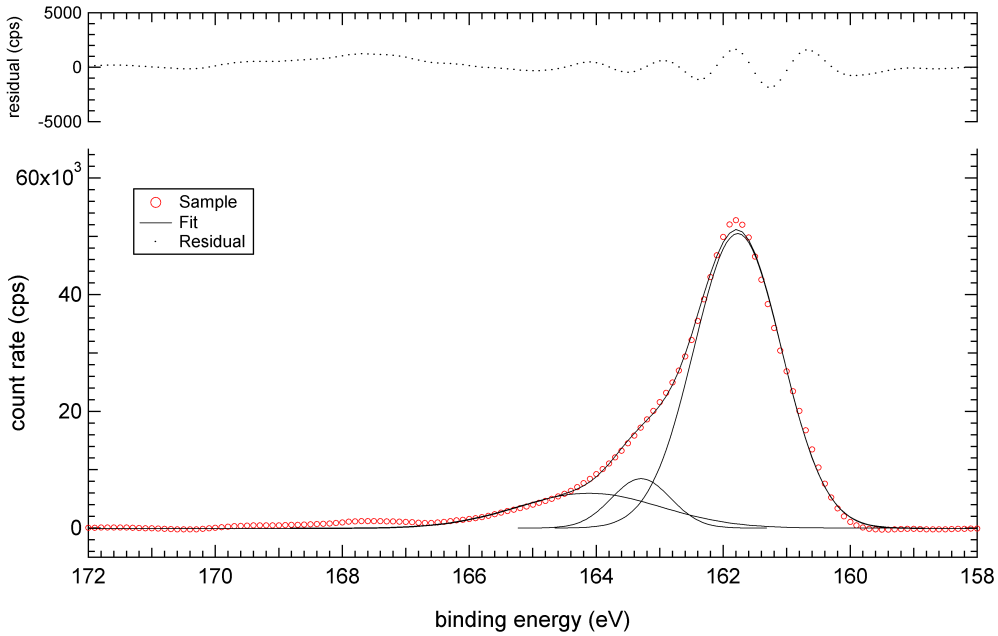

Figure A.9: *Fit of the S 2p spectrum of the covellite standard: three peaks.*

The varying number of reported peaks fitted to the S 2p spectrum makes comparisons of binding energies difficult. Nonetheless, the energies fitted in this study (161.71 and 163.10 eV) are within the range reported (Table A.3). The observed Cu $2p_{3/2}$ to S $2p_{3/2}$ binding energy separations (770.25 and 768.86 eV) compare favourably with Rupp and Weser (1976) and Leloup et al. (1993), although the binding energies suggest charge shifting may have occurred.

Table A.3: *Binding energies (eV) of covellite standards.*

Cu $2p_{3/2}$	**S $2p_{3/2}$**	**Cu $2p_{3/2}$ - S $2p_{3/2}$**	**Reference**
931.96	161.71, 163.10	770.25, 768.86	This study
931.6	161.5, 162.2	770.1, 769.4	Nakai et al. (1978)
931.7	162.3	769.4	Lianzhong (1987)
931.9	161.8	770.1	Gebhardt et al. (1986)
932.1	162.3	769.8	Brion (1980)
932.01	161.82, 164.12	770.19, 767.89	Clifford et al. (1975)
932.4	162.4	770.0	Chawla et al. (1992)
932.6	162.2, $\sim$ 163.5	770.4, 769.1	Leloup et al. (1993)
932.6	-	-	Romand et al. (1978)
932.9	162.7	770.2	Rupp and Weser (1976)
933.4	163.0	770.4	Rupp and Weser (1976)
-	162.5	-	Kelsall et al. (1992)

A.1.2.2 Cu 2p spectrum

The observed Cu 2p spectrum lineshape compares favourably with reported spectra (Rupp and Weser, 1976; Folmer and Jellinek, 1980; Lianzhong, 1987; Chawla et al., 1992; Leloup et al., 1993) and is consistent with monovalent copper because of the absence of satellite structure (Figure A.10). The Cu $2p_{3/2}$ binding energy (931.96 eV) also compares favourably with reported energies (Table A.3).

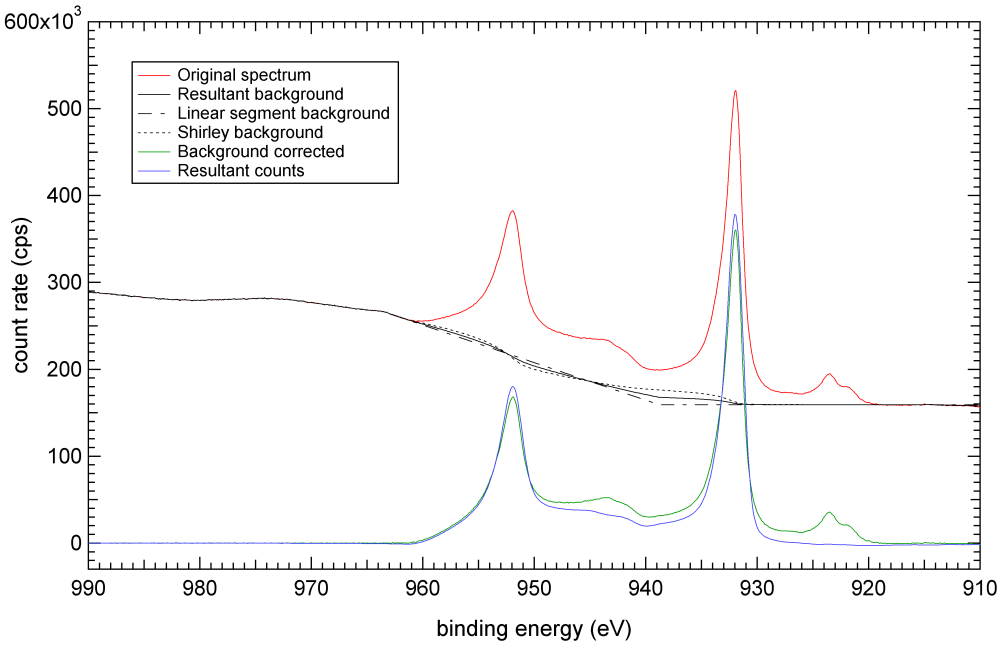

Figure A.10: *Cu 2p spectrum of the covellite standard.*

A.1.2.3 O 1s spectrum

The O 1s spectrum lineshape observed (Figure A.11) reveals minimal oxidation of the sample. The spectrum cannot be compared with reported spectra because of an absence of the latter. The observed peaks are speculatively attributed to oxide/oxyhydroxide associated with the mineral surface, adsorbed water and oxidised hydrocarbons.

A.1.2.4 Spectral intensity ratios

The observed and predicted Cu 2p:S 2p spectral intensity ratios of 14.9 and 14.5, respectively, compare favourably.

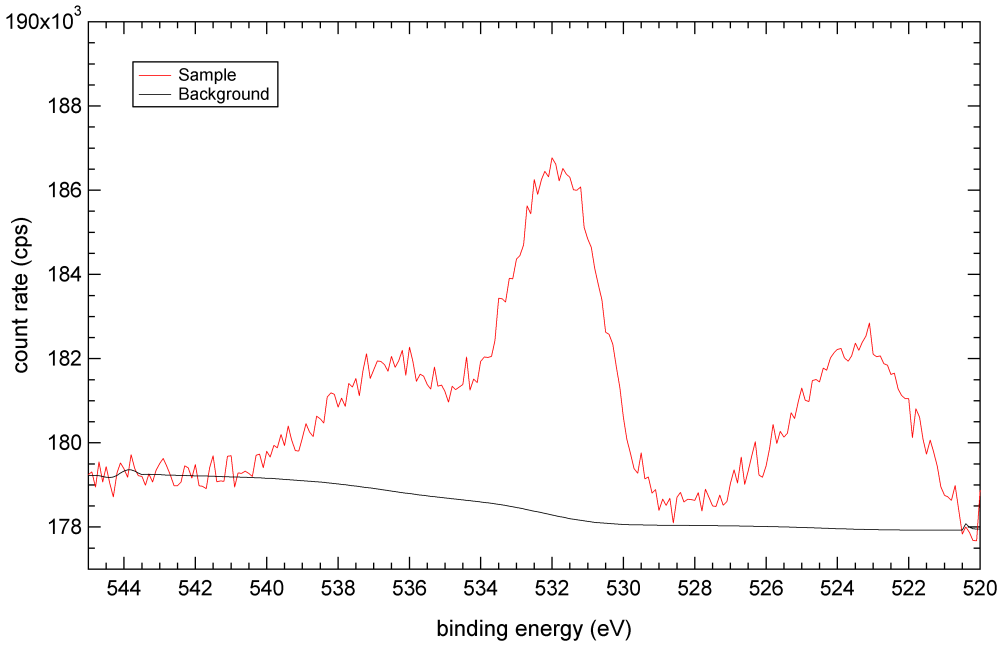

Figure A.11: *O 1s spectrum of the covellite standard.*

A.1.3 Chalcocite (Cu_2S)

A.1.3.1 S 2p spectrum

The observed S 2p spectrum lineshape (Figure A.12) compares favourably with reported spectra (Larson, 1974; Deroubaix and Marcus, 1992; Leloup et al., 1993; Kostikov and Korolkov, 1998; Velasquez et al., 2001). The observed spectrum has been fitted with one peak, in accordance with the proposed structure of Cu_2S having equivalent sulphur atoms (Figure A.13). All studies report only one peak, except Leloup et al. (1993) who reported two peaks and attribute them to S^{2-} (75 % of the intensity) and S_2^{2-} (25 % of the intensity). There is no evidence of sulphur assuming two oxidation states in this study.

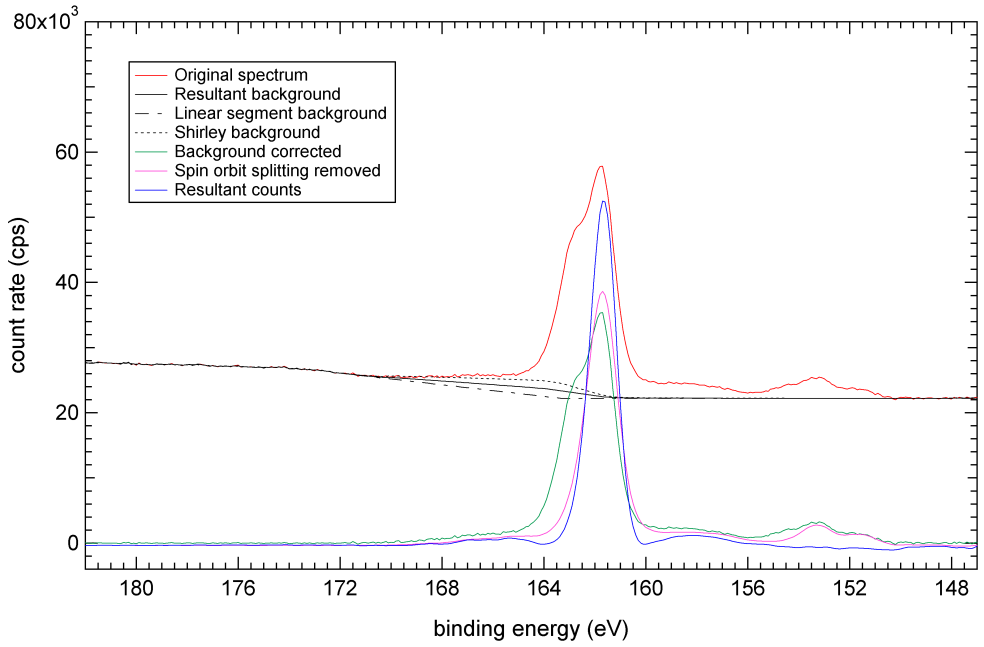

Figure A.12: *S 2p spectrum of the chalcocite standard.*

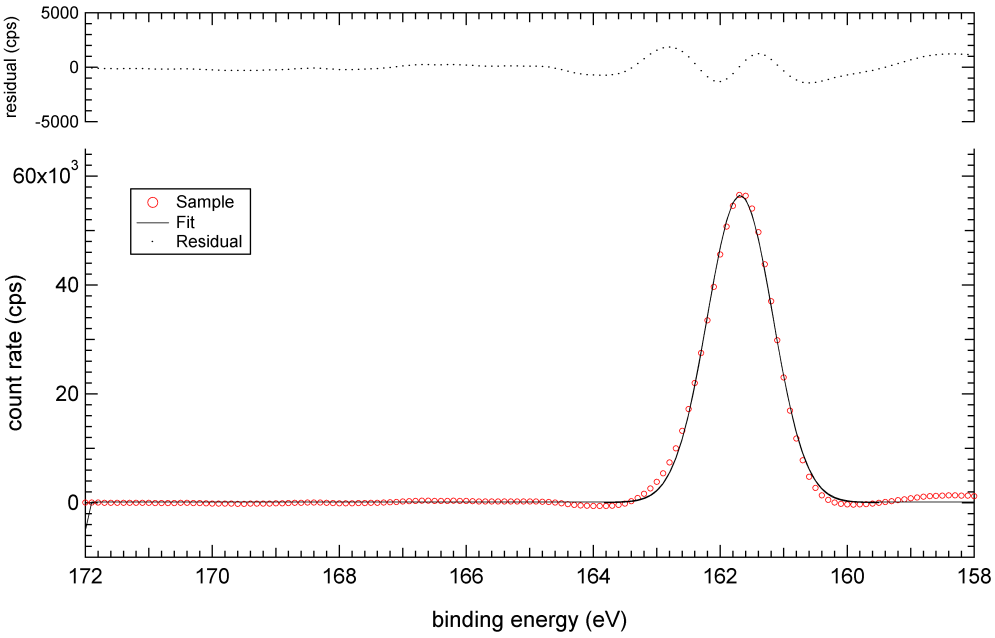

Figure A.13: *Fit of the S 2p spectrum of the chalcocite standard.*

The observed S $2p_{3/2}$ binding energy (161.69 eV) compares favourably with reported energies, although the reported range is quite broad (Table A.4). Additionally, the Cu $2p_{3/2}$ to S $2p_{3/2}$ binding energy separation (770.85 eV) also compares favourably with reported separations, although they too are quite broad.

Table A.4: *Binding energies (eV) of chalcocite standards.*

Cu $2p_{3/2}$	**S $2p_{3/2}$**	**Cu $2p_{3/2}$ - S $2p_{3/2}$**	**Reference**
932.45	161.69	770.85	This study
932.18	161.98	770.20	Clifford et al. (1975)
932.2	161.6	770.6	Nakai et al. (1978)
932.3	161.6	770.7	Gebhardt et al. (1986)
932.40	161.85	770.55	Brion (1980)
932.4	161.5	770.9	Mielczarski (1987)
932.5	161.7	770.7	Chawla et al. (1992)
932.8	162.8	770.0	Leloup et al. (1993)
932.9	161.9	771.0	Deroubaix and Marcus (1992)
934.9	163.8	771.1	Rupp and Weser (1976)
-	161.30	-	Yu et al. (1990)

A.1.3.2 Cu 2p spectrum

The observed Cu 2p spectrum lineshape (Figure A.14) compares favourably with reported spectra (Larson, 1974; Rupp and Weser, 1976; Folmer and Jellinek, 1980; Chawla et al., 1992; Leloup et al., 1993; Velasquez et al., 2001) and is consistent with monovalent copper because of the absence of satellite structure. The Cu $2p_{3/2}$ binding energy (932.45 eV) also compares favourably with reported energies (Table A.4).

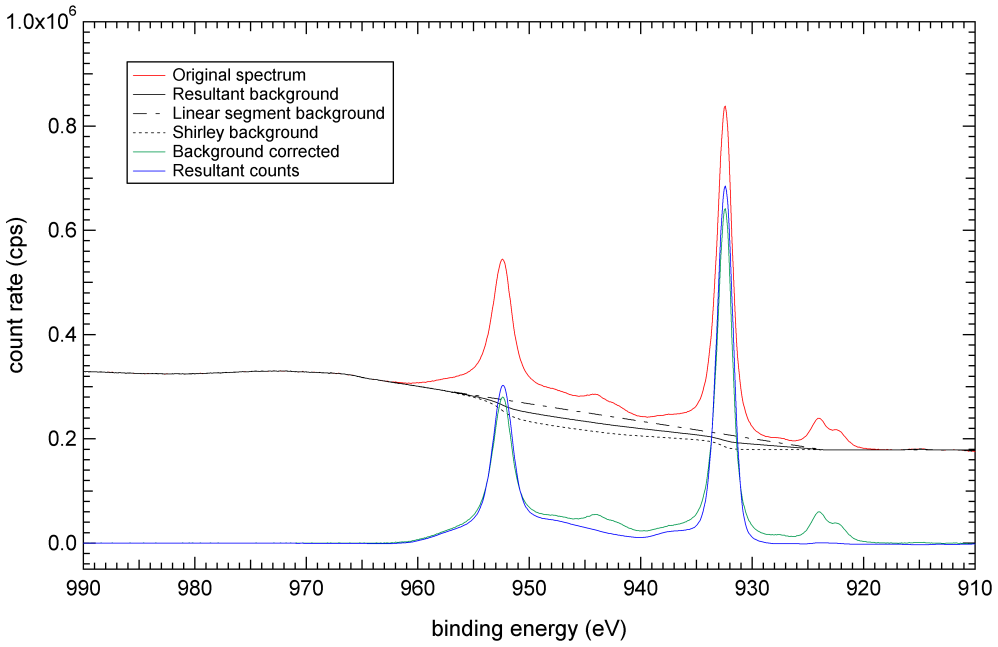

Figure A.14: *Cu 2p spectrum of the chalcocite standard.*

A.1.3.3 O 1s spectrum

The observed O 1s spectrum lineshape (Figure A.15) reveals considerable oxidation of the sample. In addition to the peak at $\sim$ 532 eV present in the spectrum reported by Mielczarski (1987), the observed spectrum displays peaks at $\sim$ 525 and $\sim$ 537 eV. The observed peaks are speculatively attributed to oxide/oxyhydroxide associated with the mineral surface, adsorbed water and oxidised hydrocarbons.

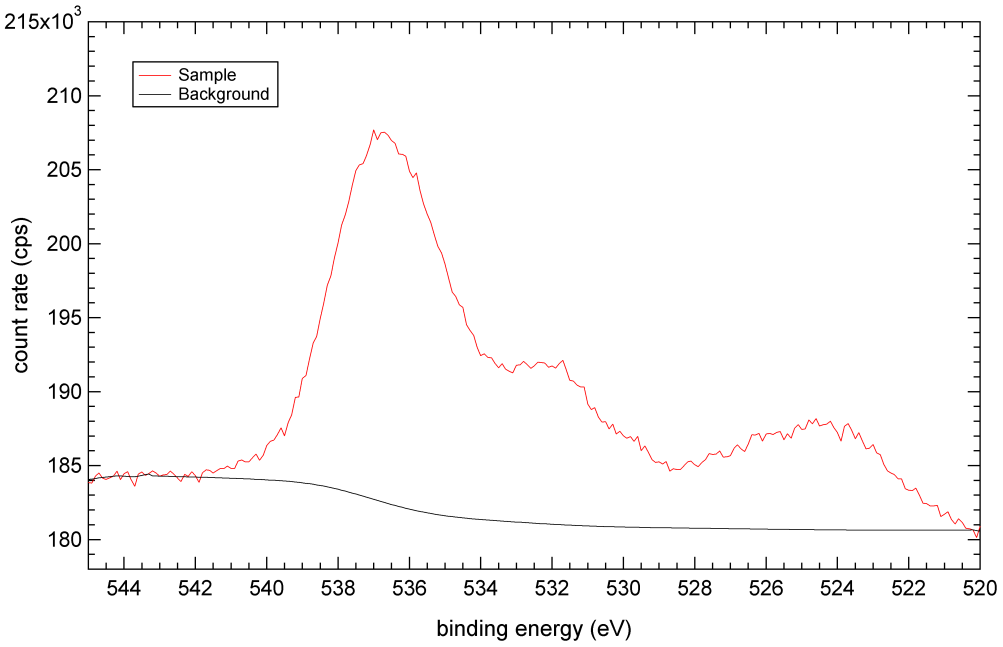

Figure A.15: *O 1s spectrum of the chalcocite standard.*

A.1.3.4 Spectral intensity ratios

The observed and predicted Cu 2p:S 2p spectral intensity ratios of 37.4 and 29.2, respectively, do not compare favourably because of an excess of copper. Although the copper excess may be due to the formation of cuprite, with the Cu 2p spectrum remaining consistent with monovalent copper and considerable intensity in the O 1s spectrum, this remains highly speculative. Chalcocite has not been used to adjust the Cu 2p or Fe 2p cross sections because of the excess of copper (Section 5.5.1.3).

A.1.4 Cuprite (Cu_2O)

A.1.4.1 Cu 2p spectrum

The observed Cu 2p spectrum lineshape compares favourably with reported spectra (Larson, 1974; Roberts, 1974; Herzog et al., 1988; Barman and Sarma, 1992; Chawla et al., 1992; Galtayries and Bonnelle, 1995; Vasquez, 1998) and is consistent with mono-

valent copper; however, minor satellite structure is apparent in the observed spectrum (Figure A.16) and reported spectra. Nonetheless, the Cu $2p_{3/2}$ binding energy (932.48 eV) and the O $1s_{1/2}$ to Cu $2p_{3/2}$ binding energy separation (402.14 eV) compare favourably with reported energies (Table A.5).

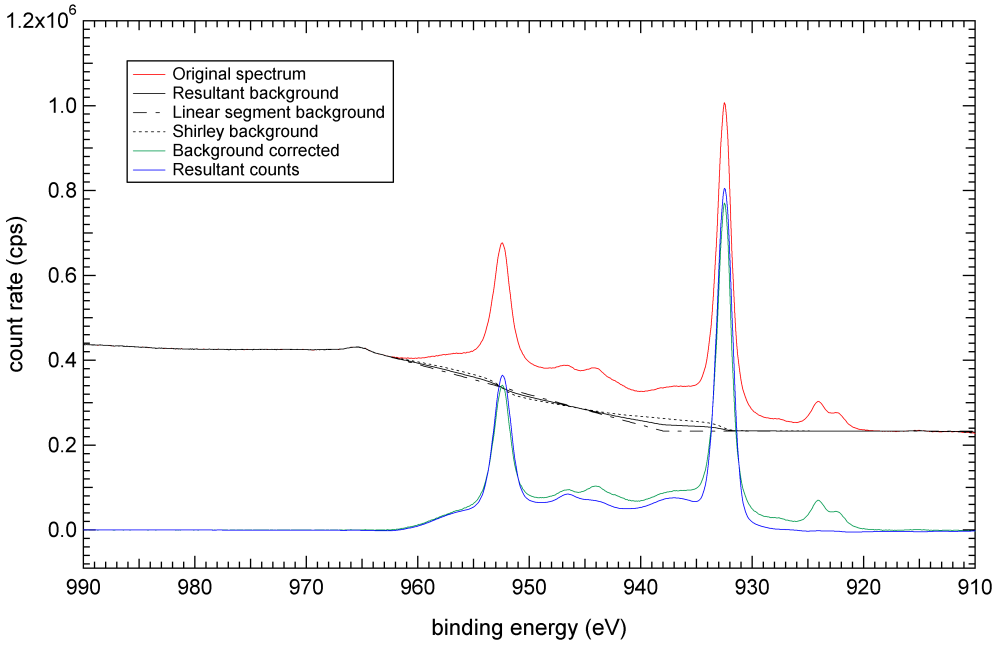

Figure A.16: *Cu 2p spectrum of the cuprite standard.*

Table A.5: *Binding energies (eV) of cuprite standards.*

Cu $2p_{3/2}$	**O $1s_{1/2}$**	**Cu $2p_{3/2}$ - O $1s_{1/2}$**	**Reference**
932.48	530.34	402.14	This study
931.4	531.4	400.0	De Filippo et al. (1988b)
931.9	-	-	Leloup et al. (1993)
932.0	530.0	402.0	McIntyre and Cook (1975)
932.0	-	-	Nakai et al. (1978)
932.2	-	-	Herzog et al. (1988)
932.4	530.0	402.4	Chawla et al. (1992)
932.5	530.4	402.1	Deroubaix and Marcus (1992)
932.5	530.3	402.2	Vasquez (1998)
932.5	529.7	402.8	Cano et al. (2001)
932.7	530.4	402.3	Haber et al. (1978)

A.1.4.2 O 1s spectrum

The observed O 1s spectrum lineshape (Figure A.17) compares favourably with the spectrum reported by Poulston et al. (1996), displaying one major peak at 530.34 eV and two minor peaks at 531.61 and 535.69 eV (Figure A.18); the minor peaks are not present in the spectra of Steiner et al. (1989) or Vasquez (1998). Poulston et al. (1996) observed the minor peak at $\sim$ 535.7 eV after annealing the cuprite at 800 K. In addition to the minor peak in the O 1s spectrum, Poulston et al. (1996) identify copper metal in the Cu $L_3M_{4,5}M_{4,5}$ spectrum. However, the Cu $L_3M_{4,5}M_{4,5}$ spectrum of the cuprite standard in this study (Figure A.19) compares favourably with the spectrum reported by Vasquez (1998) and does not suggest copper metal formation. The presence of satellite structure in the Cu 2p spectrum implies minimal oxidation; however, the minor peak appears at a binding energy much higher than binding energies reported for tenorite (CuO)(Table A.6). The nature of the minor peaks remains unresolved.

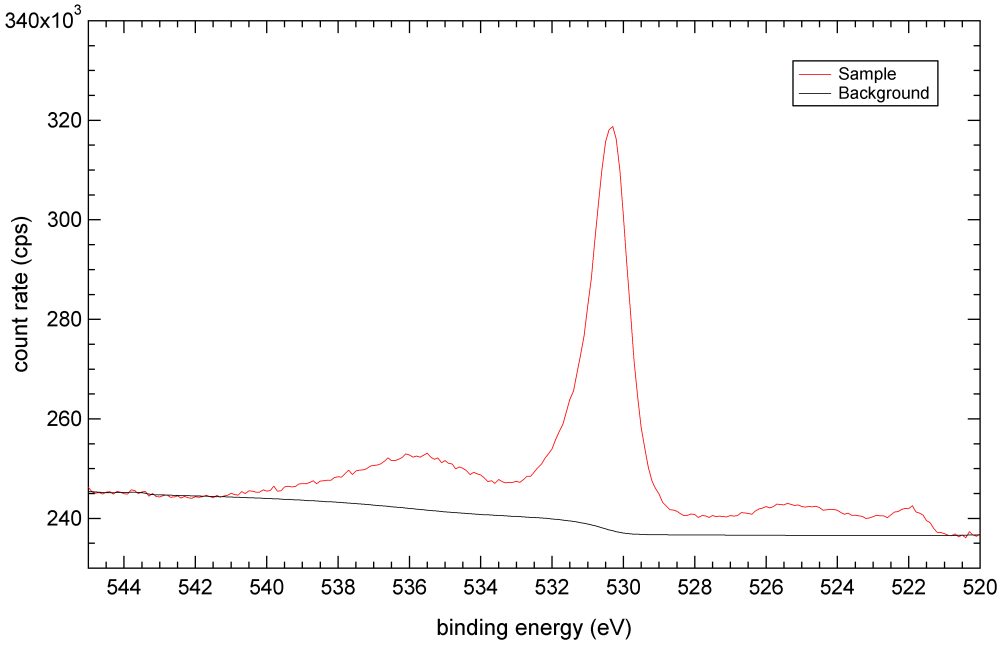

Figure A.17: *O 1s spectrum of the cuprite standard.*

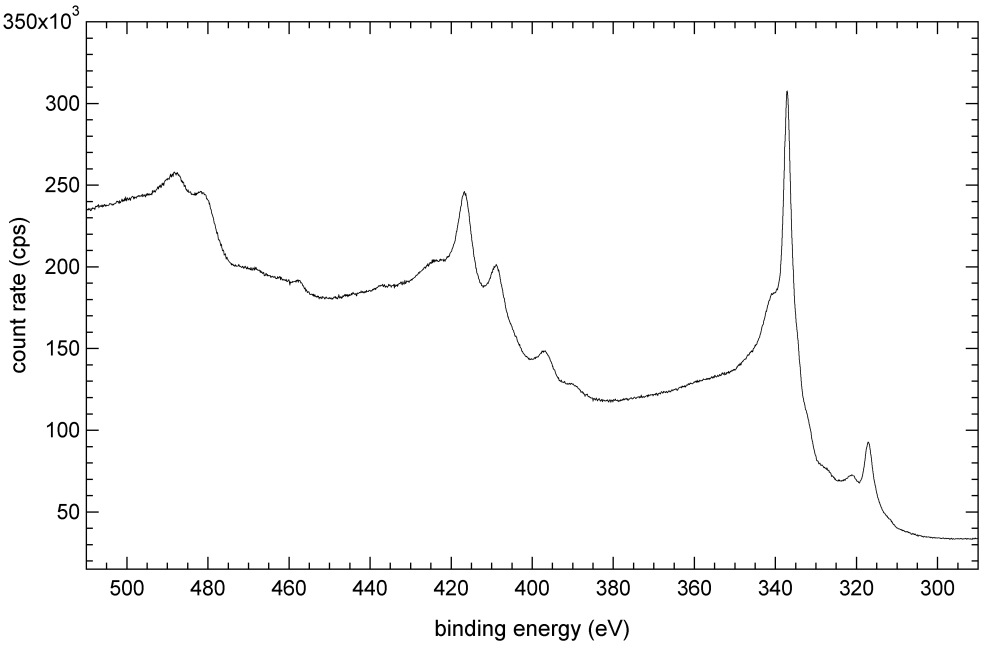

Figure A.19: *Cu $L_3M_{4,5}M_{4,5}$ spectrum of the cuprite standard fractured under anaerobic atmosphere.*

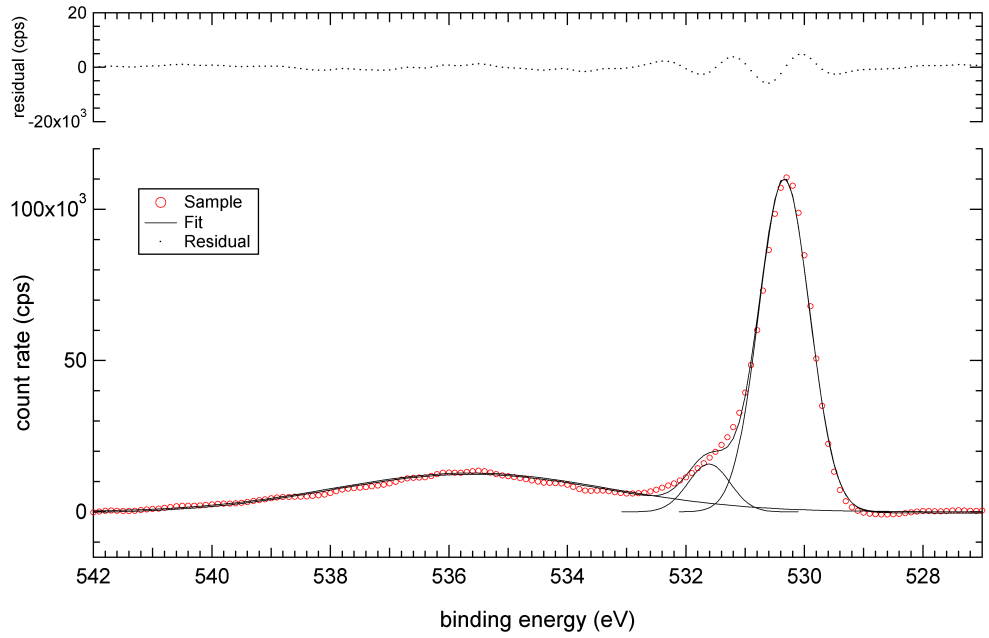

Figure A.18: *Fit of the O 1s spectrum of the cuprite standard.*

Table A.6: *Binding energies (eV) of tenorite standards.*

Cu $2p_{3/2}$	**O $1s_{1/2}$**	**Cu $2p_{3/2}$ - O $1s_{1/2}$**	**Reference**
932.7	-	-	Leloup et al. (1993)
933.2	-	-	Lianzhong (1987)
933.2	529.5-531.4	403.7	De Filippo et al. (1988b)
933.3	529.1	404.2	McIntyre and Cook (1975)
933.6	529.4	404.2	Haber et al. (1978)
933.6	-	-	Herzog et al. (1988)
933.6	529.6	404.0	Deroubaix and Marcus (1992)
933.6	-	-	Poulston et al. (1996)
933.7	529.5	404.2	Chawla et al. (1992)

A.1.4.3 Spectral intensity ratios

The observed and predicted Cu 2p:O 1s spectral intensity ratios of 18.2 and 18.2, respectively, compare favourably, if the minor peak observed in the O 1s spectrum is included. Therefore, it is speculated the minor peak is produced by the reaction of hydrocarbons with the oxygen atoms at the surface of the cuprite sample.

The consistency of the observed and predicted intensities gives confidence in the O 1s and Cu 2p cross sections, which gives confidence in the Cu 2p cross section adjustment (Section 5.5.1.3).

A.2 Iron oxides/oxyhydroxides

The iron oxide/oxyhydroxide standards analysed were hematite (Fe_2O_3), magnetite (Fe_3O_4) and goethite (FeOOH).

A.2.1 Fe 2p spectra

The observed Fe 2p spectrum lineshapes (Figures A.20 and A.22) compare favourably with reported spectra (McIntyre and Zetaruk, 1977; Brion, 1980; Harvey and Linton,

1981; Temesghen and Sherwood, 2002). The observed Fe $2p_{3/2}$ binding energies and Fe $2p_{3/2}$ to O $1s_{1/2}$ binding energy separations also compare favourably with reported energies (Table A.7).

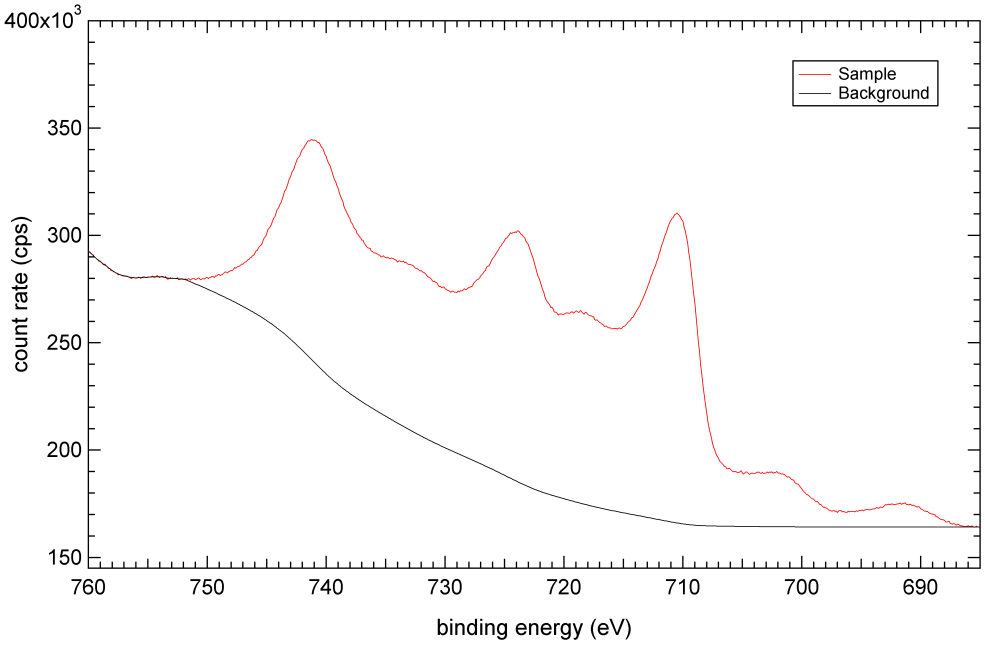

Figure A.20: *Fe 2p spectrum of the hematite standard.*

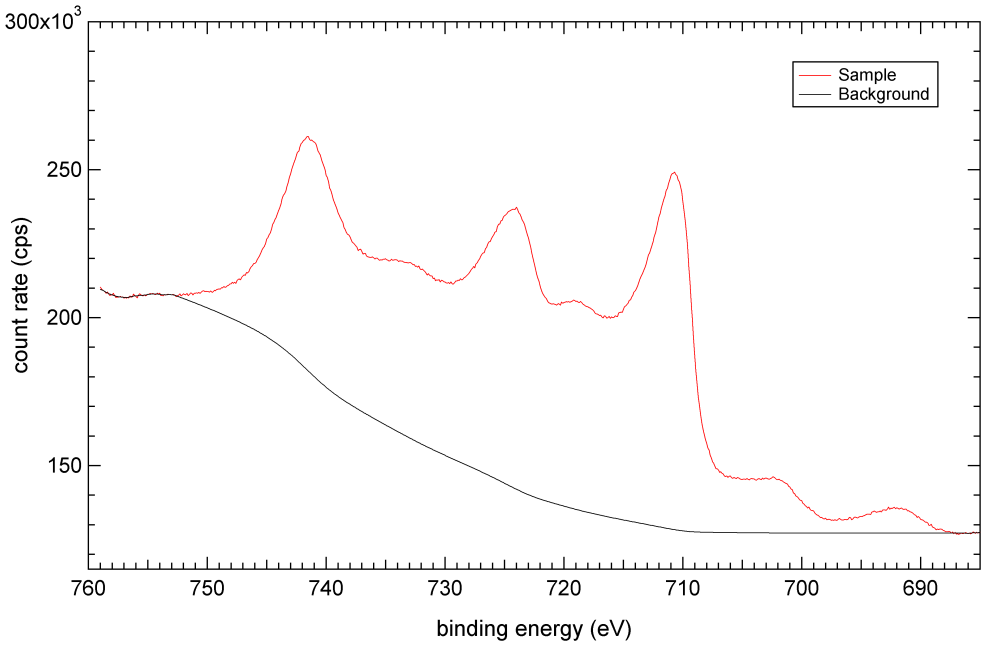

Figure A.21: *Fe 2p spectrum of the magnetite standard.*

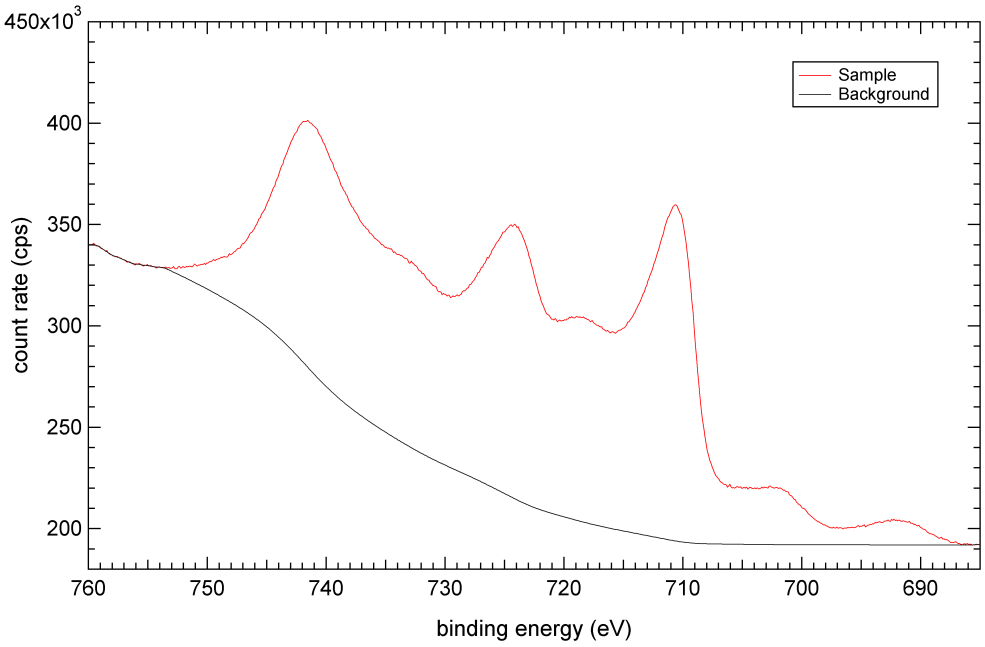

Figure A.22: *Fe 2p spectrum of the goethite standard.*

A.2.2 O 1s spectra

The observed O 1s spectrum lineshapes compare favourably with reported spectra (McIntyre and Zetaruk, 1977; Harvey and Linton, 1981)(Figures A.23, A.25 and A.27). However, fitting of the spectral envelope is a source of conjecture. The O 1s spectra of all three iron oxides were fitted with two peaks because of inequivalent oxygen atoms (Figures A.24, A.26 and A.28). However, only goethite is reported to contain more than one peak in the O 1s spectrum (Table A.7). This implies either extensive reduction has occurred in this study or multiple peaks have not been noted in previous studies. The inequivalent ratio of the peaks in the goethite fit may be due to interaction of the proton with both oxygen atoms in a phenomenon proposed by McIntyre and Zetaruk (1977).

Table A.7: *Binding energies (eV) of iron oxide/oxyhydroxide standards.*

Phase	**Fe $2p_{3/2}$**	**O $1s_{1/2}$**	**Fe $2p_{3/2}$ - O $1s_{3/2}$**	**Reference**
Fe_2O_3	710.35	529.30, 531.07	181.05, 179.28	This study
α-Fe_2O_3	710.6	529.4	181.2	McIntyre and Zetaruk (1977)
α-Fe_2O_3	710.6	529.5	181.1	Brion (1980)
α-Fe_2O_3	711.0	530.2	180.8	Temesghen and Sherwood (2002)
γ-Fe_2O_3	710.4	529.6	180.8	Temesghen and Sherwood (2002)
γ-Fe_2O_3	710.6	529.6	181.0	McIntyre and Zetaruk (1977)
$Fe_2O_3.nH_2O$	711.2	531.1	180.1	Harvey and Linton (1981)
Fe_3O_4	710.73	529.71, 530.58	181.02, 180.15	This study
Fe_3O_4	-	529.8	-	McIntyre and Zetaruk (1977)
Fe_3O_4	710.8	529.6	181.2	Temesghen and Sherwood (2002)
FeOOH	710.65	529.02, 530.37	181.63, 180.28	This study
FeOOH	711.0	529.6, 530.9	181.1, 180.0	Harvey and Linton (1981)
FeOOH	711.05	529.90, 531.00	181.15, 180.05	Brion (1980)
α-FeOOH	710.8	530.0, 531.3	180.8, 179.5	Temesghen and Sherwood (2002)
α-FeOOH	711.5	529.9, 531.0	181.2, 180.1	McIntyre and Zetaruk (1977)
γ-FeOOH	710.9	529.6, 531.0	181.3, 179.9	Temesghen and Sherwood (2002)

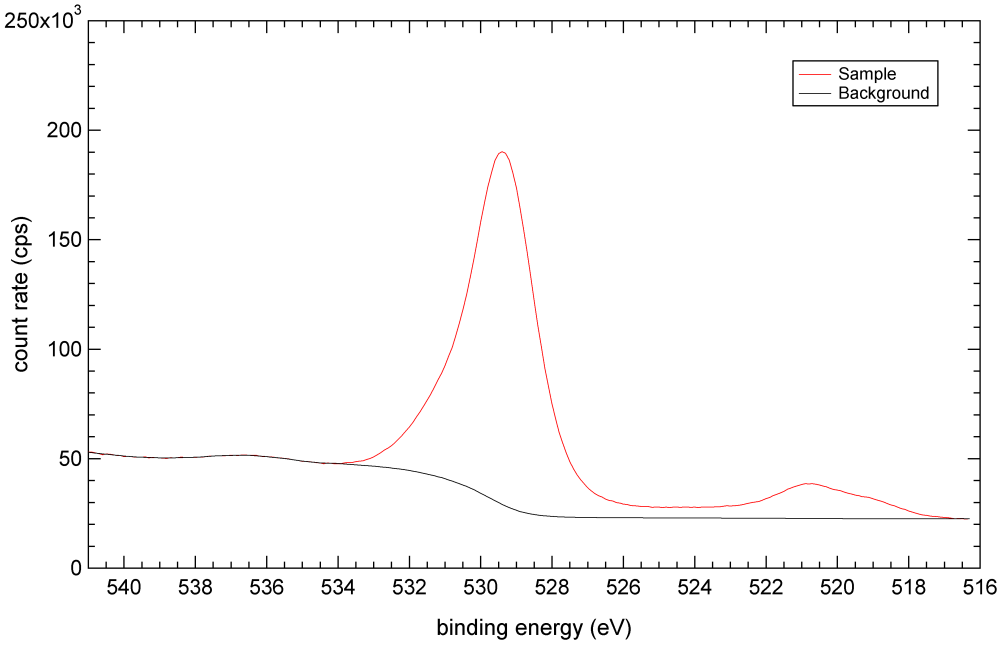

Figure A.23: *O 1s spectrum of the hematite standard.*

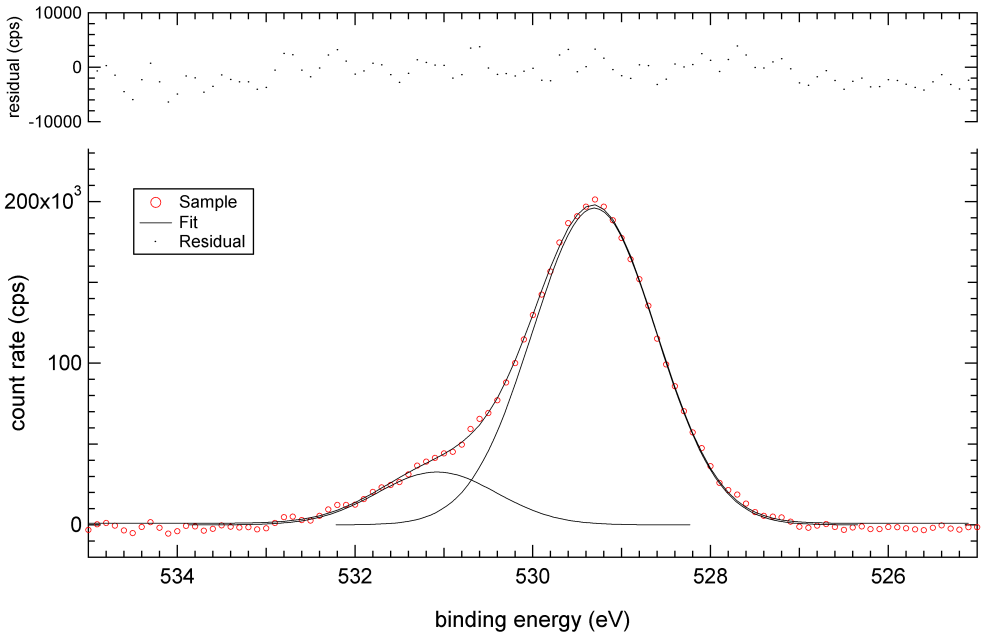

Figure A.24: *Fit of the O 1s spectrum of the hematite standard.*

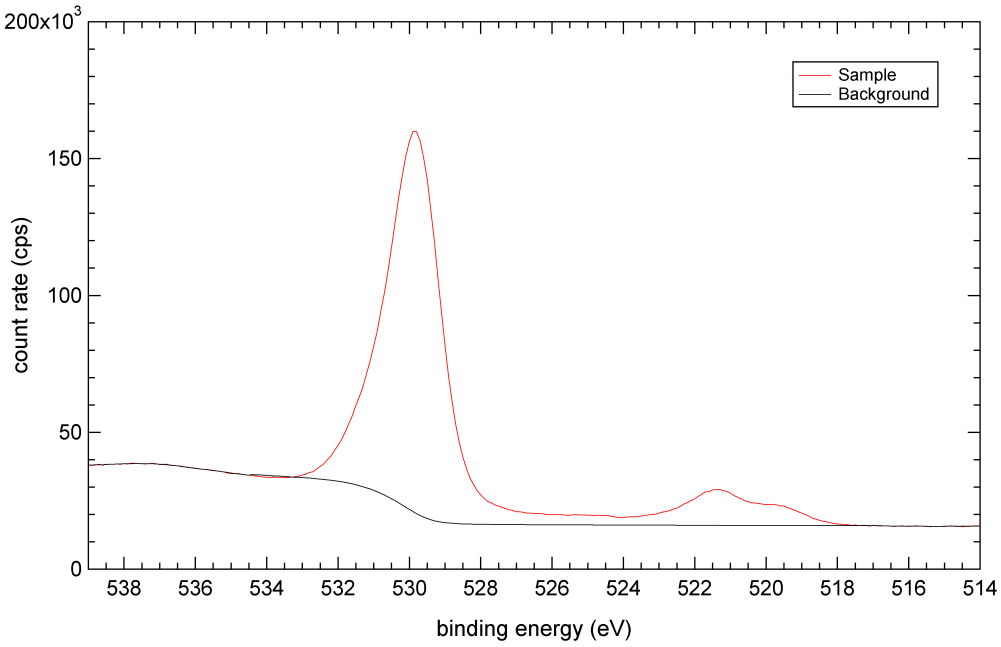

Figure A.25: *O 1s spectrum of the magnetite standard.*

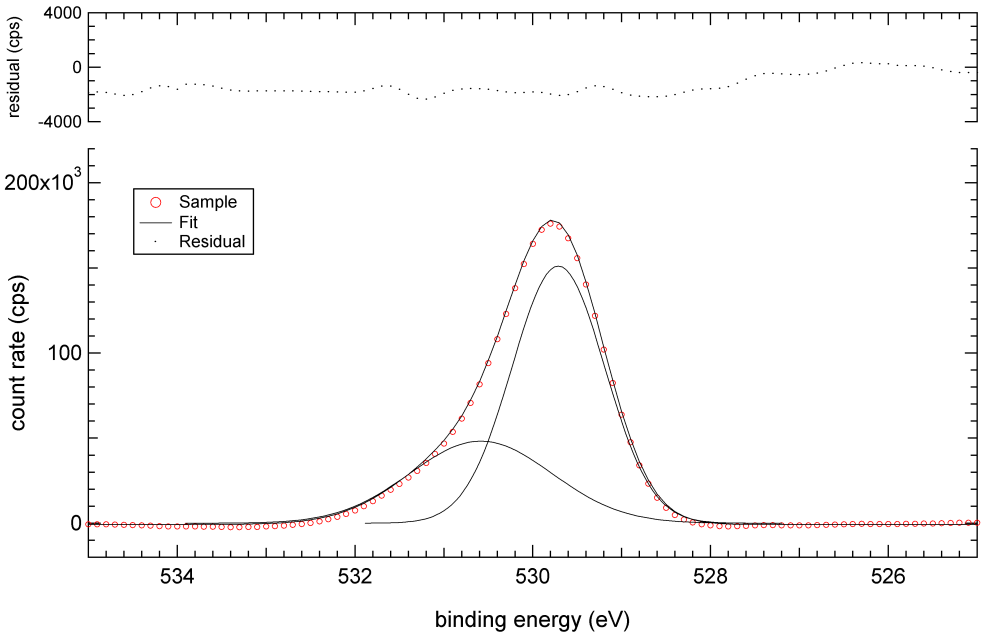

Figure A.26: *Fit of the O 1s spectrum of the magnetite standard.*

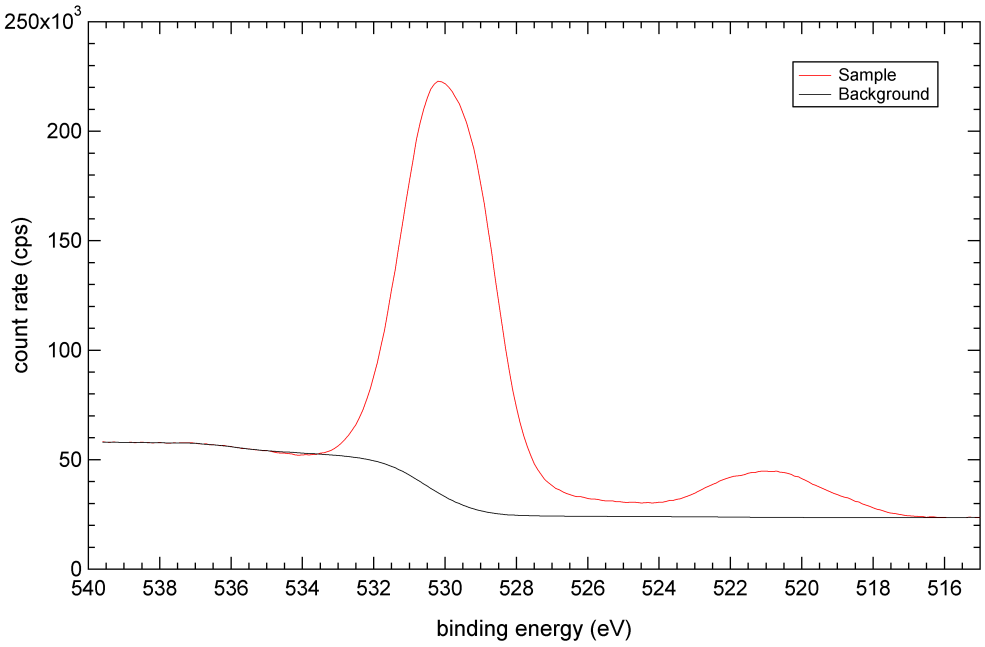

Figure A.27: *O 1s spectrum of the goethite standard.*

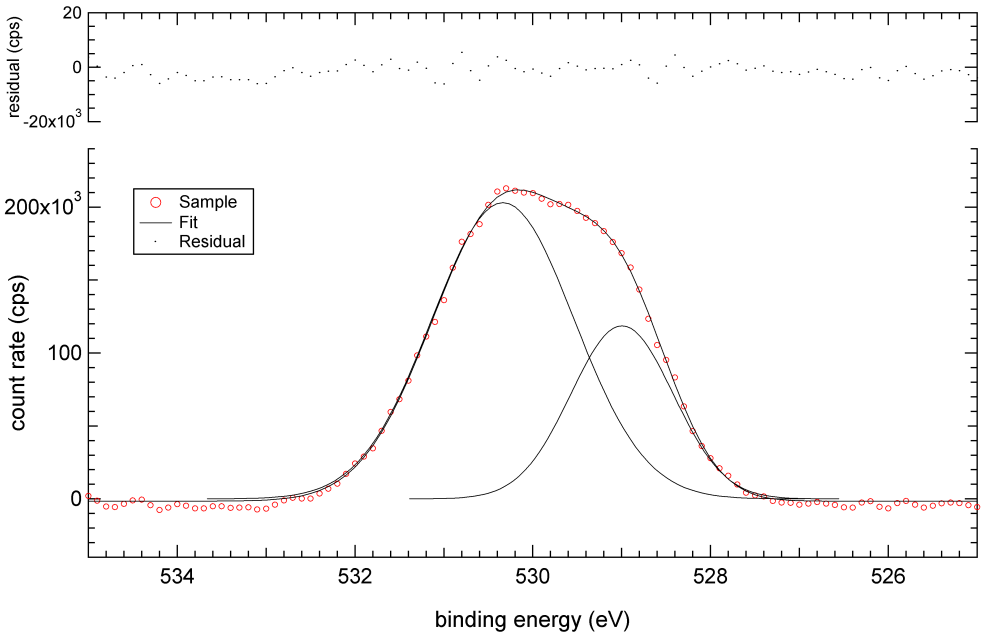

Figure A.28: *Fit of the O 1s spectrum of the goethite standard.*

A.2.3 Spectral intensity ratios

The observed and predicted Fe 2p:O 1s spectral intensity ratios compare favourably (Table A.8).

Table A.8: *Observed and predicted Fe 2p:O 1s spectral intensity ratios of the iron oxide/hydroxide standards.*

	$\mathbf{Fe_2O_3}$	$\mathbf{Fe_3O_4}$	**FeOOH**
Observed	6.74	7.77	5.46
Predicted	6.81	7.66	5.11

A.3 Iron sulphates

The iron sulphate standards analysed were hydronium jarosite $[H_3OFe_3(SO_4)_2(OH)_6]$ and ferric sulphate $[Fe_2(SO_4)_3]$.

A.3.1 S 2p spectra

The observed S 2p spectrum lineshape could not be compared with reported spectra because of an absence of the latter (Figures A.29 and A.31). However, the spectra acquired in this study consist of single peaks in accordance with equivalent sulphur atoms in each standard (Figures A.30 and A.32). The symmetry of the peaks implies photoreduction has not occurred. The observed S 2p binding energies compare favourably with reported energies (Table A.9).

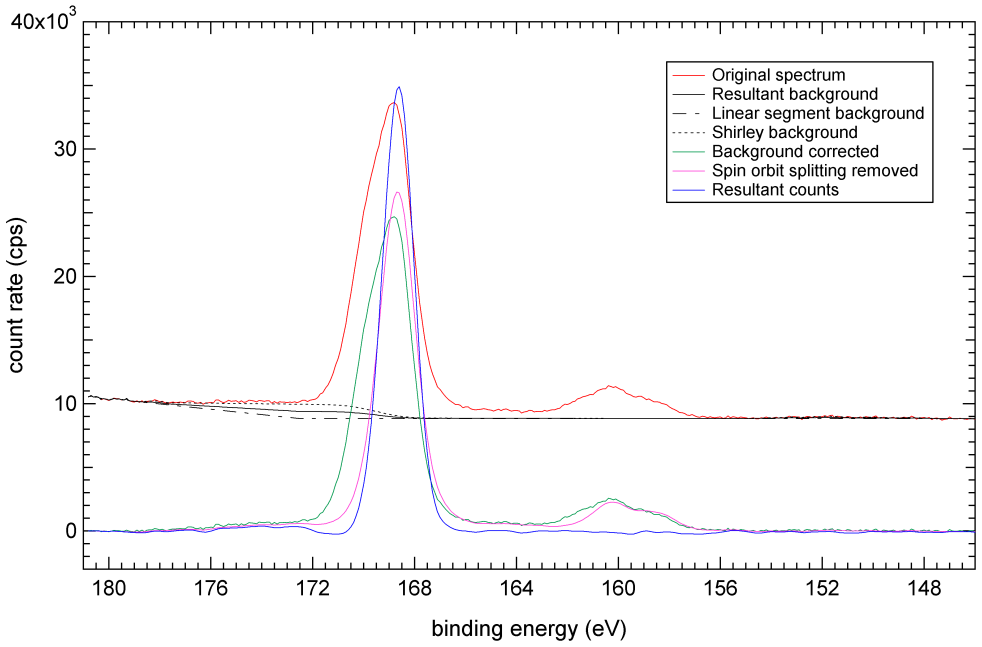

Figure A.29: *S 2p spectrum of the hydronium jarosite standard.*

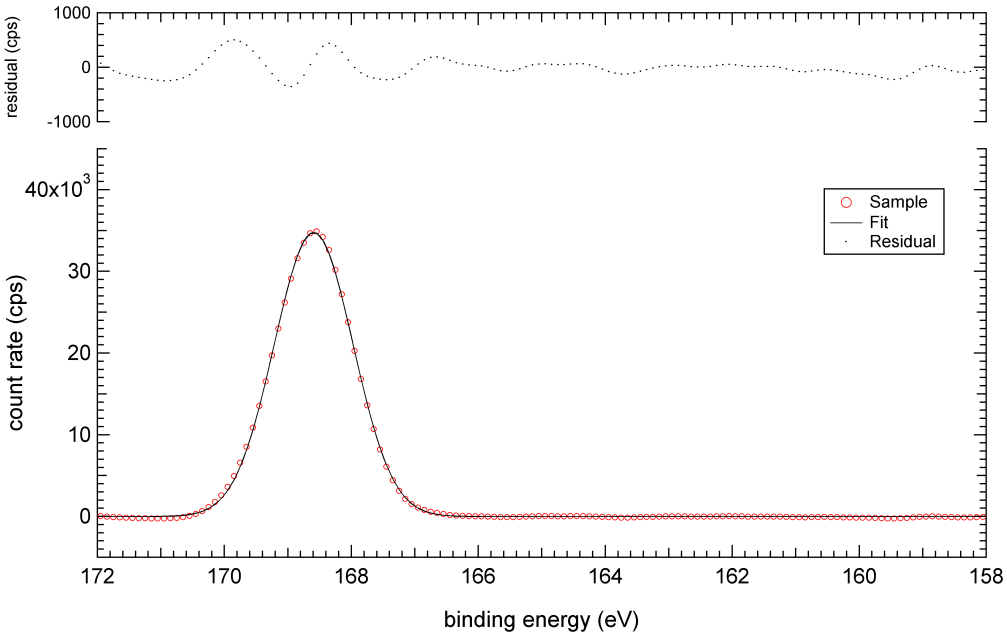

Figure A.30: *Fit of the S 2p spectrum of the hydronium jarosite standard.*

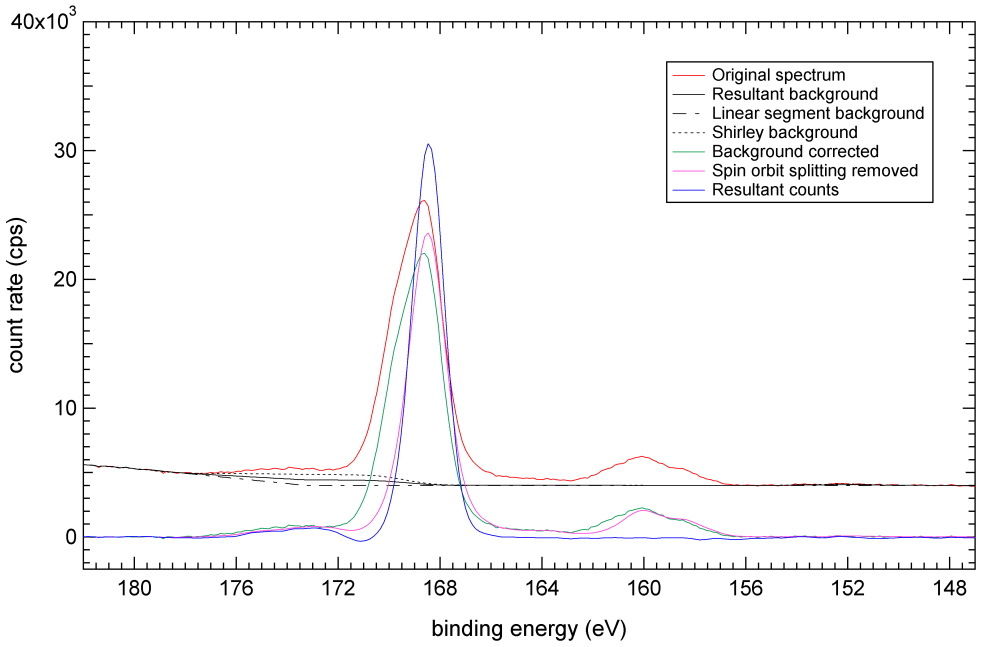

Figure A.31: *S 2p spectrum of the ferric sulphate standard.*

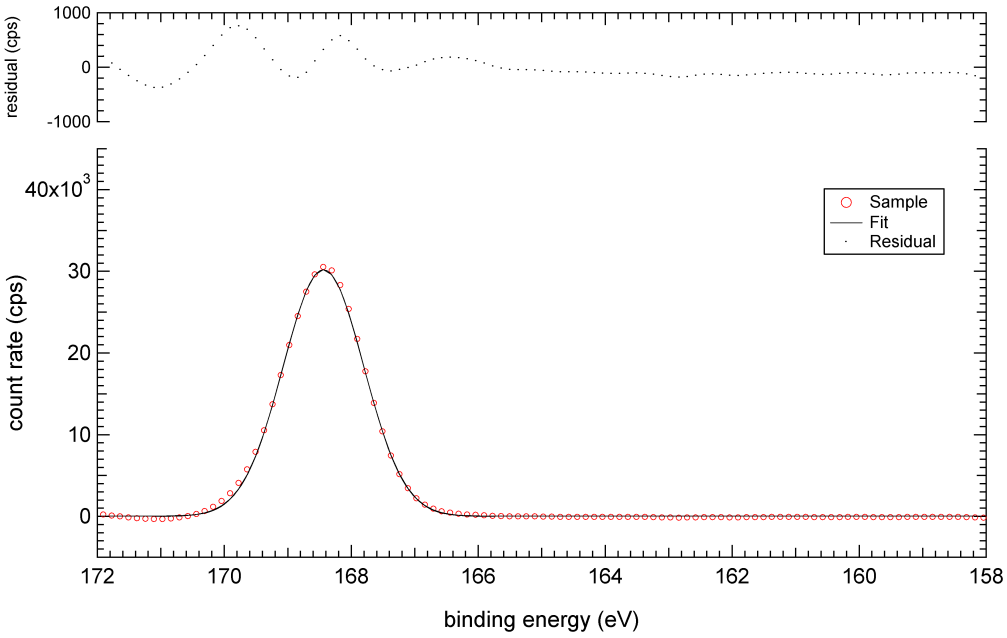

Figure A.32: *Fit of the S 2p spectrum of the ferric sulphate standard.*

Table A.9: *Binding energies (eV) of jarosite, jarosite analogue and ferric sulphate standards.*

Phase	Fe $2p_{3/2}$	O $1s_{1/2}$	S $2p_{3/2}$	Fe $2p_{3/2}$ - S $2p_{3/2}$	Reference
$H_3OFe_3(OH)_6(SO_4)_2$	712.02	531.69	168.58	543.44	This study
$KFe_3(OH)_6(SO_4)_2$	711.8	-	168.4	543.4	Brion (1980)
$FeSO_4.(NH_4)2SO_4.6H_2O$	-	-	167.90	-	Yu et al. (1990)
$Al(NH_4)(SO_4)_2.12H_2O$	-	-	168.15	-	Yu et al. (1990)
$Fe_2(SO_4)_3$	712.77	531.70	168.42	544.35	This study
$Fe_2(SO_4)_3$	713.1	532.0	169.1	544.0	Brion (1980)
$Fe_2(SO_4)_3$	714.6	532.6-9	168.0-4	-	Kelsall et al. (1992)
$Fe_2(SO_4)_3.xH_2O$	-	-	167.95	-	Yu et al. (1990)
$Fe(OH)SO_4.xH_2O$	711.2	530.2-1.6	168.6	542.6	De Filippo et al. (1988b)

A.3.2 Fe 2p spectra

The observed Fe 2p spectrum lineshape for the ferric sulphate standard displays greater definition than the spectrum reported by Brion (1980), especially for the peak at $\sim$ 719 eV (Figure A.33). Although no spectra of hydronium jarosite have been reported, the lineshape observed in this study (Figure A.34) compares favourably with the spectrum of potassium jarosite reported by Brion (1980) and the spectrum of $Fe(OH)SO_4.xH_2O$ reported by De Filippo et al. (1988b).

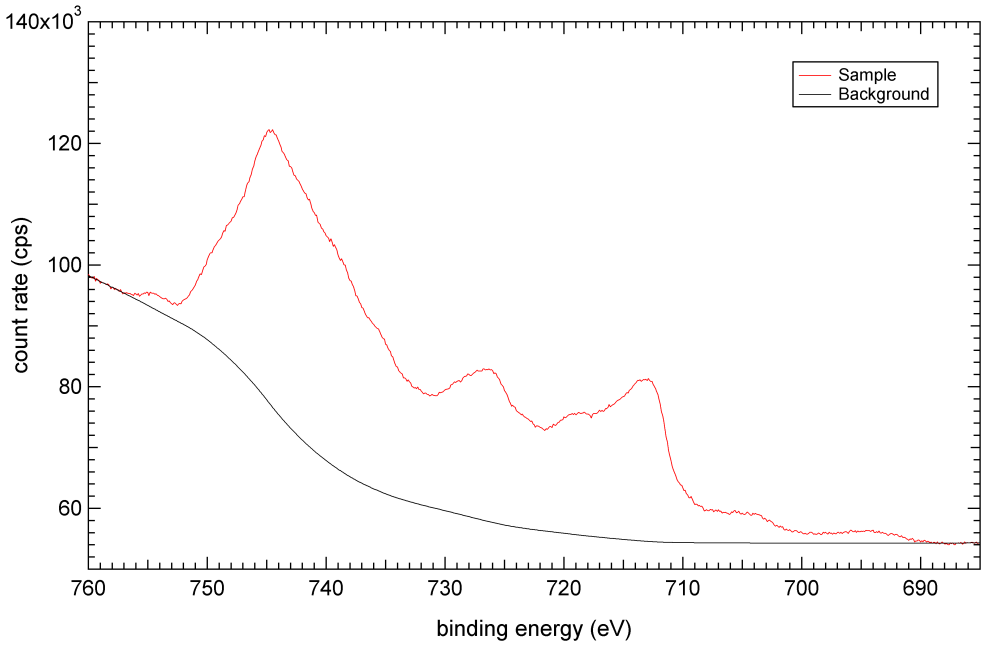

Figure A.33: *Fe 2p spectrum of the ferric sulphate standard.*

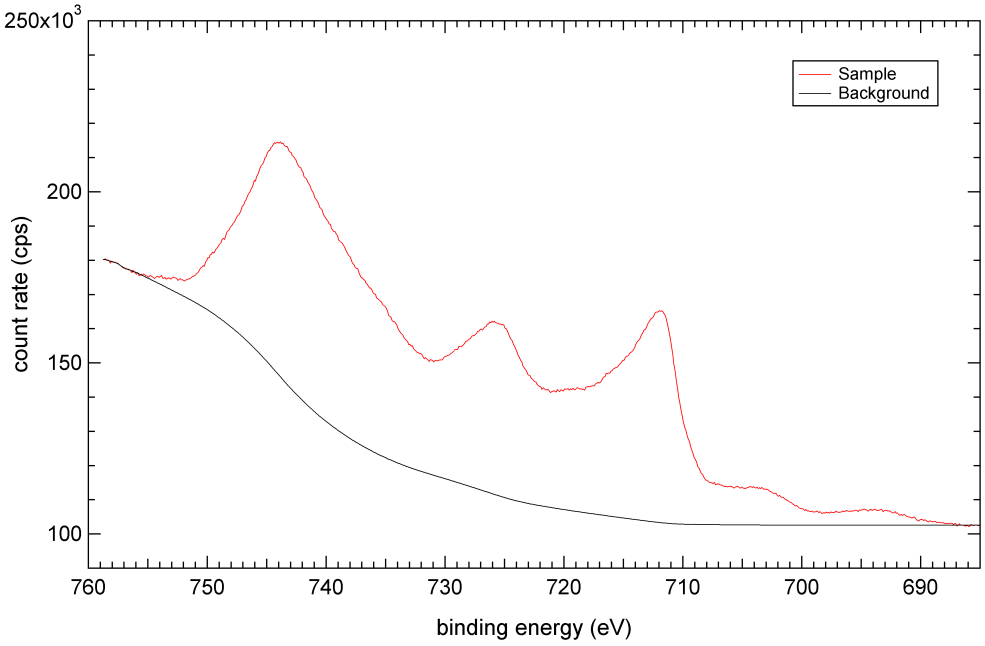

Figure A.34: *Fe 2p spectrum of the hydronium jarosite standard.*

The Fe $2p_{3/2}$ binding energies and the Fe $2p_{3/2}$ to S $2p_{3/2}$ binding energy separations for ferric sulphate and hydronium jarosite are difficult to compare with reported binding energies because of the breadth of the Fe $2p_{3/2}$ peak (Table A.9). Nonetheless, the hydronium jarosite Fe $2p_{3/2}$ to S $2p_{3/2}$ separation observed compares favourably with the potassium jarosite Fe $2p_{3/2}$ to S $2p_{3/2}$ separation reported by Brion (1980).

A.3.3 O 1s spectra

The observed O 1s spectra lineshapes (Figures A.35 - A.37) cannot be compared with reported spectra because of an absence of the latter. The ferric sulphate and hydronium jarosite spectra both display single peaks at $\sim$ 531.7 eV (Table A.9).

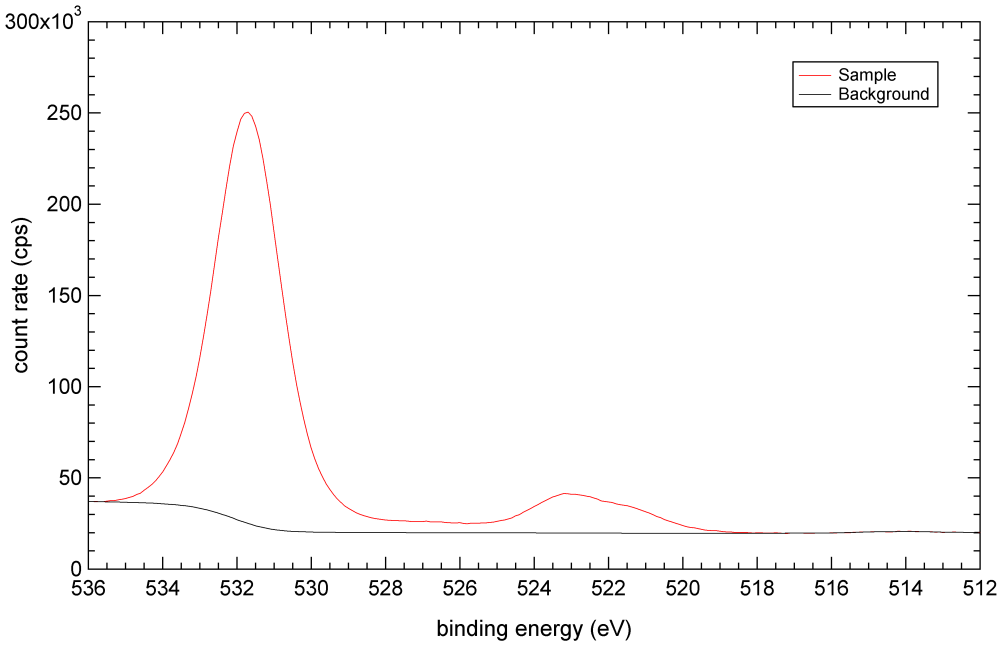

Figure A.35: *O 1s spectrum of the hydronium jarosite standard.*

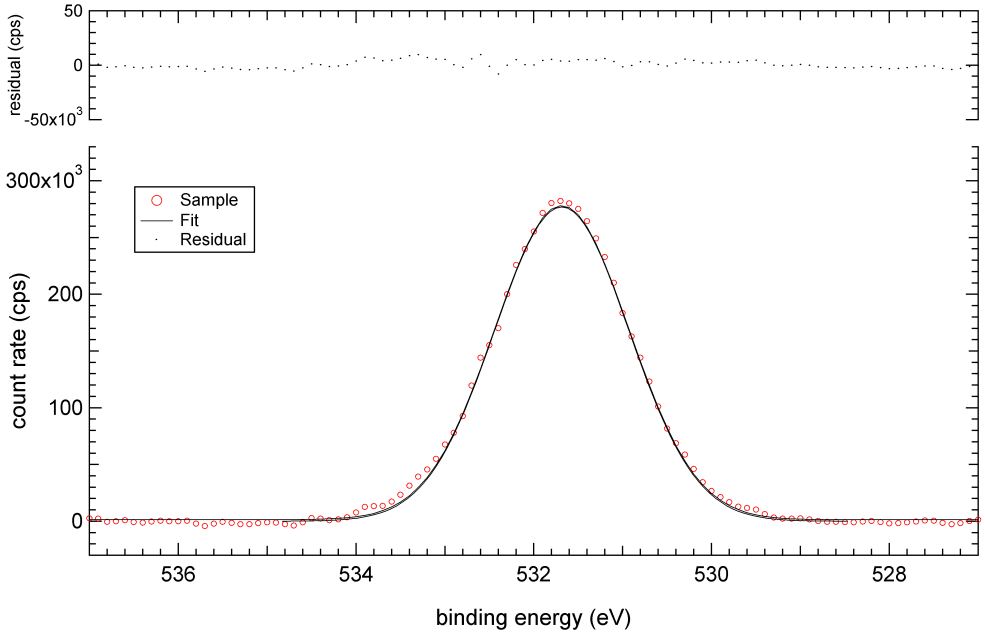

Figure A.36: *Fit of the O 1s spectrum of the hydronium jarosite standard.*

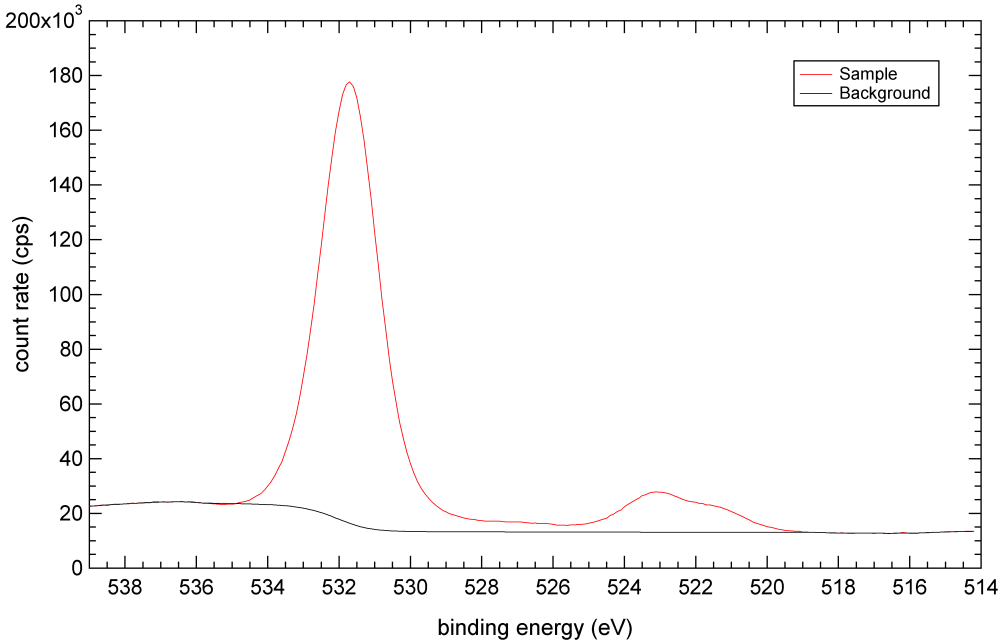

Figure A.37: *O 1s spectrum of the ferric sulphate standard.*

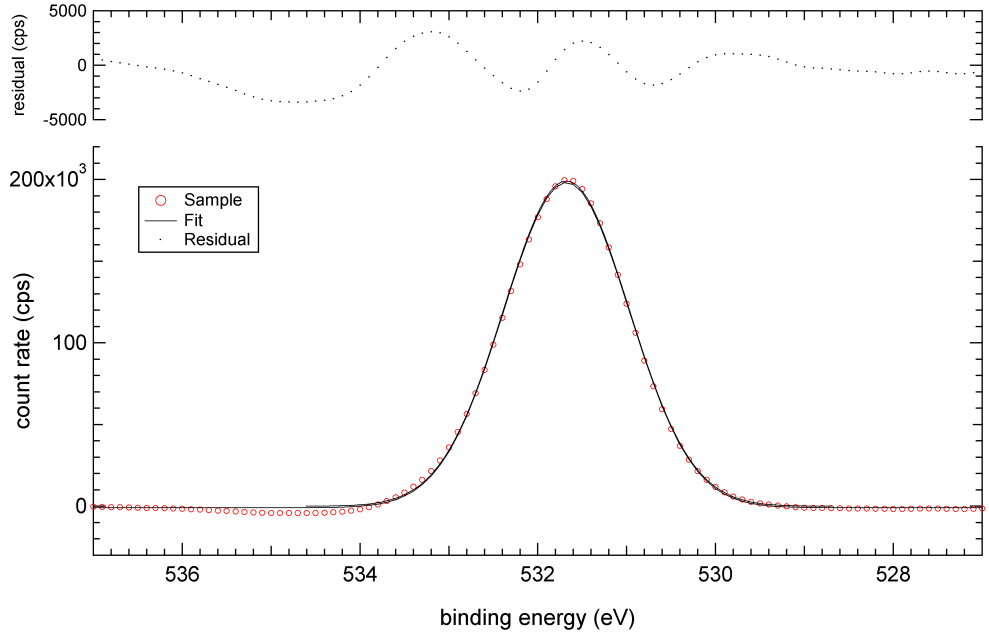

Figure A.38: *Fit of the O 1s spectrum of the ferric sulphate standard.*

A.3.4 Spectral intensity ratios

The observed and predicted Fe 2p:O 1s spectral intensity ratios for ferric sulphate and hydronium jarosite compare favourably (Table A.10). The observed and predicted Fe 2p:S 2p spectral intensity ratios for ferric sulphate also compare favourably; however, the hydronium jarosite standard appears high in sulphur. The sulphur excess is presumably caused by unreacted ferric sulphate, which is twice as rich in sulphur to iron, relative to hydronium jarosite. However, the distinctly different Fe 2p spectra of ferric sulphate and hydronium jarosite, and the consistency of the iron to oxygen intensities, suggest the ferric sulphate and hydronium jarosite standards are reliable.

Table A.10: *Observed and predicted Fe 2p:S 2p and Fe 2p:O 1s spectral intensity ratios of the iron sulphate standards.*

	$Fe_2(SO_4)_3$		$H_3OFe_3(SO_4)_2(OH)_6$	
	Fe 2p:O 1s	**Fe 2p:S 2p**	**Fe 2p:O 1s**	**Fe 2p:S 2p**
Observed	1.69	10.3	2.06	19.1
Predicted	1.69	10.9	2.03	24.6

A.4 Sulphur-oxygen salts

The sulphur-oxygen salts analysed were potassium thiosulphate and potassium sulphite. Although potassium is not present in the system (Section 3.4), analysis of the salts reveals binding energy separations and approximate binding energies for the S 2p and O 1s spectra. The binding energies observed for the potassium salts have been adjusted according to the binding energy separation observed for the S 2p peaks of potassium and sodium thiosulphate salts (0.4 eV) reported by Brion (1980) to address the charge shifting observed for potassium salts.

A.4.1 S 2p spectra

The observed S 2p spectrum lineshape for potassium thiosulphate (Figure A.39) cannot be compared with reported spectra because of an absence of the latter. The S 2p spectral envelope of thiosulphate was fitted with two major peaks and one minor peak (Figure A.40). If the minor peak is attributed to photoreduction of the high binding energy peak, the peak intensities assume a ratio of 1 to 1 in accordance with inequivalent sulphur atoms. The binding energies observed (162.61 and 168.71 eV) are higher than the binding energies reported (162.2 and 168.4 eV) by Brion (1980); however, the S $2p_{3/2}$(#1) to S $2p_{3/2}$(#2) binding energy separations (6.10 and 6.02 eV, respectively) compare favourably (Table A.11). The presence of thiosulphate in the S 2p spectra of chalcopyrite after oxidative dissolution may be difficult to detect because of the high intensities from disulphide and sulphate at 161.9 and 168.6 eV, respectively.

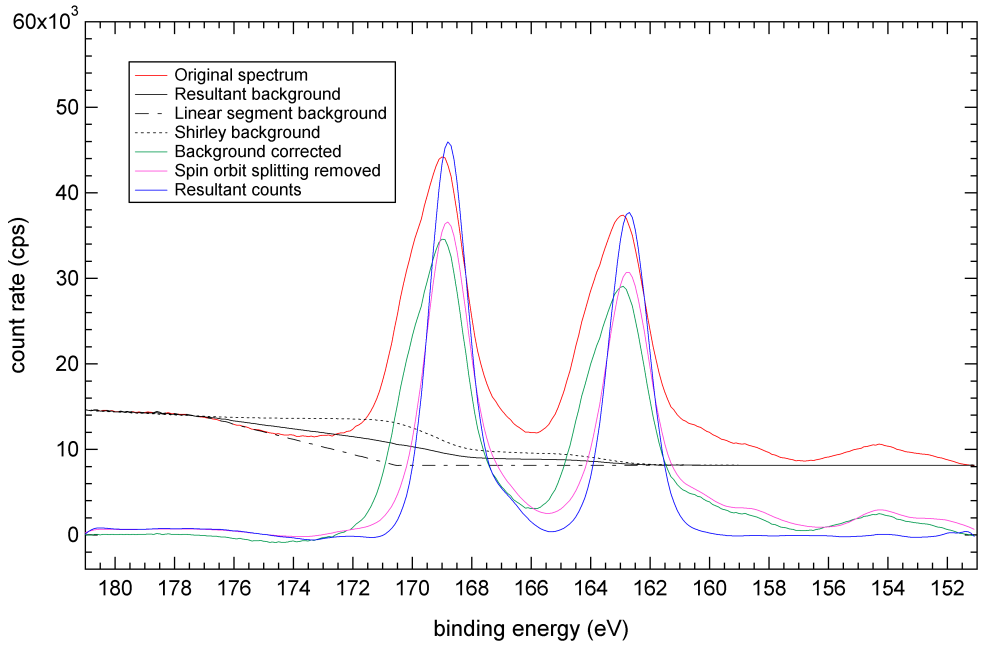

Figure A.39: *S 2p spectrum of the potassium thiosulphate standard.*

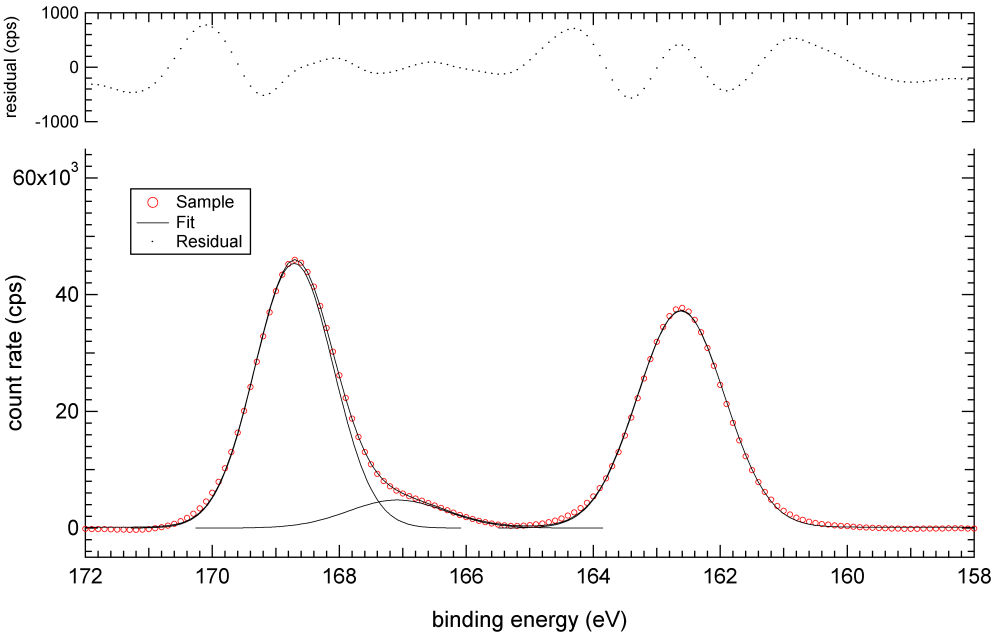

Figure A.40: *Fit of the S 2p spectrum of the potassium thiosulphate standard.*

Table A.11: *Binding energies (eV) of thiosulphate and sulphite salt standards.*

Phase	**S $2p_{3/2}$(#1)**	**S $2p_{3/2}$(#2)**	**(#1) - (#2)**	**Reference**
$K_2S_2O_3$	162.61	168.71	6.10	This study
$K_2S_2O_3$	162.2	168.4	6.2	Brion (1980)
$Na_2S_2O_3.5H_2O$	161.45	167.40	5.95	Yu et al. (1990)
$Na_2S_2O_3$	161.8	167.9	6.1	Duret-Thual et al. (1997)
$Na_2S_2O_3$	161.80	167.85	6.05	Brion (1980)
$Na_2S_2O_3$	162.3	168.4	6.1	Wagner (1978)
$Na_2S_2O_3$	162.3	168.2	5.9	Peisert et al. (1994)
K_2SO_3	166.80	169.00	2.20	This study
Na_2SO_3	164.40	-	-	Yu et al. (1990)
Na_2SO_3	166.4	-	-	Wagner and Taylor (1982)
Na_2SO_3	167.2	-	-	Peisert et al. (1994)
SO_3^{2-}	166.8	-	-	Siriwardane (1989)
SO_3^{2-}	166.6	-	-	Brion (1980)

The observed S 2p spectrum lineshape for potassium sulphite (Figure A.41) cannot be compared with reported spectra because of an absence of the latter. The S 2p spectrum of sulphite is fitted with two principal peaks in a ratio of 2 to 1 (Figure A.42). Although the emergence of a second peak suggests photoreduction might have occurred, the intensity of the peak and the integer ratio of intensities suggests the presence of two inequivalent sulphur atoms. This phenomenon may be the result of two orientations, with sulphur bonding to potassium either directly or via a bridging oxygen (Da Silva and De Andrade, 2004). The observed binding energy for the lower binding energy peak (166.80 eV) compares favourably with reported energies (164.4 - 166.8 eV), although there are no reported energies for the higher binding energy peak (Table A.11). The absence of reported lineshapes makes the issue of one or two peaks difficult to resolve. The presence of sulphite should be easily identified because of an absence of other peaks near 166 eV in the S 2p spectra of chalcopyrite after oxidative dissolution, although the precise binding energy is difficult to declare because of the association with goethite (Appendix E).

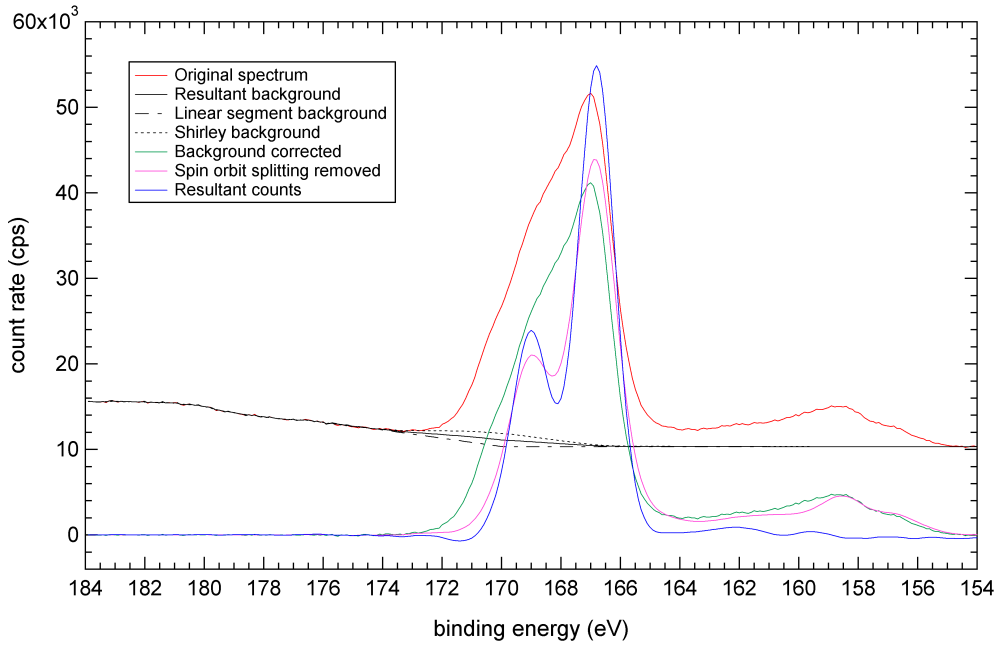

Figure A.41: *S 2p spectrum of the potassium sulphite standard.*

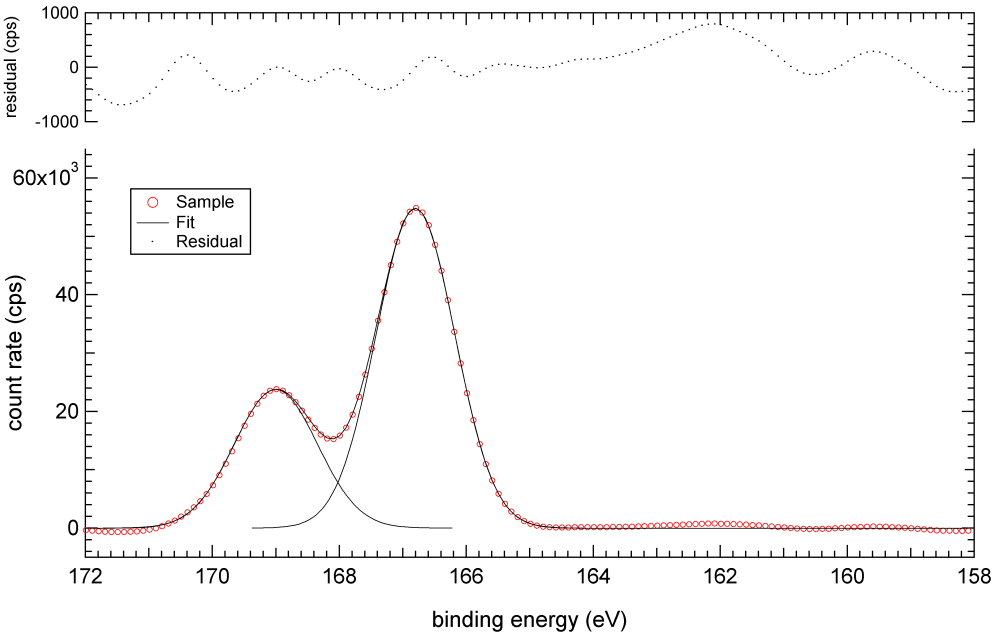

Figure A.42: *Fit of the S 2p spectrum of the potassium sulphite standard.*

A.4.2 O 1s spectra

The observed O 1s spectrum lineshapes (Figures A.43 and A.45) cannot be compared with reported spectra because of an absence of the latter. However, the O 1s spectral envelopes of thiosulphate and sulphite were fitted with single peaks, in accordance with equivalent oxygen atoms (Figures A.44 and A.46).

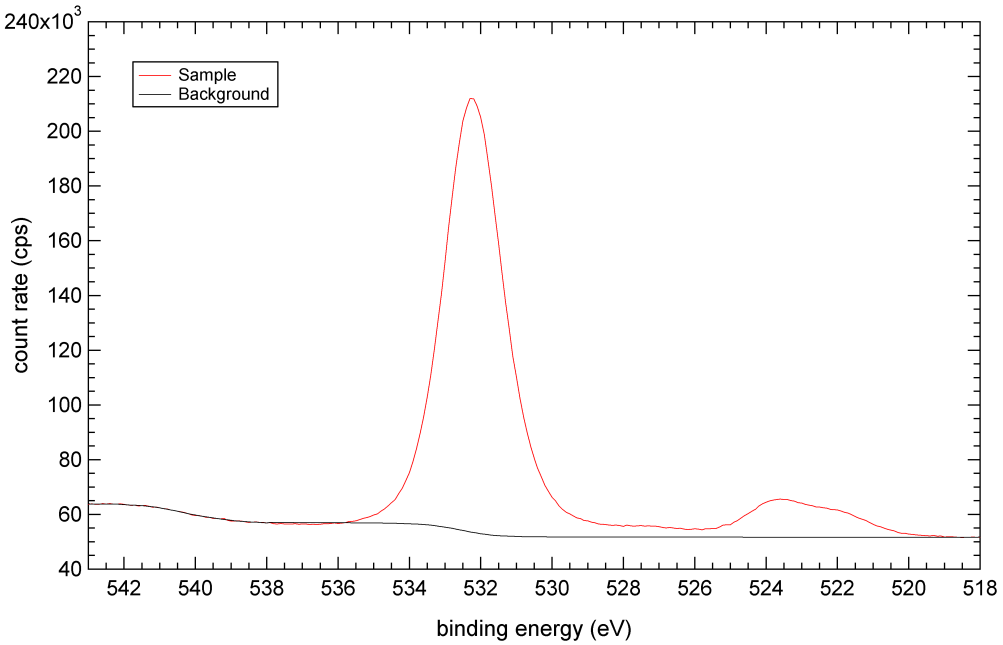

Figure A.43: *O 1s spectrum of the potassium thiosulphate standard.*

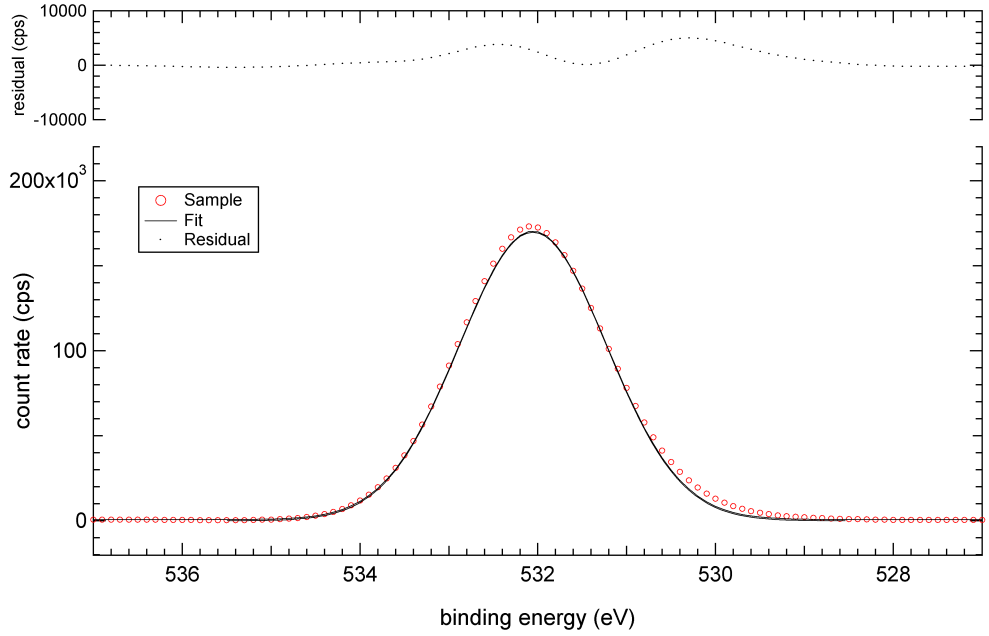

Figure A.44: *Fit of the O 1s spectrum of the potassium thiosulphate standard.*

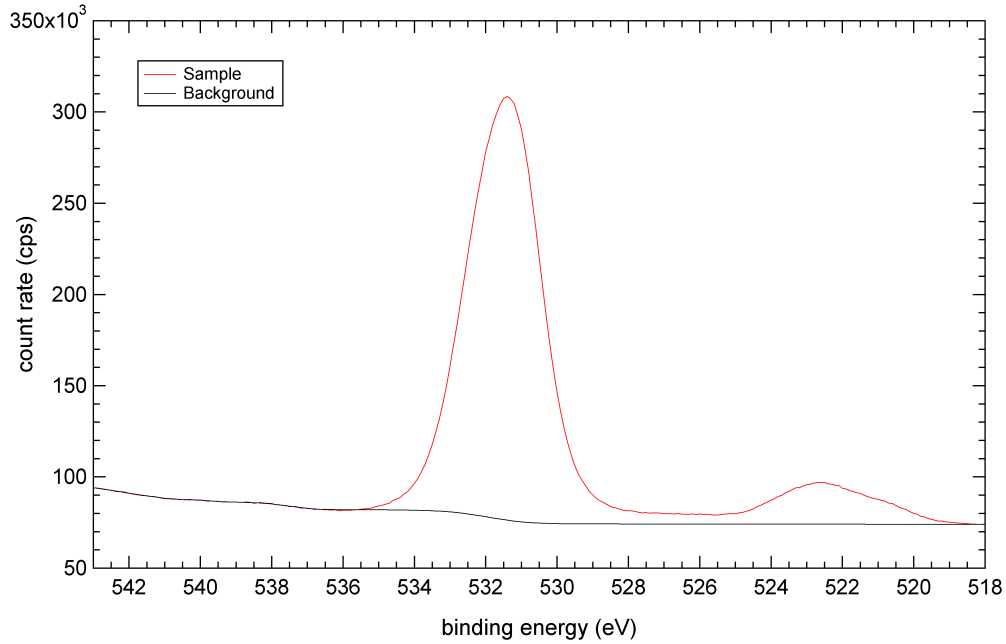

Figure A.45: *O 1s spectrum of the potassium sulphite standard.*

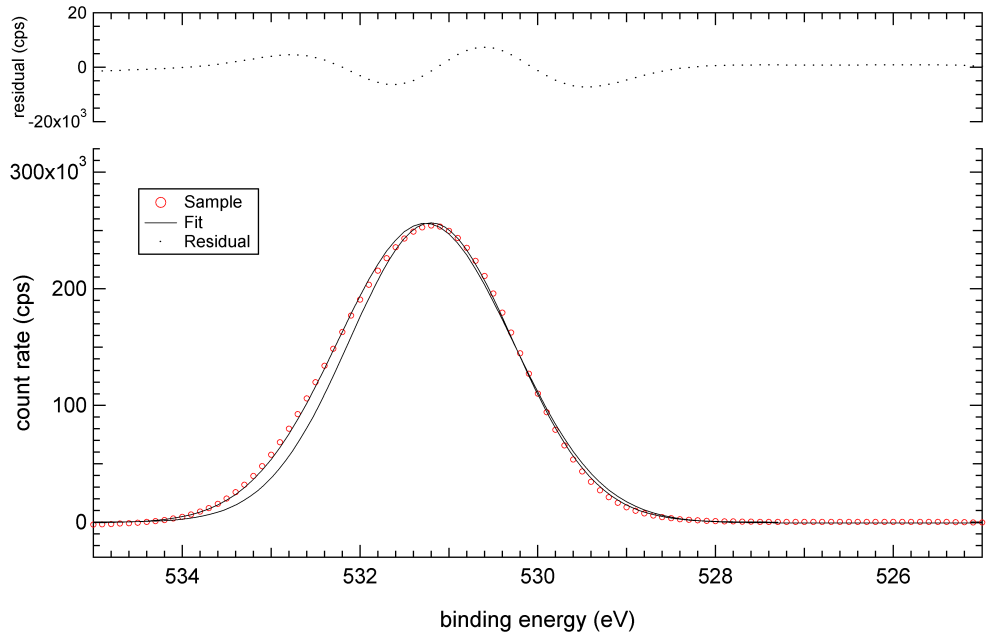

Figure A.46: *Fit of the O 1s spectrum of the potassium sulphite standard.*

A.4.3 Spectral intensity ratios

The observed and predicted S 2p:O 1s spectral intensity ratios for potassium thiosulphate compare favourably (Table A.12). However, the observed and predicted S 2p:O 1s spectral intensity ratios for potassium sulphite do not compare favourably because of either an excess of sulphur or a deficiency of oxygen (Table A.12).

Table A.12: *Observed and predicted S 2p:O 1s spectral intensity ratios of the thiosulphate and sulphite salt standards.*

	$K_2S_2O_3$	K_2SO_3
Observed	2.46	4.23
Predicted	2.39	4.82

A.5 Summary

The purity of a series of relevant standards was examined according to binding energies, binding energy separations and spectral intensity ratios. The standards of high purity include covellite, cuprite, hematite, magnetite, goethite and ferric sulphate. These standards have been used to correlate observed and predicted spectral intensity ratios (Section 5.5.1.3).

The bornite and chalcocite standards were unoxidised but displayed an excess of copper. The iron sulphates were very pure according to the iron to oxygen intensities; however, the hydronium jarosite displayed an excess of sulphur. The sulphite and thiosulphate standards were quite pure; however, the binding energies are not expected to match those observed on the surface of chalcopyrite and hence are simply used as a guide.

Appendix B

Fe 2p, O 1s and O $KL_{2,3}L_{2,3}$ spectra of standards used for Fe 2p cross section adjustment

Fe 2p and O 1s spectra of ferric sulphate, hydronium jarosite and iron-oxide/oxyhydroxide sulphate standards used for Fe 2p cross section adjustment are presented in Sections A.2 and A.3.

Note: O $KL_{2,3}L_{2,3}$ peaks are included in the Fe 2p spectra of iron-bearing standards.

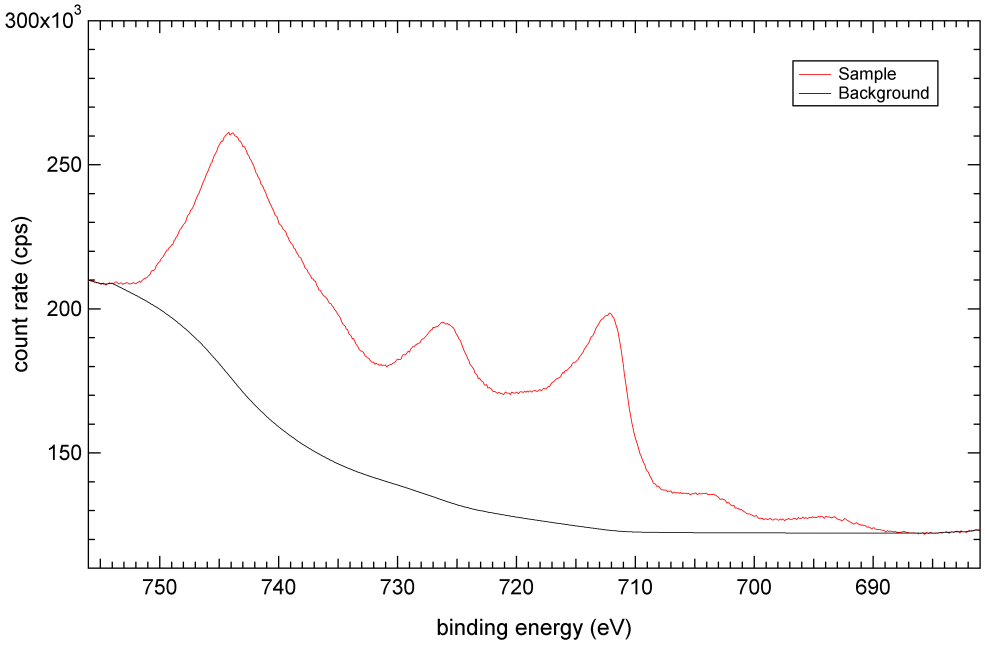

Figure B.1: *Fe 2p spectrum of the ammonium jarosite standard.*

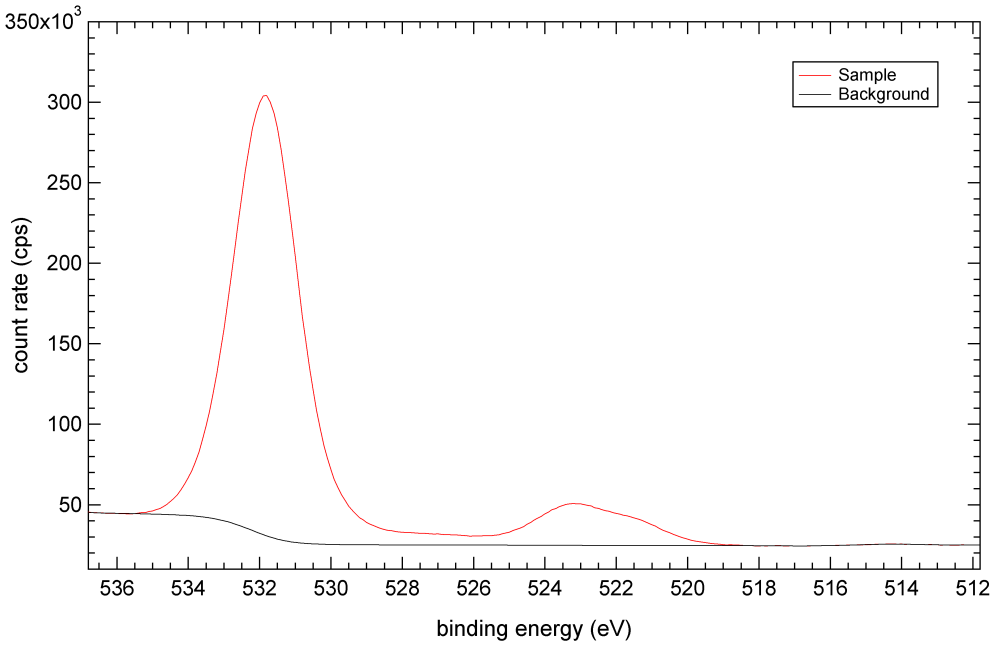

Figure B.2: *O 1s spectrum of the ammonium jarosite standard.*

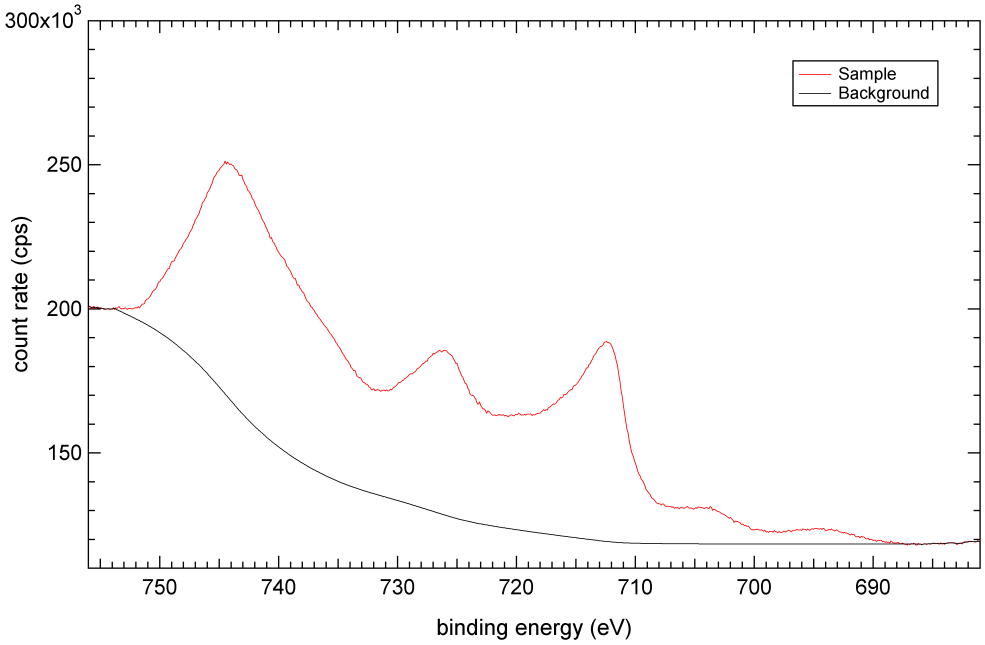

Figure B.3: *Fe 2p spectrum of the potassium jarosite standard.*

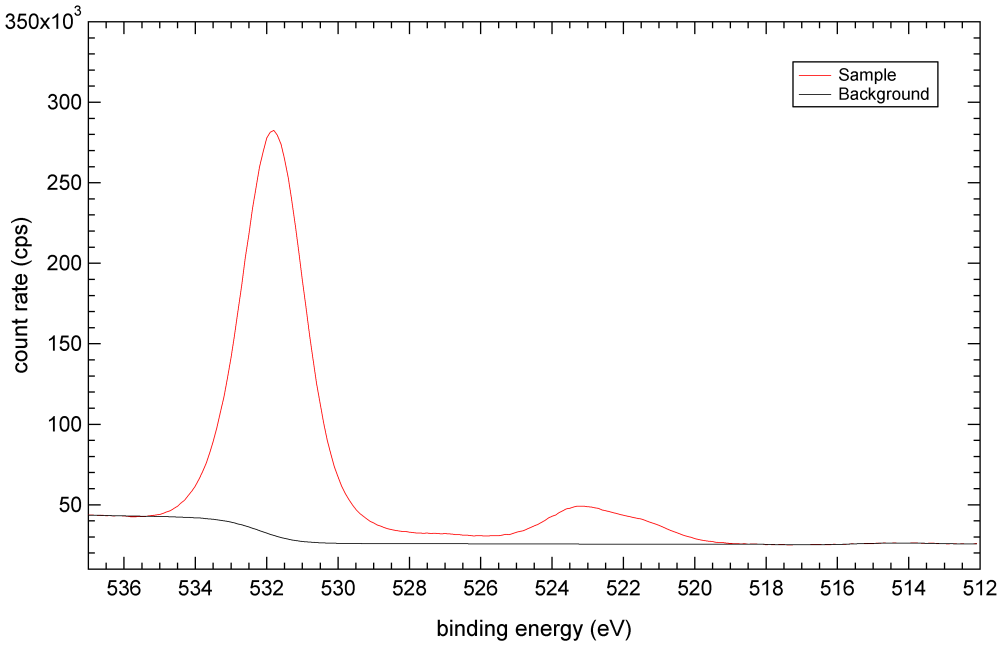

Figure B.4: *O 1s spectrum of the potassium jarosite standard.*

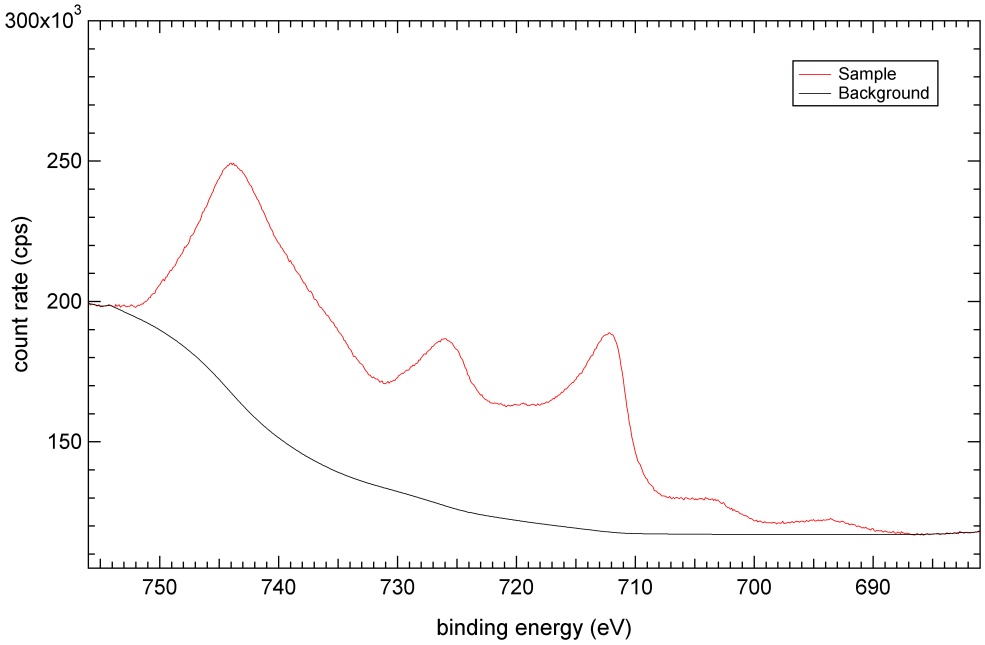

Figure B.5: *Fe 2p spectrum of the sodium jarosite standard.*

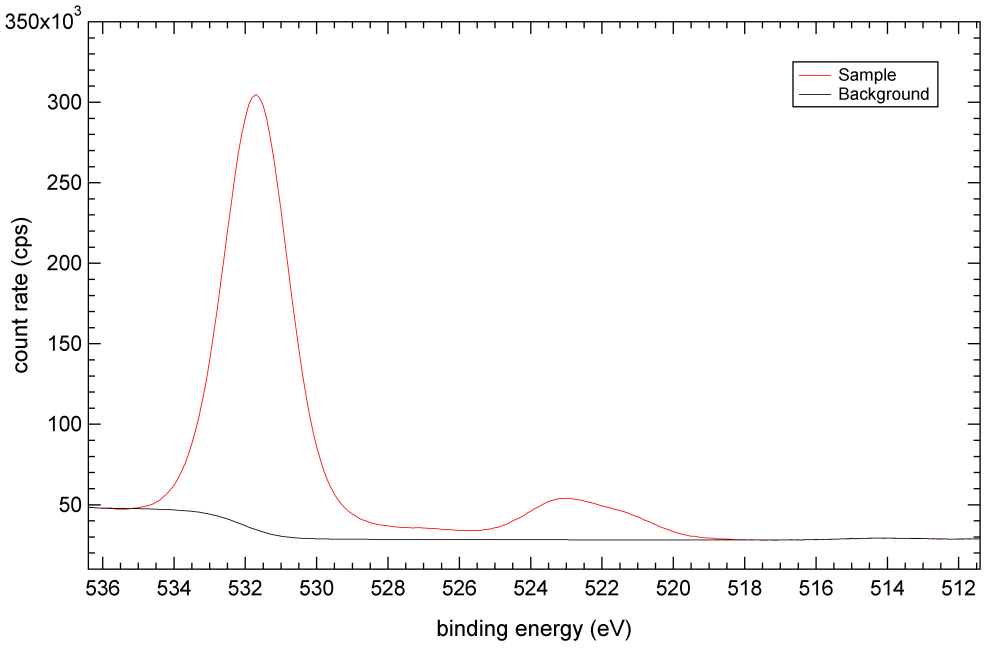

Figure B.6: *O 1s spectrum of the sodium jarosite standard.*

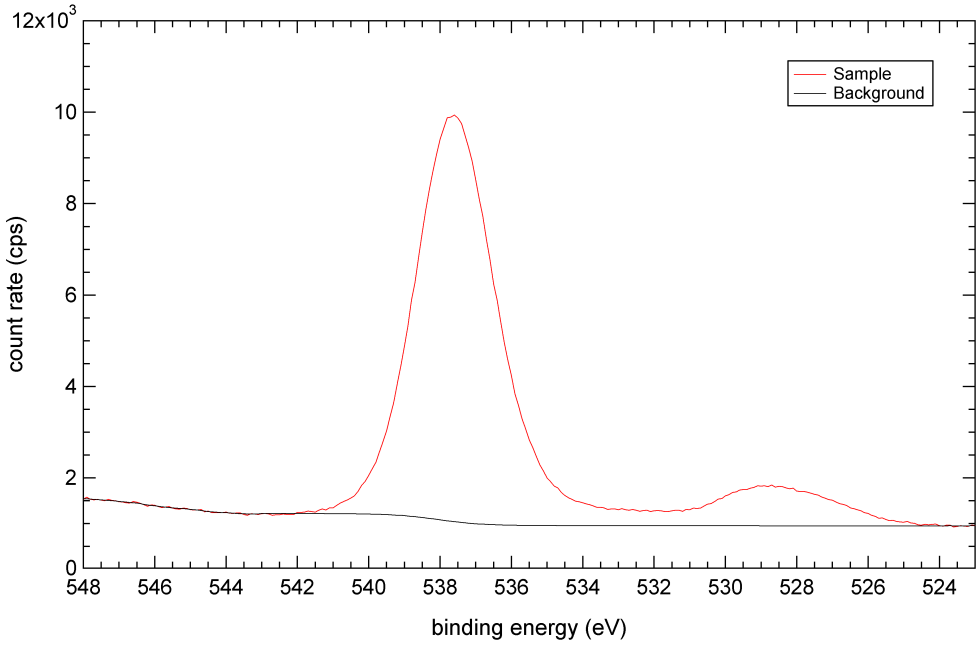

Figure B.7: *O 1s spectrum of the aluminium oxide standard.*

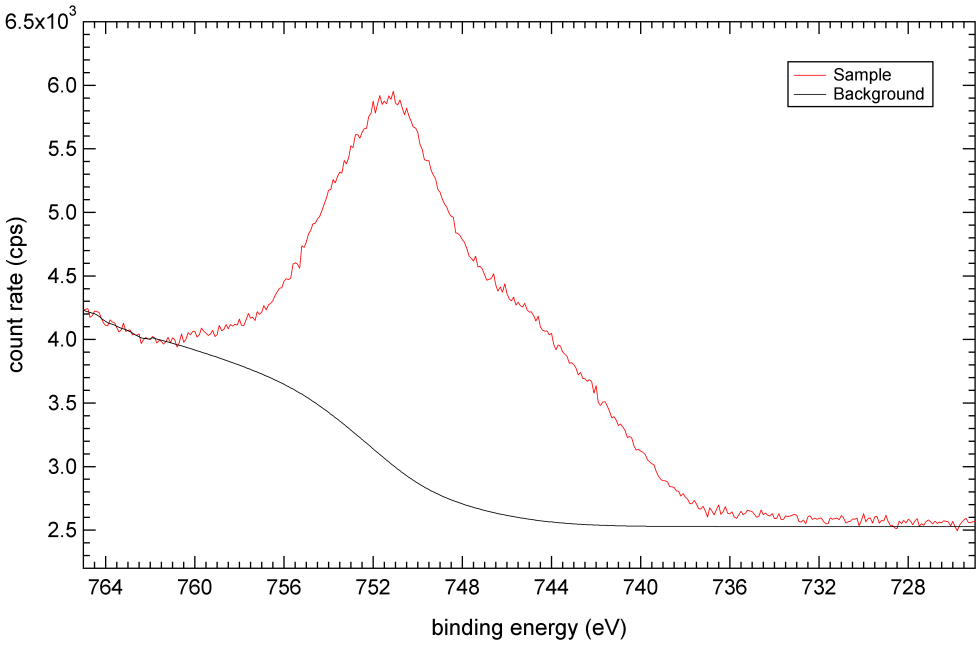

Figure B.8: *O $KL_{2,3}L_{2,3}$ spectrum of the aluminium oxide standard.*

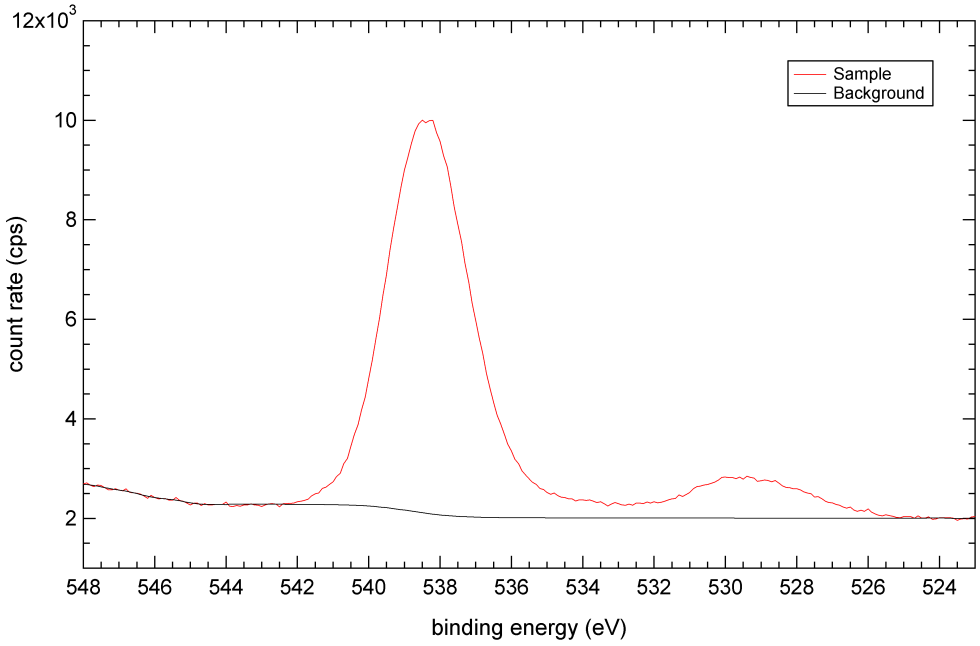

Figure B.9: *O 1s spectrum of the calcium carbonate standard (# 1).*

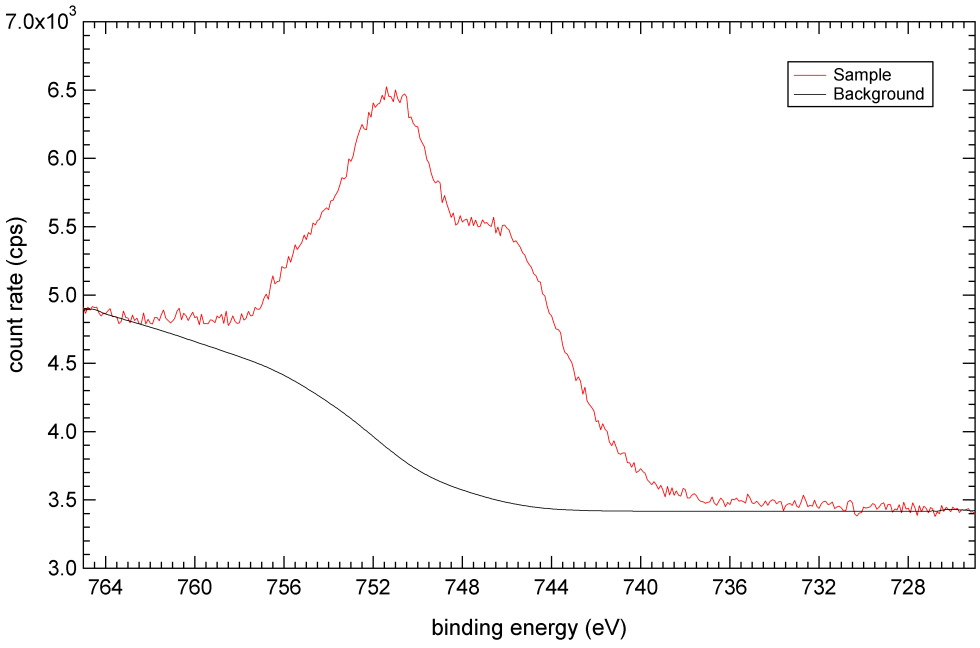

Figure B.10: *O $KL_{2,3}L_{2,3}$ spectrum of the calcium carbonate standard (# 1).*

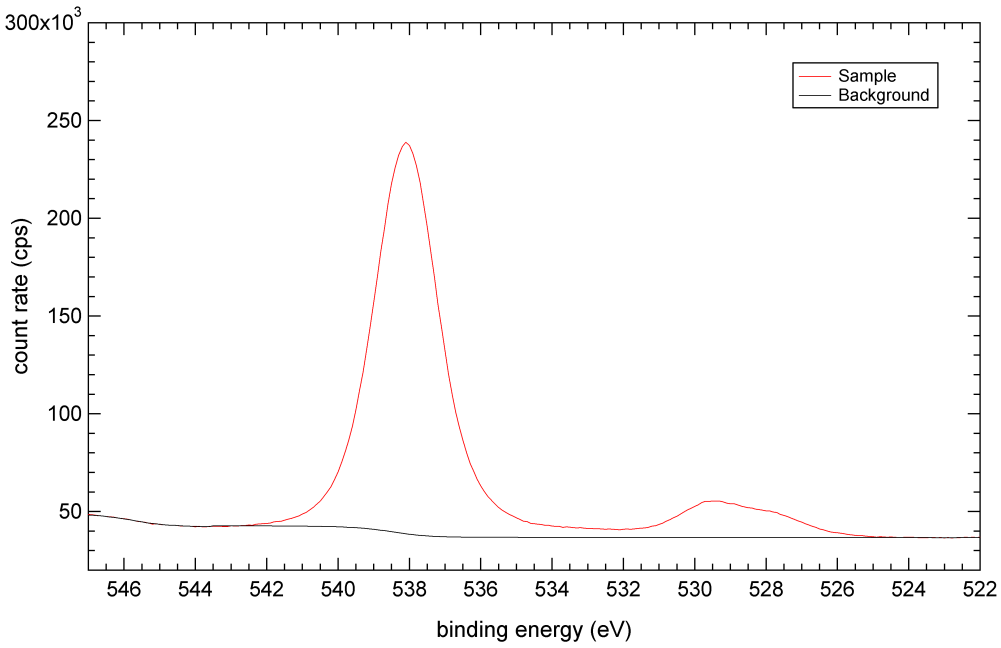

Figure B.11: *O 1s spectrum of the calcium carbonate standard (# 2).*

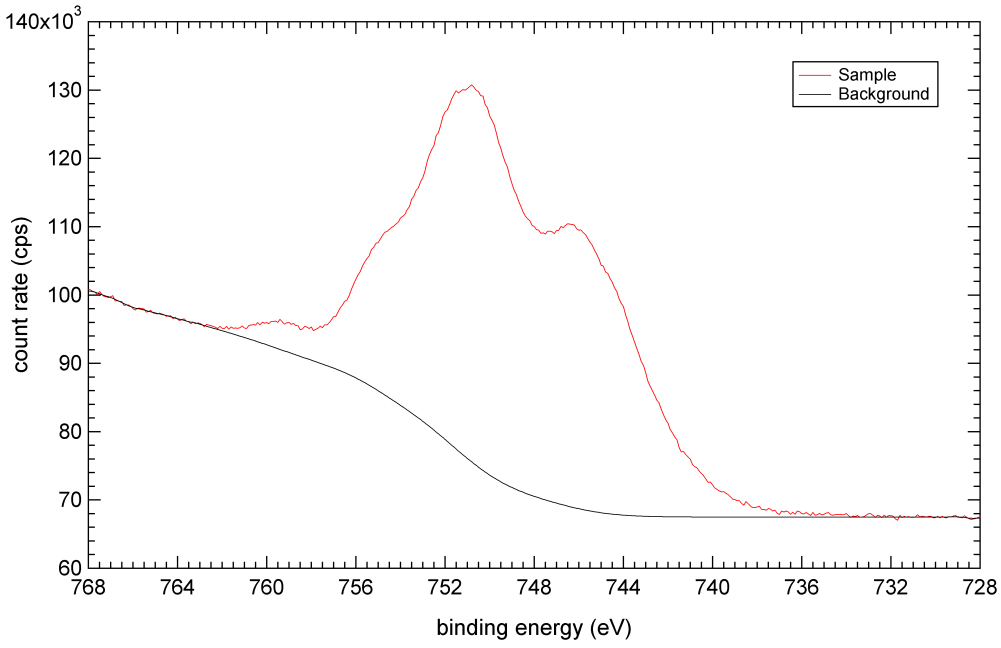

Figure B.12: *O $KL_{2,3}L_{2,3}$ spectrum of the calcium carbonate standard (# 2).*

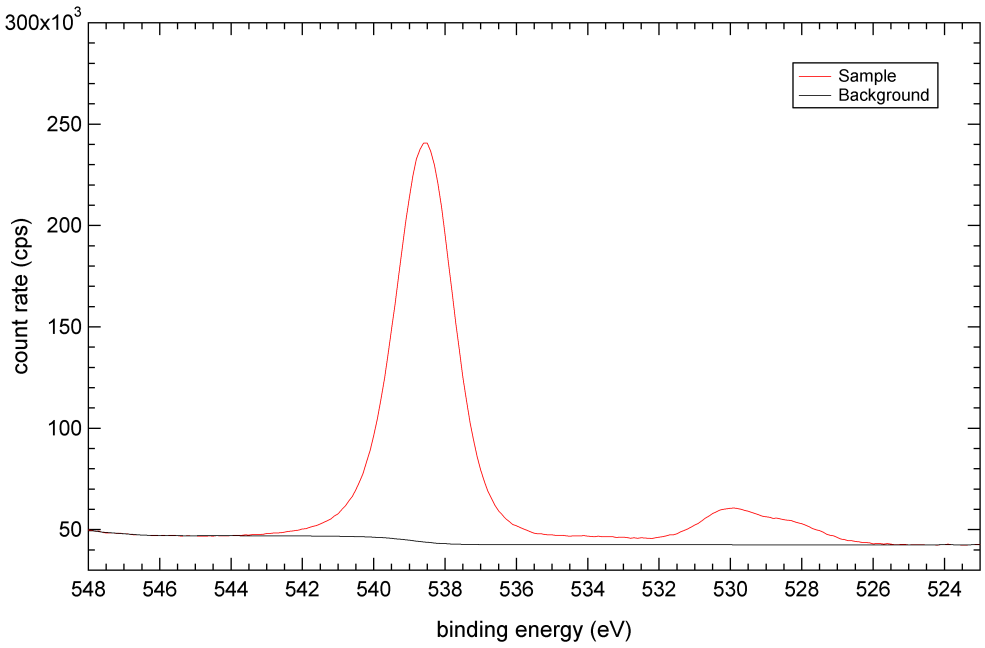

Figure B.13: *O 1s spectrum of the potassium sulphate standard (# 1).*

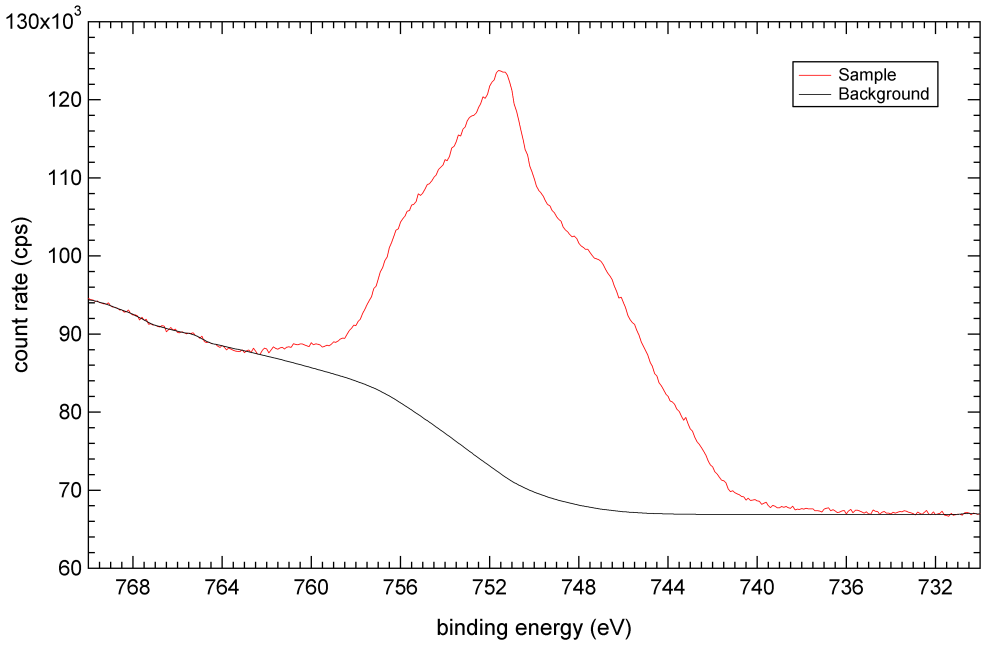

Figure B.14: *O $KL_{2,3}L_{2,3}$ spectrum of the potassium sulphate standard (# 1).*

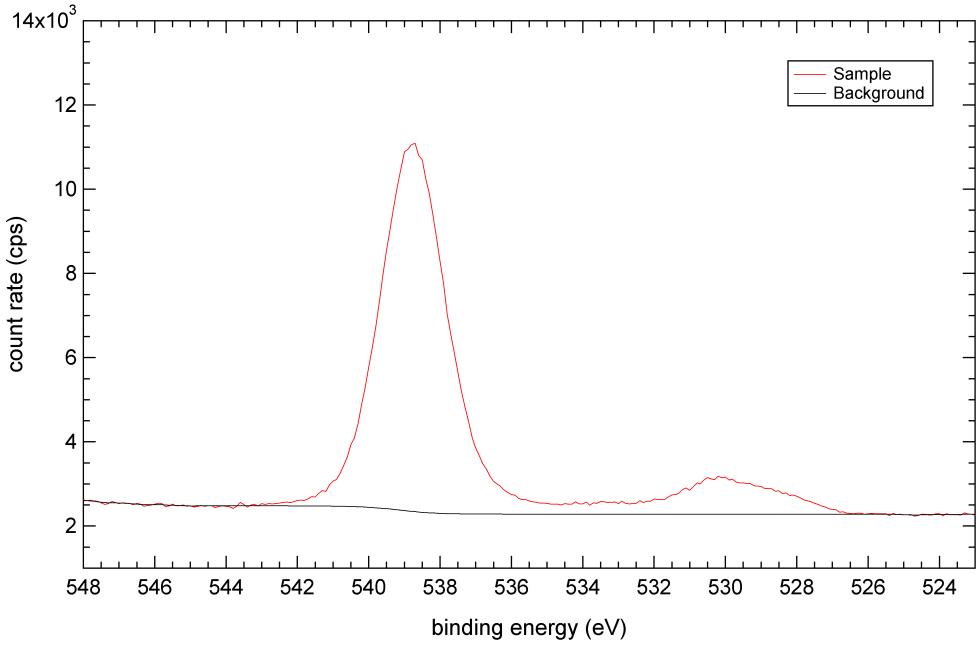

Figure B.15: *O 1s spectrum of the potassium sulphate standard (# 2).*

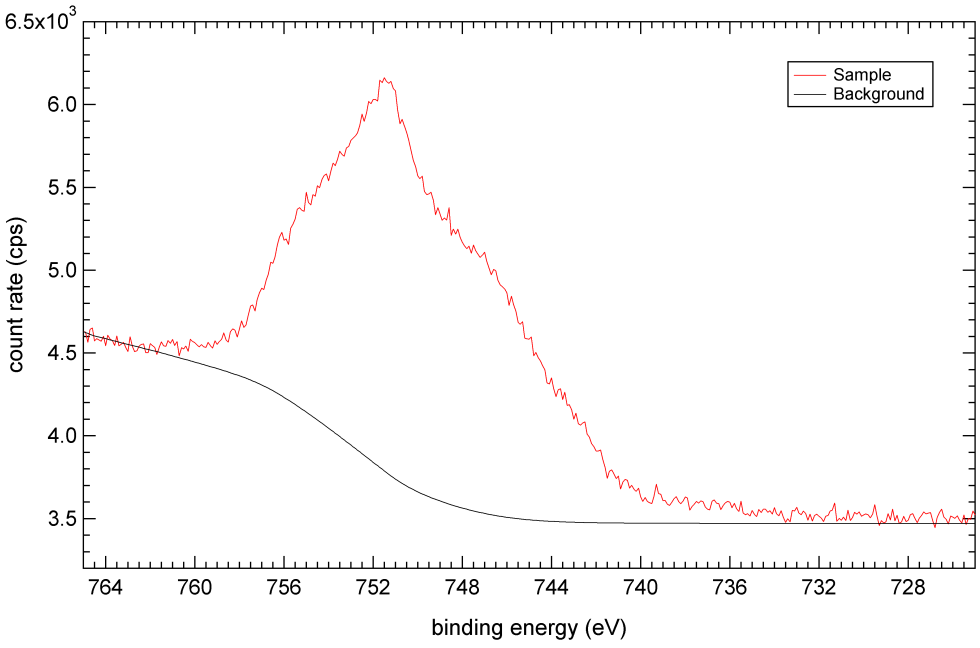

Figure B.16: *O $KL_{2,3}L_{2,3}$ spectrum of the potassium sulphate standard (# 2).*

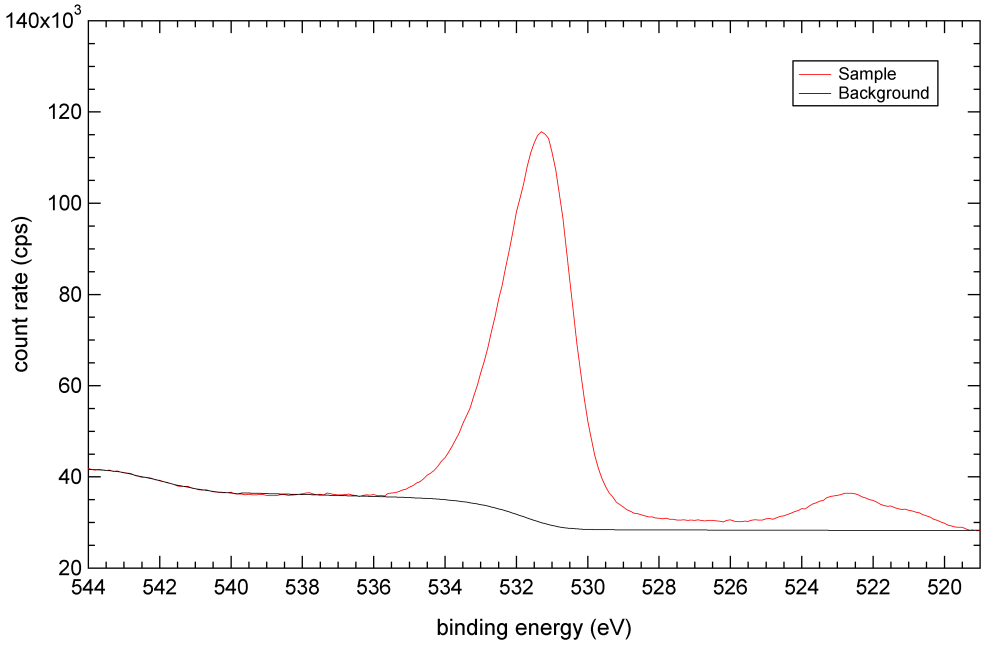

Figure B.17: *O 1s spectrum of the titanium dioxide standard.*

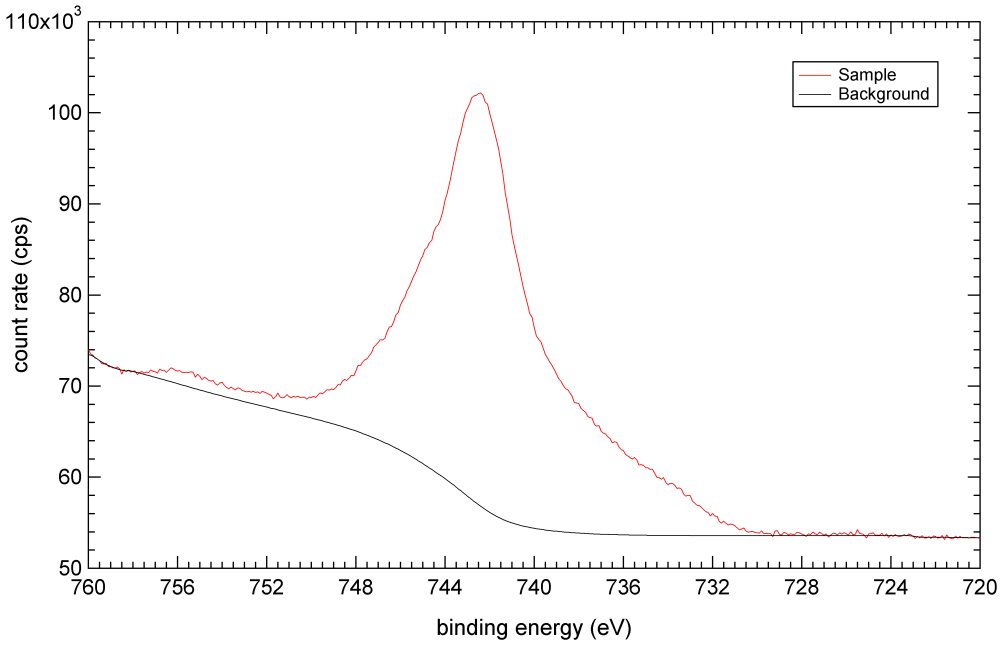

Figure B.18: *O $KL_{2,3}L_{2,3}$ spectrum of the titanium dioxide standard.*

Appendix C

S 2p, Fe 2p, Cu 2p and Si 2s spectra of chalcopyrite after oxidative dissolution

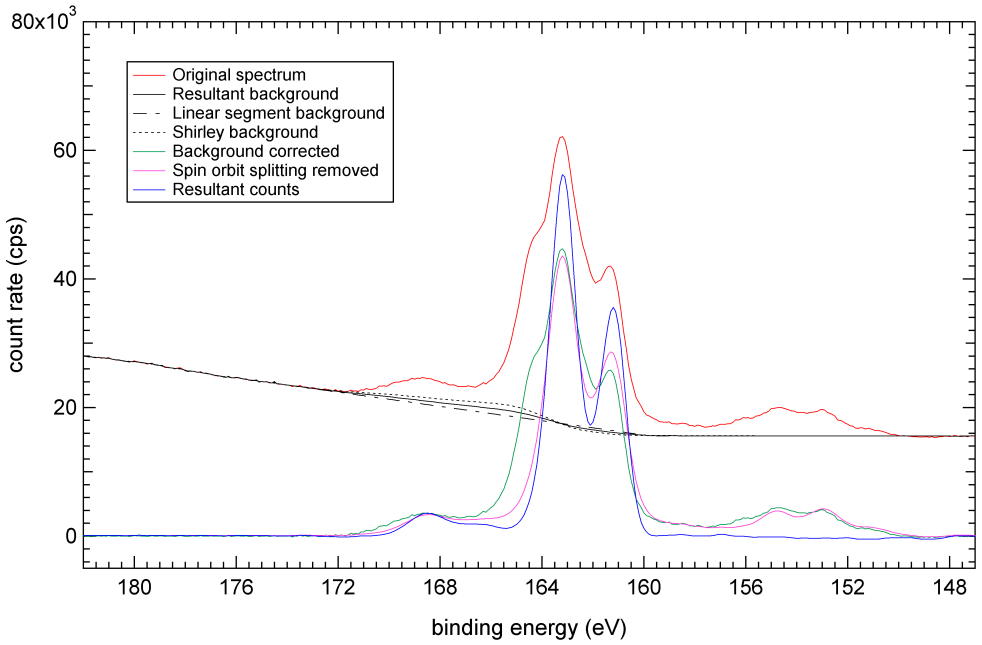

Figure C.1: *S 2p spectrum of chalcopyrite (Mass-p) after oxidative dissolution in 0.1 M ferric sulphate (pH 1.9) at 50° C for 15 minutes.*

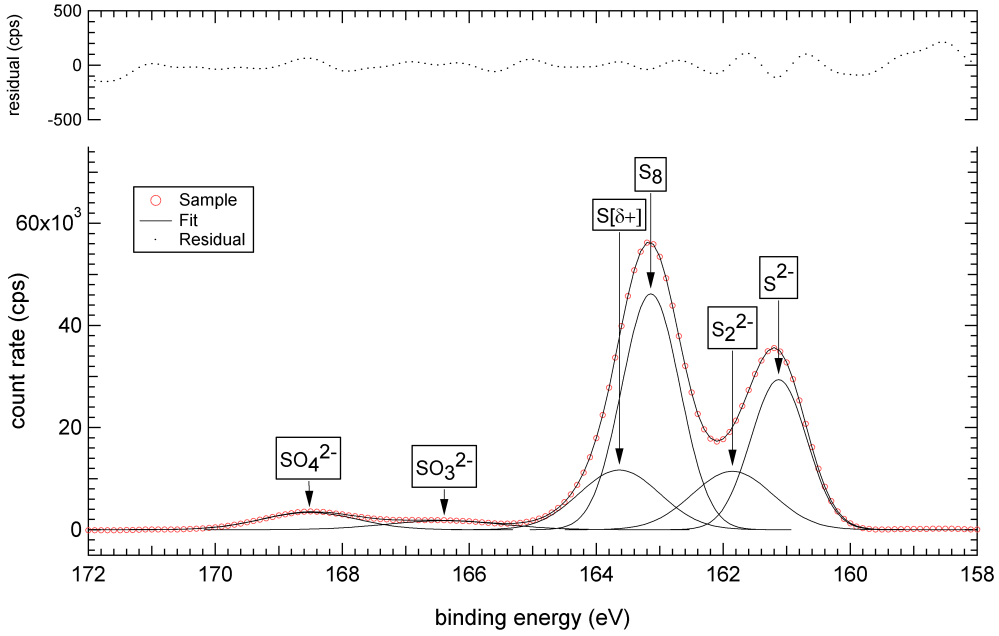

Figure C.2: *Fit of the S 2p spectrum of chalcopyrite (Mass-p) after oxidative dissolution in 0.1 M ferric sulphate (pH 1.9) at 50° C for 15 minutes.*

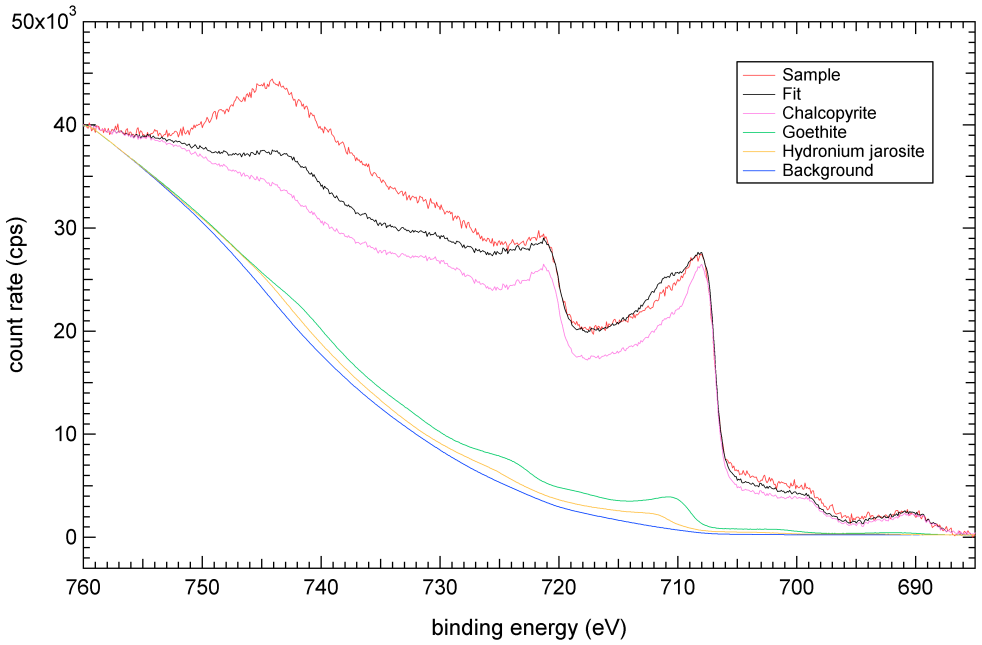

Figure C.3: *Fit of the Fe 2p spectrum of chalcopyrite (Mass-p) after oxidative dissolution in 0.1 M ferric sulphate (pH 1.9) at 50° C for 15 minutes.*

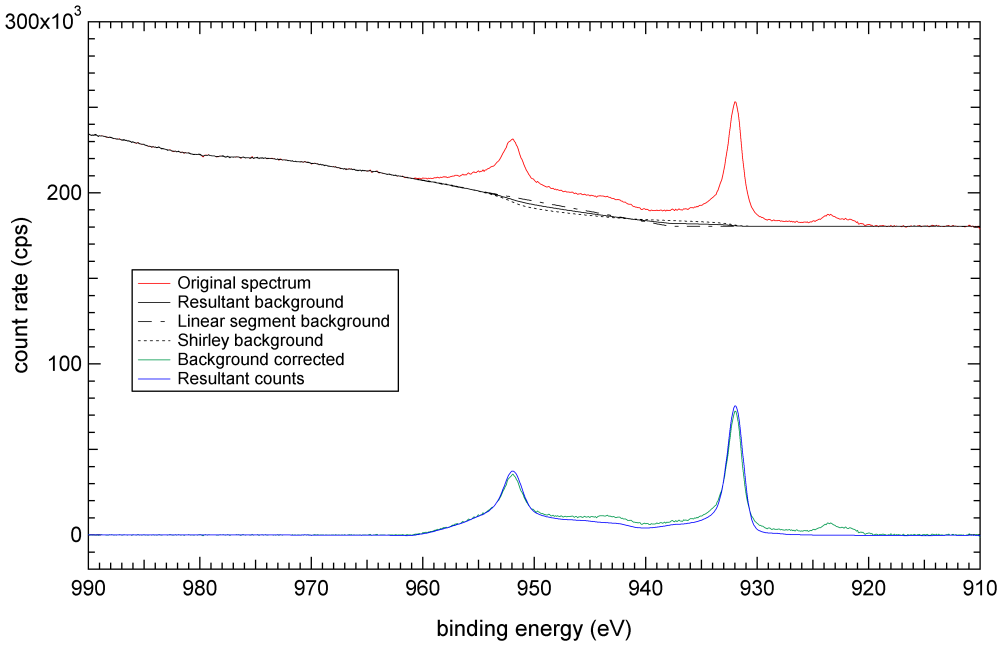

Figure C.4: *Cu 2p spectrum of chalcopyrite (Mass-p) after oxidative dissolution in 0.1 M ferric sulphate (pH 1.9) at 50° C for 15 minutes.*

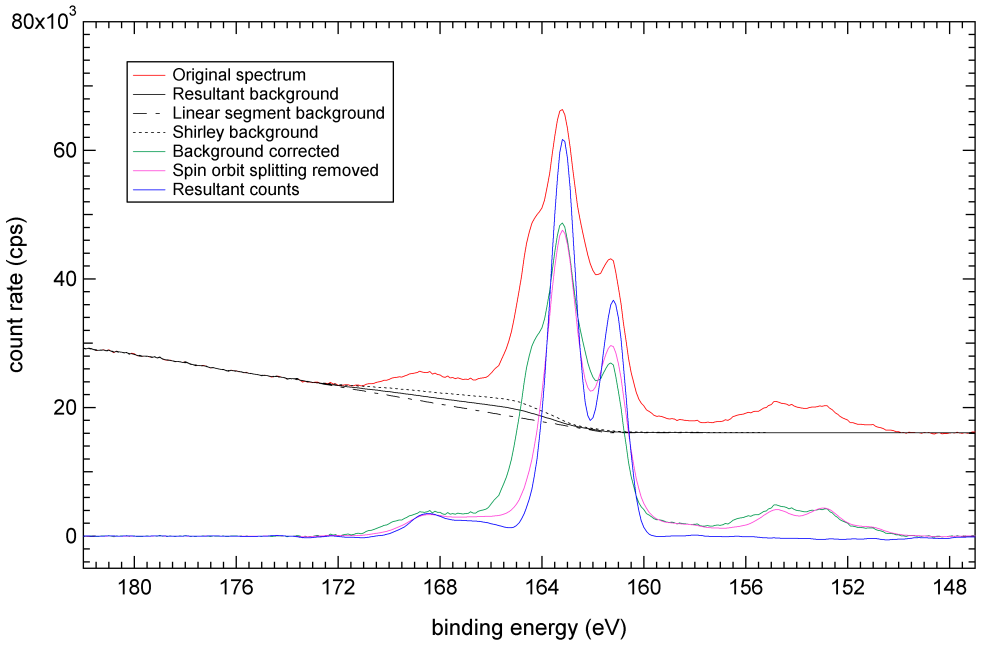

Figure C.5: *S 2p spectrum of chalcopyrite (Mass-p) after oxidative dissolution in 0.1 M ferric sulphate (pH 1.9) at 50° C for 30 minutes.*

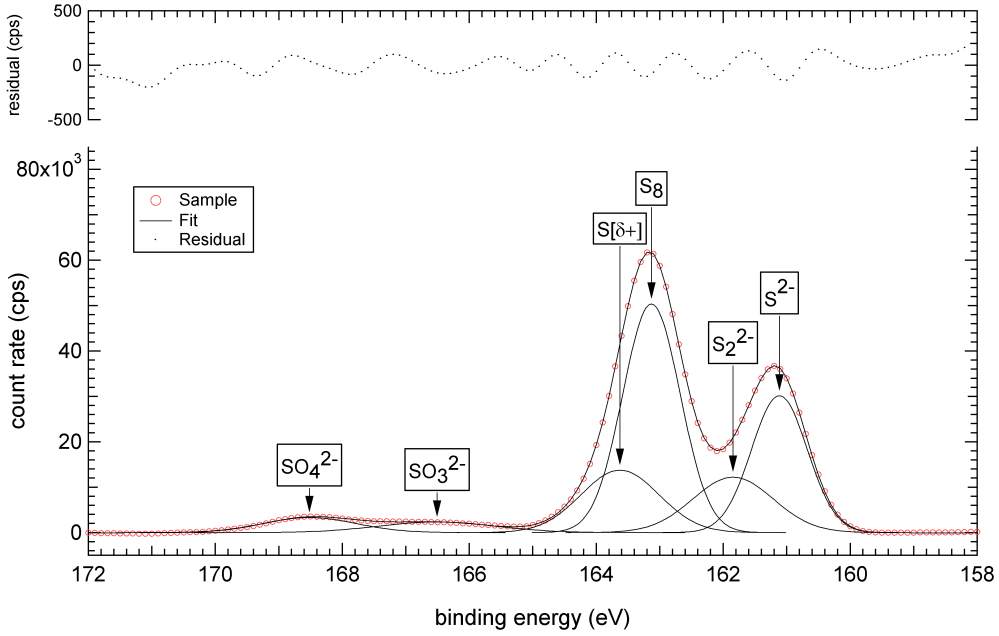

Figure C.6: *Fit of the S 2p spectrum of chalcopyrite (Mass-p) after oxidative dissolution in 0.1 M ferric sulphate (pH 1.9) at 50° C for 30 minutes.*

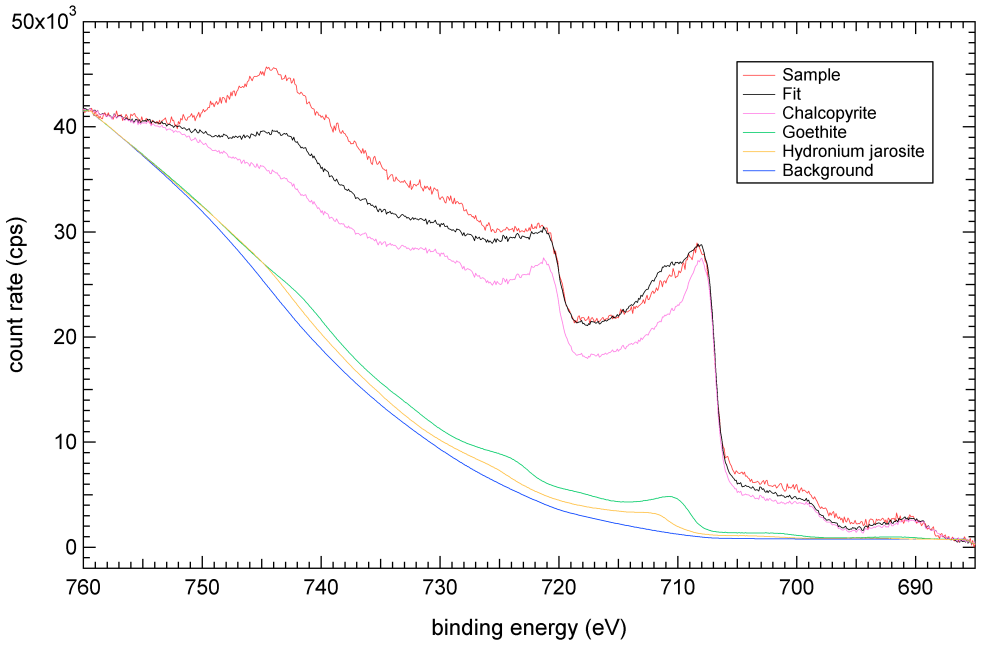

Figure C.7: *Fit of the Fe 2p spectrum of chalcopyrite (Mass-p) after oxidative dissolution in 0.1 M ferric sulphate (pH 1.9) at 50° C for 30 minutes.*

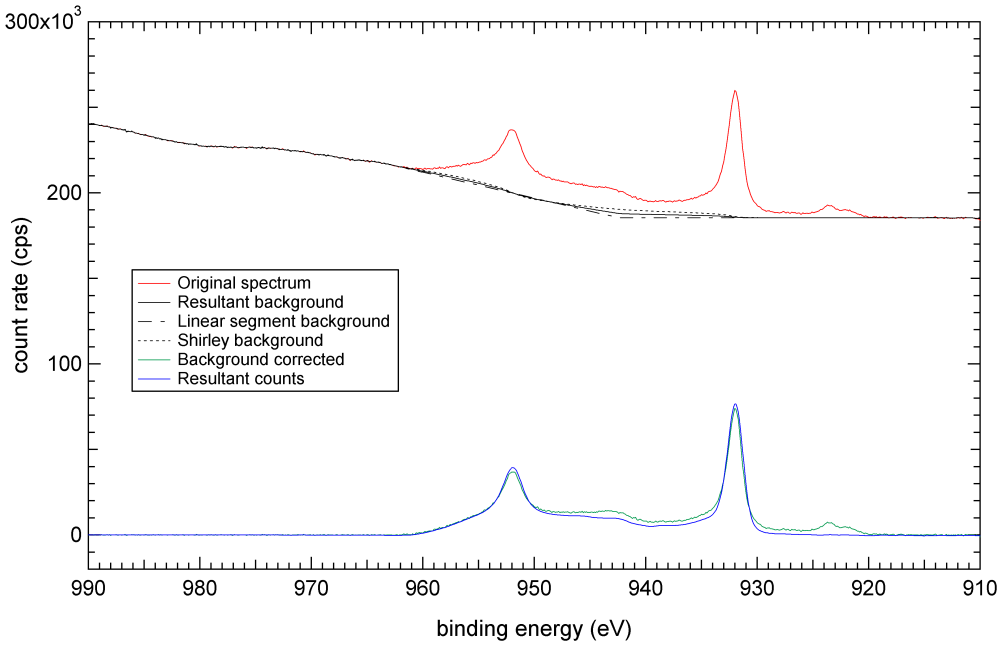

Figure C.8: *Cu 2p spectrum of chalcopyrite (Mass-p) after oxidative dissolution in 0.1 M ferric sulphate (pH 1.9) at 50° C for 30 minutes.*

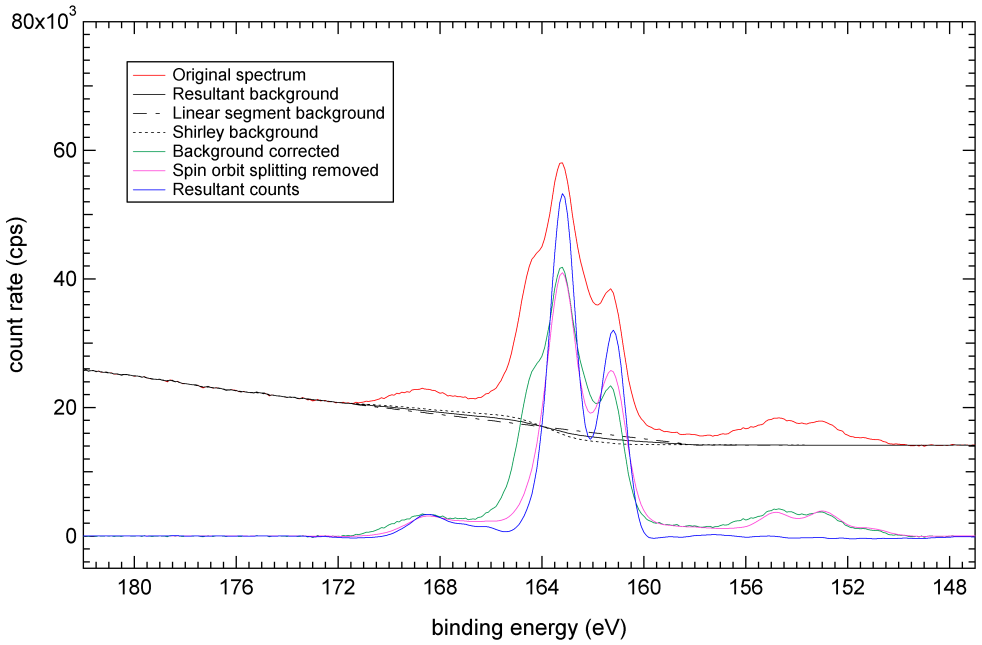

Figure C.9: *S 2p spectrum of chalcopyrite (Mass-p) after oxidative dissolution in 0.1 M ferric sulphate (pH 1.9) at 50° C for 60 minutes.*

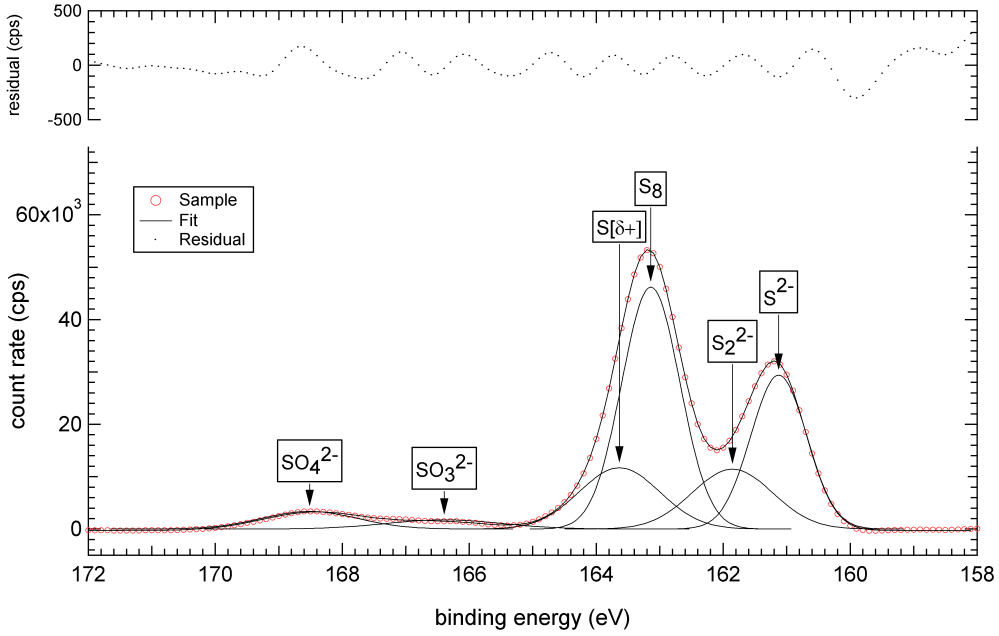

Figure C.10: *Fit of the S 2p spectrum of chalcopyrite (Mass-p) after oxidative dissolution in 0.1 M ferric sulphate (pH 1.9) at 50° C for 60 minutes.*

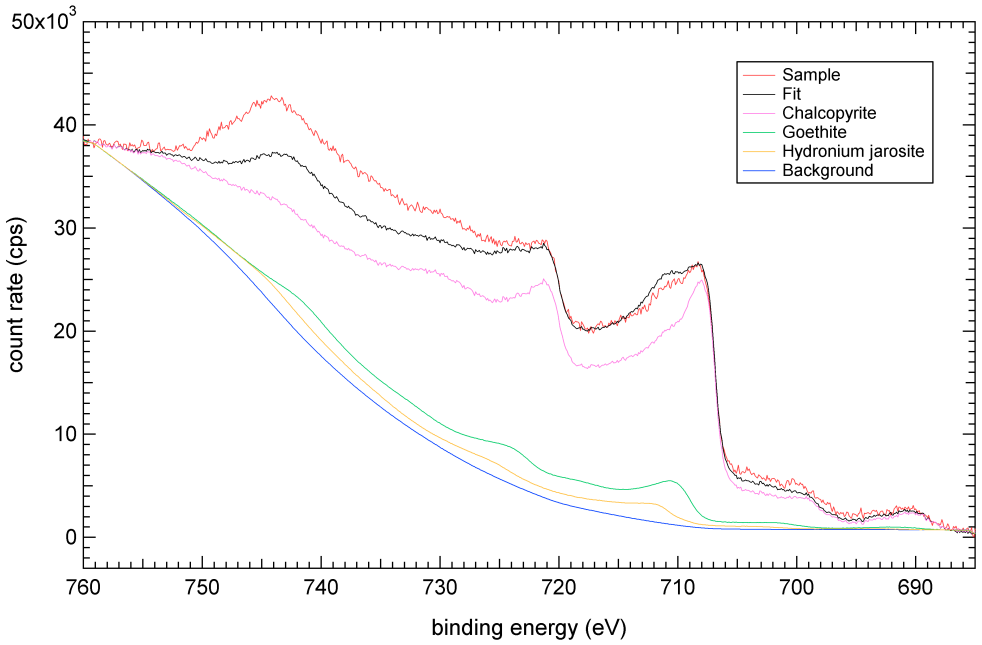

Figure C.11: *Fit of the Fe 2p spectrum of chalcopyrite (Mass-p) after oxidative dissolution in 0.1 M ferric sulphate (pH 1.9) at 50° C for 60 minutes.*

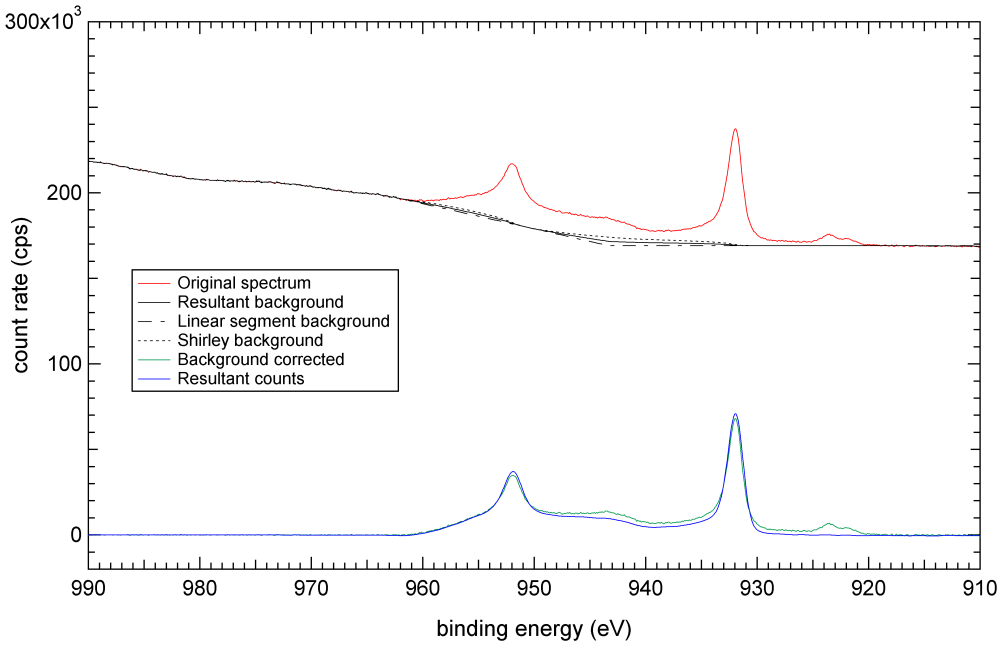

Figure C.12: *Cu 2p spectrum of chalcopyrite (Mass-p) after oxidative dissolution in 0.1 M ferric sulphate (pH 1.9) at 50° C for 60 minutes.*

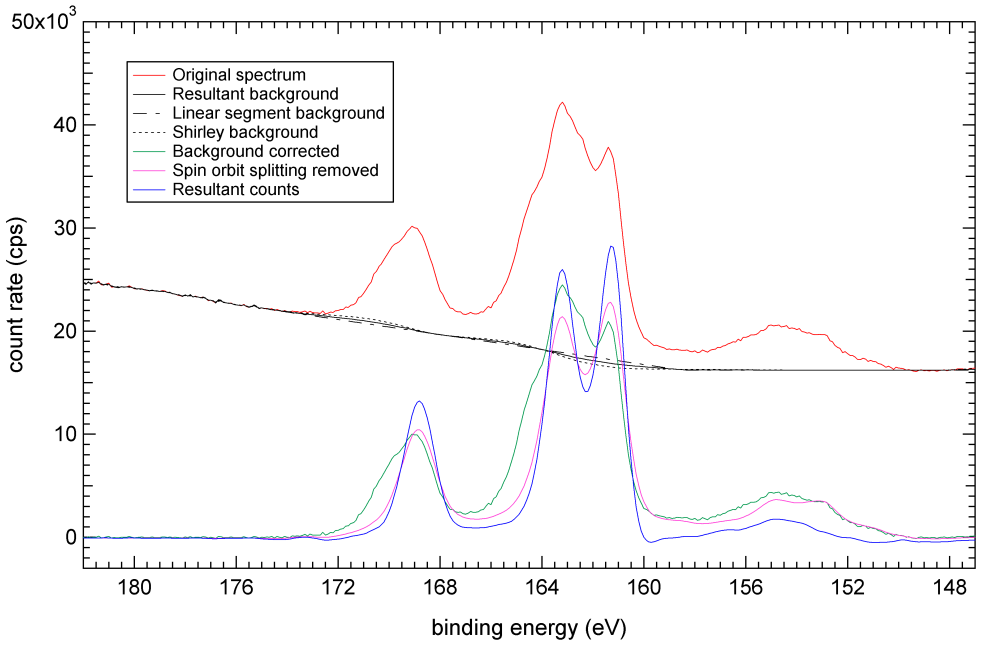

Figure C.13: *S 2p spectrum of chalcopyrite (Con-p) after oxidative dissolution in 0.1 M ferric sulphate (pH 1.9) at 50° C for 2 hours.*

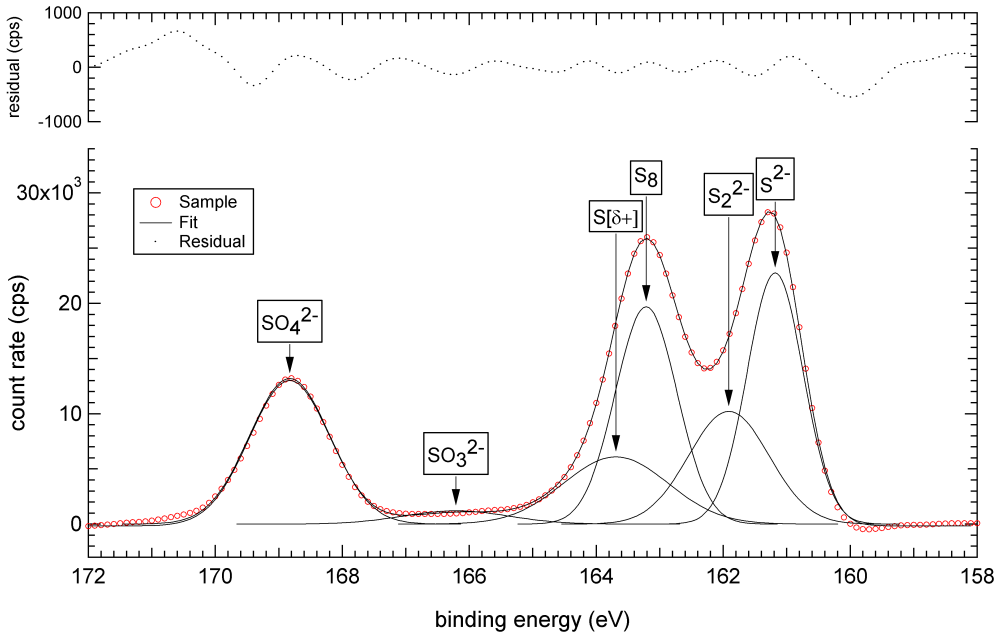

Figure C.14: *Fit of the S 2p spectrum of chalcopyrite (Con-p) after oxidative dissolution in 0.1 M ferric sulphate (pH 1.9) at 50° C for 2 hours.*

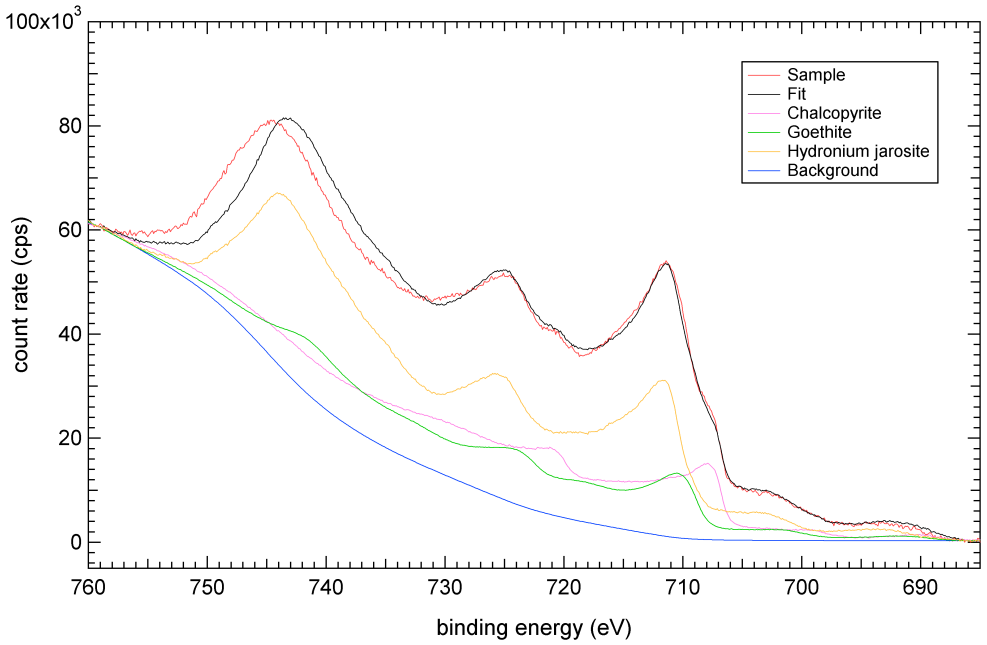

Figure C.15: *Fit of the Fe 2p spectrum of chalcopyrite (Con-p) after oxidative dissolution in 0.1 M ferric sulphate (pH 1.9) at 50° C for 2 hours.*

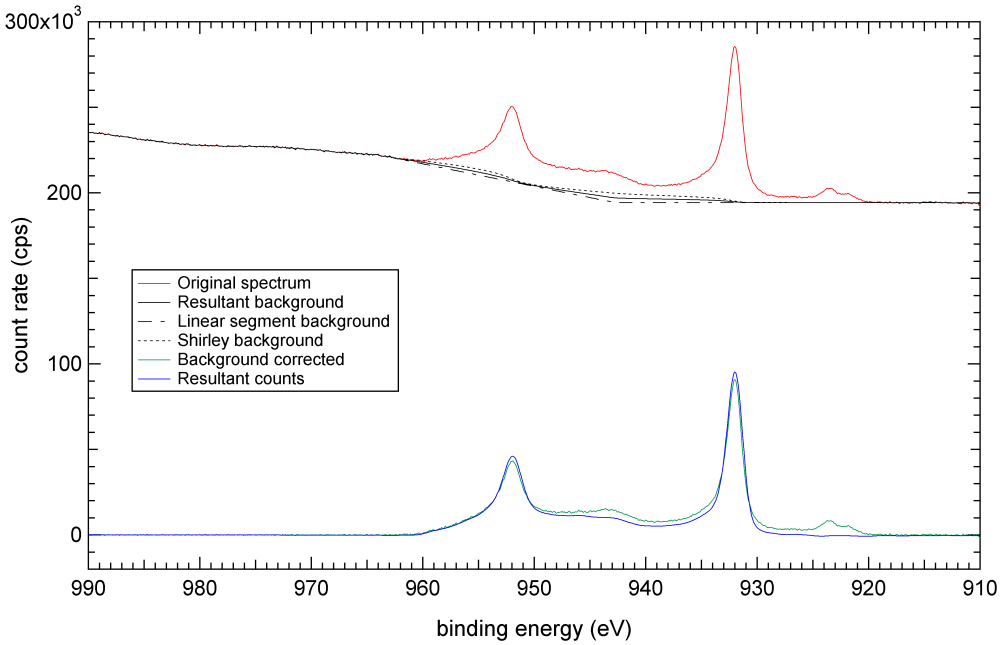

Figure C.16: *Cu 2p spectrum of chalcopyrite (Con-p) after oxidative dissolution in 0.1 M ferric sulphate (pH 1.9) at 50° C for 2 hours.*

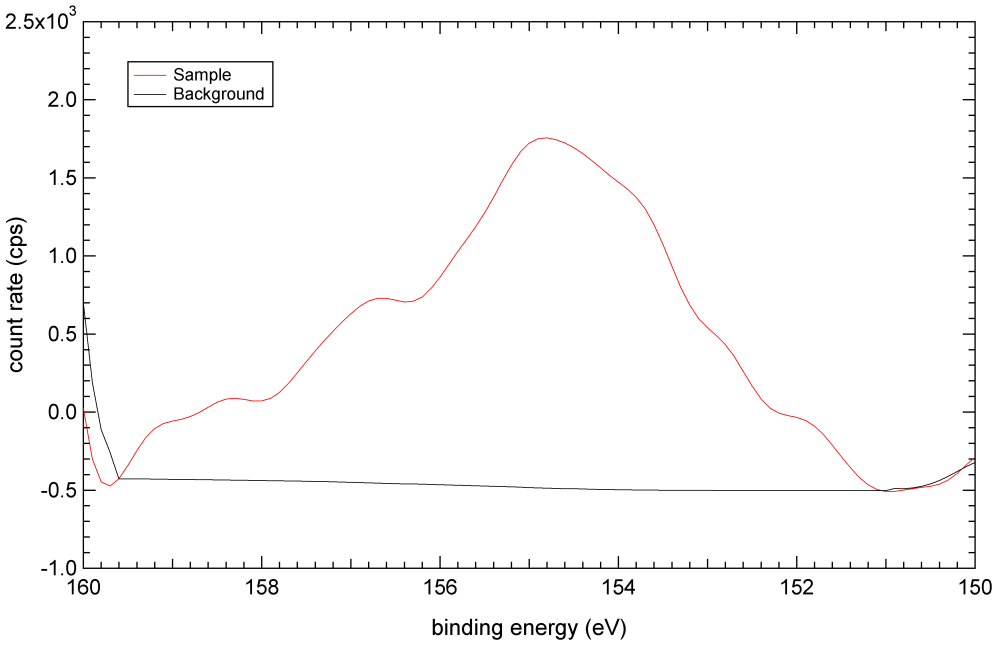

Figure C.17: *Si 2s spectrum of chalcopyrite (Con-p) after oxidative dissolution in 0.1 M ferric sulphate (pH 1.9) at 50° C for 2 hours.*

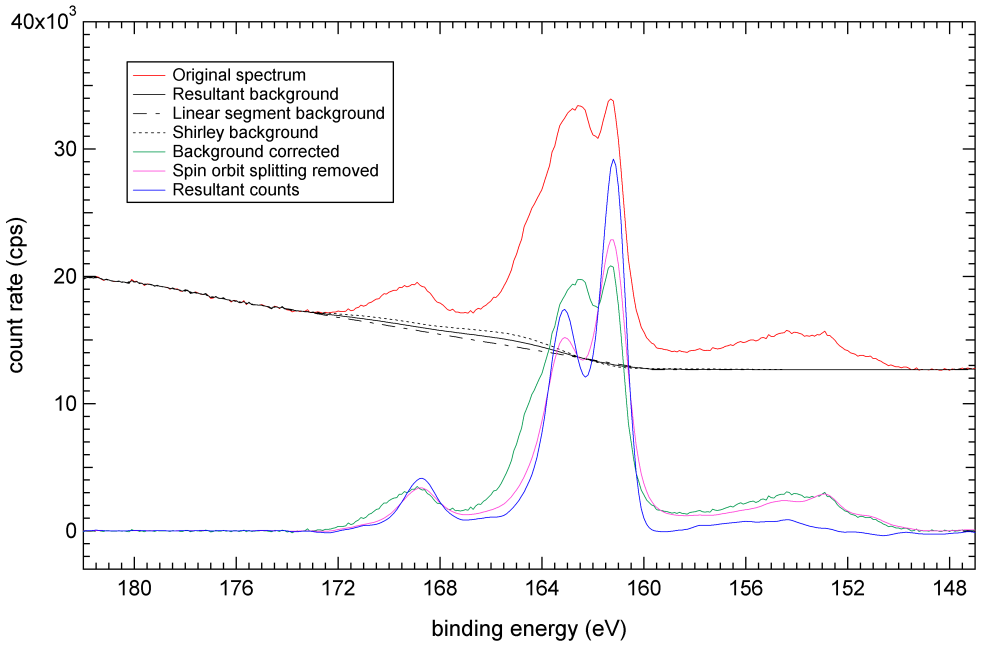

Figure C.18: *S 2p spectrum of chalcopyrite (Con-p) after oxidative dissolution in 0.1 M ferric sulphate (pH 1.3) at 50° C for 2 hours.*

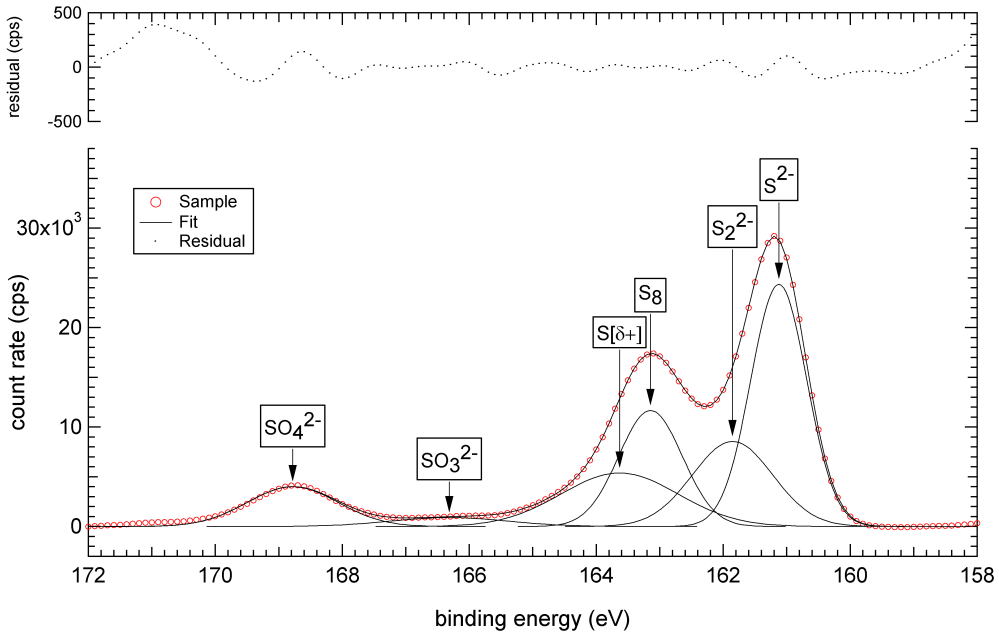

Figure C.19: *Fit of the S 2p spectrum of chalcopyrite (Con-p) after oxidative dissolution in 0.1 M ferric sulphate (pH 1.3) at 50° C for 2 hours.*

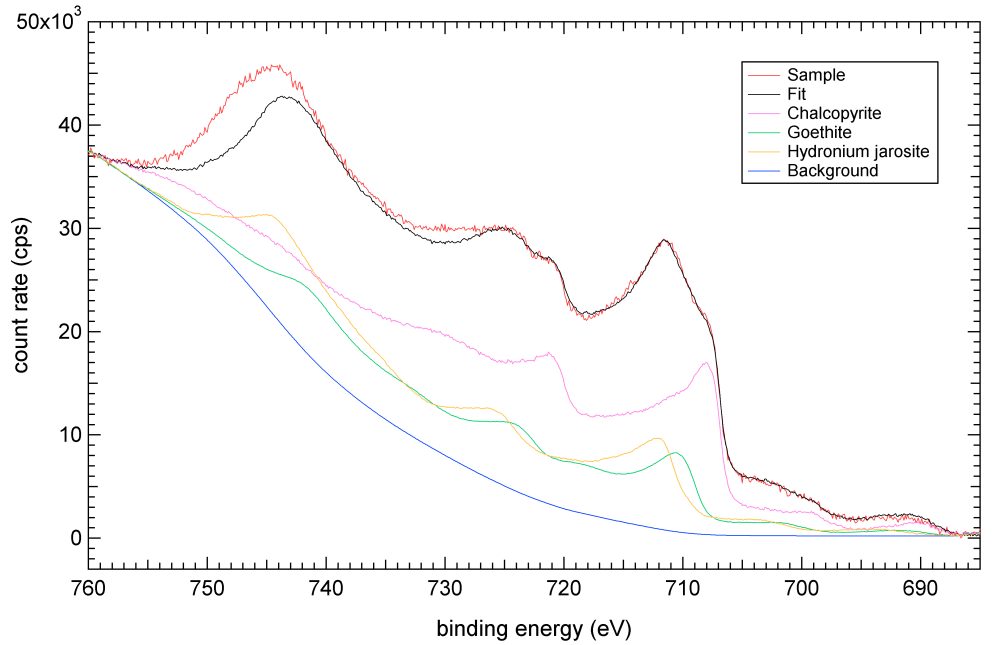

Figure C.20: *Fit of the Fe 2p spectrum of chalcopyrite (Con-p) after oxidative dissolution in 0.1 M ferric sulphate (pH 1.3) at 50° C for 2 hours.*

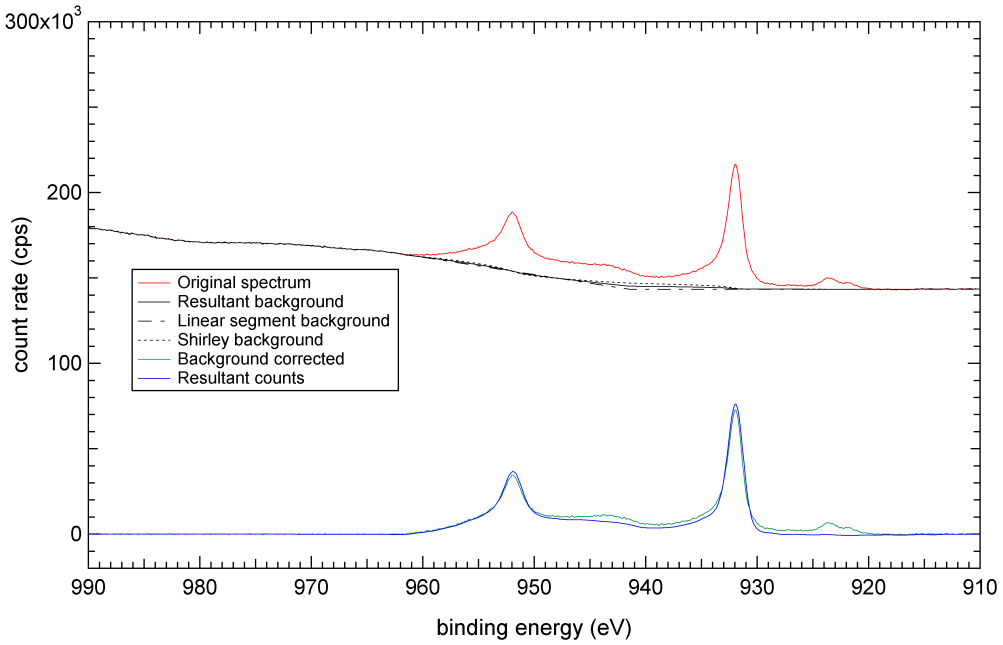

Figure C.21: *Cu 2p spectrum of chalcopyrite (Con-p) after oxidative dissolution in 0.1 M ferric sulphate (pH 1.3) at 50° C for 2 hours.*

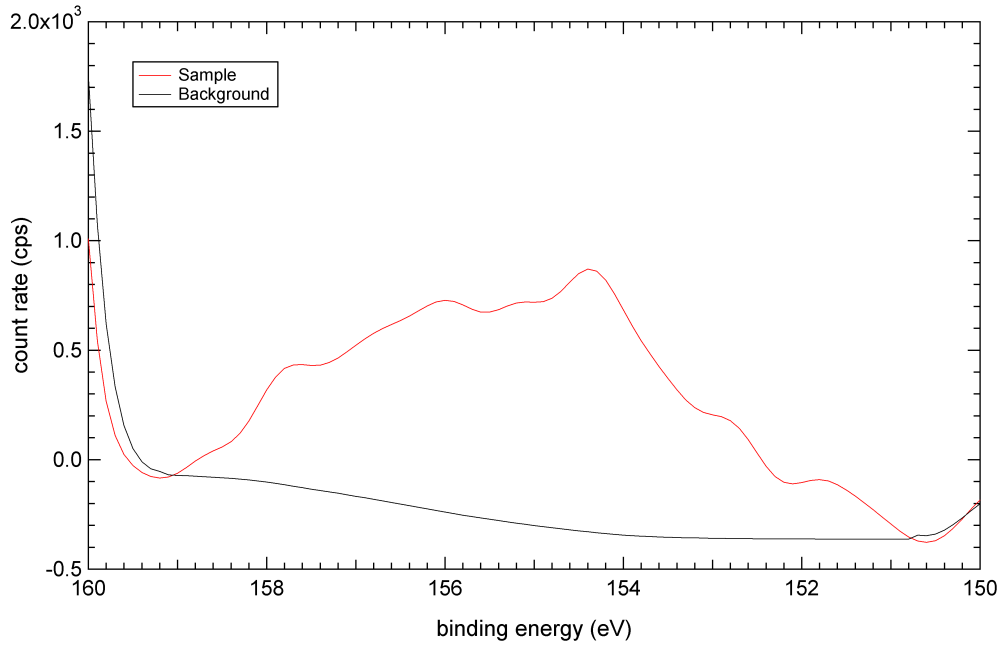

Figure C.22: *Si 2s spectrum of chalcopyrite (Mass-p) after oxidative dissolution in 0.1 M ferric sulphate (pH 1.3) at 50° C for 2 hours.*

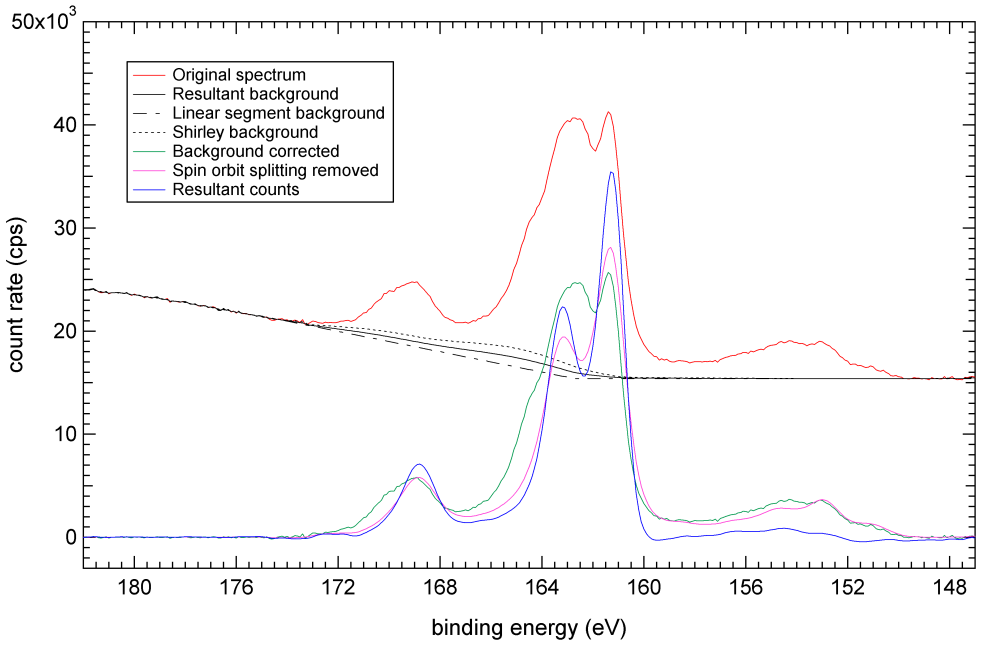

Figure C.23: *S 2p spectrum of chalcopyrite (Con-p) after oxidative dissolution in 0.1 M ferric sulphate (pH 1.3) at 65° C for 2 hours.*

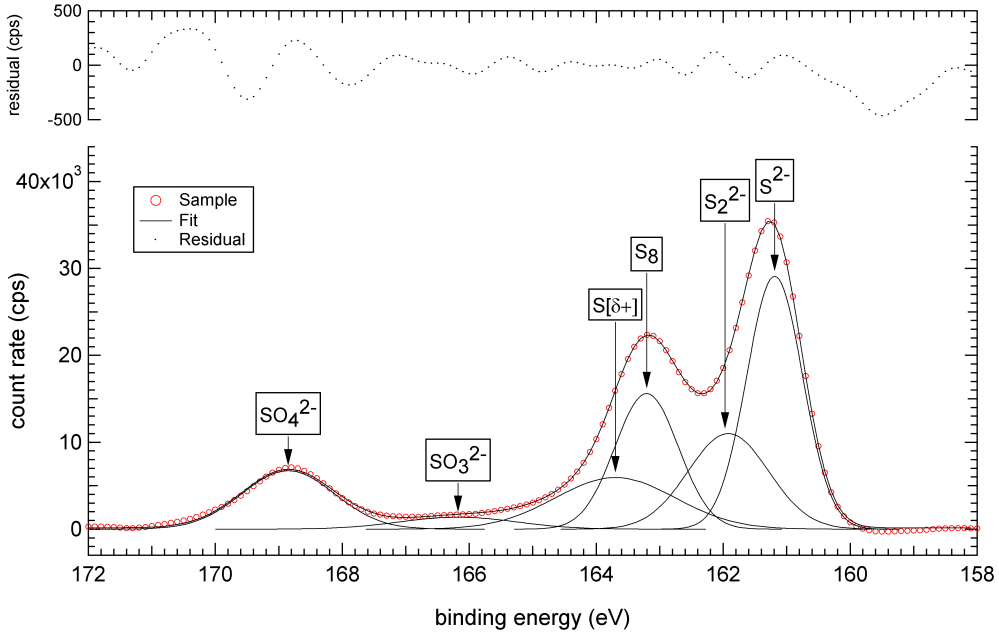

Figure C.24: *Fit of the S 2p spectrum of chalcopyrite (Con-p) after oxidative dissolution in 0.1 M ferric sulphate (pH 1.3) at 65° C for 2 hours.*

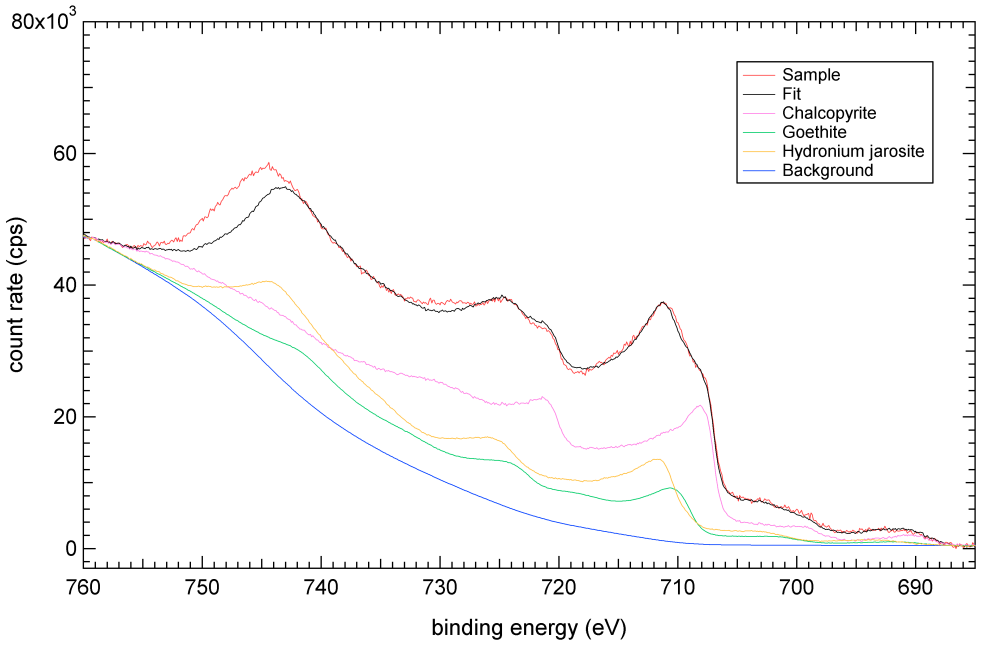

Figure C.25: *Fit of the Fe 2p spectrum of chalcopyrite (Con-p) after oxidative dissolution in 0.1 M ferric sulphate (pH 1.3) at 65° C for 2 hours.*

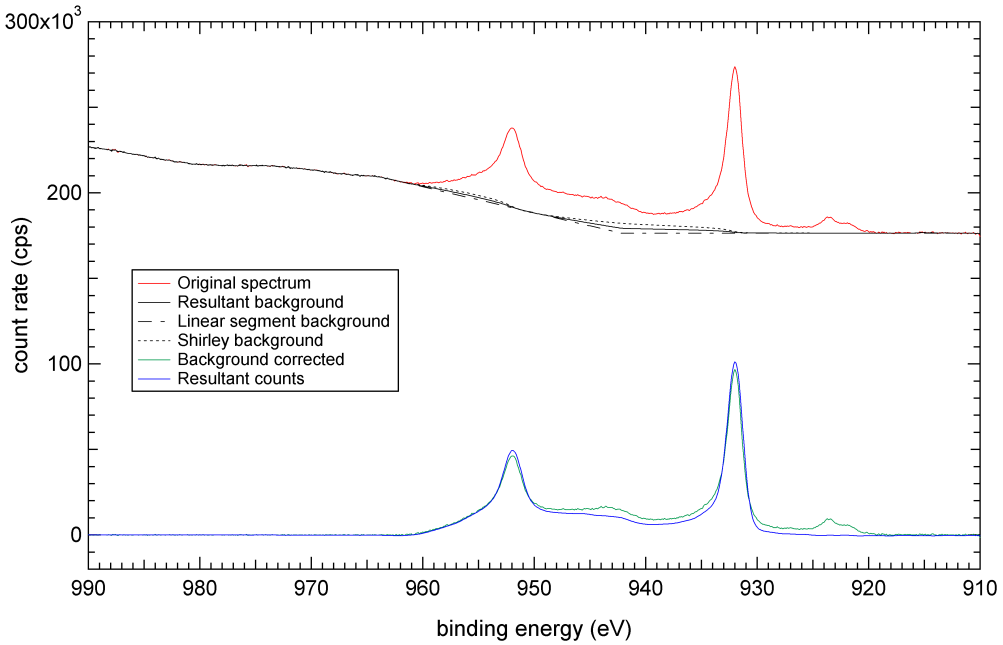

Figure C.26: *Cu 2p spectrum of chalcopyrite (Con-p) after oxidative dissolution in 0.1 M ferric sulphate (pH 1.3) at 65° C for 2 hours.*

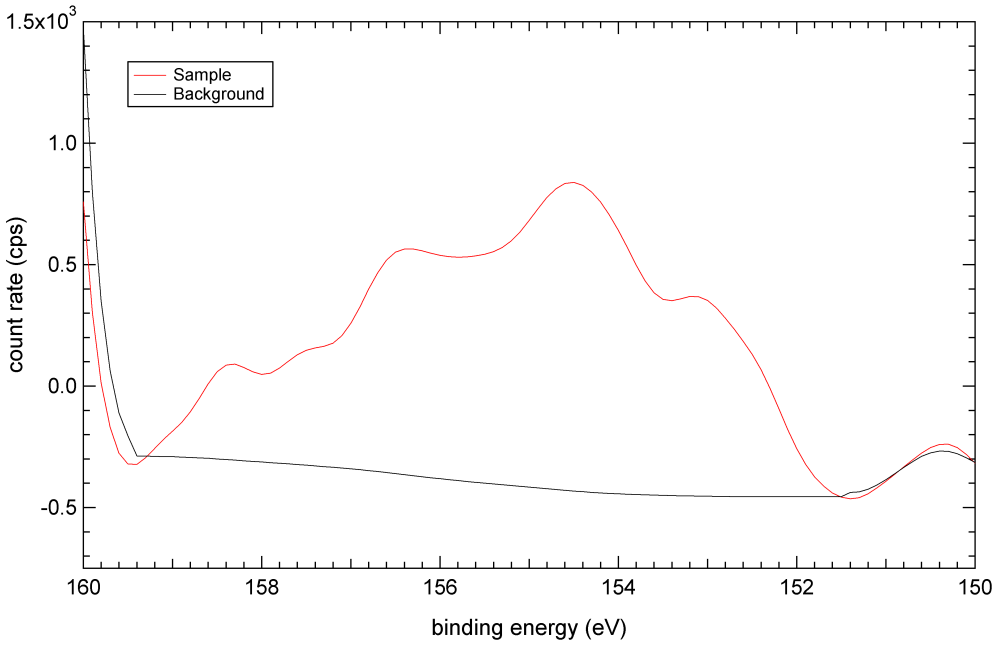

Figure C.27: *Si 2s spectrum of chalcopyrite (Mass-p) after oxidative dissolution in 0.1 M ferric sulphate (pH 1.3) at 65° C for 2 hours.*

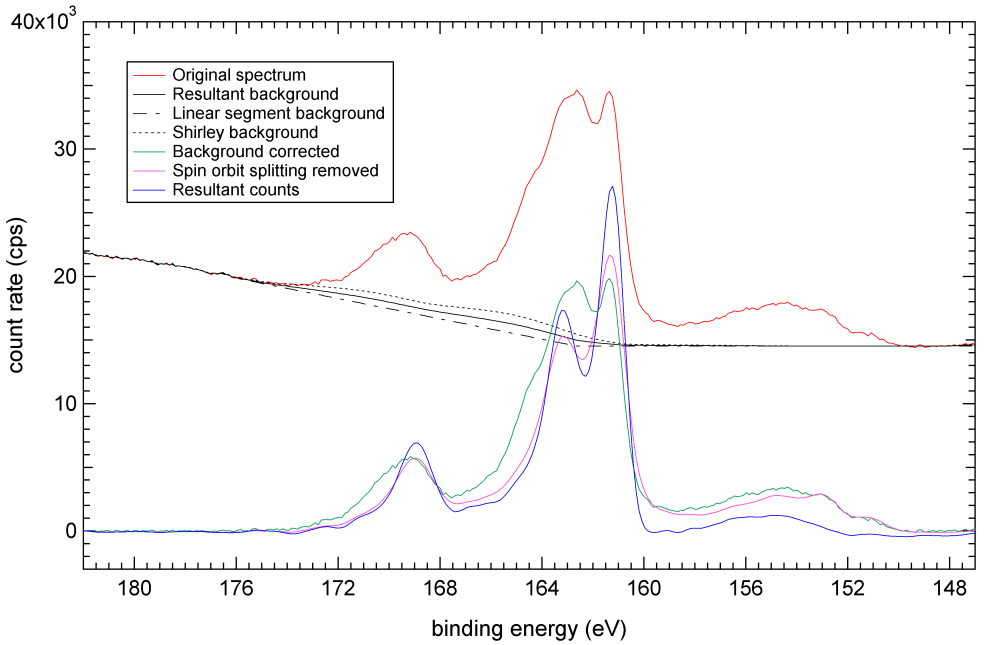

Figure C.28: *S 2p spectrum of chalcopyrite (Con-p) after oxidative dissolution in 0.1 M ferric sulphate (pH 1.3) at 80° C for 2 hours.*

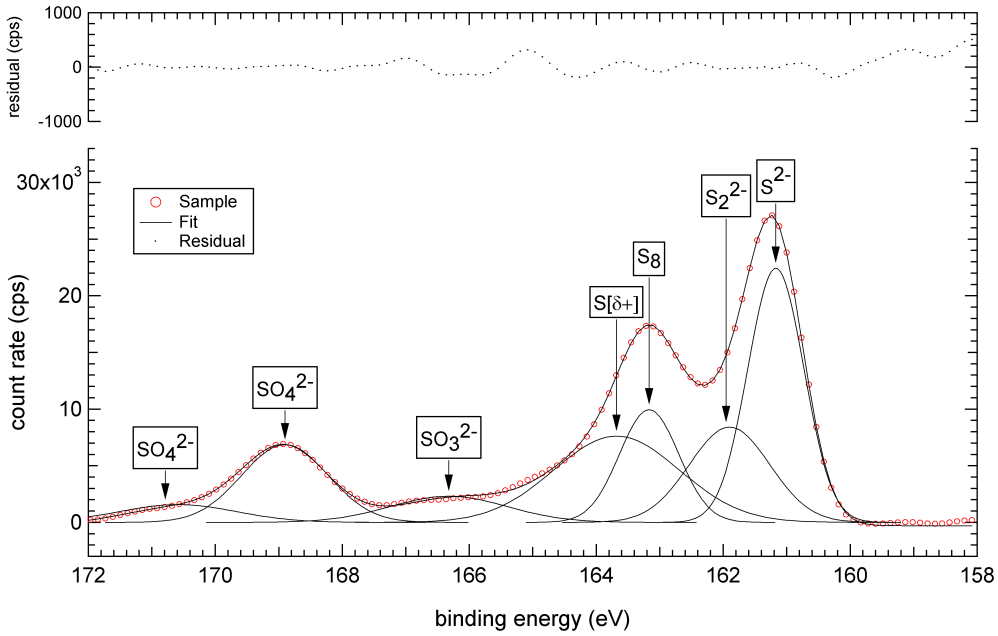

Figure C.29: *Fit of the S 2p spectrum of chalcopyrite (Con-p) after oxidative dissolution in 0.1 M ferric sulphate (pH 1.3) at 80° C for 2 hours.*

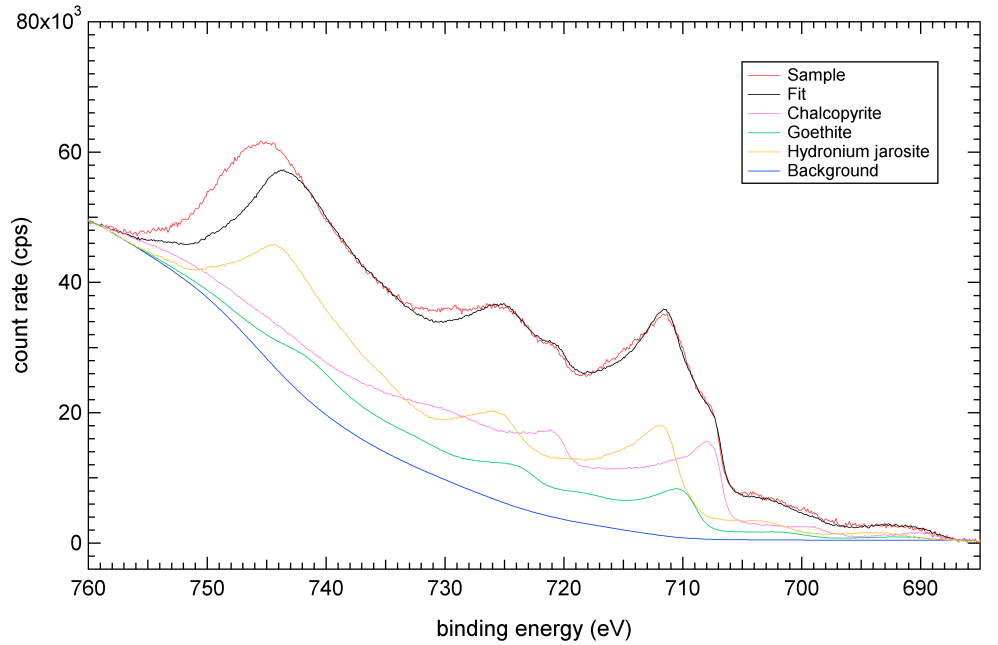

Figure C.30: *Fit of the Fe 2p spectrum of chalcopyrite (Con-p) after oxidative dissolution in 0.1 M ferric sulphate (pH 1.3) at 80° C for 2 hours.*

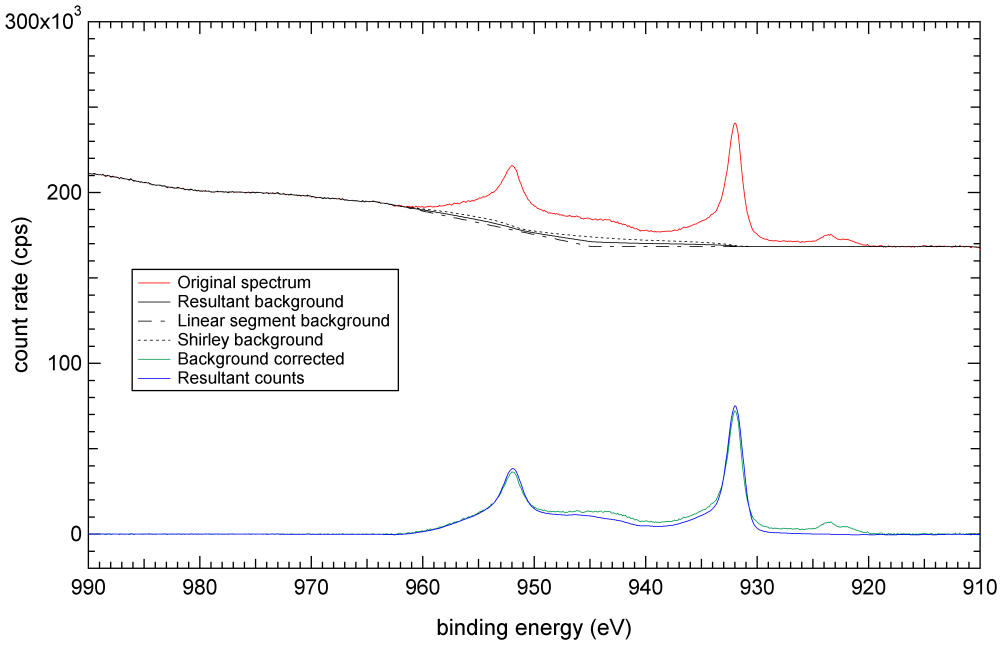

Figure C.31: *Cu 2p spectrum of chalcopyrite (Con-p) after oxidative dissolution in 0.1 M ferric sulphate (pH 1.3) at 80° C for 2 hours.*

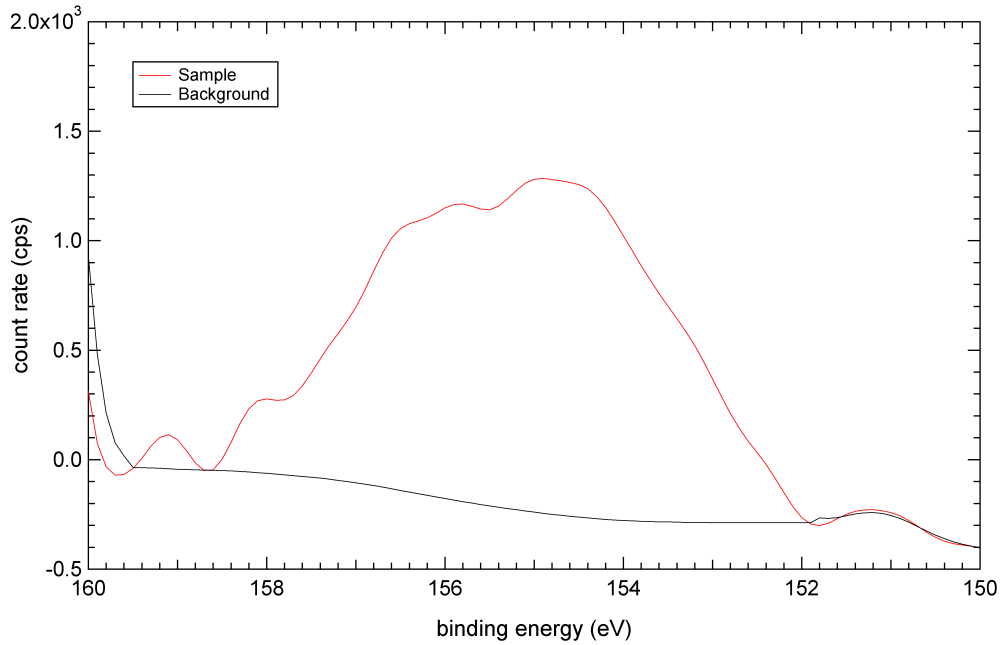

Figure C.32: *Si 2s spectrum of chalcopyrite (Con-p) after oxidative dissolution in 0.1 M ferric sulphate (pH 1.3) at 80° C for 2 hours.*

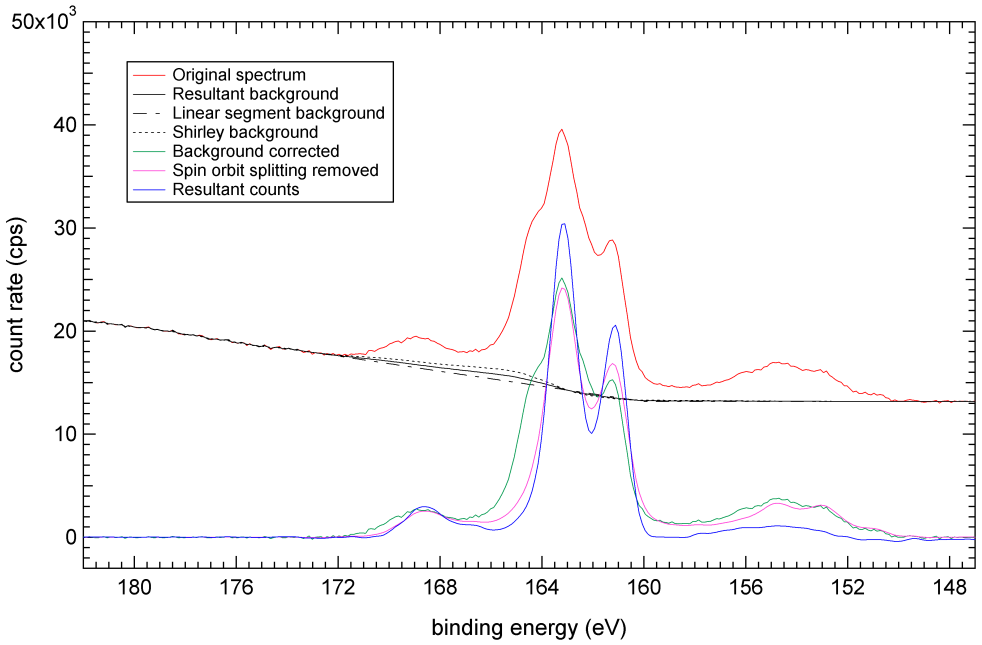

Figure C.33: *S 2p spectrum of chalcopyrite (Con-p) after oxidative dissolution in 0.2 M ferric chloride (pH 1.3) at 50° C for 2 hours.*

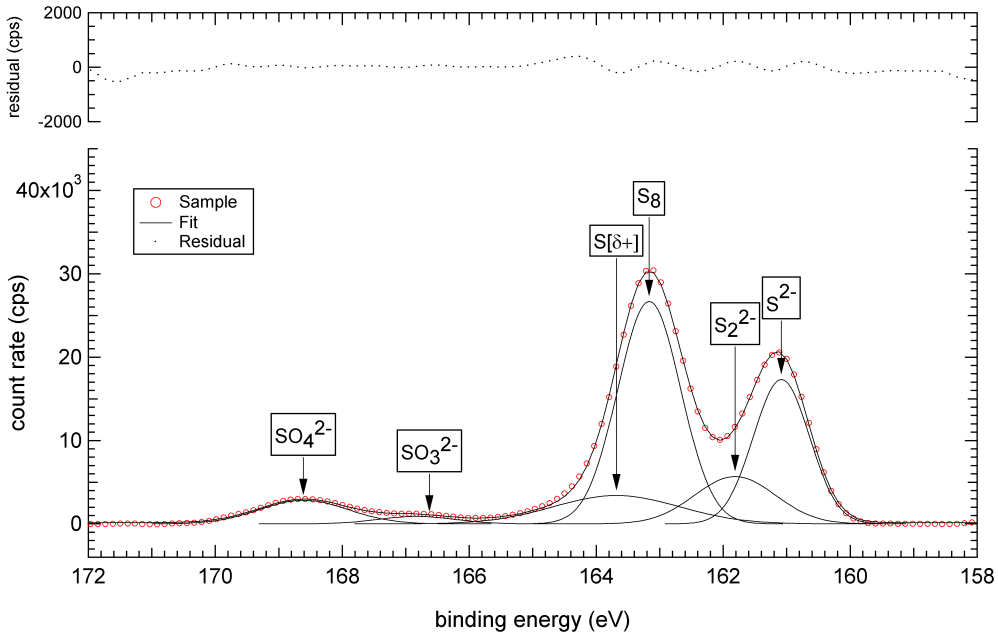

Figure C.34: *Fit of the S 2p spectrum of chalcopyrite (Con-p) after oxidative dissolution in 0.2 M ferric chloride (pH 1.3) at 50° C for 2 hours.*

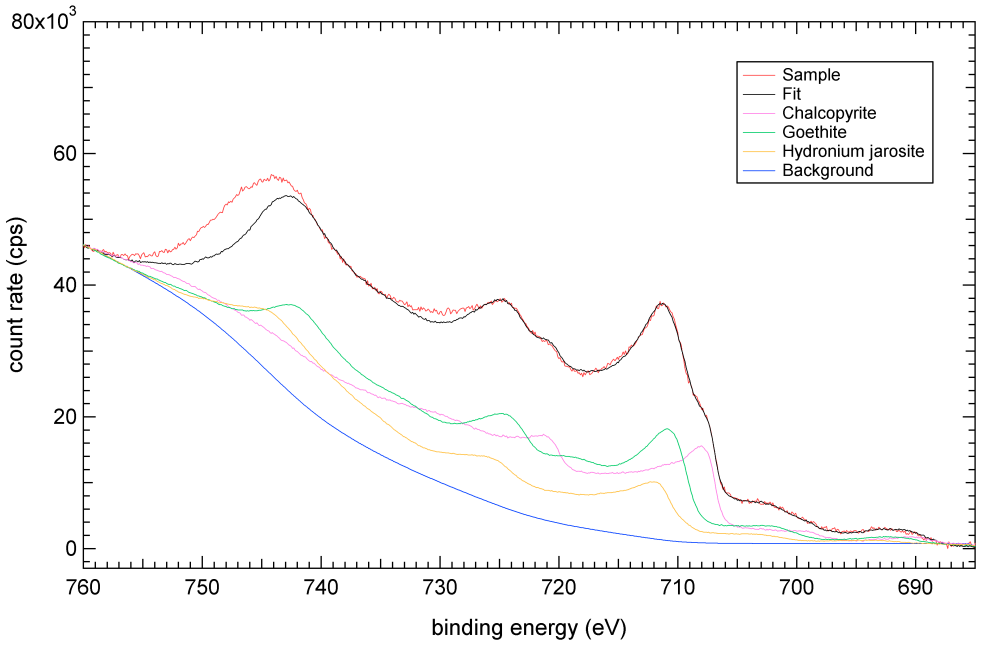

Figure C.35: *Fit of the Fe 2p spectrum of chalcopyrite (Con-p) after oxidative dissolution in 0.2 M ferric chloride (pH 1.3) at 50° C for 2 hours.*

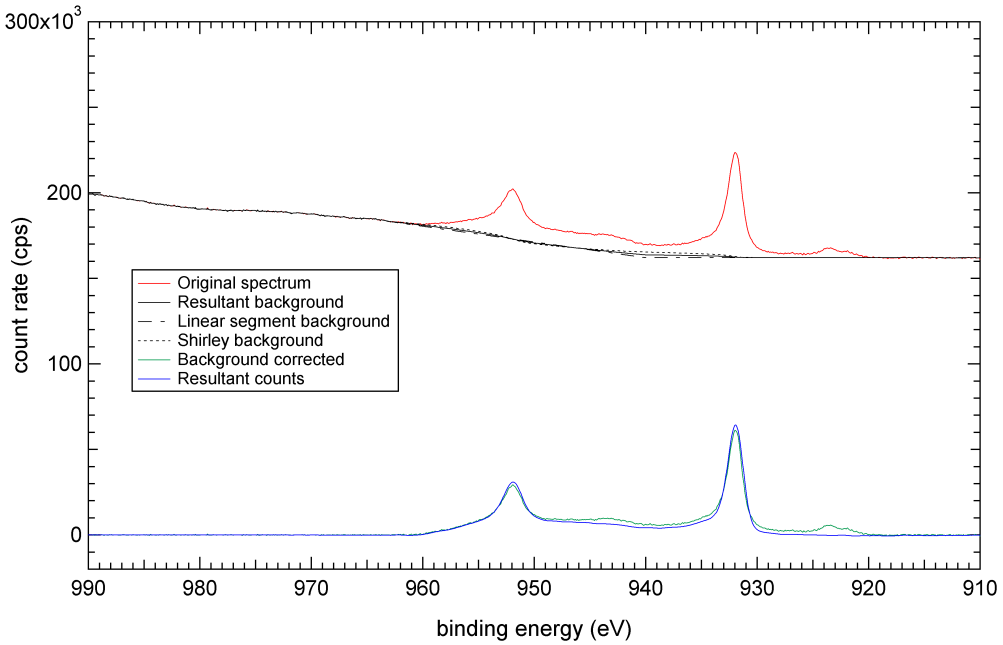

Figure C.36: *Cu 2p spectrum of chalcopyrite (Con-p) after oxidative dissolution in 0.2 M ferric chloride (pH 1.3) at 50° C for 2 hours.*

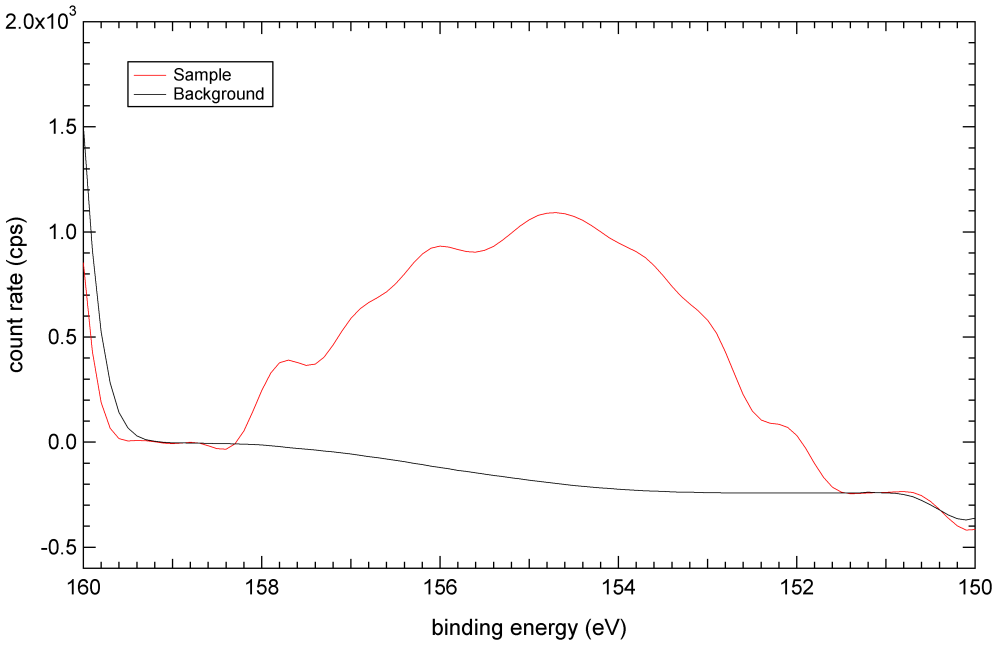

Figure C.37: *Si 2s spectrum of chalcopyrite (Con-p) after oxidative dissolution in 0.2 M ferric chloride (pH 1.3) at 50° C for 2 hours.*

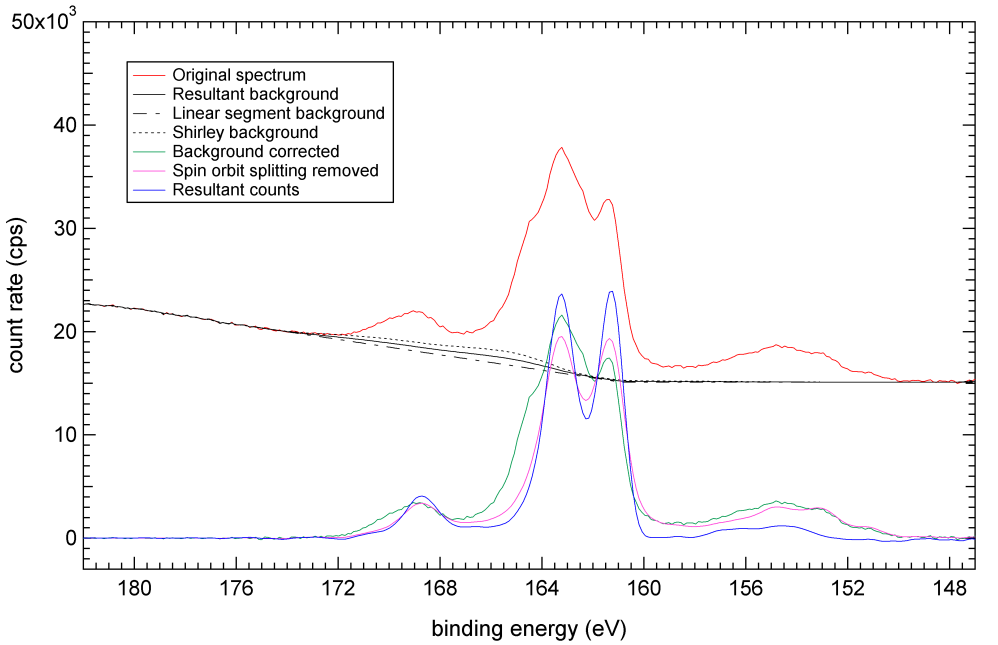

Figure C.38: *S 2p spectrum of chalcopyrite (Con-p) after oxidative dissolution in 0.2 M ferric chloride (pH 1.3) at 65° C for 2 hours.*

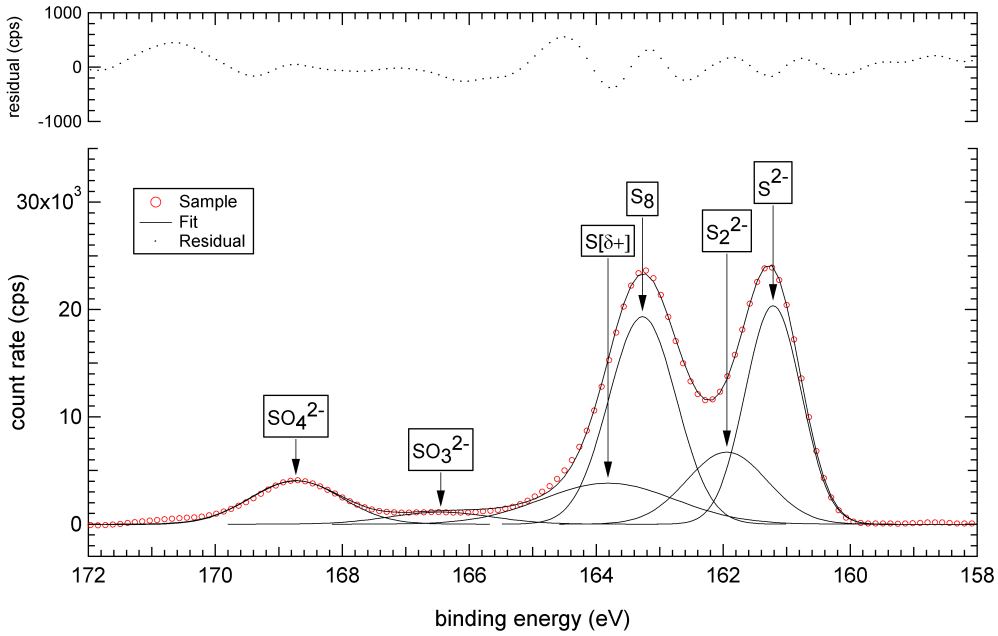

Figure C.39: *Fit of the S 2p spectrum of chalcopyrite (Con-p) after oxidative dissolution in 0.2 M ferric chloride (pH 1.3) at 65° C for 2 hours.*

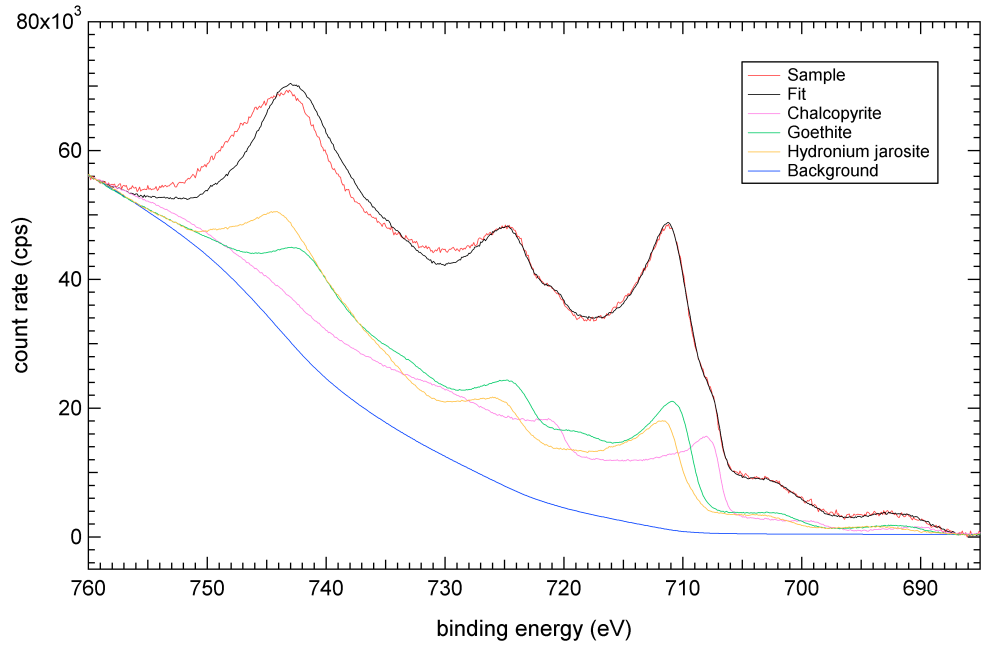

Figure C.40: *Fit of the Fe 2p spectrum of chalcopyrite (Con-p) after oxidative dissolution in 0.2 M ferric chloride (pH 1.3) at 65° C for 2 hours.*

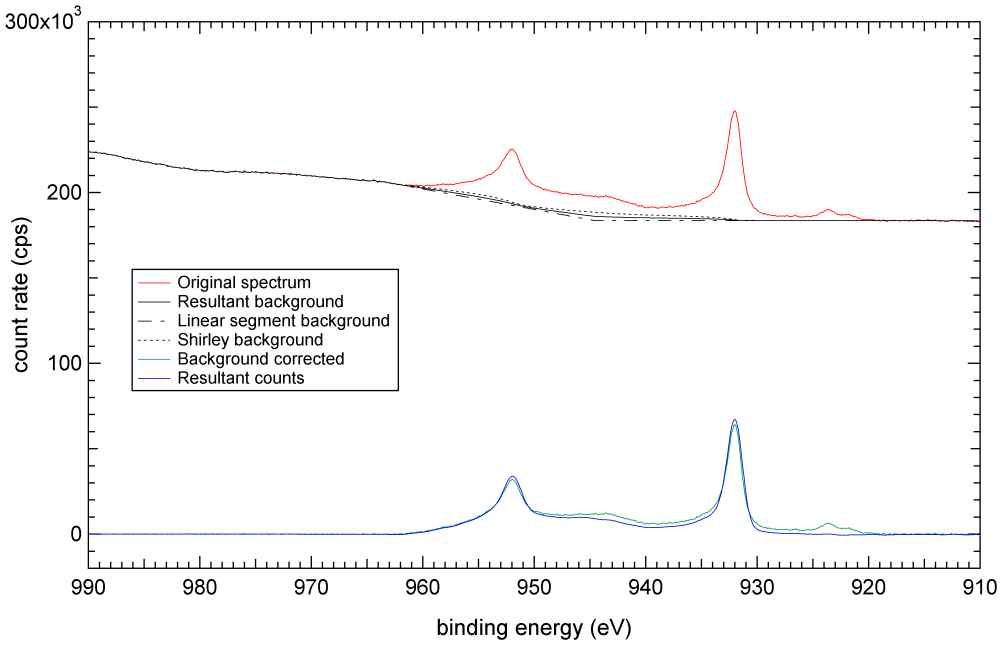

Figure C.41: *Cu 2p spectrum of chalcopyrite (Con-p) after oxidative dissolution in 0.2 M ferric chloride (pH 1.3) at 65° C for 2 hours.*

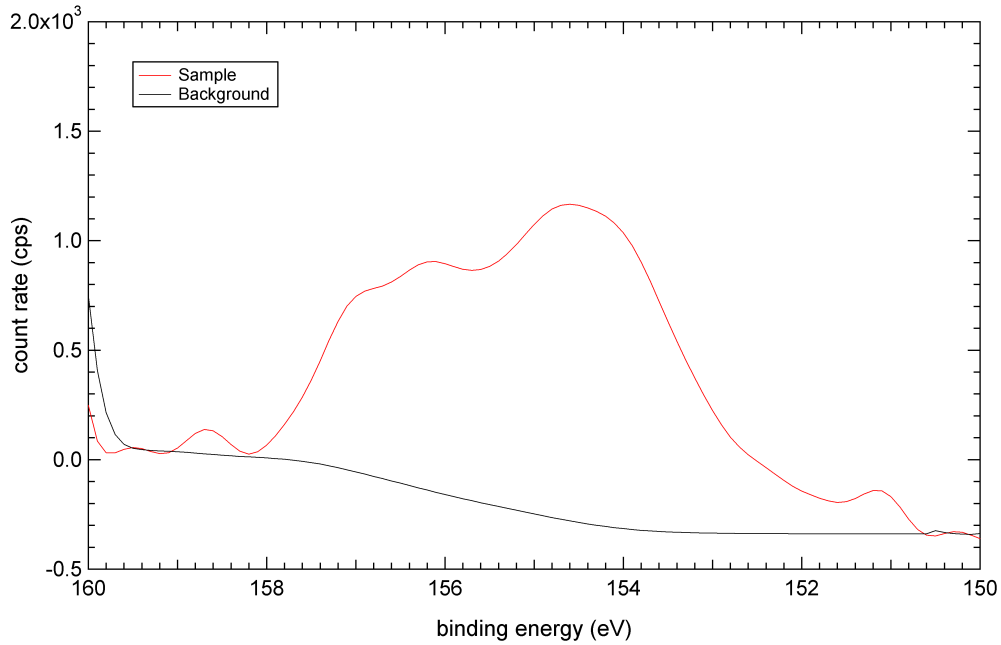

Figure C.42: *Si 2s spectrum of chalcopyrite (Con-p) after oxidative dissolution in 0.2 M ferric chloride (pH 1.3) at 65° C for 2 hours.*

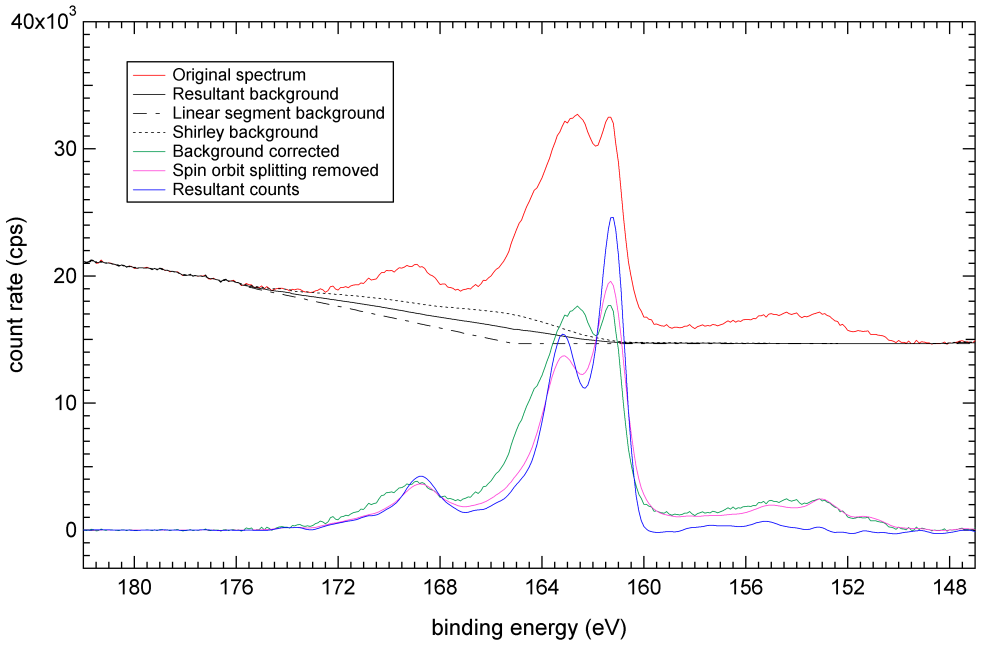

Figure C.43: *S 2p spectrum of chalcopyrite (Con-p) after oxidative dissolution in 0.2 M ferric chloride (pH 1.3) at 80° C for 2 hours.*

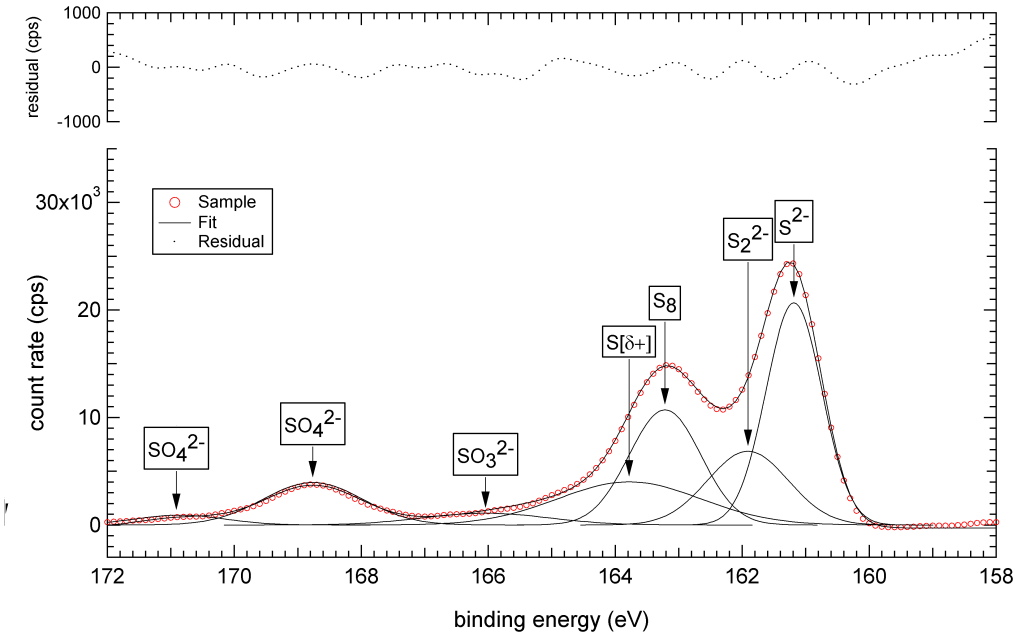

Figure C.44: *Fit of the S 2p spectrum of chalcopyrite (Con-p) after oxidative dissolution in 0.2 M ferric chloride (pH 1.3) at 80° C for 2 hours.*

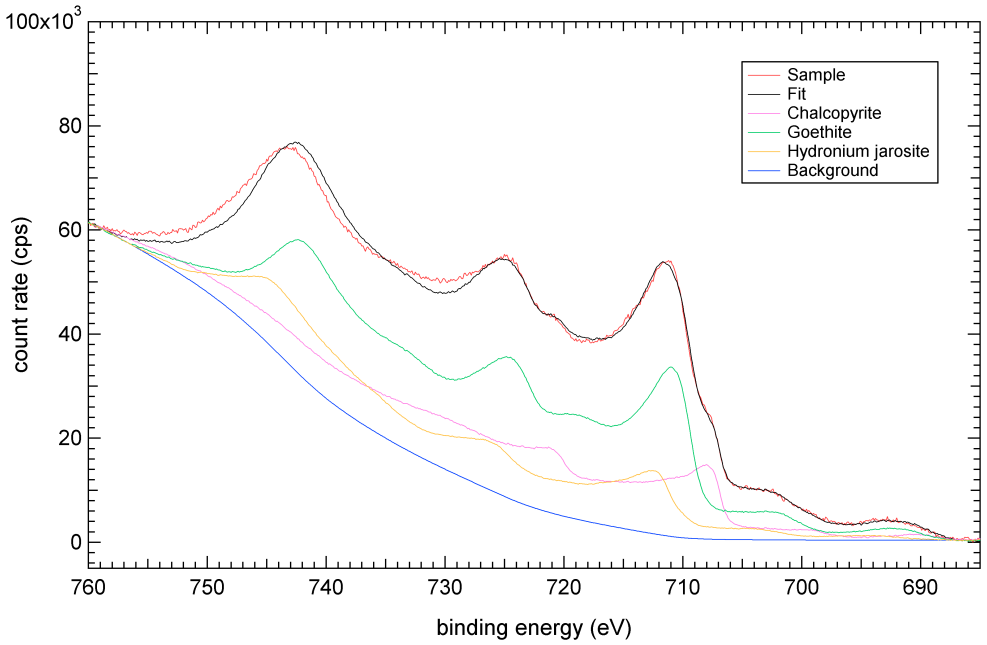

Figure C.45: *Fit of the Fe 2p spectrum of chalcopyrite (Con-p) after oxidative dissolution in 0.2 M ferric chloride (pH 1.3) at 80° C for 2 hours.*

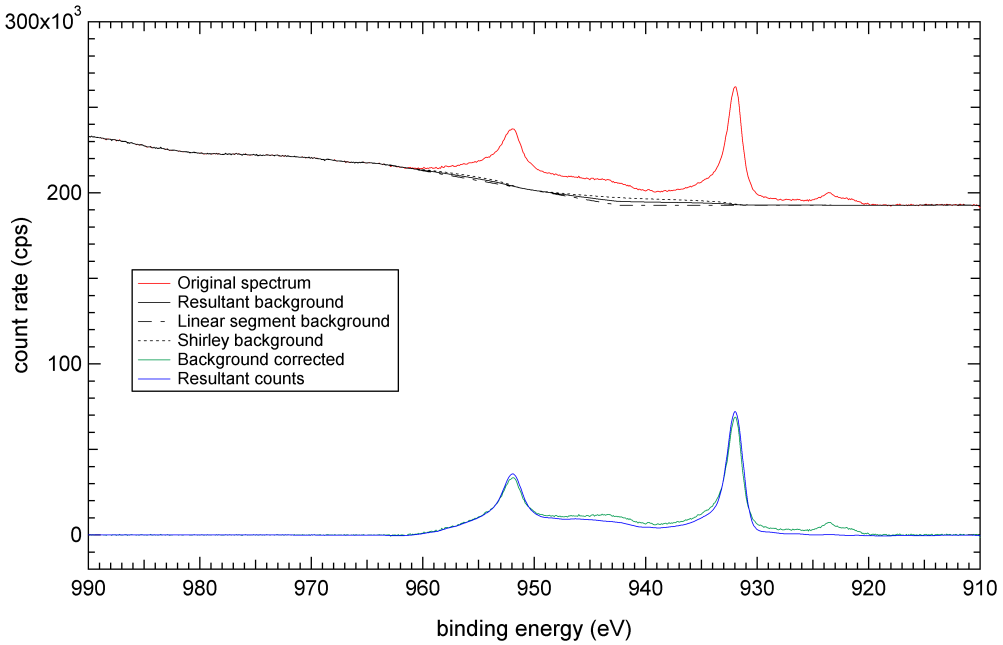

Figure C.46: *Cu 2p spectrum of chalcopyrite (Con-p) after oxidative dissolution in 0.2 M ferric chloride (pH 1.3) at 80° C for 2 hours.*

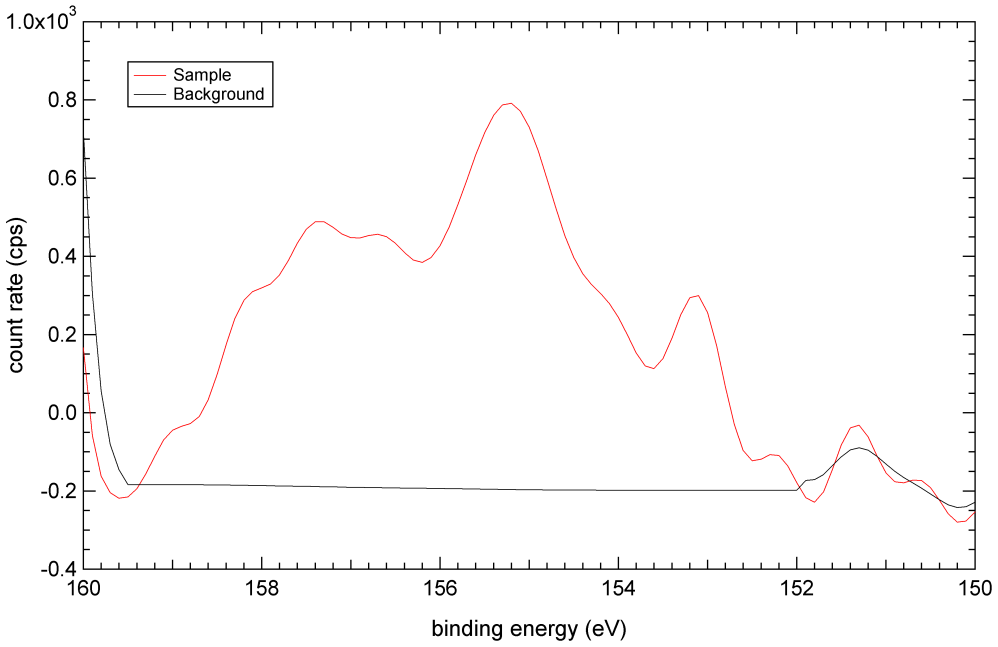

Figure C.47: *Si 2s spectrum of chalcopyrite (Con-p) after oxidative dissolution in 0.2 M ferric chloride (pH 1.3) at 80° C for 2 hours.*

Appendix D

Cu $L_3M_{4,5}M_{4,5}$ spectral analysis

The Cu $L_3M_{4,5}M_{4,5}$ spectrum and Auger parameter of chalcopyrite after oxidative dissolution were analysed to determine if additional copper sulphides form. These analyses relied on the subtle changes in electronic environment that are discernable in Auger spectra. The Cu $L_3M_{4,5}M_{4,5}$ spectrum was selected because the intensity is solely derived from bulk chalcopyrite and surface reconstruction phases, rather than deposition phases. The analysis involved comparison of spectral lineshapes and Auger parameters for chalcopyrite samples after oxidation and monovalent copper sulphide standards, including chalcopyrite, bornite, covellite and chalcocite.

D.1 Chalcopyrite before oxidative dissolution

The Cu $L_3M_{4,5}M_{4,5}$ spectrum of the chalcopyrite standard displays a peak at $\sim$ 339 eV, which is not present in the bornite, covellite or chalcocite standards, despite the overall similarity of the lineshapes (Figures D.1 - D.4). This peak was present in aditional chalcopyrite standards and is attributed to the increased relative intensity of the ^{1}G contribution based on the predicted and observed positions for the atomic terms of copper metal (Yin et al., 1972). The atomic terms used for copper metal can be used for monovalent copper because both assume the d^8 electron configuration after photoionisation.

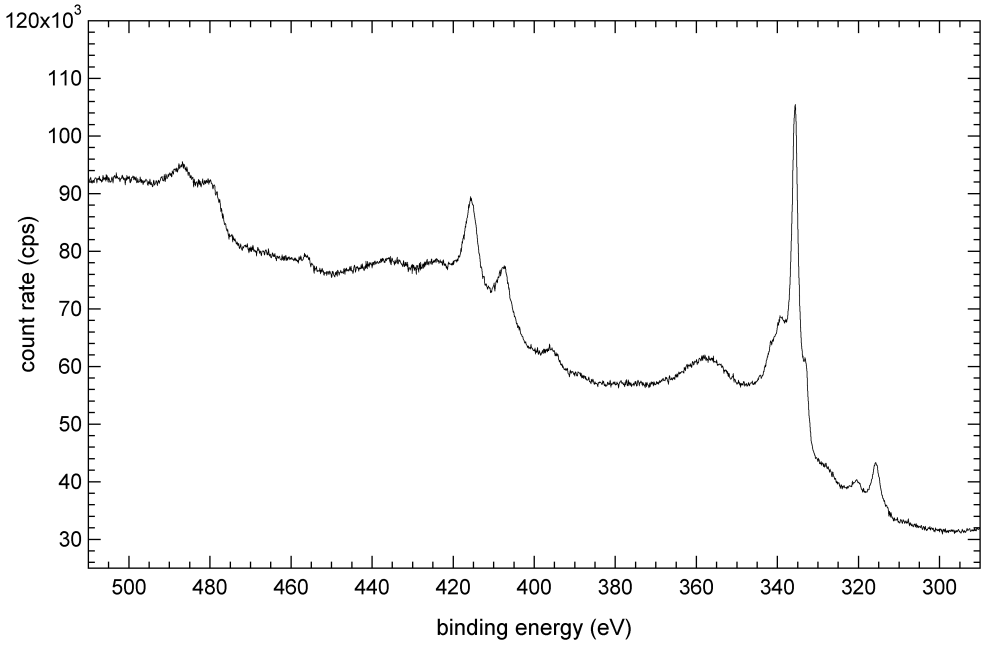

Figure D.1: *Cu $L_3M_{4,5}M_{4,5}$ spectrum of the chalcopyrite standard fractured under anaerobic atmosphere.*

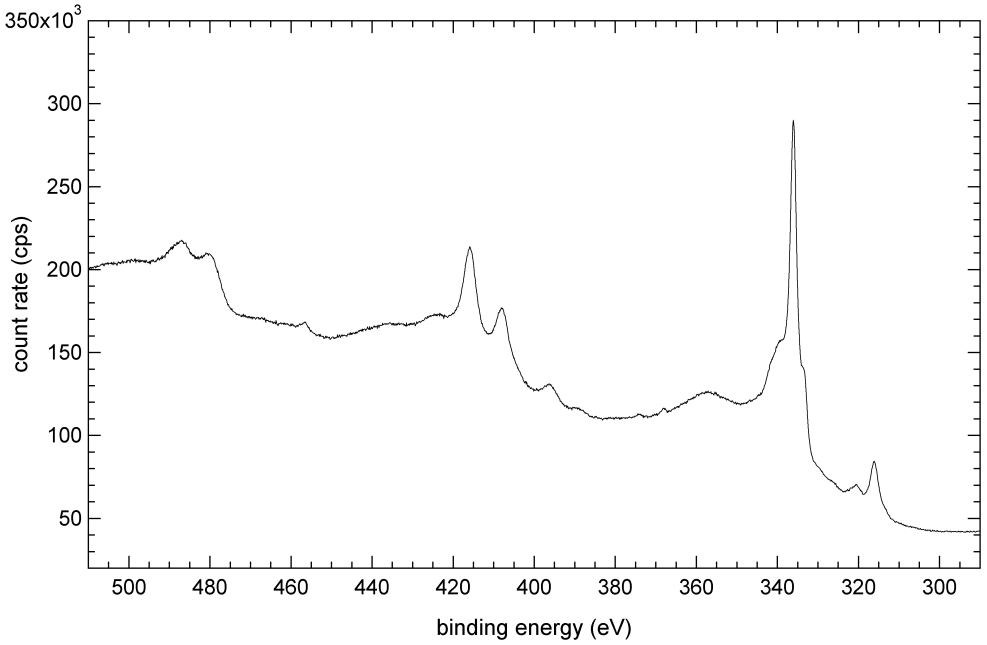

Figure D.2: *Cu $L_3M_{4,5}M_{4,5}$ spectrum of the bornite standard fractured under anaerobic atmosphere.*

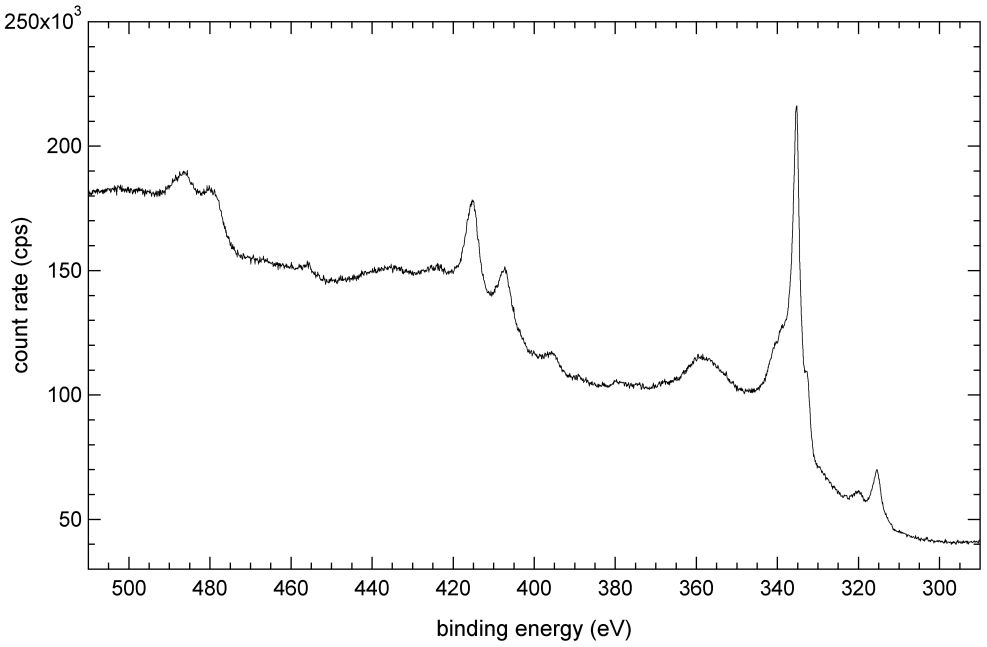

Figure D.3: *Cu $L_3M_{4,5}M_{4,5}$ spectrum of the covellite standard fractured under anaerobic atmosphere.*

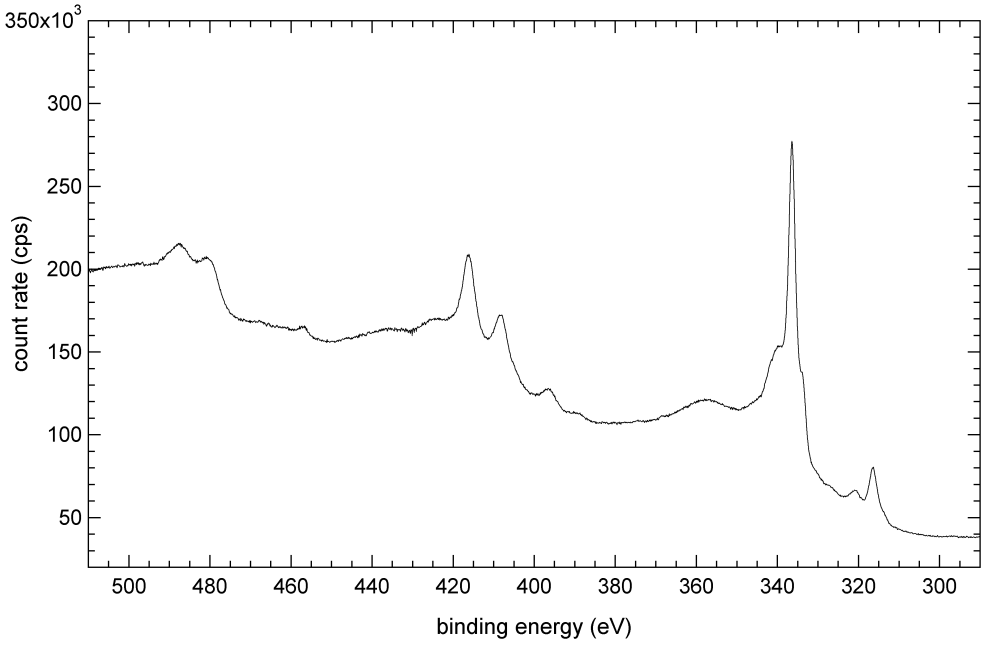

Figure D.4: *Cu $L_3M_{4,5}M_{4,5}$ spectrum of the chalcocite standard fractured under anaerobic atmosphere.*

The other contributions to the chalcopyrite Cu $L_3M_{4,5}M_{4,5}$ spectrum occur at binding energy separations that compare favourably with those reported for copper metal by Yin et al. (1972) (Table D.1).

Table D.1: *Binding energy separations (eV) of the L-S coupling interpretation of the Cu $L_3M_{4,5}M_{4,5}$ spectrum of chalcopyrite.*

Phase	^{1}**S**	^{1}**G**	^{3}**P**	^{1}**D**	^{3}**F**
Cu metal $_{(obs.)*}$	-4	-3	-2	0	3
Cu metal $_{(calc)*}$	-6	-1	-1	0	2
$CuFeS_2$ $_{(obs.)}{}^{\dagger}$	-6	-3	-	0	2

*The copper metal values are from Yin et al. (1972).

†The ^{3}P peak is not assigned because of the high intensity of the ^{1}D peak and the small separation predicted.

None of the fine structure is attributed to plasma losses because the binding energy separations observed are less than 13 eV below the parent line (Yin et al., 1972).

D.2 Chalcopyrite after oxidative dissolution

The Cu $L_3M_{4,5}M_{4,5}$ lineshapes of chalcopyrite massive (Mass-p) after oxidative dissolution in 0.1 M ferric sulphate (pH 1.9) at 50°C for up to 72 hours display the characteristic peak at $\sim$ 339 eV (Figures D.5 - D.9). The persistence of this peak suggests chalcopyrite remains the only copper sulphide present on the surface after oxidative dissolution. Chalcopyrite massive was investigated because the low surface area (relative to concentrate) was expected to produce slow dissolution kinetics and minimal phase deposition. Despite this precaution, the intensity of the peak at $\sim$ 339 eV becomes progressively weaker as a function of dissolution time. Therefore, further confirmation of chalcopyrite persistence was sought via analysis of the copper Auger parameter.

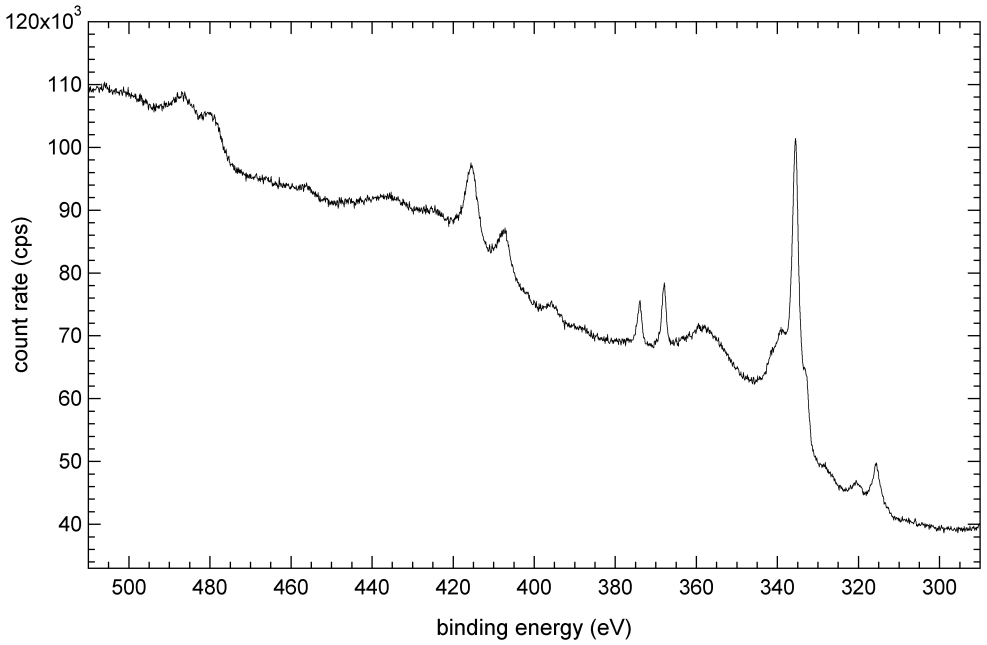

Figure D.5: *Cu $L_3M_{4,5}M_{4,5}$ spectrum of chalcopyrite (Mass-p) after oxidative dissolution in 0.1 M ferric sulphate (pH 1.9) at 50° C for 15 minutes.*

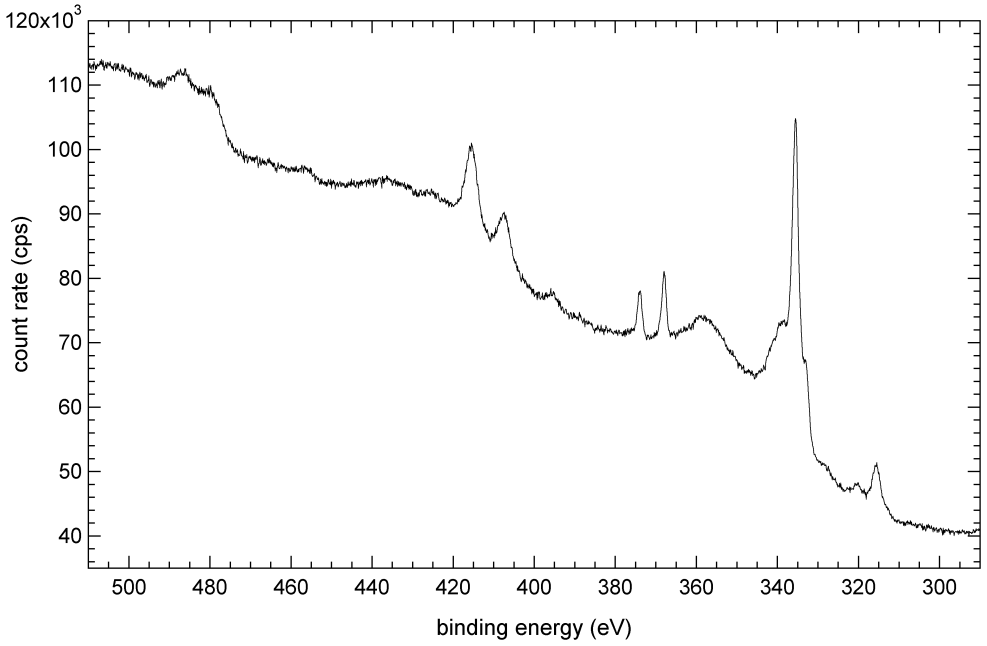

Figure D.6: *Cu $L_3M_{4,5}M_{4,5}$ spectrum of chalcopyrite (Mass-p) after oxidative dissolution in 0.1 M ferric sulphate (pH 1.9) at 50° C for 30 minutes.*

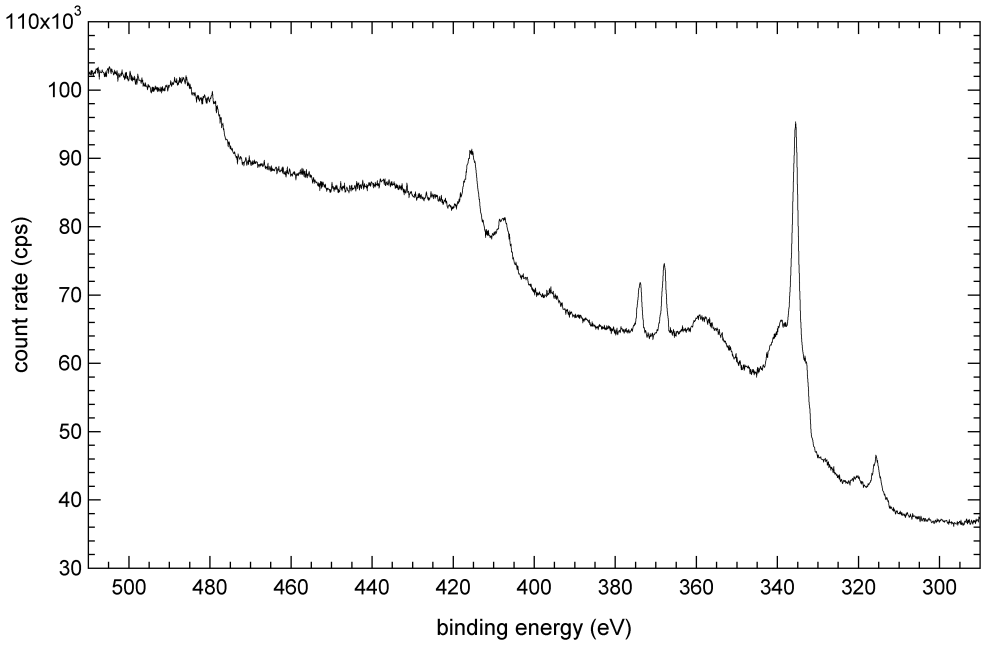

Figure D.7: *Cu $L_3M_{4,5}M_{4,5}$ spectrum of chalcopyrite (Mass-p) after oxidative dissolution in 0.1 M ferric sulphate (pH 1.9) at 50° C for 60 minutes.*

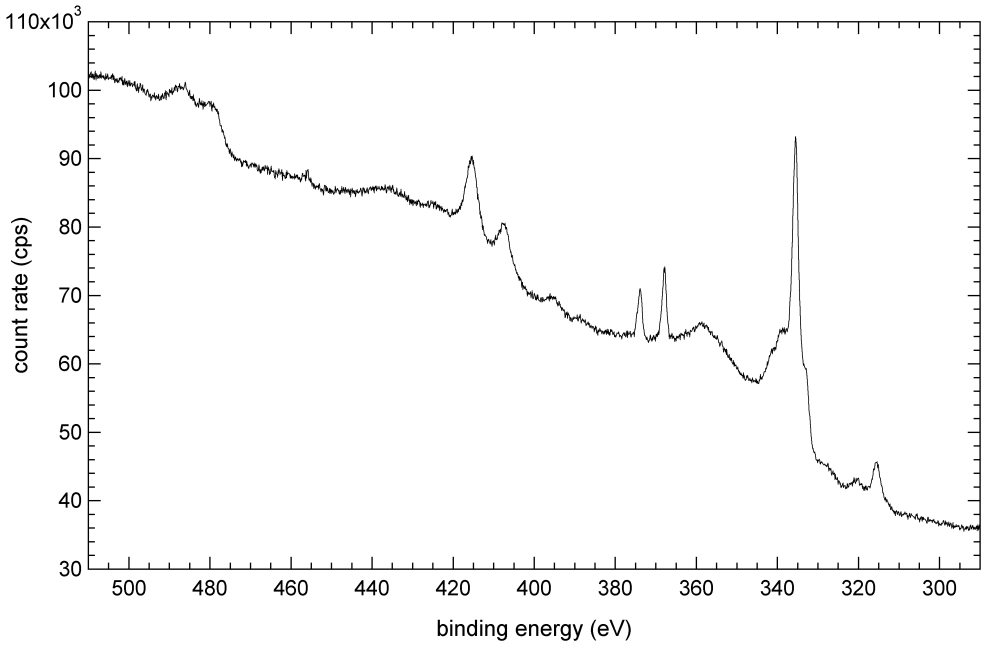

Figure D.8: *Cu $L_3M_{4,5}M_{4,5}$ spectrum of chalcopyrite (Mass-p) after oxidative dissolution in 0.1 M ferric sulphate (pH 1.9) at 50° C for 120 minutes.*

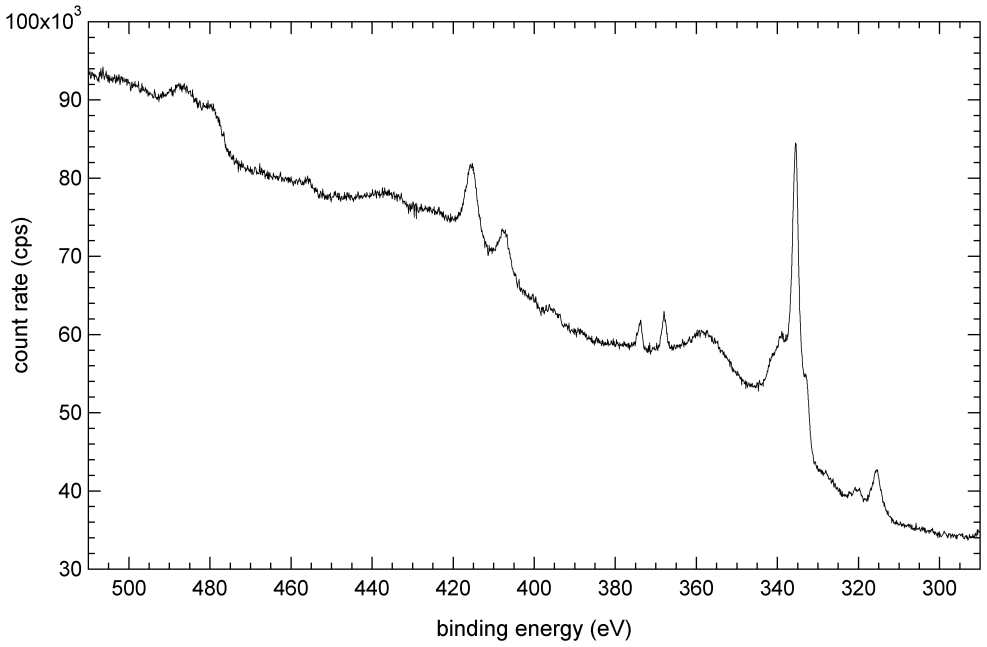

Figure D.9: *Cu $L_3M_{4,5}M_{4,5}$ spectrum of chalcopyrite (Mass-p) after oxidative dissolution in 0.1 M ferric sulphate (pH 1.9) at 50° C for 24 hours.*

D.3 Copper Auger parameter

The Auger parameter is defined as the kinetic energy separation between an Auger line and a photoelectron line (Klauber, 1995). The Cu $2p_{3/2}$ ($\sim$ 932 eV) and Cu $L_3M_{4,5}M_{4,5}$ ($\sim$ 336 eV) lines are commonly analysed because these are the most intense photoelectron and Auger lines. The Auger paramater is often used to distinguish copper phases because the extra atomic shifts caused by photoemission produce greater shifts in Auger lines than in photoelectron lines. Therefore, the changes in the binding energy separation between the Auger and photoelectron lines are greater than the changes in the binding energy of the photoelectron line. Because the Auger parameter is determined by separation, it is independent of sample charging. This is important for the analysis of chalcopyrite after oxidative dissolution because the phases depositing onto the surface are insulators that may cause charge shifting. The modified Auger parameter described by Wagner (1975) has not been used because it assumes an absence of charge shifting.

D.3.1 Chalcopyrite before oxidative dissolution

The copper Auger parameter of chalcopyrite before oxidative dissolution compares favourably with reported Auger parameters and reveals chalcopyrite can be distinguished from bornite, covellite and chalcocite (Table D.2).

Table D.2: *Copper Auger parameters (eV) observed and reported for copper sulphide standards.*

Phase	**Cu $2p_{3/2}$**	**Cu $L_3M_{4,5}M_{4,5}$**	**Auger parameter**	**Reference**
$CuFeS_2$	932.01	335.61	596.40	This study
$CuFeS_2$	931.8	335.35	596.45	Brion (1980)
Cu_5FeS_4	932.20	336.00	596.20	This study
CuS	931.96	335.36	596.60	This study
CuS	932.1	335.5	596.6	Brion (1980)
CuS	932.4	335.4	597.0	Chawla et al. (1992)
Cu_2S	932.45	336.35	596.10	This study
Cu_2S	932.3	336.0	596.3	Wagner (1975)
Cu_2S	932.4	336.4	596.0	Brion (1980)
Cu_2S	932.5	335.5	597.0	Chawla et al. (1992)
Cu_2S	932.9	336.9	596.0	Deroubaix and Marcus (1992)

Note: Some reported data were converted from kinetic energy to binding energy, including data acquired with Al K_α and Mg K_α X-ray sources. The reported data presented is limited to calibrated samples. There were no reports of copper Auger parameters for bornite.

D.3.2 Chalcopyrite after oxidative dissolution

The copper Auger parameters of chalcopyrite after oxidative dissolution are consistent with chalcopyrite remaining the only copper sulphide (Table D.3). The closest additional sulphide in terms of copper Auger parameter is covellite; however, it is 0.2 eV higher than the observed Auger parameters for chalcopyrite after dissolution (Table D.3).

Table D.3: *Copper Auger parameters (eV) observed for chalcopyrite after oxidative dissolution in ferric media.*

Sample	Lixiviate	T (°C)	pH	time (h)	Cu $2p_{3/2}$	Cu $L_3M_{4,5}M_{4,5}$	Auger para.
Mass-p	$Fe_2(SO_4)_3$	50	1.9	24	932.00	335.62	596.38
Mass-p	$Fe_2(SO_4)_3$	50	1.9	2	932.00	335.61	596.39
Con-p	$Fe_2(SO_4)_3$	50	1.9	2	932.01	335.61	596.40
Con-p	$FeCl_3$	50	1.3	2	932.04	335.66	596.38
Con-p	$FeCl_3$	50	1.5	2	932.04	335.62	596.42

D.4 Summary

The Cu $L_3M_{4,5}M_{4,5}$ spectra of chalcopyrite after oxidative dissolution were consistent with no additional copper sulphides forming. Discrimination of the chalcopyrite standards from other copper sulphide standards was possible because of the increased intensity of the ^1G peak at $\sim$ 339 eV. Although this peak became obscured as phases deposited on the surface, determination of the copper Auger parameter confirmed chalcopyrite remained the only copper sulphide present.

Appendix E

Ferric sulphate hydrolysis

Analysis of the S 2p and Fe 2p spectra provided insight into iron hydrolysis during oxidative dissolution of chalcopyrite in ferric media. The Fe 2p spectra revealed the presence of hydronium jarosite and goethite, exclusively. However, the S 2p spectra revealed sulphite and sulphate not associated with hydronium jarosite. Iron hydrolysis reports have been reviewed to establish the associations of the sulphate and sulphite identified in the S 2p spectra, while maintaining the speciation identified in the Fe 2p spectra.

Hydrolysis of ferric sulphate produces hydronium jarosite, goethite and $Fe_4(SO_4)(OH)_{10}$ (Dutrizac, 1980; Music et al., 1994). The phase composition depends on the temperature, pH and concentration of the solution. At 90°C, goethite is favoured at low (0.03 M) ferric sulphate concentration and hydronium jarosite is favoured at high (0.10 M) ferric sulphate concentration. This is consistent with the stability diagram proposed by Das et al. (1996) because high ferric concentrations produce a lower pH and hence favour jarosite formation (Figure 2.5). At 120°C, goethite remains favoured at low (0.03 M) ferric sulphate concentration, but at the higher (0.1 M) ferric sulphate concentration hydronium jarosite and $Fe_4(SO_4)(OH)_{10}$ are favoured (Music et al., 1994). The formation of $Fe_4(SO_4)(OH)_{10}$ at the higher temperature is presumably caused by a depletion of sulphate after greater jarosite precipitation at elevated temperatures.

Although $Fe_4(SO_4)(OH)_{10}$ has been described as $Fe_2O_3.SO_3.5H_2O$, based on the thermal analysis studies of Walter-Levy and Quemeneur (1968), it is more likely the iron sulphate is actually goethite (FeOOH) with sulphate either incorporated during formation, adsorbed after formation, or both (Davey and Scott, 1975; Peak et al., 1999). Sulphate incorporation during formation and sulphate adsorption after formation have been confirmed with sulphate in the inner and outer spheres of goethite identified by infrared spectroscopy (Music et al., 1993). The incorporation of sulphate during formation is caused by iron sulphate complexes (e.g., $Fe(OH)(H_2O)_4(SO_4)^+$) becoming incorporated with the growing iron oxide polymer (Section 7.2.1). The relatively high sulphate of a ferric sulphate solution favours the presence of iron sulphate complexes (Bhappu et al., 1969; Magini, 1979). The adsorption of sulphate after formation occurs with simultaneous protonation of the sulphate and the goethite surface (Hingston et al., 1972). Thus, adsorption of sulphate onto goethite is favoured at low pH (Music et al., 1993). The incorporation and adsorption of sulphate accounts for the presence of iron oxide associated with sulphate, but does not require the presence of an iron oxide (Fe_2O_3) that is unstable under the experimental conditions (Figure 2.5). Furthermore, analysis of the Fe 2p spectra of chalcopyrite performed in this study consistently discriminated against hematite (Fe_2O_3) and magnetite (Fe_3O_4) in favour of goethite (FeOOH).

The identification of sulphite in the S 2p spectra (Section 5.4.1) suggests sulphite is associated with goethite and is either incorporated during formation, adsorbed after formation, or both. Although the incorporation of sulphite during formation has not been reported, the adsorption of sulphite onto iron oxide/oxyhydroxide residing on the surface of oxidised chalcopyrite has been studied with XPS by Grano et al. (1997). Sulphite adsorption at low pH is consistent with the mechanism of sulphate adsorption and the stability of (bi)sulphite at low pH (Figure 2.4). Grano et al. (1997) concluded sulphite is oxidised to sulphate, while the ferric ions of the iron oxide/oxyhydroxide are reduced to ferrous. Because ferrous ions are more soluble than ferric ions, there is a commensurate decrease in iron oxide/oxyhydroxide on the surface. Although a decrease in iron oxyhydroxide on the surface is apparent in the Fe 2p spectra of Grano et al.

(1997), a residual amount remains. Basset and Parker (1951) propose the sulphite-iron oxyhydroxide reaction occurs via a ferric-sulphite complex intermediate [$Fe(SO_3)_2^-$]. However, there is no evidence of this complex in the Fe 2p spectra of chalcopyrite after oxidative dissolution in this study (Appendix C). It is therefore concluded some of the sulphite adsorbed onto goethite is oxidised to sulphate, but a residual amount remains adsorbed onto goethite on the chalcopyrite surface.

Iron hydrolysis reports reveal hydronium jarosite and goethite are the phases expected during oxidative dissolution of chalcopyrite in ferric media. Although another phase [$Fe_4(SO_4)(OH)_{10}$, aka $Fe_2O_3.SO_3.5H_2O$] has been reported at high temperatures and high ferric sulphate concentrations, it is likely this phase is simply goethite with sulphate either incorporated during formation, or adsorbed after formation, or both. A similar mechanism is proposed for sulphite. These interpretations are consistent with the S 2p and Fe 2p spectra of chalcopyrite after oxidative dissolution in ferric media.